

NUMERICAL MODELING AND SEISMIC PERFORMANCE ASSESSMENT
OF STEEL ECCENTRICALLY BRACED FRAMES WITH SHORT AND LONG
LINKS

A THESIS SUBMITTED TO
THE GRADUATE SCHOOL OF NATURAL AND APPLIED SCIENCES
OF
MIDDLE EAST TECHNICAL UNIVERSITY

BY

ELİF MÜGE ÜN

IN PARTIAL FULFILLMENT OF THE REQUIREMENTS
FOR
THE DEGREE OF DOCTOR OF PHILOSOPHY
IN
CIVIL ENGINEERING

JUNE 2022

Approval of the thesis:

**NUMERICAL MODELING AND SEISMIC PERFORMANCE
ASSESSMENT OF STEEL ECCENTRICALLY BRACED FRAMES WITH
SHORT AND LONG LINKS**

submitted by **ELİF MÜGE ÜN** in partial fulfillment of the requirements for the degree of **Doctor of Philosophy in Civil Engineering, Middle East Technical University** by,

Prof. Dr. Halil Kalıpçılar
Dean, Graduate School of **Natural and Applied Sciences**

Prof. Dr. Erdem Canbay
Head of the Department, **Civil Engineering**

Prof. Dr. Cem Topkaya
Supervisor, **Civil Engineering, METU**

Examining Committee Members:

Prof. Dr. Murat Altuğ Erberik
Civil Engineering, METU

Prof. Dr. Cem Topkaya
Civil Engineering, METU

Prof. Dr. Eray Baran
Civil Engineering, METU

Assoc. Prof. Dr. Saeid Kazemzadeh
Civil Engineering, Atılım University

Asst. Prof. Dr. Burcu Güldür Erkal
Civil Engineering, Hacettepe University

Date: 08.06.2022

I hereby declare that all information in this document has been obtained and presented in accordance with academic rules and ethical conduct. I also declare that, as required by these rules and conduct, I have fully cited and referenced all material and results that are not original to this work.

Name Last name : Elif Müge Ün

Signature :

ABSTRACT

NUMERICAL MODELING AND SEISMIC PERFORMANCE ASSESSMENT OF STEEL ECCENTRICALLY BRACED FRAMES WITH SHORT AND LONG LINKS

Ün, Elif Müge
Doctor of Philosophy, Civil Engineering
Supervisor : Prof. Dr. Cem Topkaya

June 2022, 192 pages

EBF links are classified into three categories as: short, intermediate and long links in terms of the normalized link length. Short links that primarily yield under shear, are usually preferred in eccentrically braced frames (EBFs) due to their high rotation and energy dissipation capacities. Long links that yield under flexure, can be used in cases where large openings are required for architectural reasons. This thesis investigates different aspects of short and long links in three independent parts.

In the first part, the effects of strain hardening ratio (SHR) on the performance assessment of eccentrically braced frame (EBF) buildings with short links were studied by using FEMA P-58 methodology. The numerical model was validated using the pseudo-dynamic test results of the DUAREM structure. Seismic performance of six archetype EBFs with different number of stories and link length to bay width (e/L) ratios were evaluated under design basis earthquake (DBE), maximum considered earthquake (MCE), and collapse level earthquake (CLE). Irreparable residual drift, repair cost and unsafe placards were calculated for SHR ranging between 0 and 0.01. The results showed that the residual interstory drift ratio is more influenced by the SHR when compared with the interstory drift ratio, link

rotation angle and story acceleration. The replacement decision was found to depend on the SHR, the number of stories, the e/L ratio, and the seismic hazard. The study demonstrated the strong influence and sensitivity of the repair cost to the SHR.

Long link behavior differs from the behavior of short links because the former is governed by flexure and subjected to significant amounts of strength and stiffness degradation. In the second part, a numerical study was undertaken to evaluate the seismic response factors for EBFs with long links using FEMA P695 methodology. Twenty-four EBF archetypes were designed by considering the bay width, number of stories, the link length to bay width (e/L) ratio and column base condition as the variables. Performances of these archetypes were evaluated under maximum considered earthquake (MCE), and collapse level earthquake (CLE). The effects of degradation were studied by considering degrading and non-degrading responses separately.

A nonsymmetrical loading protocol for long links was developed in the last part of the thesis. Twenty-four long link EBF archetypes with variable floor plans, bay widths, number of stories and link length to bay width (e/L) ratios were designed according to the US standards. The responses of EBFs under maximum considered earthquake (MCE) and collapse level earthquake (CLE) were obtained by making use of numerical analysis employing degrading link models. The link rotation angle time histories were reduced and converted into a series of cycles and the peaks of the LRA response were identified by using the rainflow counting algorithm. The nonsymmetrical loading protocol was represented as a function of maximum rotation range, which depends on the seismic hazard and e/L ratio.

Keywords: Eccentrically Braced Frames, Strain Hardening Ratio, Short Links, Long Links, Load Protocols

ÖZ

KISA VE UZUN BAĞ KİRİŞLİ DIŞMERKEZ ÇAPRAZLI ÇELİK ÇERÇEVELERİN NÜMERİK MODELLENMESİ VE PERFORMANS DEĞERLENDİRMESİ

Ün, Elif Müge
Doktora, İnşaat Mühendisliği
Tez Yöneticisi: Prof. Dr. Cem Topkaya

Haziran 2022, 192 sayfa

Dışmerkez çaprazlı çerçevelerin (*DÇÇ*) bağ kirişleri kısa, orta ve uzun bağ kirişleri olmak üzere üç sınıfa ayrılmıştır. Yüksek dönme açısı ve enerji emme kapasitelerinden dolayı *DÇÇ*'lerde tercih edilen kısa bağ kirişleri, genel olarak kesme kuvveti altında akarlar. Genel olarak eğilme kuvveti altında akan uzun bağ kirişleri ise sağladığı geniş açıklıklar sebebiyle *DÇÇ*'lerde mimari açıdan tercih edilmektedir. Bu tez çalışması, kısa ve uzun bağ kirişlerini üç bağımsız çalışmada farklı açılardan incelemiştir.

Birinci kısımda, FEMA P-58 metodolojisi kullanılarak, gerinim sertleşme değerinin (*GSD*), kısa bağ kirişli *DÇÇ* çelik yapıların performansı üzerindeki etkileri çalışılmıştır. Nümerik model, DUAREM yapısının benzeşik-dinamik test sonuçları kullanılarak doğrulanmıştır. Farklı kat yüksekliği ve bağ kiriş uzunluğu-açıklık oranına (*e/L*) sahip altı *DÇÇ* çelik arketip yapının sismik performansı geliştirilmiştir. Tamir edilemez kalıcı görelî kat ötelenmesi, tamir masrafı ve yapının mühürlenme ihtimali, 0 ve 0.01 değerleri arasındaki *GSD* kullanılarak hesaplanmıştır. Sonuçlar, *GSD* değerindeki değişimin; kalıcı görelî kat ötelenmesi değerini, görelî kat ötelenmesi, bağ kiriş dönme talebi ve kat ivmesine göre daha fazla etkilendiğini

göstermektedir. Eğer görelî kat ötelenmeleri dikkate alınîrsa, *GSD* deęerinin tamir masrafı üzerinde önemli bir etkisi bulunduęu gözlemlenmiştir.

Uzun baę kirişlerinin davranışı kısa baę kirişlerine göre farklılık göstermektedir. Uzun baę kirişleri genellikle eğilme kuvveti altında akarlar ve önemli miktarlarda mukavemet ve rijitlik azalımına maruz kalırlar. İkinci kısımda, uzun baę kirişli *DÇÇ*'lerin sismik davranışı, FEMA P695 metodolojisi kullanılarak incelenmiştir. Farklı açıklık, kat yükseklikleri, baę kirişi uzunluęu-açıklık oranları (e/L) ve farklı mesnet koşulları düşünülerek 24 adet *DÇÇ* çelik arketip yapı tasarlanmıştır. Bu arketiplerin sismik performansları maksimum ve çökme depremleri altında incelenmiştir. Mukavemet ve rijitlik azalımının etkisi, azalımın-varsayıldığı ve azalımın-varsayılmadığı modeller kullanılarak çalışılmıştır.

Çalışmanın son kısmında, uzun baę kirişleri için simetrik olmayan bir yükleme protokolü geliştirilmiştir. Farklı kat planı, açıklık, kat yükseklikleri, baę kirişi uzunluęu-açıklık oranları (e/L) ve farklı mesnet koşulları düşünülerek Amerikan standartlarına göre 24 adet *DÇÇ* çelik arketip yapı tasarlanmıştır. Mukavemet ve rijitlik azalımının modellendięi modeller ile, tasarlanan *DÇÇ*'lerin maksimum ve çökme depremleri altındaki performansı analiz edilerek nümerik olarak elde edilmiştir. Çevrim sayma metodu kullanılarak, baę kiriş dönme talebi zaman tanım alanı deęerleri azaltılmış ve bu deęerlerin çevrim sayıları ve pik deęerleri belirlenmiştir. Simetrik olmayan yükleme protokolü, maksimum dönme talep aralığı, sismik tehlike ve e/L oranının fonksiyonu olarak tanımlanmıştır.

Anahtar Kelimeler: Dış merkezli çelik çapraz çerçeveler, Gerinim sertleşme deęeri, Kısa baę kirişi, uzun baę kirişi, yükleme protokolü

To my mother

ACKNOWLEDGMENTS

I would like to express my deepest gratitude to my supervisor Prof. Dr. Cem Topkaya. I cannot put into words how lucky I feel for studying with him. His guidance and support illuminated every moment of this work. He is one of the most brilliant, smart, understanding, and supportive people I know and the best supervisor I could imagine. It seems like an understatement no matter how much I thank him.

I would also like to thank my thesis monitoring committee members, and the examining committee members one by one for their precious time and comments.

I would like to express my appreciation to Prof. Dr. Musab Aied Qissab Al-Janabi for the great collaborative work we have carried out in this period. I am honored to take a part in these studies.

I owe my deep gratitude to Dr. Burhan Aleessa Alam for his endless encouragement and care throughout this period. Working with him was one of the best parts of my academic career. I am indebted so much to my dear friend Bilgin Koçak who helped me a lot to prepare my post-processor tools which accelerated my analyses. I would also like to thank my friend Dr. Ahmet Kuşyılmaz for his valuable time whenever I needed his support.

I have been partially supported by the Scientific and Technological Research Council of Turkey (TUBITAK) throughout this period under grant number TUBITAK 2211-A and I would like to express my sincere acknowledgment to TUBITAK for this support.

I would like to thank my husband, Engin Balıkçı for his endless support to complete my thesis. My gorgeous daughters Ela and Ada; thank you very much for your mature understanding of the time I stole from you despite your young age. I love you more than you can imagine. I would also want to thank my aunt Hasibe İmre for her everyday moral support. My deepest love belongs to all my family who deserves all the gratitude.

Finally, I dedicate this thesis to my lovely mother to thank her one last time. With all my heart and being, I am grateful to be her daughter.

TABLE OF CONTENTS

ABSTRACT	v
ÖZ.....	vii
ACKNOWLEDGMENTS.....	x
TABLE OF CONTENTS	xii
LIST OF TABLES	xvi
LIST OF FIGURES.....	xviii
LIST OF ABBREVIATIONS	xxiii
LIST OF SYMBOLS.....	xxiv
CHAPTERS	
1 INTRODUCTION.....	1
1.1 General.....	1
1.2 Objectives and Scope.....	3
1.3 Thesis Organization	5
2 EFFECTS OF CYCLIC STRAIN HARDENING ON PERFORMANCE OF ECCENTRICALLY BRACED FRAMES	7
2.1 Background.....	7
2.1.1 Performance Based Design.....	7
2.1.2 Summary of Past Research Considered the Effect of Strain Hardening Ratio on the Engineering Demand Parameters.....	13
2.1.3 Summary of Past Research on the Modeling of Structural Steel Members under Cyclic Loading	15

2.2	Modeling of Shear Links	23
2.3	Numerical Modeling of EBFs and Verification of Numerical Models	26
2.3.1	DUAREM Structure.....	26
2.4	Details of Parametric Study on Performance of EBF Archetypes	39
2.5	Results of Time History Analysis	42
2.5.1	Link Rotation Angle	43
2.5.2	Interstory Drift Ratio.....	46
2.5.3	Residual Interstory Drift Ratio.....	49
2.5.4	Story Acceleration	52
2.6	Seismic Performance Assessment of Archetypes	54
2.6.1	Probabilistic Distribution of Repair Cost.....	57
2.6.2	Irreparable Residual Drift	64
2.6.3	Unsafe Placards.....	65
2.7	Summary And Evaluation of Results	66
3	SEISMIC PERFORMANCE EVALUATION OF ECCENTRICALLY BRACED FRAMES WITH LONG LINKS USING FEMA P695 METHODOLOGY	69
3.1	Background	69
3.1.1	Summary of FEMA P-695 Methodology	69
3.1.2	Summary of Past Research on Long Links.....	72
3.1.3	Link Deterioration Model	80
3.2	Design of Archetypes	84
3.3	Numerical Modeling Details and Verification of Flexural Link Models .	91
3.4	Ground Motion Selection and Scaling	97

3.5	Results of Time History Analysis	98
3.5.1	Effects of Strength and Stiffness Degradation	98
3.5.2	Effect of Seismic Intensity	108
3.5.3	Effect of Floor Plan	115
3.5.4	Responses of All Archetypes.....	117
3.6	Remedial Measures.....	119
3.6.1	Modifications to the Response Modification Coefficient	120
3.6.2	Using Stocky Link Beams	122
3.6.3	Modifying Link Length to Bay Width Ratio.....	123
3.6.4	Support Conditions.....	125
3.6.5	Effect of Gravity Framing	128
3.7	Summary.....	130
4	DEVELOPMENT OF A LOADING PROTOCOL FOR LONG LINKS IN ECCENTRICALLY BRACED FRAMES	131
4.1	Background.....	131
4.1.1	Summary of Past Protocols on Structural Members.....	131
4.1.2	Loading Protocol Developed by Richards (2004) and Richards and Uang (2006).....	133
4.1.3	Loading Protocol Developed by Al-Janabi and Topkaya (2020)....	134
4.2	Archetype Development	135
4.3	Ground Motion Selection and Scaling:.....	140
4.4	Time History Analysis Results:	142
4.4.1	Representation of Time History Response as Ordered Cycles.....	143
4.4.2	Number of Cycles.....	144

4.4.3	Maximum Link Rotation Angle and Cumulative Damage	147
4.4.4	Maximum Rotation Range, Mean Rotation Range and Distribution of Cycles	150
4.5	Development of Nonsymmetrical Loading Protocols.....	153
4.6	Effects of Column Base Fixity and Link Axial Force.....	157
4.7	Future Research Needs.....	161
4.8	Summary	162
5	CONCLUSIONS.....	163
5.1	Conclusions on the Effects of Cyclic Strain Hardening on the Performance of Eccentrically Braced Frames.....	163
5.2	Conclusions on the Seismic Performance Evaluation of Eccentrically Braced Frames with Long Links using FEMA P695 Methodology	165
5.3	Conclusions on the Development of a Loading Protocol for Long Links in Eccentrically Braced Frames	167
	REFERENCES	169
	CURRICULUM VITAE.....	191

LIST OF TABLES

TABLES

Table 2.1 Summary of previous research on the SHR value.....	20
Table 2.2 Summary of Giuffre-Menegotto-Pinto material parameters proposed by past researchers.....	22
Table 2.3. Details of the Structural Steel components of the DUAREM Structure	28
Table 2.4. Comparison of Maximum Base Shear Values between the Experimental and Numerical Results.....	34
Table 2.5. Comparison of Maximum Story Displacement and Link Rotation Angle Values between the Experimental and Numerical Results.....	35
Table 2.6. Comparison of Maximum Residual Story Displacement and Link Rotation Angle Values between the Experimental and Numerical Results	35
Table 2.7. Archetype Properties and Scaling Factors.....	41
Table 2.8. Member Sizes of Archetypes	41
Table 2.9 Structural and nonstructural fragilities used in PACT Model.....	55
Table 3.1. Total LRA values of long links from previous experiments	84
Table 3.2. Archetype Properties and Scaling Factors.....	88
Table 3.3. Member Sizes of FP-I Archetypes	89
Table 3.4. Member Sizes of FP-II Archetypes	90
Table 3.5. Parameters of bilin material model	93
Table 3.6. Redesigned member sizes of AT1-I-R with $R=4$ $Cd=3$ and AT1-I-S with stocky link sections.....	121
Table 3.7. Member sizes of archetypes with $e/L=0.65$	124
Table 4.1. Archetype Properties and Scaling Factors.....	137
Table 4.2. Member Sizes of FP-I Archetypes	138
Table 4.3. Member Sizes of FP-II Archetypes	139
Table 4.4. Statistical measures for number of cycles, damage index (DI), and maximum LRA	145

Table 4.5. Statistical measures for rotation range and mean of the rotation range	149
Table 4.6. The statistical information on the ratio of response quantities (Fixed based archetype over pin-based archetype)	159

LIST OF FIGURES

FIGURES

Figure 1.1. A typical EBF configuration and deformation pattern.....	1
Figure 2.1. Cyclic Stress Strain Behavior for A36 steel and Dafalias and Popov's (1975) bounding surface plasticity model	15
Figure 2.2. Shear Force Deformation Relationship Proposed by Richards and Uang (2004 and 2006).....	24
Figure 2.3. Simulation of Link Response using Different Material Models and Cyclic Stress Strain Behavior of Structural Steel (a) Bilinear (b) Steel 02 (c) Multilinear	26
Figure 2.4. Experimental mock-up structure (Sabau et al. (2014)).....	27
Figure 2.5. South Frame of the DUAREM Structure	28
Figure 2.6. Acceleration time history for 15613_H2 record	29
Figure 2.7. Response spectrum of the selected scaled GM record versus target spectrum.	30
Figure 2.8. Comparison of Experimental and Numerical Results for Story Displacements.....	32
Figure 2.9. Comparison of Experimental and Numerical Results for Link Rotation Angles.....	33
Figure 2.10. Comparison of Experimental and Numerical Results for (a) Link Rotation Angle versus Link Shear at Story 1 (b) Link Rotation Angle versus Link Shear at Story 2 (c) Link Rotation Angle versus Link Shear at Story 3 (d) Base Shear-First Story Displacement.....	34
Figure 2.11. Effect of <i>SHR</i> on the Residual Response of the DUAREM Structure	37
Figure 2.12. Effect of <i>SHR</i> on the Maximum Response of the DUAREM Structure	38
Figure 2.13. Effect of <i>SHR</i> on the Maximum Base Shear of the DUAREM Structure	39

Figure 2.14. Floor Plan and Elevation View of Archetypes	40
Figure 2.15. Link Rotation Angle Response for AT1, AT5 and AT9 ($e/L=0.08$) .	44
Figure 2.16. Link Rotation Angle Response for AT3, AT7 and AT11 ($e/L=0.12$)	45
Figure 2.17. Effect of <i>SHR</i> on Normalized Link Rotation Angle.....	45
Figure 2.18. Interstory Drift Response for AT1, AT5 and AT9 ($e/L=0.08$).....	47
Figure 2.19. Interstory Drift Response for AT3, AT7 and AT11 ($e/L=0.12$).....	48
Figure 2.20. Effect of <i>SHR</i> on Normalized Interstory Drift.....	48
Figure 2.21. Residual Interstory Drift Response for AT1, AT5 and AT9 ($e/L=0.08$)	50
Figure 2.22. Residual Interstory Drift Response for AT3, AT7 and AT11 ($e/L=0.12$)	51
Figure 2.23. Effect of <i>SHR</i> on Normalized Residual Interstory Drift.....	51
Figure 2.24. Story Acceleration Response for AT1, AT5 and AT9 ($e/L=0.08$)....	52
Figure 2.25. Story Acceleration Response for AT3, AT7 and AT11 ($e/L=0.12$)..	53
Figure 2.26. Effect of <i>SHR</i> on Story Acceleration.....	53
Figure 2.27. Probabilistic Distribution of Repair Costs under DBE, MCE and CLE Level Seismic Events (3-story archetypes).....	59
Figure 2.28. Probabilistic Distribution of Repair Costs under DBE, MCE and CLE Level Seismic Events (6-story archetypes).....	60
Figure 2.29. Probabilistic Distribution of Repair Costs under DBE, MCE and CLE Level Seismic Events (9-story archetypes).....	61
Figure 2.30. Ratio of Median Repair Cost to Initial Cost.....	62
Figure 2.31. Comparison of the Ratio of Median Repair Cost to Initial Cost for EBFs with $e/L = 0.08$ and $e/L = 0.12$	63
Figure 2.32. Irreparable Residual Drift.....	64
Figure 2.33. Probabilistic Distribution of Repair Costs under MCE Level Seismic Events for AT5 (Irreparable Residual Drifts not Considered).....	65
Figure 2.34. Unsafe Placards	66
Figure 3.1. Link shear versus link rotation angle responses of short and long links	79

Figure 3.2. Modified IMK model: backbone deterioration curve for monotonic loading	80
Figure 3.3. Modified IMK model: basic modes of cyclic deterioration	81
Figure 3.4. Floor plans.....	85
Figure 3.5. Typical elevation view	86
Figure 3.6. Schematic diagram of OpenSees simplified model	92
Figure 3.7. Test setup used by Okazaki et al. (2005) and deformation pattern.....	95
Figure 3.8. Comparison of numerical simulation of degrading and non-degrading models with the experimental results	96
Figure 3.9. Static Pushover Curve of AT5-I.....	98
Figure 3.10. LRA versus LS interactions that belong to 1st story link of AT5-I under ground motion 2 (GM02) scaled to CLE10% for (a) degrading model and (b) non-degrading model.....	99
Figure 3.11. The variation of median Link Rotation Angle for 3 story FP-I archetypes	100
Figure 3.12. The variation of median Link Rotation Angle for 3 story FP-II archetypes	101
Figure 3.13. The variation of median Link Rotation Angle for 6 story FP-I archetypes	102
Figure 3.14. The variation of median Link Rotation Angle for 6 story FP-II archetypes	103
Figure 3.15. The variation of median Link Rotation Angle for 9 story FP-I archetypes	104
Figure 3.16. The variation of median Link Rotation Angle for 9 story FP-II archetypes	105
Figure 3.17. Ratios of LRA for degrading model over non-degrading model of 3 story FP-I and FP-II archetypes.....	106
Figure 3.18. Ratios of LRA for degrading model over non-degrading model of 6 story FP-I and FP-II archetypes.....	107

Figure 3.19. Ratios of LRA for degrading model over non-degrading model of 9 story FP-I and FP-II archetypes	108
Figure 3.20. Variation of LRA for 3 story FP-I archetypes under MCE, CLE20% and CLE10% events.....	109
Figure 3.21. Variation of LRA for 3 story FP-II archetypes under MCE, CLE20% and CLE10% events.....	110
Figure 3.22. Variation of LRA for 6 story FP-I archetypes under MCE, CLE20% and CLE10% events.....	111
Figure 3.23. Variation of LRA for 6 story FP-II archetypes under MCE, CLE20% and CLE10% events.....	112
Figure 3.24. Variation of LRA for 9 story FP-I archetypes under MCE, CLE20% and CLE10% events.....	113
Figure 3.25. Variation of LRA for 9 story FP-II archetypes under MCE, CLE20% and CLE10% events.....	114
Figure 3.26. Variation of median LRA of degrading model for 6 story FP-I and FP-II archetypes under MCE event	116
Figure 3.27. Variation of median LRA of degrading model for 6 story FP-I and FP-II archetypes under CLE20% event	116
Figure 3.28. Variation of median LRA of degrading model for 6 story FP-I and FP-II archetypes under CLE10% event	117
Figure 3.29. Median link rotation angle (LRA) for all archetypes	119
Figure 3.30. Variation of LRA under CLE10% level seismic hazard for AT12-I: a) Modification to response modification coefficient, b) Using stocky link beams .	121
Figure 3.31. Variation of LRA under CLE10% level seismic hazard for AT4-II: a) Modification to response modification coefficient, b) Using stocky link beams .	122
Figure 3.32. Variation of LRA under CLE10% level seismic hazard for $e/L=0.65$: a) 3 Stories b) 6 Stories c) 9 stories d) Maximum LRA values of all stories for FP-I and FP-II archetypes.	125
Figure 3.33. Median LRA distribution for fixed and pin-based 6 story archetypes of FP-I under CLE10% seismic hazard.....	127

Figure 3.34. Median LRA for fixed-based archetypes: a) Height wise distribution for 9-story buildings, b) Responses of all archetypes.....	127
Figure 3.35. Response of EBFs with gravity frames.....	130
Figure 4.1. Loading Protocols (a) Richards (2004) Loading Protocol for Long links (b) AISC 341-16 Protocol for Short Links	134
Figure 4.2. Loading protocol proposed for short links for $n_{max}=15$ (Al-Janabi and Topkaya (2020))	135
Figure 4.3. Floor plans.....	136
Figure 4.4. Floor plans.....	136
Figure 4.5. Nonlinear Static Pushover Curve of AT5-I.....	141
Figure 4.6. Scaling of the far-field record set for AT5-I.....	142
Figure 4.7. Time history analysis results for AT3-I: (a) link rotation versus time, (b) ordered symmetric cycles, and (c) ordered nonsymmetrical cycles	144
Figure 4.8. Number of cycles, maximum link rotation angle, and damage index.	147
Figure 4.9. Cycle range and mean of cycle range for the three most damaging cycles	151
Figure 4.10. Distribution of cycle ranges	153
Figure 4.11. Proposed loading protocol for long links.....	154
Figure 4.12. Distribution of cycle ranges and accumulation of damage with cycle number.....	155
Figure 4.13. Comparison of loading protocols.....	156
Figure 4.14. Behavior of Specimen 3 under different loading scenarios	157
Figure 4.15. Comparisons of the distribution of normalized cycle ranges of pin-based and fixed based archetypes.....	159
Figure 4.16. Normalized link axial forces for 6 story FP-I archetypes	160

LIST OF ABBREVIATIONS

ABBREVIATIONS

BRBF	Buckling Restrained Braced Frames
CBF	Concentrically Braced Frames
CLE	Collapse Level Earthquake
ACMR	Adjusted Collapse Margin Ratio
CMR	Collapse Margin Ratio
DBE	Design Basis Earthquake
D-EBF	Dual-Eccentrically Braced Frames
EBF	Eccentrically Braced Frames
EDP	Engineering Demand Parameters
IDR	Interstory Drift Ratio
LRA	Link Rotation Angle
LS	Link Shear
MCE	Maximum Considered Earthquake
MRF	Moment Resisting Frames
PSBD	Performance Based Seismic Design
RIDR	Residual Interstory Drift Ratio
SA	Story Acceleration
SDC	Seismic Design Category
SDOF	Single Degree of Freedom
SHR	Strain Hardening Ratio
YBS	Yielding Brace Systems

LIST OF SYMBOLS

SYMBOLS

ρ	normalized link length
γ_p	inelastic deformation of the link
θ_p	pre-capping plastic rotation
θ_{pc}	post-capping plastic rotation
θ_u	ultimate rotation capacity
θ_y	yield rotation
Ω_0	overstrength factor
μ_t	period based ductility
Λ	reference cumulative rotation capacity
δ_u	roof displacement
C_d	displacement amplification factor
b	flange width
d	depth of the section
E	modulus of elasticity
e	link length
F_y	yield stress
h	web depth
L	bay width
M_c	capping moment
M_p	plastic moment capacity
M_r	residual moment
M_y	effective yield moment
q	behavior factor
R	response modification coefficient
t_f	flange thickness
t_w	web thickness

V_{\max} maximum base shear capacity
 V_p plastic shear capacity
 W building weight
 Z plastic section modulus

CHAPTER 1

INTRODUCTION

1.1 General

An *eccentrically braced frame* (EBF) is a steel lateral load resisting system that consists of columns, link beams, beam segments outside the link, and braces. They can be considered as hybrid systems that are capable of integrating the benefits of concentrically braced frames (CBFs) having high initial stiffness and moment resisting frames (MRFs) having high energy dissipation capacity. Figure 1.1 shows the typical configuration and deformation pattern of an EBF. The energy dissipation is provided by the yielding of the link members, which are the short horizontal segments between the eccentrically configured braces. The stiffness, strength, ductility and performance of an EBF system can be modified by altering the length (e) of the link beam. All the other members are designed to remain elastic during a seismic event.

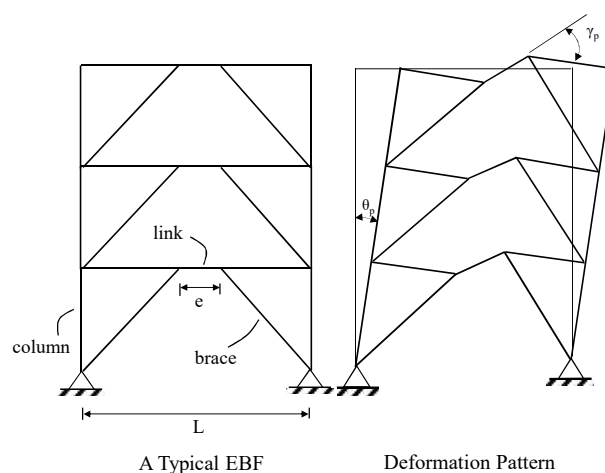


Figure 1.1. A typical EBF configuration and deformation pattern

EBF links are classified into three categories as: short, intermediate and long links in terms of the normalized link length $\rho = e/(M_p/V_p)$ where, M_p and V_p are the plastic moment and plastic shear capacities of I-shaped links respectively. These capacities can be calculated according to the AISC Seismic Provisions for Structural Steel Buildings (AISC 341-16) as follows:

$$M_p = ZF_y \quad (1.1)$$

$$V_p = 0.6F_y(d - 2t_f)t_w \quad (1.2)$$

where Z = plastic section modulus, d = depth of the section, t_f = flange thickness, t_w = web thickness, F_y = nominal yield strength. The inelastic rotation capacity of a link depends on its normalized link length (ρ) and the limits that distinguish link behavior depend on the specification being used. According to AISC341, short links ($\rho \leq 1.6$) predominantly yield in shear whereas long links ($\rho \geq 2.6$) predominantly yield in flexure. Intermediate links ($1.6 < \rho < 2.6$) yield in shear and flexure. A typical deformation pattern of an EBF is shown in Figure 1.1 where γ_p represents the inelastic deformation of the link and is defined as the plastic rotation angle between the link and the beam segment outside the link.

AISC Seismic Provisions for Structural Steel Buildings (AISC 341-16) and Eurocode 8 (2004) are one of the widely used design specifications which adopt a force-based design procedure for EBF systems. According to AISC341, the inelastic rotation limits are defined as $\gamma_p = 0.08$ rad for short links and $\gamma_p = 0.02$ rad for long links. Linear interpolation between 0.08 rad and 0.02 is used for intermediate links. Recent years have also witnessed the development of Performance Based Seismic Design (PBSD) procedures. Unlike traditional force-based designs, PBSD targets to satisfy predetermined damage levels under different performance levels.

Different EBF systems (short, intermediate and long) have particular advantages over each other. For example, short links perform considerably better than long links when subjected to cyclic loadings while long links provide more freedom for architectural design. Although past researchers have investigated EBF systems in

many different aspects, there still exists some research gaps for both short- and especially long-link EBF systems. This thesis consists of three independent studies considering either short- or long-link EBF systems, which aim to provide a contribution to a part of these areas with lack of research. The first part investigates the effects of strain hardening ratio (*SHR*) on the performance assessment of short link eccentrically braced frame (EBF) buildings by using FEMA P-58 methodology. The second part provides a comprehensive numerical evaluation of the seismic response factors for EBFs with long links using FEMA P695 methodology. The third part proposes a nonsymmetrical loading protocol for long-link EBFs. The objectives and scopes of each study are discussed separately in the following section.

1.2 Objectives and Scope

Strain hardening ratio (*SHR*) is defined as the ratio between post-yield stiffness and initial elastic stiffness, which can be calculated at the material level or member level. Past researchers have examined the effect of strain hardening ratio (*SHR*) on residual deformation demands of different types of steel structural systems and single degree-of freedom systems and concluded that the response is very sensitive to the *SHR*. These studies will be summarized in Chapter 2. However, there exists no study reported to date which focuses on a systematic evaluation of the strain hardening effects on the performance of EBF buildings.

The first objective of this thesis is to investigate the effect of strain hardening on the engineering demand parameters and performance of short-link EBFs by giving particular emphasis on residual deformations. Next-Generation Performance Design Procedures were adopted to correlate EDPs (i.e. inter-story drift ratio, residual drift ratio, link rotation angle, story displacement, floor acceleration, etc.) to the performance level of interest. Pursuant to this goal, numerical models were calibrated using pseudo-dynamic (*PSD*) test results to identify the influence of material parameters on system response. A parametric study was conducted to investigate the strain hardening effects on the EDPs. Short-link EBF archetypes with

different number of stories were analyzed under different seismic hazard levels. The performances of EBF archetypes were evaluated in terms of repair/replacement cost.

Short links usually show a stable response with a sudden loss in capacity due to fracture of the link. On the other hand, long links experience significant strength and stiffness degradation due to local buckling of the web and flanges. In addition, the rotation capacities of short and long links are markedly different as mentioned in the previous section. Based on these observations, there is a clear need for a systematic evaluation of the performance of EBFs with long links. Pursuant to this goal, second part of this thesis has undertaken a numerical study to evaluate the performance of EBFs with long links using the FEMA P695 methodology. A total of 24 EBF archetypes were designed and analyzed under different seismic hazards. Effects of degradation were studied by comparing the responses of degrading and non-degrading models. Design recommendations were developed based on the evaluation of archetype EBFs.

Loading protocols are required to examine the response of structural systems or members under a seismic event. The fundamental responses of a structural component are strength and deformation capacities, ductility, energy dissipation capacity and failure modes. Under cyclic loads, these capacities depend on cumulative deformation and are functions of damaging cycles. The loading protocols should be developed for different structural systems separately with a wide range of earthquake data because of the highly uncertain natures of earthquakes and structural response. The only protocol that can be used for long links is the one developed by Richards (2004). Long links are subjected to strength and stiffness degradation, which is not a characteristic of short links. The available loading protocol for long links was developed using a non-degrading moment rotation response. Furthermore, the nonsymmetrical nature of link rotation demands due to mean effects was neglected. The third part of the thesis aims to develop nonsymmetrical loading protocols for long links considering strength and stiffness deterioration behavior in addition to the mean effects. Pursuant to this goal, 24 EBF archetypes were designed with a variable range of e/L ratio, number of stories and bay widths. The archetypes

were subjected to two different seismic hazard intensities by conducting time history analysis. The developed loading protocol can be used for testing of long EBF links.

1.3 Thesis Organization

The present thesis consists of five chapters. The first chapter is the Introduction. Chapter 2 is related with short-link EBF topics and Chapters 3 and 4 are related with long-link EBF topics.

Chapter 2 investigates the effects of *SHR* on the engineering demand parameters (EDPs) and the performance assessment of short-link eccentrically braced frame (EBF) buildings by using FEMA P-58 methodology.

Chapter 3 undertakes a comprehensive numerical study to evaluate the seismic response factors for EBFs with long links using FEMA P695 methodology. The acceptable performance of long-link EBFs and remedial measures to improve this performance were investigated for a wide range of link lengths under different seismic levels.

Chapter 4 presents a nonsymmetrical loading protocol developed for long link EBFs. The proposed protocol is a function of maximum rotation range, which depends on the seismic hazard and e/L ratio.

The concluding remarks of the above independent studies are summarized in Chapter 5.

CHAPTER 2

EFFECTS OF CYCLIC STRAIN HARDENING ON PERFORMANCE OF ECCENTRICALLY BRACED FRAMES

2.1 Background

2.1.1 Performance Based Design

Performance of structures is generally quantified in terms of engineering demand parameters (EDPs). PBSB correlates EDPs (i.e. inter-story drift ratio, residual drift ratio, link rotation angle, story displacement, floor acceleration, etc.) to the performance level of interest. Traditional PBSB procedures adopted a wide range of different performance levels (i.e. Immediate Occupancy, Life Safety, Collapse Prevention, Scenario Expected Loss, Probable Maximum Loss, Scenario Upper Loss, etc.). Incremental dynamic analysis (IDA) was used in a number of studies (Khorami et al. (2017 and 2017), Shariati et al. (2020)) to assess performance of structural systems using traditional PBSB procedures. Next-Generation Performance Design Procedures (i.e. FEMA P-58 (2018)) revised discrete performance levels in traditional PBSB procedures and proposed continuous and universal definitions of performance measures as casualties, repair/replacement costs, repair time, environmental impacts and unsafe placarding in the form of probable impacts with uncertainties. PBSB enables comparing the repair/replacement costs of traditional structural systems with more specialized ones such as systems with base isolation (Kelly (1997)), self-centering systems (Tong et al. (2019)), or systems with dampers (Jalali et al. (2012)).

2.1.1.1 Summary of FEMA P-58 Methodology

FEMA P-58 is a set of methodology and procedures that are applicable to new and existing structures. The methodology was developed to assess the probable seismic performance of individual buildings and archetypes based on their unique site, structural, nonstructural and occupancy characteristics which improves the understanding of the total building. Performance is measured in terms of probability of incurring casualties, repair and replacement costs, repair time, environmental impacts and unsafe placarding. As a result, a better and easy understanding of seismic performance of a building, not only to engineers but also to the non-engineers like investors, renters, decision makers and insurance market can be provided.

FEMA P-58 methodology consists of eight basic steps, namely: selection of the assessment type, selection of the performance measures, assembling the building performance model, selection of the analysis method, constructing the building analytical model, definition of earthquake hazards, analyzing the building response, input the response data, calculating the performance and reviewing the results.

There exists three types of assessments in FEMA P-58. The first one is the intensity-based assessment where, the building is assumed to be subjected to a specified earthquake shaking intensity from 5% damped elastic acceleration response spectra. The second one is the scenario-based assessments which evaluate the performance of a building considering an earthquake scenario with a specific magnitude and location. The last one is the time-based assessment. Time-based assessments consider all earthquakes and their probability of occurrences at a specified time period.

The performance measures are developed to quantify the consequences of a structural response under a seismic event. Apart from traditional PBSO procedures, FEMA P-58 intended to propose continuous and universal definitions of

performance measures which can be meaningful to non-engineer decision makers.

Five different performance measures were defined as:

- **Casualties:** loss of life/ serious injury
- **Repair cost:** dollar cost required to restore the building to its pre-earthquake condition. If the repair cost exceeds a certain percentage of the initial cost defined by the decision maker, the repair cost modifies into replacement cost. Replacement cost is the dollar cost to replace the building of a similar construction.
- **Repair time:** time (weeks) required to restore the building to its pre-earthquake condition.
- **Environmental Impact:** the amount of carbon emission and embodied energy required to restore the building to its pre-earthquake condition.
- **Unsafe Placarding:** a post-earthquake inspection rating that determines whether entrance or occupancy of a building (or a part of a building) is safe or should be restricted.

The building assets that are at risk under a seismic event are described by assembling the building performance model. The building performance model assemblage includes the information of:

- **Basic building data:**

Basic building data includes the building size, replacement cost, replacement time .. etc.

- **Occupancy:**

Occupancy is the primary intended purpose of the building. FEMA P-58 provides a Performance Assessment Calculation Tool (PACT) to assess next-generation performance measures as a function of EDPs. Once the type of occupancy is defined to PACT, it estimates the distribution of people over time as well as time and quantity of non-structural components exist in the building.

- **Vulnerable structural and non-structural components and assemblies:**

PACT includes over 700 fragility curves in its database, generated for different types of structural and nonstructural components and can categorize all structural and non-structural components into fragility groups and performance groups. Each group has its own damage state, damage correlation and damage parameters. These curves are derived using analysis results, experimental results and expert judgement. However, the embedded fragility curves can be modified or replaced manually by the user. In the absence of floor plans, FEMA P-58 offers an additional tool that estimates the nonstructural component distribution on a gross square foot basis, for each occupancy type called “Normative Quantity Estimation Tool”. These quantities are derived by investigating 3000 buildings in detail.

The damage state of each fragility group is a function of different key response parameters (link rotation angles, floor accelerations, story drift ratios, residual drift ratios...etc) associated with the fragility specification used to assess the performance. The median values of these key response parameters are estimated using structural analysis. FEMA P-58 structural analysis procedures include non-linear response history and simplified analysis.

For the analytical model in a nonlinear response history analysis, the building is recommended to be modeled as a three-dimensional (3-D) assemblies including all elements which provide measurable strength and stiffness. Two dimensional (2-D) models are not advised, but if the building is to be modeled in 2-D, each ground motion pair should be applied separately to its corresponding building direction. The analytical model in the simplified analysis estimates the median values of the structural response using a linear elastic structural model and an estimate of the building’s lateral yield strength.

The method of selection and scaling of ground motions show variation among different assessment types. However, for all assessment types, the selected ground motions should match the target spectrum over the period range T_{min} and T_{max} where

T_{min} is taken as 0.2 times the smaller of T_I^X and T_I^Y and T_{max} is taken as the larger of the fundamental periods, T_I^X and T_I^Y . The spectral shape of the selected ground motion records is recommended to be similar to the one of the target spectrum. If this condition cannot be satisfied, eleven or more ground motion pairs are required to estimate reasonable median responses. However, independent from the level of the fit, FEMA P-58 prescribes that at least seven ground motion pairs should be selected. Each ground-motion pair should then be amplitude-scaled.

The methodology calculates the performance as a function of component damage. For the cases that the total or partial collapse of a building is the major reason of earthquake losses, the users should define a collapse fragility function which relates the probability of structural collapse as a function of the seismic intensity.

Once the analyses are completed, the response parameters should be inputted into Performance Assessment Calculation Tool (PACT) to assess next-generation performance measures as a function of EDPs. PACT calculates the value of each performance measure as well as the percentage contribution of each component to the overall losses using a Monte Carlo process.

2.1.1.2 Summary of Past Research that used FEMA P-58 Methodology

The FEMA P-58 methodology is a practical and convenient tool for estimating next-generation performance measures. Recently, researchers have paid an increased attention to FEMA P-58 procedures (Xu et al. (2019), Silva et al. (2020), Cardone et al. (2015), Guerrero et al. (2017)). Papadopoulos et al. (2019) defined FEMA P-58 procedure as a trade off between accuracy and simplicity and a valuable tool for performance assessment. Majidi et al. (2021) applied FEMA P-58 methodology for a RC educational building in Iraq and concluded that the obtained results are very clear for the owner and decision makers. Sani et al. (2018) adopted PACT software based on FEMA P-58 procedure, to compare the expected annual losses (EAL) of SMRFs of 4, 6 and 8 stories with and without base isolation systems. Cook et al.

(2017) compared FEMA P-58 method results with other commonly used performance assessment methods (the Thiel Zsutty Method, ST Risk software) and concluded that, FEMA P-58 gives similar results on average. However FEMA P-58 methodology provides detailed building specific risk information and varies between buildings when compared with the other performance assessment methods, because it has an ability to quantify the effect of building-specific features. In a more recent study, Cook et al. (2021) compared the FEMA P-58 outcomes and empirical data from 1994 Northridge Earthquake for a regional scenario assessment. They concluded that FEMA P-58 over-predicts repair cost and unsafe placards especially for wood frames and proposed a calibration to the FEMA P-58 procedure. Del Gobbo et al. (2018) investigated the seismic performance and repair costs of Eurocode compliant concentric braced frame buildings. Sullivan et al. (2018) examined the performance of 22-story steel framed building in Christchurch. They pointed the significant effects of non-structural element positioning, modeling the cladding and the aftershocks on the loss assessment. Engineering Demand Parameter (EDP) estimation using FEMA P-58 methodology is also preferred by the other researchers (Cremen and Baker (2018) and Saldana et al. (2018)).

Along with all other EDPs, the residual frame deformation has a dominant impact on the seismic performance for some structural systems such as buckling restrained braced frames (BRBFs) (Ariyaratana and Fahnestock (2011) and Guner and Topkaya (2020)). McCormick et al. (2008) found out that a residual drift ratio of 0.5% is perceivable by the occupants and proposed this ratio as a limit of permissible residual deformation level. According to FEMA P-58, repair of a structure is not economically and practically feasible if the residual drift ratio exceeds 1%. While accurate estimation of EDPs is essential, they are highly dependent on the modeling assumptions. Research conducted to date has demonstrated that residual deformation is substantially sensitive to the post-yield stiffness of the steel material.

In a recent study by Prasai (2021), seismic performances of nine newly designed and one existing EBF structures were evaluated using FEMA P-58 procedure. In another recent study, Arifin et al. (2017, 2021) examined the seismic performance of a 22-

story EBF building in New Zealand which was subjected to a series of earthquakes. The sensitivity of peak accelerations and drifts to the *SHR* was examined within the context of this study.

2.1.2 Summary of Past Research Considered the Effect of Strain Hardening Ratio on the Engineering Demand Parameters

Strain hardening ratio (*SHR*) is the ratio between the post-yield stiffness and the initial elastic stiffness. *SHR* can be calculated at the material level or member level. Past researchers have examined the effect of *SHR* on the performance of different steel structural systems and single degree-of-freedom (*SDOF*) systems.

Mahdavi-pour and Deylami (2014) conducted a probabilistic assessment study for 3, 6, 9 and 12 story buckling-restrained braced frames (*BRBFs*) and investigated the effect of *SHR* on the residual deformations under 10 ground motion pairs presented in SAC studies for Los Angeles (FEMA 2000). Giuffre-Menegotto-Pinto (Steel02) nonlinear material model defined in the OpenSees (2006) computer program, was selected with *SHRs* of 1%, 2%, 3% and 4%. They demonstrated that the effect of *SHR* on the residual deformations of *BRBFs* is more pronounced as the ground motion intensity increases and the responses other than residual deformations were not significantly influenced by the *SHR*.

Asgharkhani et al (2020) studied approximate methods for residual drift estimation in *BRBFs*. Two , 4, 6, 8, 10 and 12 story *BRBFs* were analyzed under 78 ground motion records which were scaled into different intensities. They investigated the effect of *SHR* ratio on the accuracy of the proposed and the evaluated methods. Giuffre-Menegotto-Pinto (Steel02) material model was defined in the OpenSees (2006) program with parameters: $R_0=20$, $CR_1=0.925$, $CR_2=0.15$, $a_1=0.07$, $a_2=1.0$, $a_3=0.05$ and $a_4=1.0$. Three values of kinematic hardening were considered as: $\alpha=0.003$, 0.01 and 0.02. Their study showed that the accuracy of the residual drift methods depends on the *SHR*.

Bojorques and Ruiz Garcia (2013) studied the residual drift demands in moment resisting frame (*MRF*) structures, which were subjected to narrow band earthquake ground motions. The influence of post-yield stiffness ratio on the residual drifts had been investigated on a 4-story study-case frame with $SHR=0.03$ and $SHR=0.01$. The authors showed that, as the SHR increases, the residual inter-story drift demand in moment resisting frames (MRFs) decreases with increasing ground motion intensity.

Christopolous et al. (2003) studied the characteristics and factors affecting the permanent deformations on *SDOF* structures. $SHRs$ are considered as 0.05, 0.00, -0.05 and -0.10. Three different hysteretic models, Elastoplastic, Takeda and Flag shaped were adopted. Elastoplastic hysteretic model was selected as a representative of steel structures, Takeda hysteretic model was representative of reinforced concrete structures and Flag Shaped model represents the self-centering structures. The study concluded that while the response is very sensitive to the SHR for the elasto-plastic systems, self-centering systems are insensitive to the reduction in SHR even for the negative slopes.

Kawashima et al. (1998) defined two parameters namely bilinear factor, r which is the ratio of post yield stiffness to the initial elastic stiffness; and SRDR which is the ratio of residual displacement to the maximum possible value of residual displacement. They aimed to generate a residual displacement response spectrum on *SDOF* structures with different periods, ductilities and bilinear factors based on 63 ground motions. Three bilinear factors (r) are considered as -0.05, 0.0 and 0.1. They have concluded that the response spectrum significantly depends on the bilinear factor and approaches to zero as the r value increases. On the other hand, SRDR value almost reaches to 1.0 when the bilinear factor is smaller than 0.0.

2.1.3 Summary of Past Research on the Modeling of Structural Steel Members under Cyclic Loading

A limited literature survey on modeling assumptions was conducted to investigate the range of *SHR* considered in studies on different steel structural systems. FEMA 356 (2000) adopts bilinear hardening and permits *SHR* of 0.03 for modeling the behavior of beams and columns, unless a greater value is justified by test data.

2.1.3.1 Material level

A representative cyclic stress-strain curve (Cofie and Krawinkler (1985)) obtained from a uniaxial test on A36 steel is given in Figure 2.1. Dafalias and Popov (1975) formulated bounding surface plasticity model which is based on stress bounds. The nonlinear portions of the stress-strain curve can be defined by continuously changing tangent modulus whose magnitude is a function of the distance between a stress bound and the instantaneous stress. At large inelastic strains, the stress-strain curve approaches a straight line bound as shown in Figure 2.1. The slope of the stress bound, which is directly related to the *SHR*, depends on the grade and heat of steel. The *SHR* value was reported as $0.0075 (E/133)$ for the A36 specimen (Cofie and Krawinkler (1985)), where E is the elastic modulus of steel material.

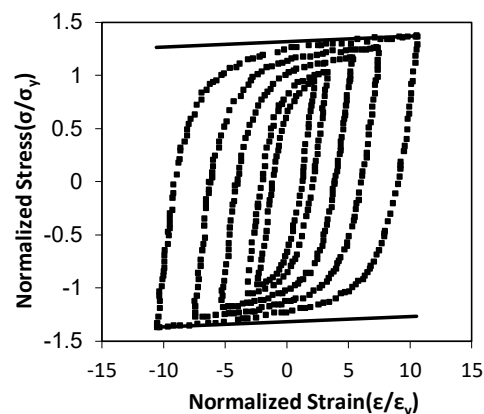


Figure 2.1. Cyclic Stress Strain Behavior for A36 steel and Dafalias and Popov's (1975) bounding surface plasticity model

Shen et al (1992) proposed a two-surface model for steel plates using three types of structural steels: SS400, SM490 and SM570 to predict the elastoplastic behavior under cyclic loading. *SHR* values were reported as 0.009 ($E/111$), 0.014 ($E/71$), and 0.005 ($E/200$) for SS400, SM490, and SM570 steels, respectively. Usami et al. (2000) and Shen et al. (1995) observed that the slope of stress bound is not a constant and decreases with the amount of plastic work.

Duscika et al. (2007) modeled cyclic stress strain using an elastic model for the plastic strain component as in Equation 2.1:

$$\varepsilon = \frac{\sigma}{E} + \left(\frac{\sigma}{K}\right)^{1/n} \quad (2.1)$$

The Modulus of Elasticity (E) is measured, the cyclic strain (K) and cyclic hardening coefficient (n) are obtained from data regression of the coupon stress and corresponding plastic strain values for different grade structural steel plates. The stress-strain curve for each structural steel was plotted and the post yielding stiffness ratios of steel plates are found to vary between 0.0029 ($E/345$) and 0.004 ($E/250$).

Carreño et al (2020) have conducted a detailed optimization study on Grade 60 ASTM A615 and ASTM A706 steel reinforcing bars to calibrate and propose material model parameter values for Steel02 material model. The recommended *SHR* values are 0.012 ($E/83$) and 0.02 ($E/50$) for A706 and A615 steels, respectively where $R_0=20$, $CR_1=0.9$, $CR_2=0.08$, $a_1=0.039$, $a_2=1.0$, $a_3=0.029$ and $a_4=1.0$.

Wang et al. (2015) proposed a uniaxial trilinear kinematic hardening model for high strength steel specimens, where the calibrated *SHR* is reported as 0.019 ($E/53$). Based on these studies it can be considered that the *SHR* value has a wide range that changes between 0.0029 ($E/345$) and 0.02 ($E/50$).

2.1.3.2 *BRBFs, SMRFs and STMFs*

Guerrero et al. (2016) conducted a preliminary design and assessment study on low rise BRBF structures. They have considered tension compression asymmetry in the hysteretic behavior, assumed SHR value as 0.3% and calibrated Steel02 material model parameters according to the experiments carried out by Merrit et al (2003).

Gray et al (2014) compared the performances of Yielding Brace Systems (*YBSs*) and *BRBFs* on a 12-story sample building. Post yield stiffness and strength at large displacement of these systems are different from each other. Steel02 material model in OpenSees computational program had been assigned to each *BRBF* component and the calibrated SHR value is reported as 0.025.

Howidae et al. (2015) performed a numerical investigation on the seismic behavior of full-length and short-core buckling restrained braces using the OpenSees (2006) software. The Steel02 material model parameters were calibrated according to Tremblay et al. (2006) and Duscika et al (2007). The value of *SHR* is reported as 0.008.

Erochko et al. (2011) compared the residual drifts of special moment resisting frames (*SMRFs*) and *BRBFs* of 2 to 12 stories. 2D frames were modeled with the nonlinear seismic analysis program Ruaumokko (2005). The *SHR* was assumed to be 0.02. The study concluded that the *BRBFs* are more sensitive to the initial residual drifts than the *SMRFs* because of the P- Δ effects. Similarly, tall buildings are more sensitive to the residual drifts than the short buildings.

Sahoo and others conducted numerous studies between 2013 and 2019 on *BRBFs* including the seismic performance, drift response evaluation of *BRBFs* and drift mitigation techniques developed for *BRBFs*, analytical evaluation of the hysteretic response of BRBs of variable lengths. They also investigated the effect of loading histories and restraining parameters on the cyclic response of Steel BRBs. The SHR values in these studies were reported in the range of 0.01 to 0.044. Gade and Sahoo

(2016) also evaluated the collapse-resistance of special truss moment frames according to FEMA P695 methodology. The ratio of strain-hardening slopes to the elastic slopes is assumed as: 0.03 for beams and columns, 0.06 for panel zones and 0.1 for channel sections.

2.1.3.3 Isolated Members

Iraj et al (1996) conducted a deflection analysis of pin ended columns and fixed ended tubular beam columns employing FEAP (1977) computer program. Based on the experimental results, the kinematic and isotropic hardening ratios are assumed to be 0.00896.

Lamarche et al (2010) performed an experimental and numerical study on isolated columns to investigate the effect of relaxing design requirements of the columns of multistory concentrically braced frame (*CBF*) structures. The isolated column is modeled with OpenSees (2006) software using calibrated Steel02 material (Lamarche et al 2008). The *SHR* parameters are reported as 0.0036 and 0.0055 for the web and the flange respectively.

Uriz et al. (2008) modeled steel braces in OpenSees (2006) computational platform based on Giuffre-Menegotto-Pinto (Steel02) material model. The validated (Black et al. (1980)) *SHR* value was reported as 0.003.

2.1.3.4 Eccentrically Braced Frames

Koboevic et al. (2012) conducted a numerical study with four EBF structures with different frame heights which are designed for different locations. Analysis were conducted using three computer programs: ANSR-1 (1975), DRAIN-2DX (1993) and OpenSees (2006) using both Giuffre-Menegotto-Pinto (Steel02) and Multilinear hysteretic material models whose parameters were calibrated with the test data of Okazaki et al. (2005). The *SHR* value was reported as 0.0045. The authors concluded

that, the effect of modeling is less pronounced on the force response. However, small variations in the modeling assumptions or ground motion input may end up with very high variations in deformation response. Ramadan and Ghobarah (1995) developed an analytical model for shear-link behavior and assumed *SHR* value as 0.002.

Richards and Uang (2006) proposed a testing protocol for short links in *EBFs*. 3- and 10 story prototype buildings were designed according to IBC (ICC2000) and AISC Seismic Provision (AISC 2002) analyzed with DRAIN-2DX (Prakash et al. 1993) and the *SHR* value was reported as 0.002.

O-Reilly and Sullivan (2016) proposed a direct displacement based seismic design of *EBFs*. The Giuffre Menegotto-Pinto hysteresis rule was considered in OpenSees (2006) to represent the cyclic shear behavior. The *SHR* was considered equal to 0.001 after calibration with test results.

Al-Janabi and Topkaya (2020) proposed non-symmetrical loading protocols for shear links in *EBFs*. They designed 20 *EBF* archetypes according to ASCE7-16 with different number of stories and e/L ratios. The OpenSees (2006) computational platform was adopted for the analysis and *SHR* value was considered as 0.002.

Arifin (2017) conducted a sensitivity study of peak accelerations and drifts of a 22-story *EBF* building in New Zealand to the *SHR*. The control value of the post-yield stiffness was assumed as 0.03 and modified to 0.02 for the sensitivity study.

To summarize, numerical studies conducted on BRBs and BRBFs considered *SHR* in the wide of range of 0.003 and 0.044. For MRFs *SHR* between 0.01 and 0.03 was taken into account. Investigation on isolated columns considered *SHR* in the range of 0.0036 and 0.0090 and steel braces were modeled with $SHR=0.003$. *EBF* links were modeled with *SHR* in the range of 0.001 and 0.03. Table 2.1 and 2.2 summarize the *SHR* assumptions of past researchers presented above and Giuffre-Menegotto-Pinto material parameters considered by these researchers in case OpenSees (2006) computational platform was used. It can be observed that a wide range of *SHR* values

were adopted in modeling and the value considered in a study depends on the calibration with experimental observations.

Table 2.1 Summary of previous research on the SHR value.

Author	Frame/ Element/ System	Strain hardening ratio (b)	Post Yielding Stiffness (E/(1/b))	Source of Validation/ Calibration	Analysis Software
Mahdavi pour & Deylami (2014)	BRBF	0.01, 0.02, 0.03, 0.04	E/100, E/50, E/33, E/25	-	OpenSees
Asgharkhani et al. (2020)	BRBF	0.003, 0.01, 0.02	E/333	Merrit et al. (2003)	OpenSees
Bojorques and Ruiz Garcia (2013)	MRF	0.01, 0.03	E/100, E/33	-	Ruaumokko
Christopolous et al. (2003)	SDOF	0.05, 0, -0.05, -0.1	E/20, -E/20, E/10	-	-
Kawashima et al. (1998)	SDOF	0.1, 0, -0.05	E/10, 0, -E/20	-	-
Cofie and Krawinkler (1985)	Structural Steel	0.0075	E/133	Cofie and Krawinkler (1985)	-
Shen et al. (1992)	2SM	0.009 (SS400), 0.014 (SM490), 0.005 (SM570)	E/111 (SS400), E/71 (SM490), E/200 (SM570)	Shen et al. (1992)	-
Duscika et al. (2007)	Plate Steel	0.0029-0.004	E/345-E/250	Duscika et al. (2007)	-
Carreño et al. (2020)	Rebars	0.012 (A706), 0.02 (A615)	E/83 (A706), E/50 (A615)	Carreño et al. (2020)	OpenSees
Wang et al. (2015)	High strength steel	0.0019	E/53	Wang et al. (2015)	ANSYS
Guerrero et al. (2016)	BRBF	0.003	E/333	Merrit et al. (2003)	OpenSees
Gray et al. (2014)	BRBF	0.025	E/40	-	OpenSees
Howidae et al. (2015)	Full length & short core BRB	0.008	E/125	Tremblay et al. (2006) and Duscika et al. (2007)	OpenSees

Table 2.1 (continued)

Author	Frame/ Element/ System	Strain hardening ratio (b)	Post Yielding Stiffness (E/(1/b))	Source of Validation/ Calibration	Analysis Software
Erochko et al. (2011)	BRBF&S MF	0.02	E/50	FEMA356	Ruaumokko
Sahoo and Chao (2015)	BRBFs	0.03	E/33	Merrit et al. (2003)	PERFORM- 3D
Pandikkadavath and Sahoo (2016)	BRBs	0.023	E/43	-	ABAQUS CAE
	SBRBs	0.025-0.044	E/40-E/23	-	ABAQUS CAE
Ghowsi and Sahoo (2019)	BRBs	0.01	E/100	Wu et al. (2014)	ABAQUS
Pandikkadavath and Sahoo (2017)	BRBs	0.025	E/40	Merrit et al. (2003)	PERFORM- 3D
	SBRBs and HBRBs	0.03	E/33	-	PERFORM- 3D
Ghowsi and Sahoo	BRBs	0.02	E/50	-	SAP2000
Gade and Sahoo (2016)	STMF- beams and columns	0.03	E/33	-	SAP2000
	STMF- panel zones	0.06	E/17	-	SAP2000
	STMF- channel sections	0.10	E/10	Parra- Montesinos et al. (2006)	SAP2000
Iraj et al. (1996)	Pin & ended columns	0.00896	E/111	Shen et al. (199)	FEAP
Lamarche et al. (2008)	Isolated columns	0.0036 (web), 0.0055 (flange)	E/278 (web), E/182 (flange)	Lamarche et al. (2008)	OpenSees
Uriz et al (2008)	Single Steel Brace	0.003	E/333	Black et al. (1980)	OpenSees
Koboevic et al. (2012)	EBF	0.0045	E/222	Okazaki et al. (2005)	Drain2DX, ANSR1, OpenSees
Richards and Uang (2006)	EBF	0.002	E/500	Arce (2002)	Drain2DX

Table 2.1 (continued)

Author	Frame/ Element/ System	Strain hardening ratio (b)	Post Yielding Stiffness (E/(1/b))	Source of Validation/ Calibration	Analysis Software
O'Reilley and Sullivan (2016)	EBF	0.001	E/1000	Mansour (2010) Okazaki et al. (2005)	OpenSees
Al-Janabi and Topkaya (2020)	EBF	0.002	E/500	Okazaki et al. (2005)	OpenSees
Arifin (2022)	EBF	0.03 and 0.02	E/33 and E/50	-	Ruaumokko

Table 2.2 Summary of Giuffre-Menegotto-Pinto material parameters proposed by past researchers

Author	Giuffre-Menegotto-Pinto material parameters							
	b (SHR)	Ro	cR1	cR2	a1	a2	a3	a4
Mahdavi pour & Deylami (2014)	0.01, 0.02, 0.03, 0.04	-	-	-	-	-	-	-
Asgharkhani et al. (2020)	0.003, 0.01, 0.02	20	0.925	0.15	0.007	1.0	0.05	1.0
Carreño et al. (2020)	0.012 (A706), 0.02 (A615)	20	0.9	0.08	0.039	1.0	0.029	1.0
Guerrero et al. (2016)	0.003	20	0.925	0.15	0.007	1.0	0.05	1.0
Gray et al. (2014)	0.025	19	0.9	0.15	0.035	1.0	0.01	1.0
Howidae et al. (2015)	0.008	20-40	-	-	0.34	11.1	0.34	11.1
Lamarche et al. (2008)	0.0036 (web), 0.0055 (flange)	25	0.925	0.15	0.005	1.0	0.005	1.0
Uriz et al (2008)	0.003	-	-	-	-	-	-	-
Koboovic et al. (2012)	0.0045	22	0.925	0.15	0.12	7.0	0.12	7.0
O'Reilley and Sullivan (2016)	0.001	20	0.925	0.1	0.02	1.0	0.02	1.0
Al-Janabi and Topkaya (2019)	0.002	20	0.925	0.15	0.02	1.0	0.02	1.0

Specimens tested by Okazaki et al. (2005) and Bozkurt and Topkaya (2018) were considered to determine the *SHR* values observed during experiments on shear links. The post-yield stiffnesses of 4CRLP, 8RLP and 10RLP specimens of Okazaki et al. (2005) were calculated as 0.0016, 0.0012 and 0.0033 respectively at the end of 0.13 rad rotation cycle. Similarly the post yield stiffnesses of specimens 1 and 6 of Bozkurt and Topkaya (2018) were calculated as 0.0047 and 0.002 respectively at the end of 0.09 rad rotation cycle. The observations justify that the *SHR* values obtained for shear links can vary between 0.001 and 0.005.

2.2 Modeling of Shear Links

Accurate modeling of link beams is essential for estimating the response of EBF systems because links are the primary source of energy dissipation. Observations from experiments conducted in the past (Malley and Popov (1984) and Kasai and Popov (1986)) revealed that both isotropic and kinematic hardening occur in links yielding predominantly in shear. Ramadan and Ghobarah (1995) developed an analytical model for shear links. This model adopts 3 translational and 3 rotational springs at the ends of the link to simulate the shear and flexural responses, respectively. A bilinear load-deformation response was considered for the springs and a multi-linear load deformation response was obtained by combining the 3 springs in parallel. The overall load-deformation response was calibrated using test results. The yield points and strain hardening ratio were also calculated according to University of Texas Austin (UTA) link tests with A992 steel (Arce 2002). This modeling approach was modified by Richards and Uang (2004 and 2006). The rotational springs were removed and the overall multi-linear load deformation response of translational springs was modified as shown in Figure 2.2. A shear overstrength of 1.5 is adopted in this model. The load-deformation response varies from $1.1V_p$ to $1.3V_p$ finally reaching to $1.5V_p$, where V_p is the plastic shear strength of the I-shaped link. The slope at each loading increment is indicated in Figure 2.2,

where the *SHR* (K_{V4}) was considered as 0.002. In other words, the post yield hardening slope is taken as 0.002 times the initial slope.

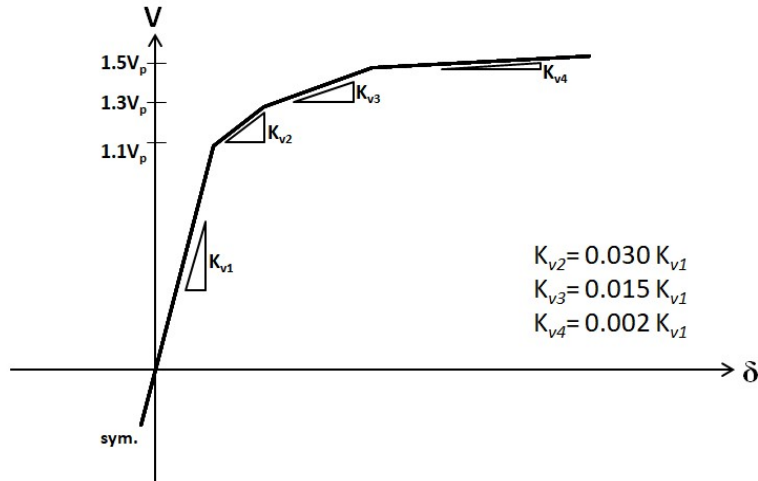


Figure 2.2. Shear Force Deformation Relationship Proposed by Richards and Uang (2004 and 2006)

Malakoutian et al. (2013) developed a modeling technique to be used with OpenSees (2006) routines. The axial and flexural responses were modeled with a beam-column element with fiber cross-section. A shear force versus shear deformation section was aggregated to represent the shear response. This technique eliminated the need for translational and flexural springs used at the link ends. O'Reilly and Sullivan (2016) modified the material model for the shear behavior to account for combined isotropic and kinematic hardening possessed by the links. The very same modeling technique was adopted by Al-Janabi and Topkaya (2020)

Response of a shear link under different material modeling approaches is given in Figure 2.3. The 4C-RLP specimen tested by Okazaki et al. (2005) was considered for comparison purposes. The modeling technique recommended by Malakoutian et al. (2013) was used with three different material behaviors. The first one is bilinear kinematic model with a *SHR* of 0.012. The second one is the Giuffre Menegotto-Pinto hysteresis rule (Steel02 material model) with the material parameters considered in Al-Janabi and Topkaya (2020). The third one employs a multi-linear

material model with the model parameters considered in Richards and Uang (2004 and 2006). Comparisons with tests results show that the Giuffre Menegotto-Pinto hysteresis rule and the multi-linear material model are capable of representing the global shear link versus rotation response with the former being more successful in simulating the transition from elastic to plastic behavior. The bilinear material model has a tendency to over-estimate the resistance for link rotations larger than 0.1 rad because of the large value of the *SHR*.

Preliminary studies were conducted to evaluate the accuracy of different material modeling techniques in estimating the results of PSD tests. The comparisons revealed that the model with the multi-linear hardening provides more accurate results when compared with the model employing the Giuffre Menegotto-Pinto hysteresis rule. Therefore, the multi-linear material modeling approach was employed for the studies described in this chapter.

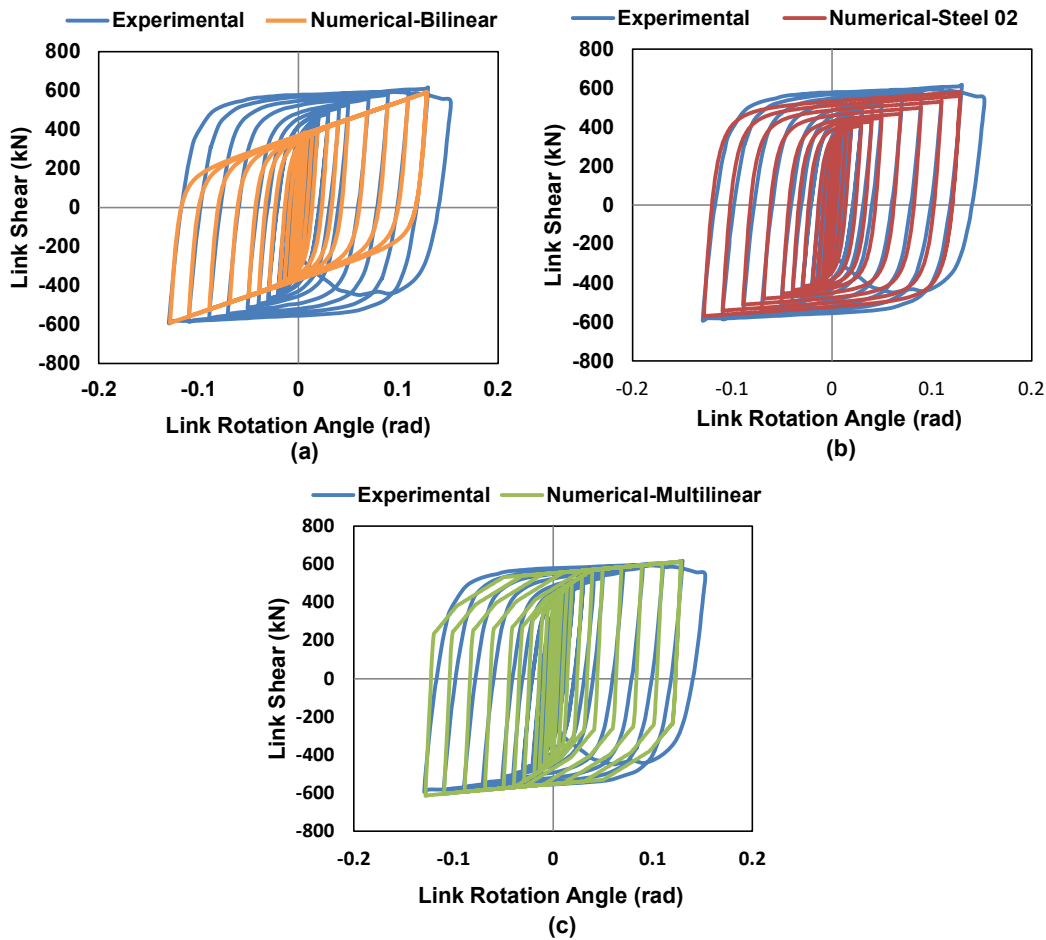


Figure 2.3. Simulation of Link Response using Different Material Models and Cyclic Stress Strain Behavior of Structural Steel (a) Bilinear (b) Steel 02 (c) Multilinear

2.3 Numerical Modeling of EBFs and Verification of Numerical Models

2.3.1 DUAREM Structure

The performance of dual-eccentrically braced frames (*D-EBF*) with replaceable links was studied as a part of the DUAREM Project (Sabau et al. (2014) and Ioan et al. (2016)). DUAREM Project was conducted in 2014, in order to assess the performance of *D-EBFs* with replaceable links, to validate the re-centering capability

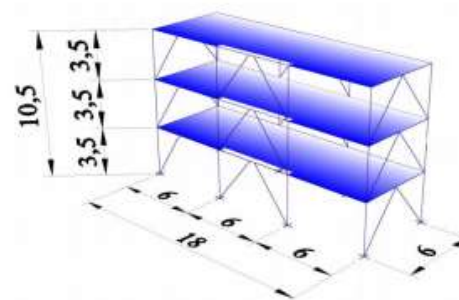
of these structures and to investigate concrete slab-steel structure interaction in the link region.

A three story prototype dual system with 18m×30m plan dimensions was designed according to the European norms (EN1990, EN1991, EN1992, EN1993, EN1994 and EN1998). The story height of the structure is 3.5 m, and the bay widths of all spans are 6 m.

A 1- by 3-bay part of the dual system with equal spans of 6 m was tested in the European Laboratory for Structural Assessment (ELSA) of the Joint Research Centre (JRC) in Ispra, Italy. Two external frames of the prototype building in the transversal direction were considered and named as North and South frames. The two frames differed in the way that the concrete floor slab is attached to the links. The floor slab was not connected to the links in the South frame, which was used in this study for verification of the numerical models. The 3 story experimental mock-up structure with a story height of 3.5 m is presented in Figure 2.4 and the geometry of the framing is indicated in Figure 2.5. The yield strength and dimensions of steel components are presented in Table 2.3.



(a) Full Set-up



(b) 3D view

Figure 2.4. Experimental mock-up structure (Sabau et al. (2014))

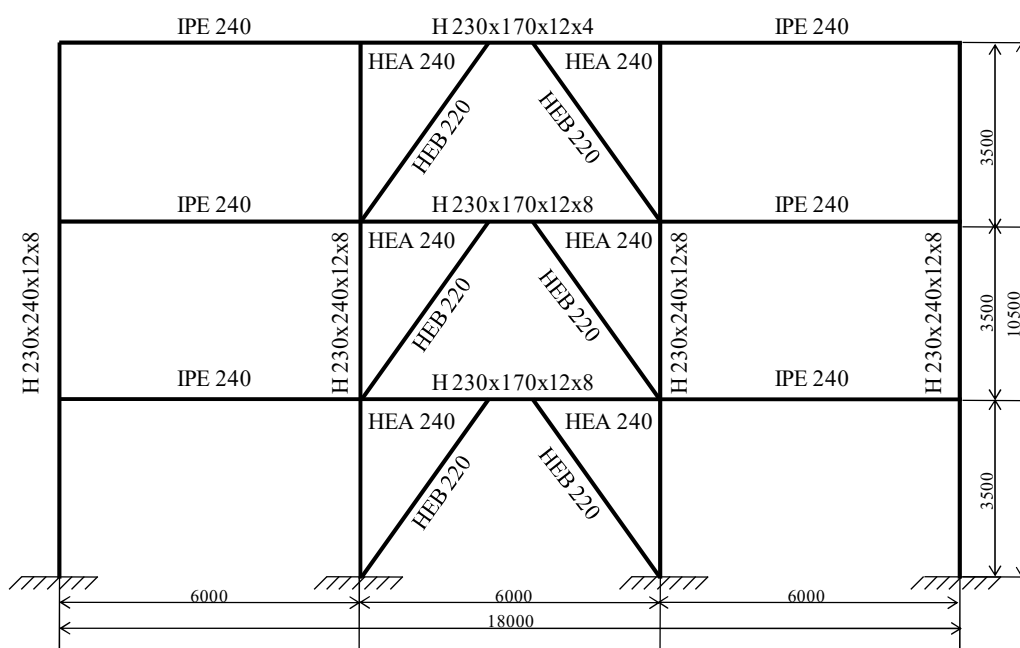


Figure 2.5. South Frame of the DUAREM Structure

Table 2.3. Details of the Structural Steel components of the DUAREM Structure

Component	F _y (N/mm ²)	Dimensions (mm)
Column	507.5*	230x240x12x8
MRF beams	425	240x120x9.8x6.2
EBF beams	384	230x240x12x8
Braces	405	200x200x15x9
1 st and 2 nd story Links	293	230x170x12x8
3 rd story link	303	230x120x12x4

* web yield strength of the column web and flange were reported to be 512 N/mm² and 503 N/mm² respectively. The overall yield strength of the columns was assumed to be 507.5 N/mm² in this study.

EN 1991 provisions were used to determine the gravity loads. In addition to the self-weight of structure, an additional vertical loading was applied on the structure based on the load combination presented in Equation 2.2:

$$1.00 G_K + 0.3 Q_K \quad (2.2)$$

where G_k is the total dead load of 4.9 kN/m^2 and Q_k is the variable load of 3.0 kN/m^2 .

The masses of the first, second and third stories were reported to be 165 tons, 165 tons and 168 tons respectively.

The test frame was subjected to the İzmit Yarımca 15613_H2 ground motion record (Figure 2.6) selected from a set of 7 ground motions from RESORCE database (<http://www.resorce-portal.eu/>, Akkar et al. (2014)) that matches EN1998 type-1 target response spectrum (Figure 2.7) for soil type C and $a_{gr} = 0.19g$.

The selected ground motion record was scaled to different levels of peak ground acceleration (PGA) as:

- 1) Full operation (0.02 g)
- 2) Damage Limitation (DL): $a_g=0.191 \text{ g}$, 95 years return period
- 3) Significant Damage (SD): $a_g=0.324 \text{ g}$, 475 years return period
- 4) Near Collapse (NC) : $a_g=0.557 \text{ g}$, 2475 years return period

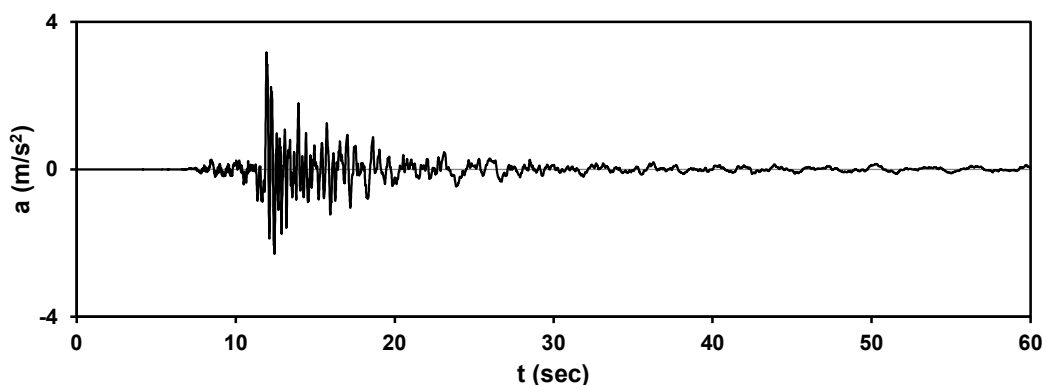


Figure 2.6. Acceleration time history for 15613_H2 record

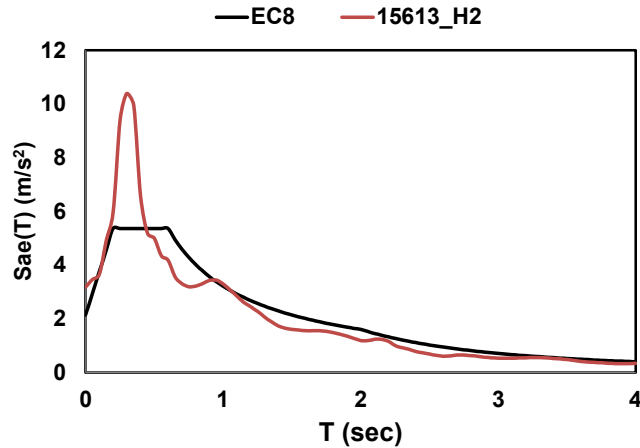


Figure 2.7. Response spectrum of the selected scaled GM record versus target spectrum.

The OpenSees computational platform was used for analysis of the 2-D dual-eccentrically braced frame (D-EBF). The columns, moment resisting frame beams, beam outside of the link and braces were modeled with force-based nonlinear beam-column elements with fiber sections. Ten integration points were used along the length of each member . The yield strengths of each member were adopted from the DUAREM report (Sabau et al. (2014)), where mechanical characteristics of steel components according to the independent tests had been provided. The links were modeled using the approach presented in Section 2.2 and by adopting the non-linear shear force versus deformation response proposed by Richards and Uang (2004 and 2006).

Flush end-plated replaceable links were used in the DUAREM frame where thick end plates and bolts were used to connect the links to the collector beams. This type of a connection has considerable rotational flexibility which must be accounted for in the numerical models (Zimbru et al. (2017, 2017 and 2018)). Zero length elements were defined at the ends of the links and the elastic flexural stiffness of the end connections was taken as $6.0E+7$ Nm/rad based on calculations according to EN1993-1-8 (2005). The initial shear rigidity of the links was equal to GA_{web} , where G is the shear modulus of steel, and A_{web} is the area of the link section that resists the

shear force. Reported floor mass was equally distributed to each column node at each story. The column bases were considered fixed according to the actual base condition.

During the PSD tests, the equation of motion was solved for the restoring force coming from the south frame. In this process, no viscous damping matrix was used. Consequently, damping was not assigned to any of the D-EBF members in the numerical model.

The natural periods of the first three modes of the DUAREM structure were determined from the Spatial-Model Frequency (Hz) plots as $T_1=0.520$ sec, $T_2=0.180$ sec and $T_3=0.125$ sec. The numerical model calculates the natural periods of the first three modes using eigenvalue analysis as $T_1=0.521$ sec, $T_2=0.214$ sec and $T_3=0.144$ sec.

Time history of story displacements and link rotation angles obtained from the numerical model are compared with the experimental findings in Figures 2.8 and 2.9, respectively. The load case with a PGA of 0.324g was considered for verification purposes because this was the ground motion input with the highest PGA that can be fully completed. A PGA of 0.324g corresponds to Significant Damage limit state with a return period of 475 years. In other words, the level of input is representative of the design basis earthquake (DBE). The link shear versus link rotation angle responses are compared with experimental results in Figure 2.10(a), 2.10 (b), 2.10 (c). The base shear versus first story displacement responses are compared in Figure 2.10 (d). In addition, the maximums of base shear, story displacement, residual story displacement, link rotation angle, residual link rotation angle are reported in Tables 2.4 through 2.6 and are compared with the experimental results.

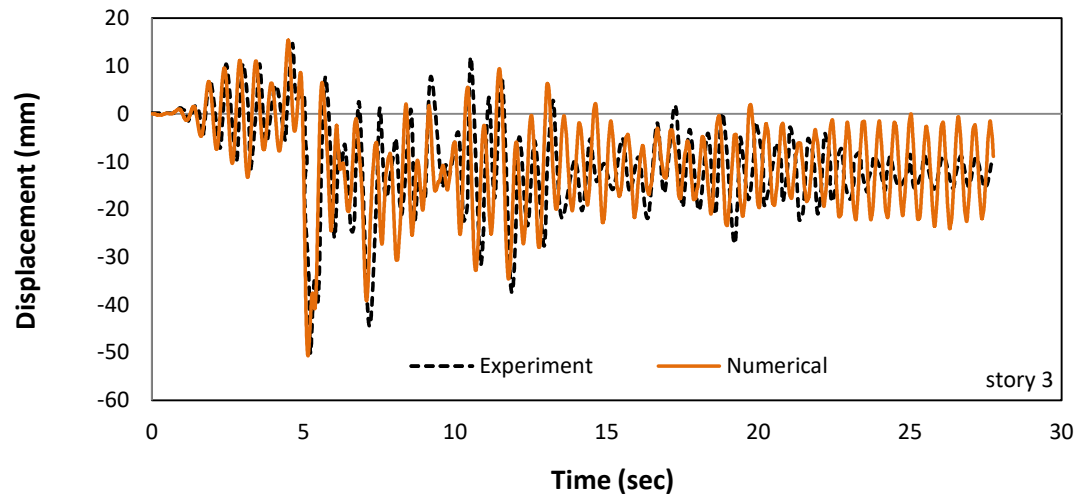
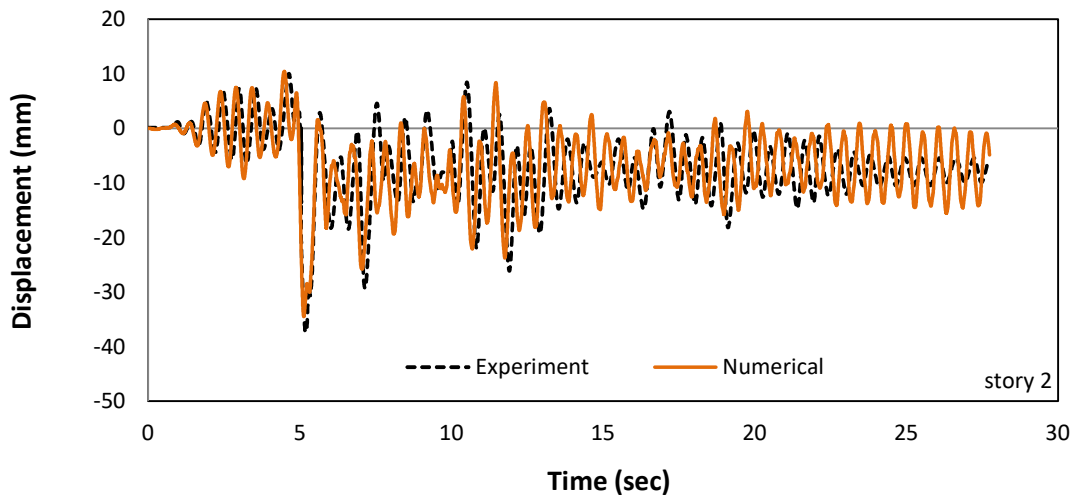
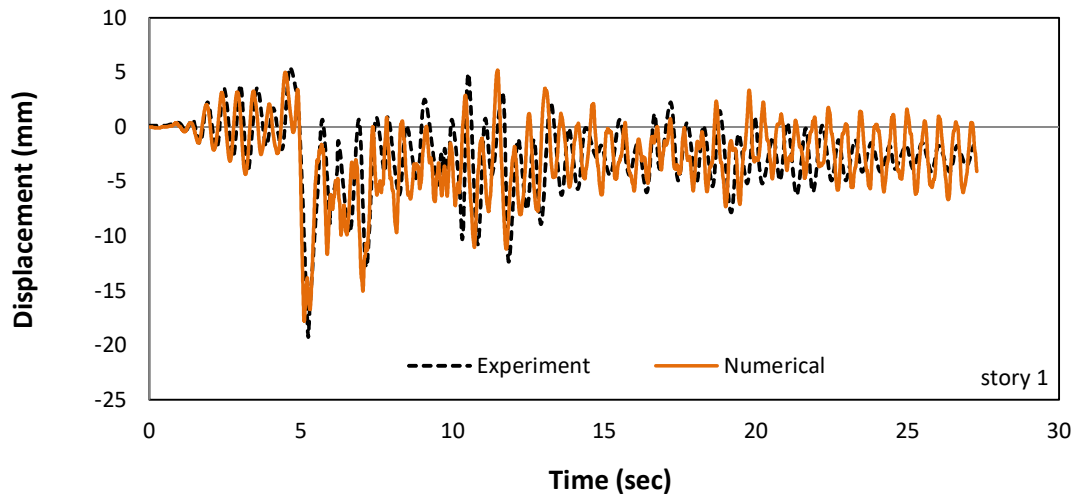


Figure 2.8. Comparison of Experimental and Numerical Results for Story Displacements

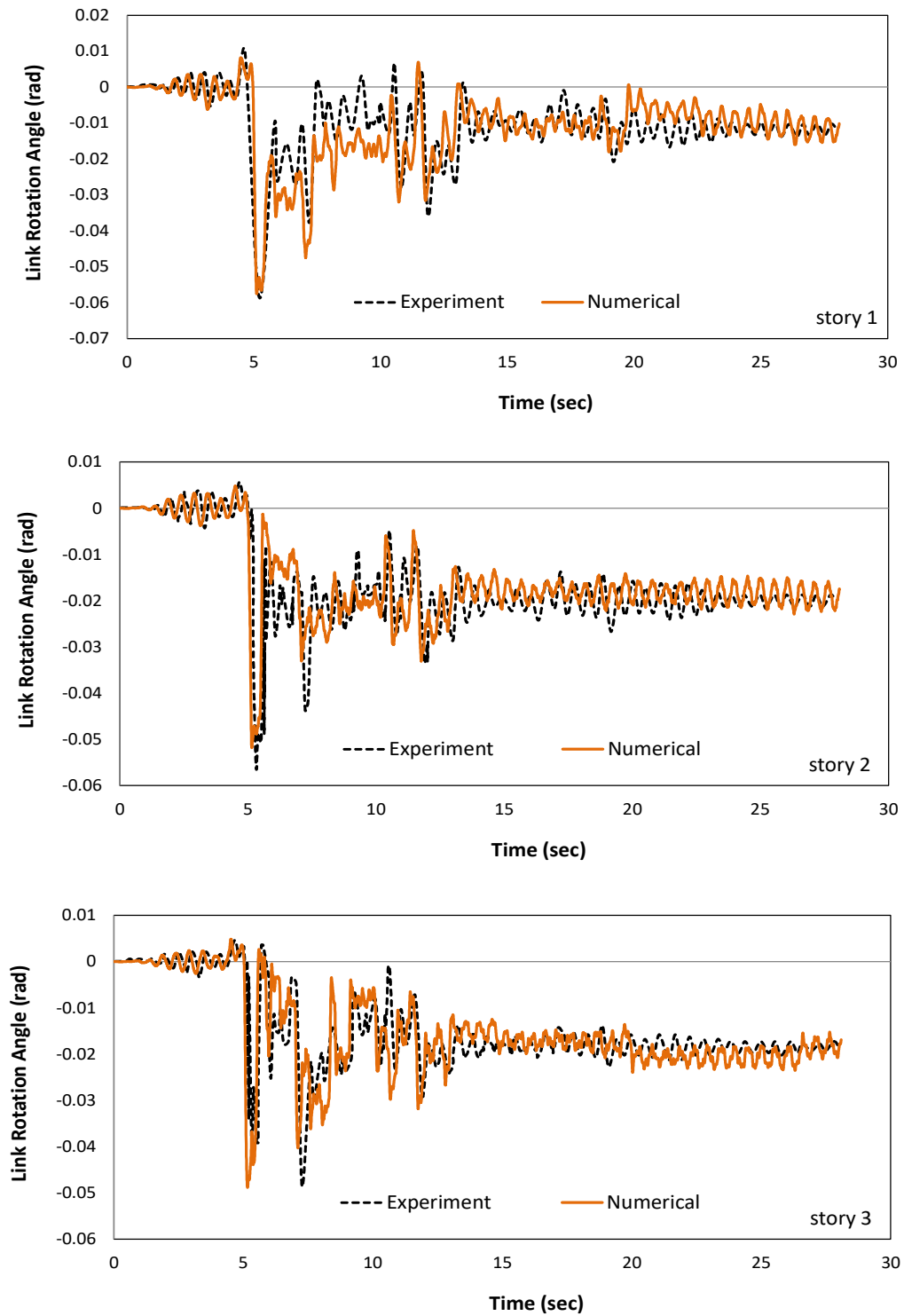


Figure 2.9. Comparison of Experimental and Numerical Results for Link Rotation Angles

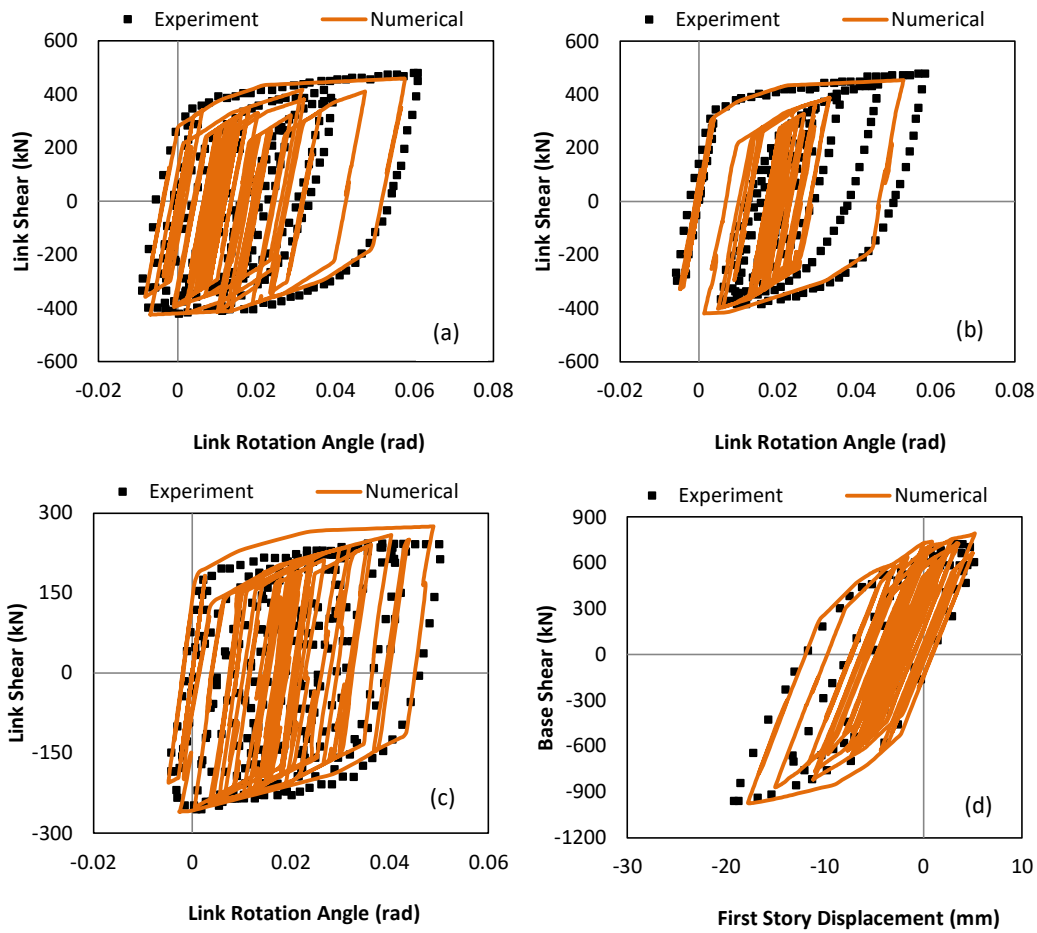


Figure 2.10. Comparison of Experimental and Numerical Results for (a) Link Rotation Angle versus Link Shear at Story 1 (b) Link Rotation Angle versus Link Shear at Story 2 (c) Link Rotation Angle versus Link Shear at Story 3 (d) Base Shear-First Story Displacement

Table 2.4. Comparison of Maximum Base Shear Values between the Experimental and Numerical Results

	Experimental	Numerical	Experimental/ Numerical
Base Shear Positive (kN)	720.94	793.73	0.91
Base Shear Negative (kN)	-960.26	-973.28	0.99

Table 2.5. Comparison of Maximum Story Displacement and Link Rotation Angle Values between the Experimental and Numerical Results

	Maximum Story Displacement			Maximum Link Rotation		
	Exp. (mm)	Num. (mm)	Exp/ Num	Exp. (rad)	Num. (rad)	Exp/ Num
First Story Positive	5.43	5.20	1.04	0.0096	0.0082	1.17
First Story Negative	-18.94	-17.79	1.06	-0.0585	-0.0575	1.02
Second Story Positive	9.93	10.39	0.96	0.0056	0.0048	1.16
Second Story Negative	-37.22	-34.47	1.08	-0.0565	-0.0518	1.09
Third Story Positive	14.70	15.40	0.95	0.0046	0.0048	0.95
Third Story Negative	-50.20	-50.68	0.99	-0.0486	-0.0489	0.99

Table 2.6. Comparison of Maximum Residual Story Displacement and Link Rotation Angle Values between the Experimental and Numerical Results

	Residual Story Displacement			Residual Link Rotation		
	Exp. (mm)	Num. (mm)	Exp/ Num	Exp. (rad)	Num. (rad)	Exp/ Num
First Story	-2.58	-2.79	0.93	-0.0116	-0.0116	1.00
Second Story	-7.42	-7.37	1.01	-0.0198	-0.0190	1.04
Third Story	-11.88	-11.88	1.00	-0.0183	-0.0187	0.98

The residual displacements reported in Table 2.4 were obtained by averaging the response in the last 5 seconds of the displacement history. The ratios of experimental to numerical responses are close to unity in most of the cases. The numerical estimates are within 10% of the experimental results indicating that the numerical model is capable of describing the overall behavior of the specimen. Responses presented in Figure 2.10 show that the adopted link model is also capable of

representing the response of shear links. When the displacement histories are examined, larger oscillations than the experimental ones are obtained for the last part of the loading. These differences can be attributable to the material damping effects and frictional response of bolted connections which are not simulated in the numerical model.

The sensitivity of the responses of the DUAREM structure to *SHR* was investigated using complementary numerical analysis. *SHR* values of 0.00001, 0.0005, 0.001, 0.002, 0.003, 0.005, 0.01 were considered. Three different seismic hazard levels were taken into account. The first one is with a PGA of 0.324g which corresponds to DBE level ground motion. The second one is with a PGA of 0.486g and corresponds to Maximum Considered Earthquake (MCE) level ground motion. The MCE level was obtained by amplifying the PGA for DBE with 1.5. The third one is with a PGA of 0.632g and corresponds to Collapse Level Earthquake (CLE). The CLE level was obtained by amplifying the PGA for MCE with 1.3. Complementary analyses results for the residual response, maximum response and base shear are given in Figures 2.11, 2.12 and 2.13 respectively. In these figures, the maximums of displacement, residual displacement, maximum link rotation angle, residual link rotation angle for all stories and the base shear are given as a function of the *SHR* for different hazard levels. The results show that among the EDPs the residual drift and residual link rotation are the most sensitive to the *SHR*. The observations of Mahdavi-pour and Deylami (2014) on BRBFs were found to be applicable to EBF systems. In other words, as the intensity of the ground motion increases, the effect of *SHR* is much more pronounced. The *SHR* has negligible effect on the maximum roof drift and maximum link rotation angle when the DUAREM structure is subjected to a DBE level ground motion. As the ground motion intensity increases, the effects of *SHR* are more noticeable.

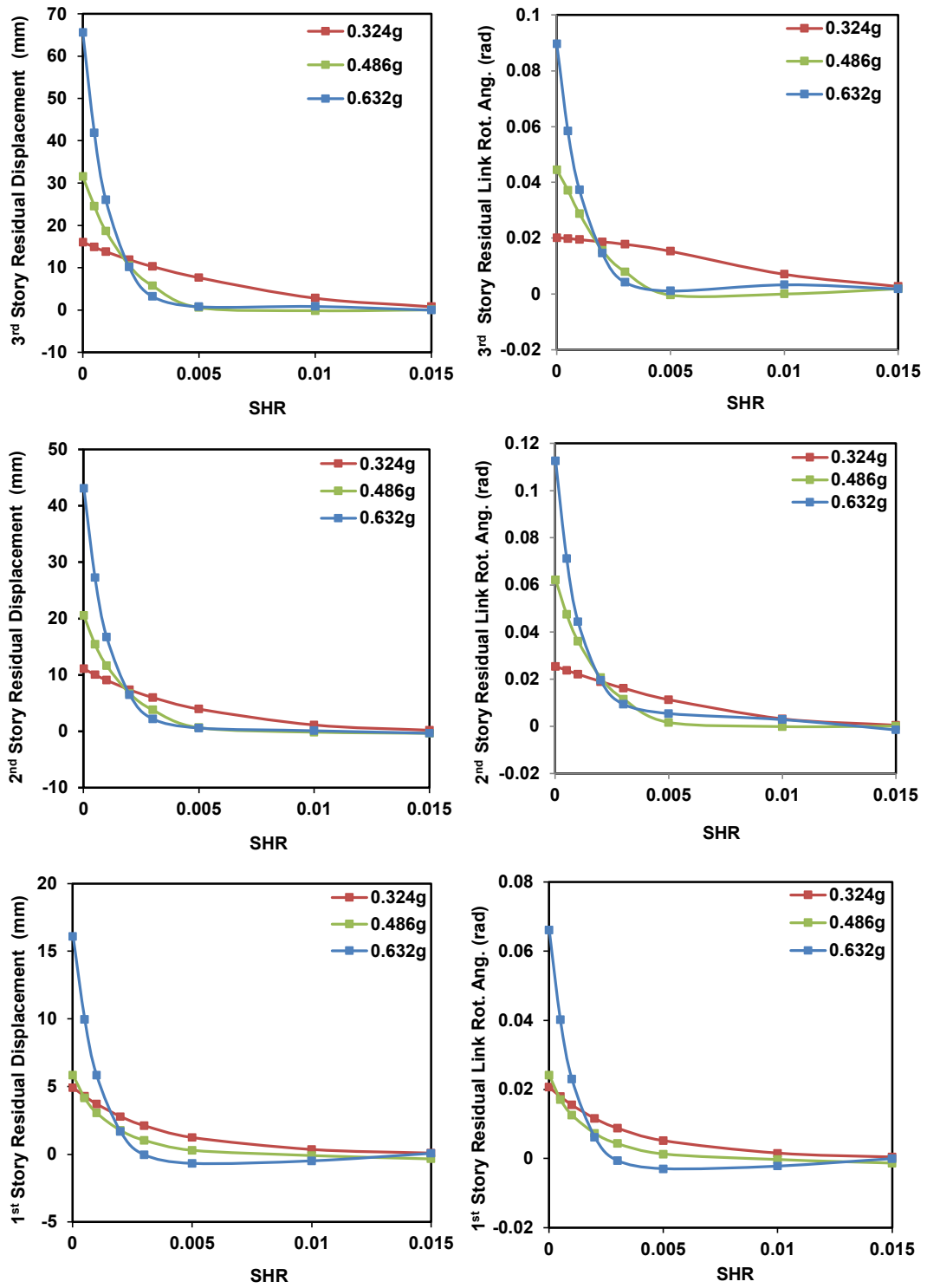


Figure 2.11. Effect of *SHR* on the Residual Response of the DUAREM Structure

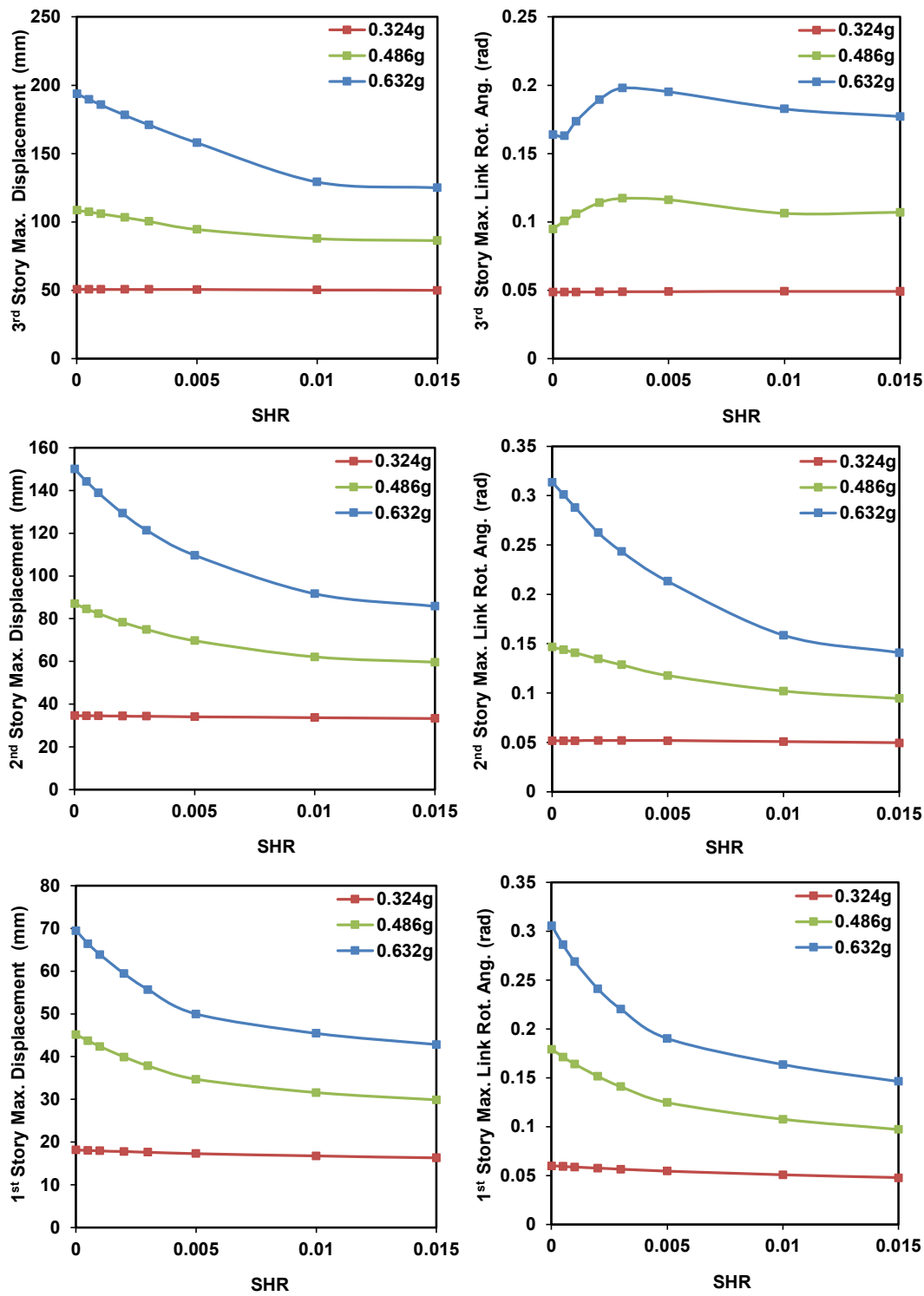


Figure 2.12. Effect of *SHR* on the Maximum Response of the DUAREM Structure

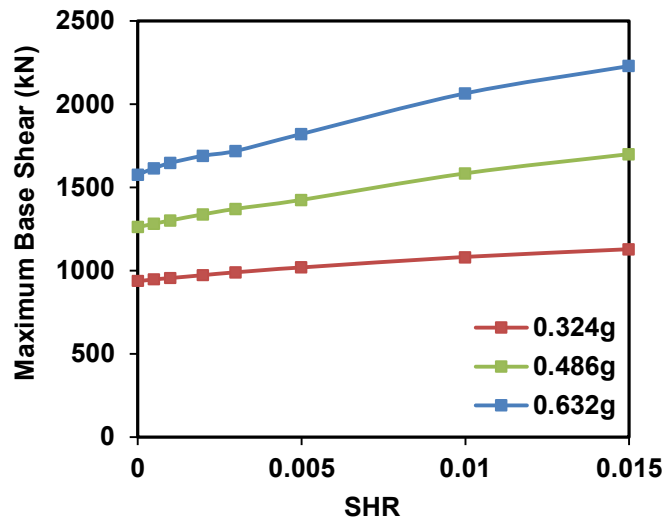


Figure 2.13. Effect of *SHR* on the Maximum Base Shear of the DUAREM Structure

2.4 Details of Parametric Study on Performance of EBF Archetypes

Six archetypes designed by Al-Janabi and Topkaya (2020) were considered for the parametric study. The archetypes have a floor plan of 54m×54m with bay widths of 9m in each direction as shown in Figure 2.14. The story height was 4m for all stories. Number of stories of 3, 6, 9 and link length to bay width ratios (e/L) of 0.08 and 0.12 were considered. The archetype EBFs were designed using equivalent lateral force (ELF) procedure proposed in ASCE 7-16 (2016). Seismic hazard level was determined according to FEMA P695 (2009) methodology where a Seismic Design Category (SDC) D_{max} was considered. The details of the archetypes are given in Tables 2.7 and 2.8 by using the identical naming convention used by Al-Janabi and Topkaya (2020). All links are shear yielding links.

The numerical modeling technique adopted for the simulation of DUAREM structure was used for the parametric study. An elastic leaning column was attached to the EBF by making use of stiff truss elements. The gravity loads tributary to each EBF was applied to the leaning column to take into account the P- Δ effects. All members were modeled to have a yield stress of 345 MPa. The links were modeled

using the approach presented in Section 2.2 and by adopting the non-linear shear force versus deformation response proposed by Richards and Uang (2004 and 2006). The *SHR* values of 0.0, 0.001, 0.002, 0.003, 0.005, 0.01 were considered in order to investigate the effect of *SHR* on engineering demand parameters (EDPs) and repair costs. The case with no strain hardening was designated as *SHR* = 0.0 in this section. However, *SHR* was defined as 0.00001 in the OpenSees numerical model because zero post yielding stiffness causes numerical instabilities in the MultiLinear Material model. A 2% damping was assigned to all members in the numerical model except the link members (Al-Janabi and Topkaya (2020)).

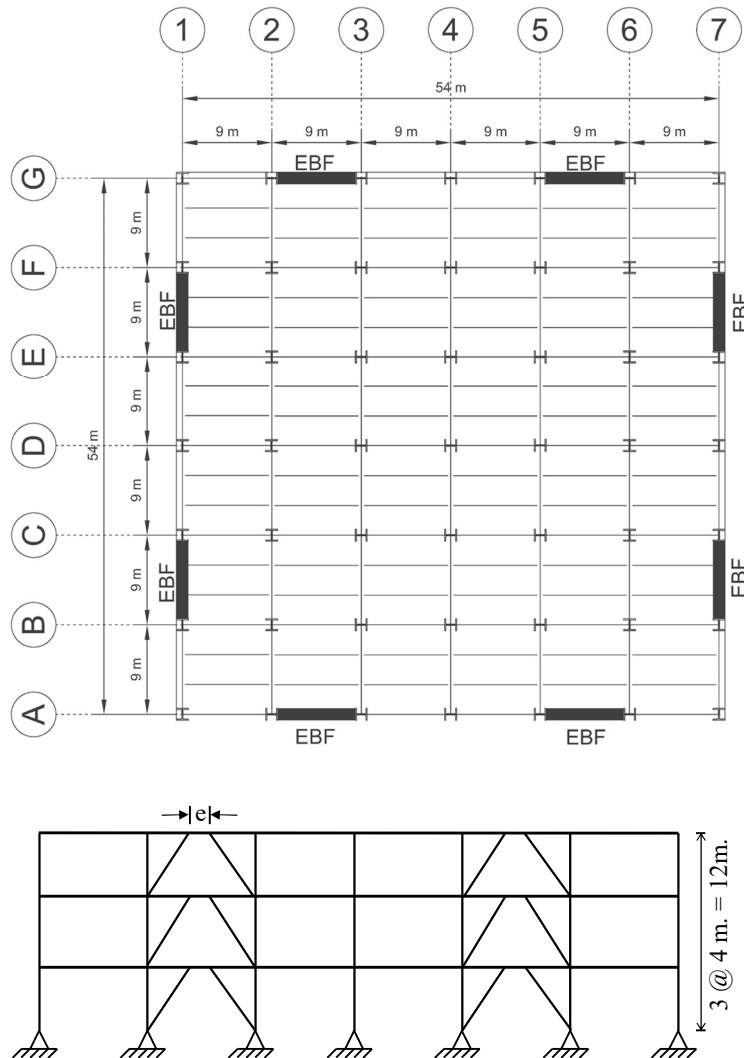


Figure 2.14. Floor Plan and Elevation View of Archetypes

Table 2.7. Archetype Properties and Scaling Factors

AT	Ns	e/L	Tanalysis (s)	Median MCE Scale Factor	Median CLE Scale Factor
AT1	3	0.08	0.67	2.44	3.20
AT3	3	0.12	0.74	2.50	3.20
AT5	6	0.08	1.25	2.61	3.34
AT7	6	0.12	1.39	2.49	2.99
AT9	9	0.08	1.70	3.10	4.03
AT11	9	0.12	2.07	3.02	3.53

Table 2.8. Member Sizes of Archetypes

AT	Story	Links	Braces	Columns	AT	Story	Links	Braces	Columns
AT1	1	18×35	16×67	14×132	AT3	1	16×50	12×72	14×132
	2	16×36	10×54	14×132		2	16×40	10×60	14×132
	3	14×22	10×49	14×132		3	10×39	10×49	14×132
AT5	1	21×44	12×72	14×159	AT7	1	18×55	12×72	14×159
	2	21×44	12×72	14×159		2	18×50	12×72	14×159
	3	21×44	12×72	14×159		3	16×50	12×72	14×159
	4	16×40	12×58	14×82		4	16×40	10×60	14×82
	5	16×31	12×53	14×82		5	12×40	10×49	14×82
	6	16×26	10×49	14×82		6	10×39	10×49	14×82
AT9	1	24×55	12×87	14×311	AT11	1	21×55	12×79	14×257
	2	24×55	12×87	14×311		2	21×55	12×79	14×257
	3	24×55	12×87	14×311		3	18×55	12×72	14×257
	4	24×55	12×87	14×211		4	16×50	12×72	14×159
	5	24×55	12×87	14×211		5	16×50	12×72	14×159
	6	21×62	12×79	14×211		6	14×61	10×60	14×159
	7	21×57	12×79	14×132		7	16×40	10×60	14×74
	8	21×57	12×79	14×132		8	12×40	10×49	14×74
	9	21×50	12×79	14×132		9	10×39	10×49	14×74

FEMA P-58 (2018) suggests that at least seven ground motion pairs should be used, regardless of the match with the target spectrum. If there exists a poor fit to the target spectrum, eleven or more pairs should be selected for a proper estimate of median response. Time history analyses in this study used the 22-pair far-field ground motion set of FEMA P695 (2009). Individual ground motions were scaled up to the MCE spectral demand of SDC D_{max} at the structure's fundamental period which was obtained from eigenvalue analysis (Table 2.7). Medians of individual scale factors of each archetype EBFs are given in Table 2.7. DBE, MCE, and CLE level ground motions were considered to take into account the variation in seismic hazard. DBE spectral demands were considered as 2/3 of the MCE spectral demands. Scaling factors for Collapse Level Earthquake (CLE) were determined by using Collapse Margin Ratio ($CMR_{10\%}$) values reported by Al-Janabi and Topkaya (2020). The MCE scaling factors were amplified by the $CMR_{10\%}$ to arrive at the CLE scaling factors (Table 2.7). Five-seconds of free vibration were added at the end of each individual ground motion. The residual drifts were calculated by averaging the response in the last 5 seconds.

2.5 Results of Time History Analysis

PACT (Performance Assessment Calculation Tool) program determines the required EDPs according to the structural system of interest. For EBFs, the required EDPs are the link rotation angle (LRA), interstory drift ratio (IDR), residual interstory drift ratio (RIDR) and story acceleration (SA). The sensitivity of each of these parameters to SHR is investigated in this section. The results of over 1500 time history analysis are too voluminous to present in every detail. Therefore, the maximum of any EDP from an analysis was recorded and the median of the responses from 44 ground motions are reported in the following subsections. The results are presented by considering the variation of EDPs along the height of the three-, six- and nine-story archetypes. In addition, the median response for any particular SHR was normalized by the median response obtained for $SHR=0.002$. The variations of the normalized

responses are presented for all the six archetypes studied within the context of the parametric study.

2.5.1 Link Rotation Angle

The variation of median link rotation angle for $e/L=0.08$ and $e/L=0.12$ archetypes is given in Figures 2.15 and 2.16 respectively where the responses under DBE, MCE and CLE level seismic hazards are presented separately. The median LRA reduced with increasing *SHR*. The differences become more pronounced at lower stories and at higher ground motion intensity levels. For 6- and 9-story archetypes, independent from the magnitude of the ground motion, *SHR* has no effect on LRA at the roof level. The normalized link rotation angles are reported in Figure 2.17 for the two e/L ratios studied. The LRA responses are observed to be more sensitive to *SHR* for $e/L=0.08$ when compared with the responses for $e/L=0.12$ regardless of the number of stories. For example, maximum LRA at MCE level ground motion, reduced from 0.319 rad to 0.215 rad as *SHR* increased from zero to 0.01 for AT1. On the other hand, maximum LRA at MCE level reduced only from 0.183 rad to 0.172 rad within the same *SHR* range for AT3. *SHR* values different than 0.002 resulted in changes less than 20 percent in the LRA response of archetypes with $e/L=0.12$. On the other hand, the changes are less than 40 percent for archetypes with $e/L=0.08$.

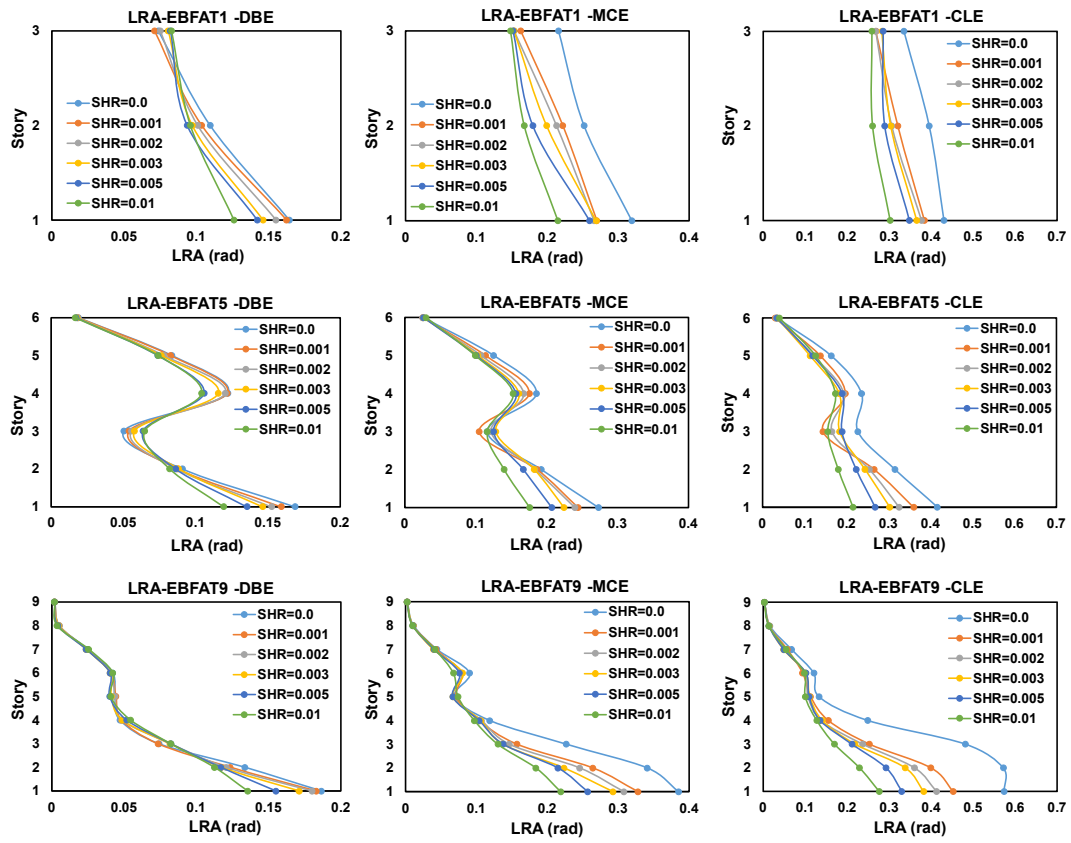


Figure 2.15. Link Rotation Angle Response for AT1, AT5 and AT9 ($e/L=0.08$)

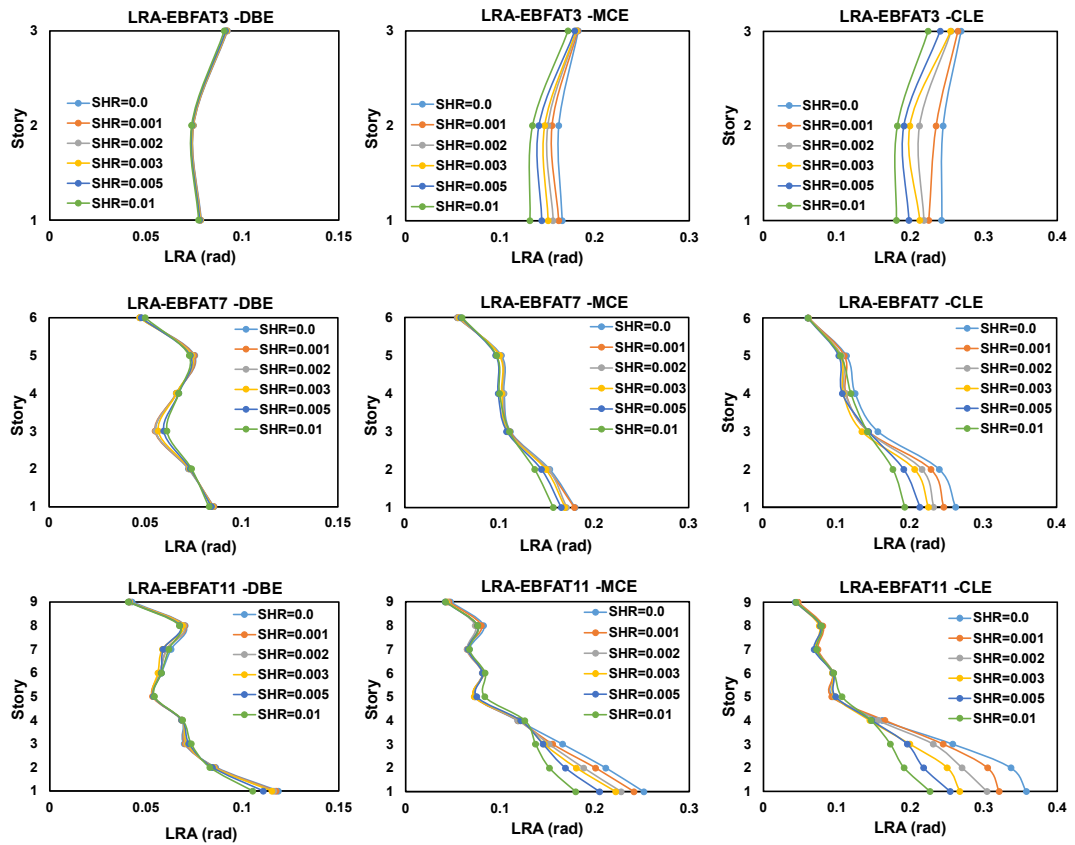


Figure 2.16. Link Rotation Angle Response for AT3, AT7 and AT11 ($e/L=0.12$)

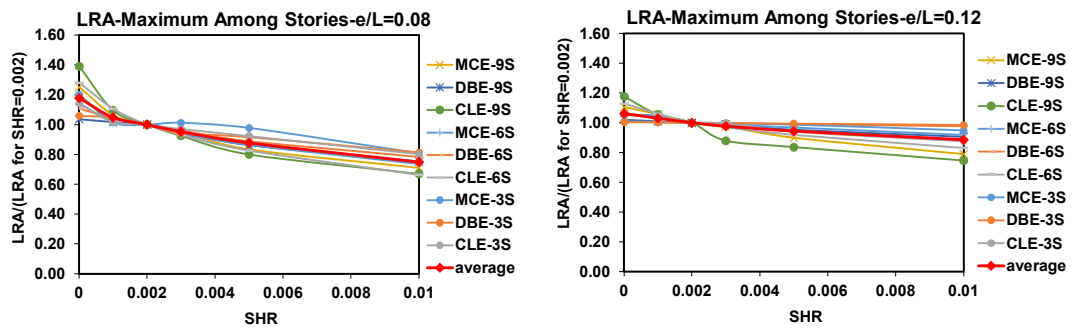


Figure 2.17. Effect of *SHR* on Normalized Link Rotation Angle

2.5.2 Interstory Drift Ratio

The variation of interstory drift ratios for all archetypes is given in Figure 2.18 and 2.19. Similar to the LRA, the median IDR is observed to decrease with an increase in *SHR*. The changes in IDR are more pronounced as the intensity of the ground motion increases. The normalized IDRs are reported in Figure 2.20 for the two *e/L* ratios studied. The changes in IDR are less when compared with the changes in LRA. In fact LRA and IDR are interdependent EDPs. The LRA can be calculated from IDR using the rigid-plastic mechanism recommended in AISC341. This approach, however, does not take into account the deformations of the members other than the links. The IDR is influenced by the LRA and also by the elastic deformation of the columns, collector beams and braces. A change in the value of *SHR* directly influences the value of LRA. On the other hand, the effect of *SHR* on IDR is less pronounced because the *SHR* influences the LRA but not the elastic deformations of the members other than the links. Data presented in Figure 2.20 suggests that *SHR* values different than 0.002 resulted in changes less than 20 percent in the LRA response of archetypes with $e/L=0.08$ and $e/L=0.12$. There are only a few cases where the differences exceed 20 percent and these belong to $SHR=0$.

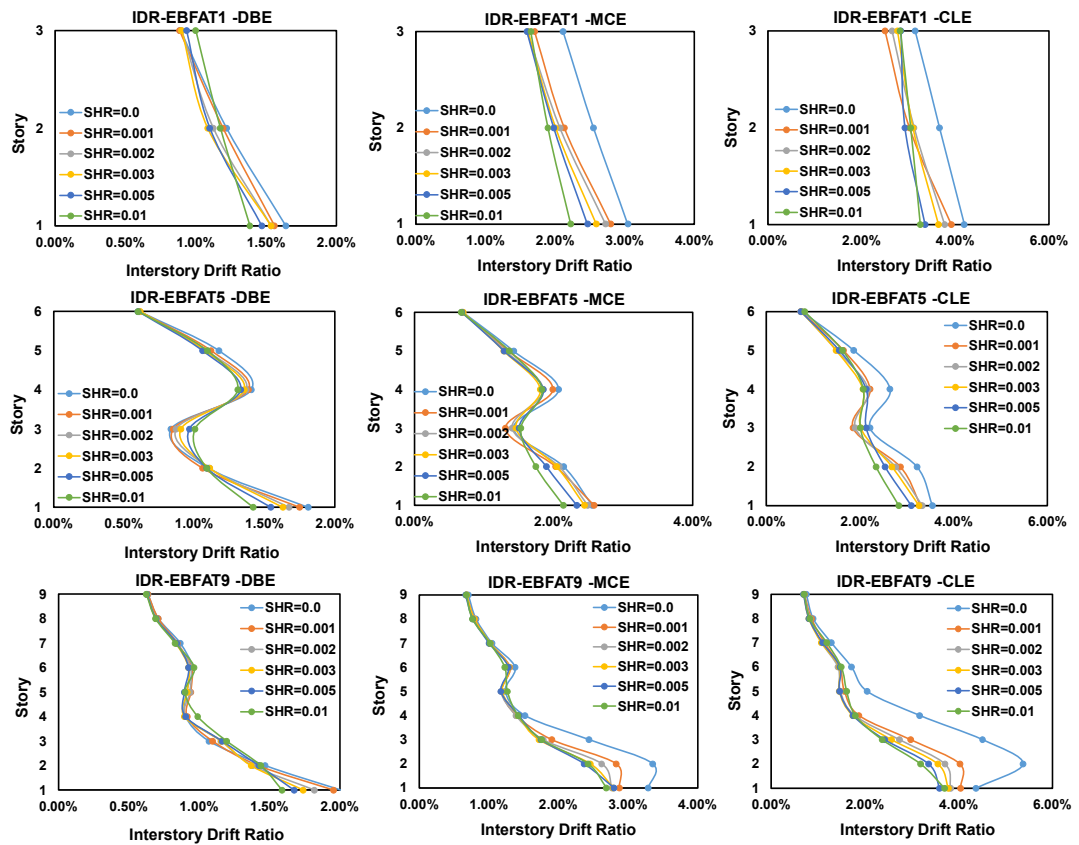


Figure 2.18. Interstory Drift Response for AT1, AT5 and AT9 ($e/L=0.08$)

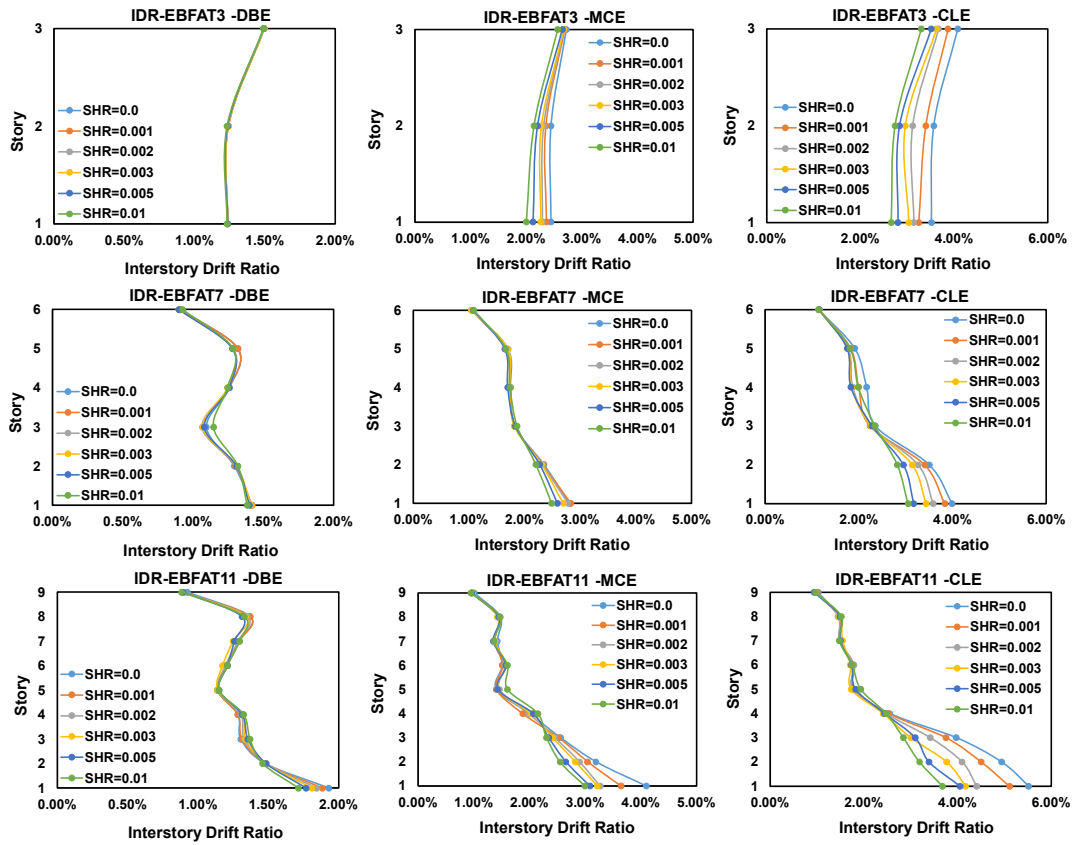


Figure 2.19. Interstory Drift Response for AT3, AT7 and AT11 ($e/L=0.12$)

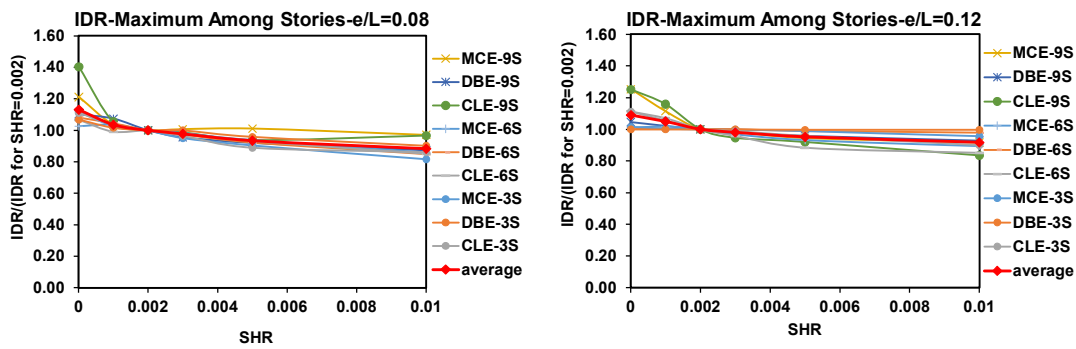


Figure 2.20. Effect of SHR on Normalized Interstory Drift

2.5.3 Residual Interstory Drift Ratio

The variation of residual interstory drift ratio for $e/L=0.08$ archetypes is given in Figure 2.21 and $e/L=0.12$ archetypes is given in Figure 2.22. Similar to the LRA and IDR responses, the RIDR reduces by increasing SHR . The changes are more significant for the CLE seismic hazard. Unlike LRA and IDR, the RIDR responses are significantly influenced by the value of SHR . A similar outcome was obtained by the parametric study on the DUAREM structure. The normalized RIDRs are reported in Figure 2.23 for the two e/L ratios studied. There are marked differences in the behaviors of archetypes with $e/L=0.08$ and $e/L=0.12$. For both the e/L ratios there is a similar decrease in RIDR with an increase in SHR from 0.002 to 0.01 where the decreases for $e/L=0.08$ is slightly more than the ones for $e/L=0.12$. For SHR values less than 0.002, the RIDR ratios can be as high as 3.5 times for $e/L=0.08$ and 1.67 times for $e/L=0.12$. The results are in line with the findings of Mahdavi-pour and Deylami (2014) in terms of the dependence of RIDR on the SHR and seismic hazard.

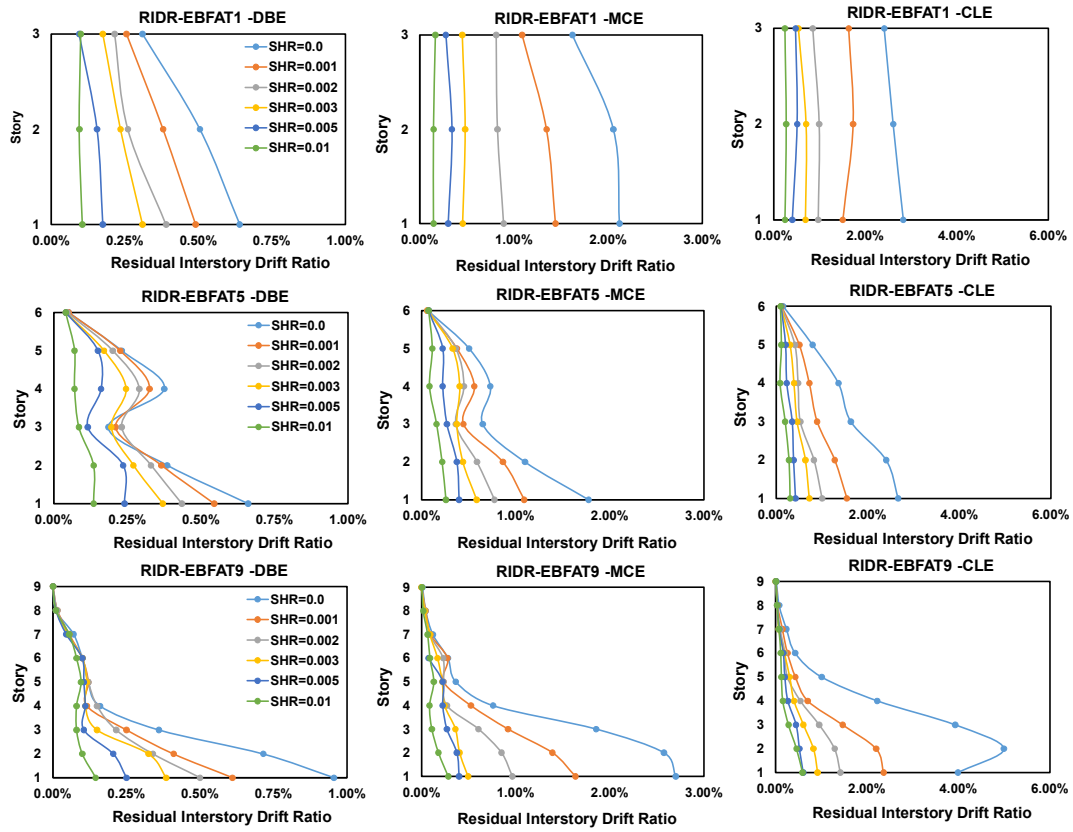


Figure 2.21. Residual Interstory Drift Response for AT1, AT5 and AT9 ($e/L=0.08$)

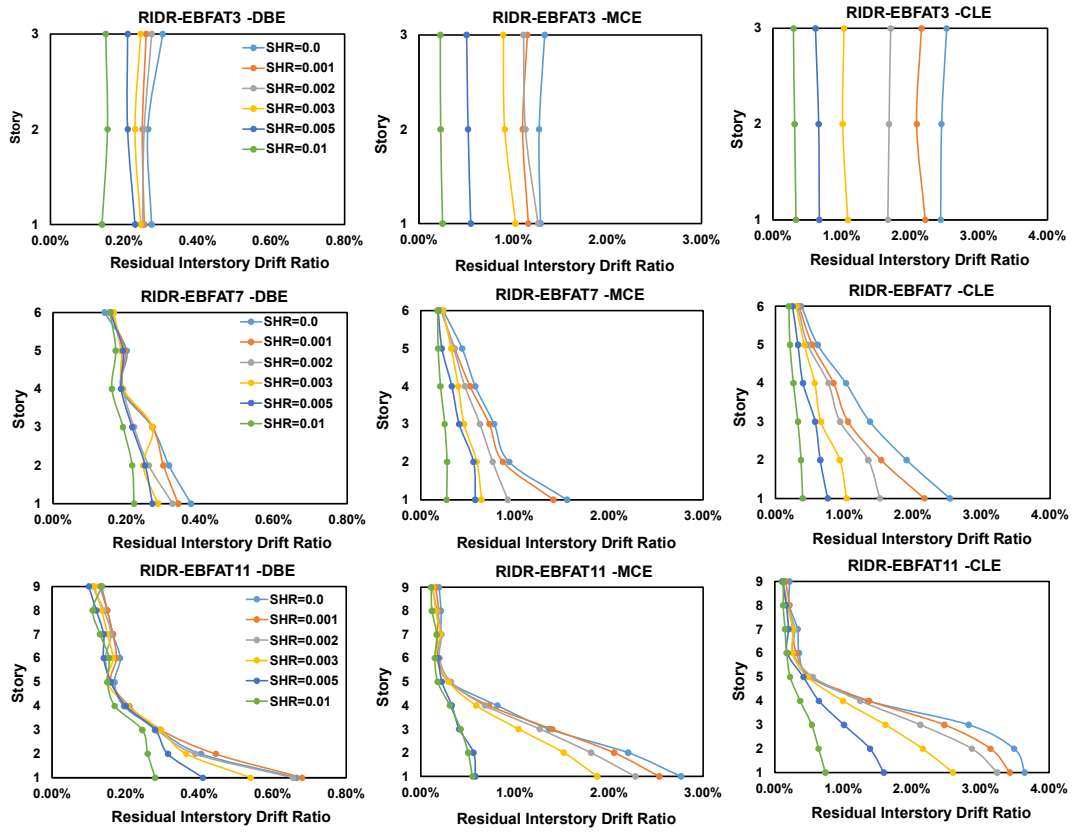


Figure 2.22. Residual Interstory Drift Response for AT3, AT7 and AT11 ($e/L=0.12$)

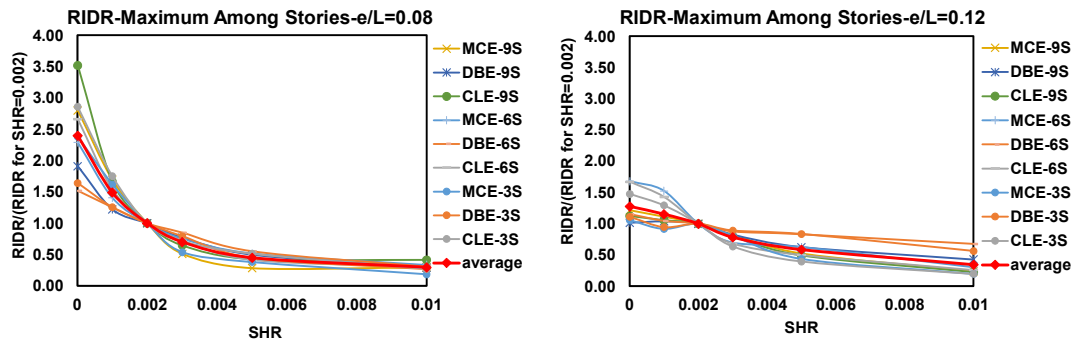


Figure 2.23. Effect of SHR on Normalized Residual Interstory Drift

2.5.4 Story Acceleration

The variation of story acceleration for all archetypes and normalized maximum story accelerations is given in Figure 2.24, 2.25 and 2.26 respectively. The effect of *SHR* on the SA response is negligible. Among all EDPs, the SA is the one that has almost no dependency on *SHR*.

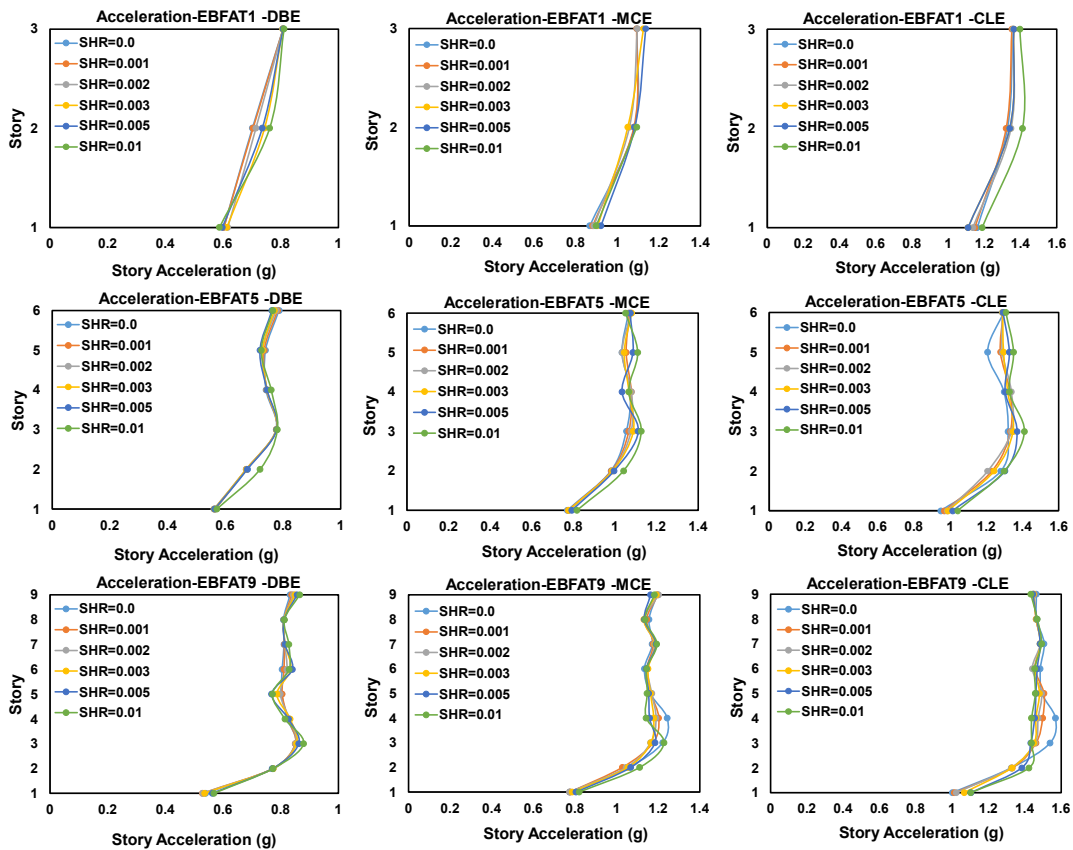


Figure 2.24. Story Acceleration Response for AT1, AT5 and AT9 ($e/L=0.08$)

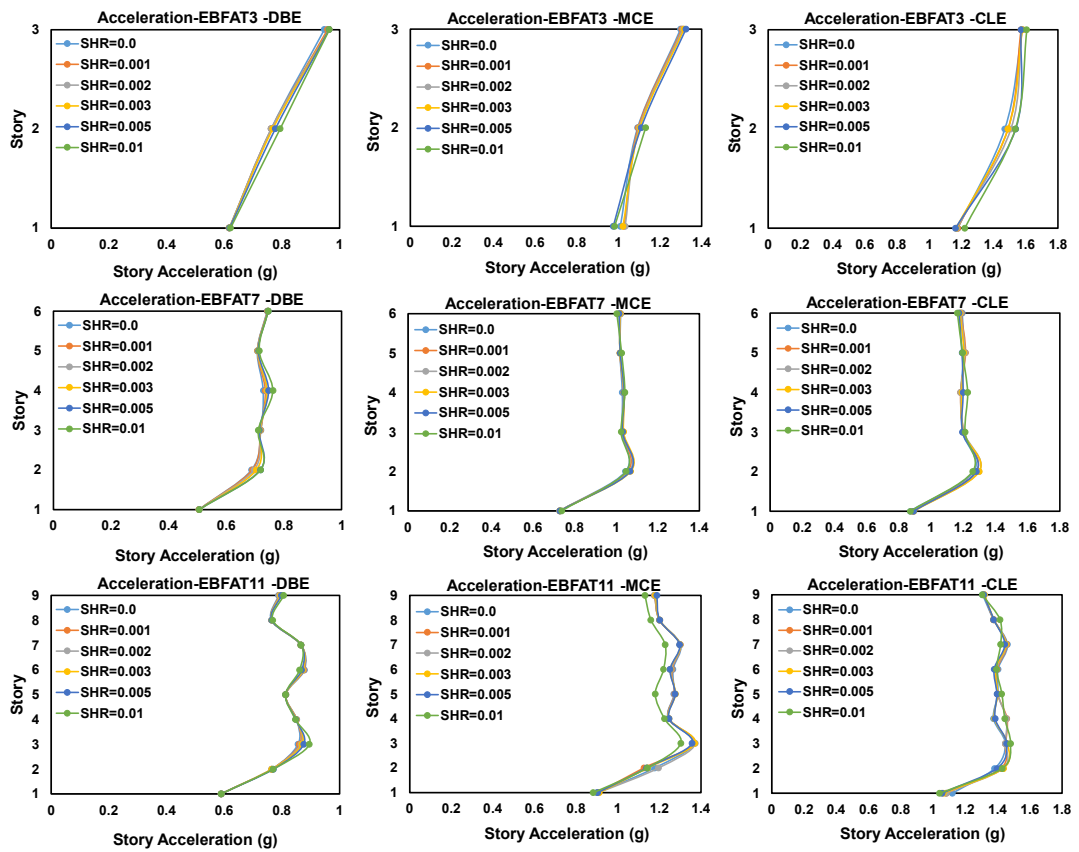


Figure 2.25. Story Acceleration Response for AT3, AT7 and AT11 ($e/L=0.12$)

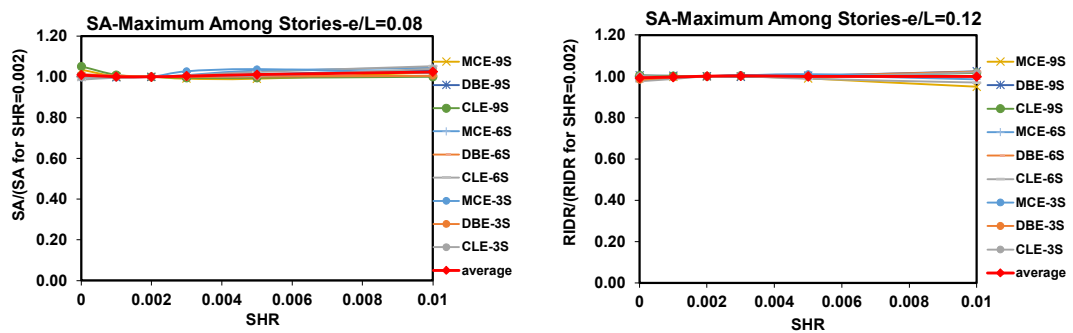


Figure 2.26. Effect of SHR on Story Acceleration

2.6 Seismic Performance Assessment of Archetypes

Seismic performances of the archetypes were evaluated by making use of FEMA P-58 (2018) methodology which quantifies the performance measures as repair cost, repair time and unsafe placards. PACT software, which is used alongside FEMA P-58 (2018) methodology, requires building information, total replacement cost, total loss threshold, occupancy type, structural and non-structural components, and engineering demand parameters to calculate performance measures. Building information can be obtained from plan and elevation views of archetype structures (Figure 2.14). Güner and Topkaya (2020) considered a constant replacement cost of \$1,900 per square meter for 3-, 6- and 9-story buildings using the RSMeans square foot cost estimator (<https://www.rsmeans.com>, 2020) based on 2011 data. Total replacement costs were determined as \$16,621,200, \$33,242,400 and \$49,863,600 for 3-, 6- and 9-story archetypes, respectively.

Total loss threshold is the limiting ratio of repair cost to the replacement cost. When this limiting ratio is exceeded, the stakeholder is advised to replace the structure rather than repair it. Based on past studies, FEMA P-58 (2018) suggest that it is reasonable to replace the building when the repair cost exceeds 40% of the replacement cost (i.e. total loss threshold = 0.4). In this study, the total loss threshold is considered as 1.0 in order to provide a fair comparison between the true consequences of the repair costs of archetype EBFs.

The occupancy type was considered as commercial office for all archetypes. Structural components were determined using floor plan and elevation view in Figure 2.14. Non-structural component quantities were determined using a supplementary file, Normative Quantity Spreadsheet provided by FEMA P-58. In this study, default fragility functions provided in FEMA P-58, for structural and non-structural components were adopted. FEMA P-58 allows identifying seismic performance using either correlated or uncorrelated damage. Correlated damage means, all components within a performance group experiences an identical damage (Hamburger et al. (2012)). This reduces the computational effort but increases the

uncertainty. All performance groups were assumed to be correlated because the intent of the current study is to compare repair costs for different *SHR* values rather than estimating an accurate repair cost. Table 2.9 shows the structural and non-structural fragilities per each story for 3-story archetype EBFs. For 6- and 9-story archetype EBFs, the fragilities which were assigned to “All” stories are the same as reported in Table 2.9. Fragilities that were assigned only to the “Roof” level and D1014.011 Traction Elevator change in quantity for different number of stories.

Table 2.9 Structural and nonstructural fragilities used in PACT Model

Stories	No.	Component Name	Quan.	Dir.	Demand Parameter
All	B1031.001	Bolted shear tab gravity connections	76	Yes	Story Drift Ratio
1st	B1031.011a	Steel Column Base Plates, Column W < 150 plf	8	Yes	Story Drift Ratio
All	B1035.062a	EBF Shear Link, with floor beams, link w < 100 PLF	4	Yes	Link Rotation Angle
All	B2022.001	Curtain Walls	313.88	Yes	Story Drift Ratio
All	C1011.001a	Wall Partition, Type: Gypsum with metal studs	31.39	Yes	Story Drift Ratio
All	C2011.001b	Prefabricated steel stair	4	Yes	Story Drift Ratio
All	C3011.001a	Wall Partition, Type: Gypsum + Wallpaper	2.37	Yes	Story Drift Ratio
All	B3011.011	Concrete tile roof	84.75	No	Acceleration
All	C3027.001	Raised Access Floor	235.41	No	Acceleration
All	C3032.001a	Suspended Ceiling	125.55	No	Acceleration
All	C3034.001	Independent Pendant Lighting	941.64	No	Acceleration
1st	D1014.011	Traction Elevator	3	No	Acceleration
All	D2021.011a	Cold or Hot Potable	1.32	No	Acceleration
All	D3041.011a	HVAC Galvanized Sheet Metal Ducting	2.35	No	Acceleration
All	D3041.012a	HVAC Galvanized Sheet Metal Ducting	0.63	No	Acceleration

Table 2.9 (continued)

Stories	No.	Component Name	Quan.	Dir.	Demand Parameter
All	D3041.031a	HVAC Drops / Diffusers is Suspended Ceilings	28.25	No	Acceleration
All	D3041.041a	Variable Air Volume (VAV) box with in-line coil	21.97	No	Acceleration
All	D4011.021a	Fire Sprinkler Water Piping	6.28	No	Acceleration
All	D4011.031a	Fire Sprinkler Drop Standard Threaded Steel	2.82	No	Acceleration
Roof	D3031.011a	Chiller - Capacity: < 100 Ton	3.58	No	Acceleration
Roof	D3031.021a	Cooling Tower - Capacity: < 100 Ton	3.58	No	Acceleration
Roof	D3041.101a	HVAC Fan - Capacity: all	1	No	Acceleration
Roof	D3052.011a	Air Handling Unit - Capacity: <5000 CFM	16.48	No	Acceleration
Roof	D5011.011a	Transformer/primary service - Capacity: <100 kVA	1	No	Acceleration
Roof	D5012.013a	Motor Control Center - Capacity: all	3.77	No	Acceleration
Roof	D5012.031a	Distribution Panel - Capacity: 100 to <350 Amp	1	No	Acceleration

Time history analyses were conducted for DBE, MCE and CLE level seismic hazards as explained in the previous section. The time history analysis results were paired and defined in two perpendicular directions in PACT analysis. Twenty-two pairs of link rotation angle, interstory drift and story acceleration were calculated for 6-archetypes, 3 ground motion intensity levels and 6 different *SHR* values at each floor. Maximum residual interstory drift ratios among all stories, for each 22 ground motion pair were also defined in PACT. Two-hundred Monte Carlo Realizations were used as suggested by FEMA P-58 (2018).

FEMA P-58 (2018) suggests a median irreparable residual drift ratio and dispersion of 1% and 0.3 respectively. According to McCormick et al. (2008), 0.5% residual deformation is perceivable by the occupants and after this limit the structure may

need to be replaced. Preliminary performance assessment of the archetype buildings showed that majority of the buildings would have to be replaced if irreparable residual drift ratio limit is considered as 0.5%. As a result, the effect of *SHR* values on the repair cost could not be fairly compared. Therefore, default median irreparable residual drift ratio (1%) and dispersion (0.3) values of PACT were considered in this study. The repair cost performance of the archetypes with different *SHR* values were compared in terms of median confidence level. The following subsections provide information about the performance metrics.

2.6.1 Probabilistic Distribution of Repair Cost

The probabilistic distribution of repair costs for 3-, 6- and 9-story archetypes under different ground motion intensity levels are presented in Figures 2.27, 2.28, and 2.29, respectively. In these figures, the black dashed line represents the median confidence level. The results indicate that the repair costs depend significantly on the *SHR*. An increase in the value of *SHR* results in a reduction in the repair costs.

For a median confidence level, 3-story EBFs do not require replacement under DBE level ground motion for all *SHR* values considered. A 3-story EBF with $SHR = 0.002$ (i.e. the reference case) is expected to be replaced when subjected to MCE or CLE level earthquakes. Similar observations can be drawn for 6-story EBFs. However, for these cases, EBFs with low *SHR* values are expected to be replaced even after DBE level earthquakes. A 9-story EBF had a larger probability of replacement when compared with 3- and 6-story archetypes.

The median repair costs were normalized by the initial costs and the ratios are presented in Figure 2.30 for EBFs subjected to DBE, MCE, and CLE level ground motions. If replacement is not required because of irreparable residual drift, the ratio between the median repair cost to the initial cost would be approximately 23%, 37% and 48% for DBE, MCE and CLE level events, respectively. These ratios are slightly sensitive to the *SHR* value. On the other hand, *SHR* plays an important role in

deciding whether a structure should be replaced or repaired especially for 6- and 9-story EBFs. The decision of replacement depends on e/L ratio, number of stories, seismic hazard and SHR value as given in Figure 2.30. Figure 2.31 shows the comparison between the normalized median repair costs of EBFs with $e/L = 0.08$ and $e/L = 0.12$. EBFs with shorter link length ratios are expected to have lower probability of replacement. Repair times are not reported for brevity; however these were observed to show a very similar trend with the repair costs. If the structure should be replaced, then the time required for total replacement is obtained. Otherwise, a repair time is determined which is slightly sensitive to the SHR value.

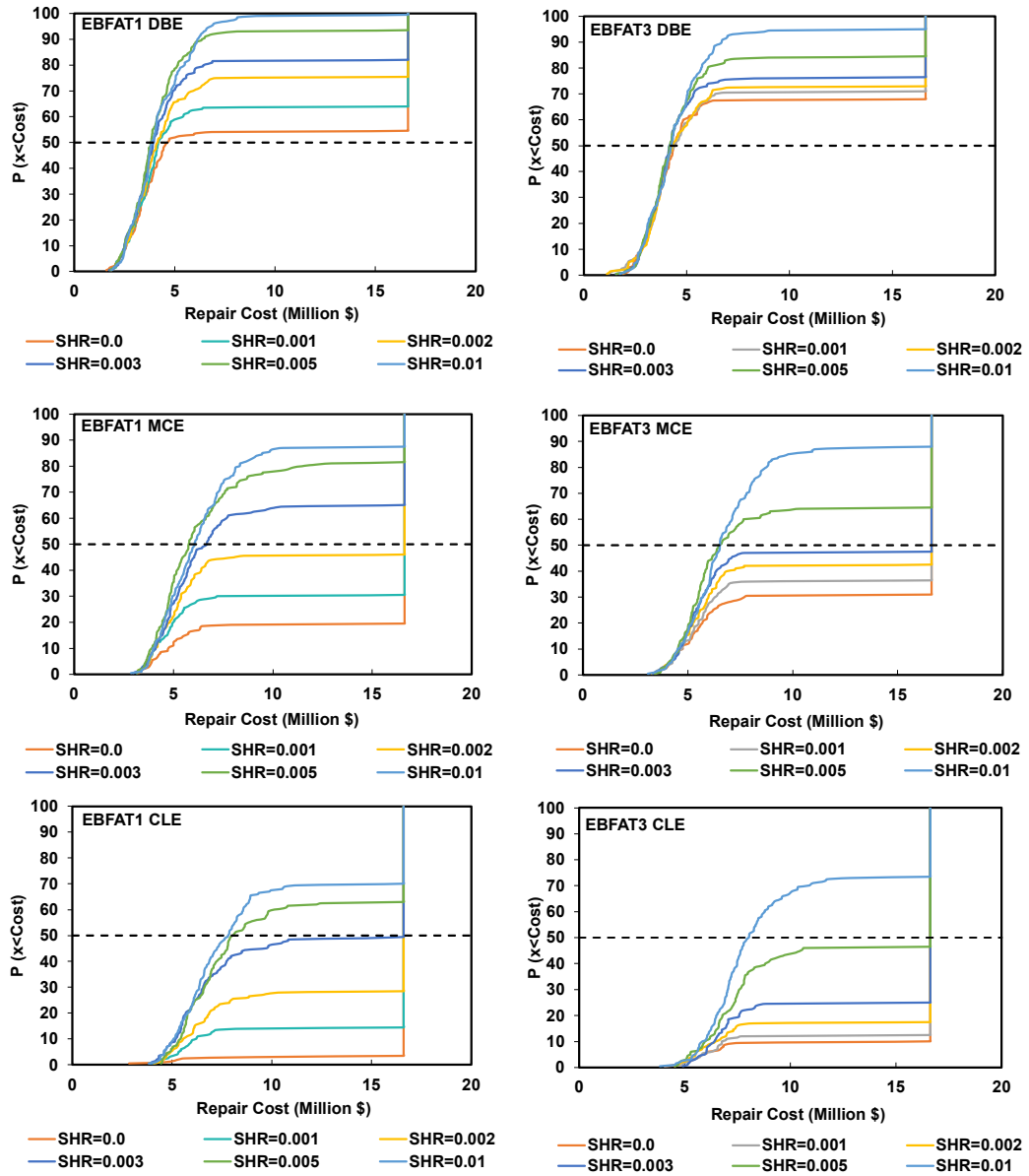


Figure 2.27. Probabilistic Distribution of Repair Costs under DBE, MCE and CLE Level Seismic Events (3-story archetypes)

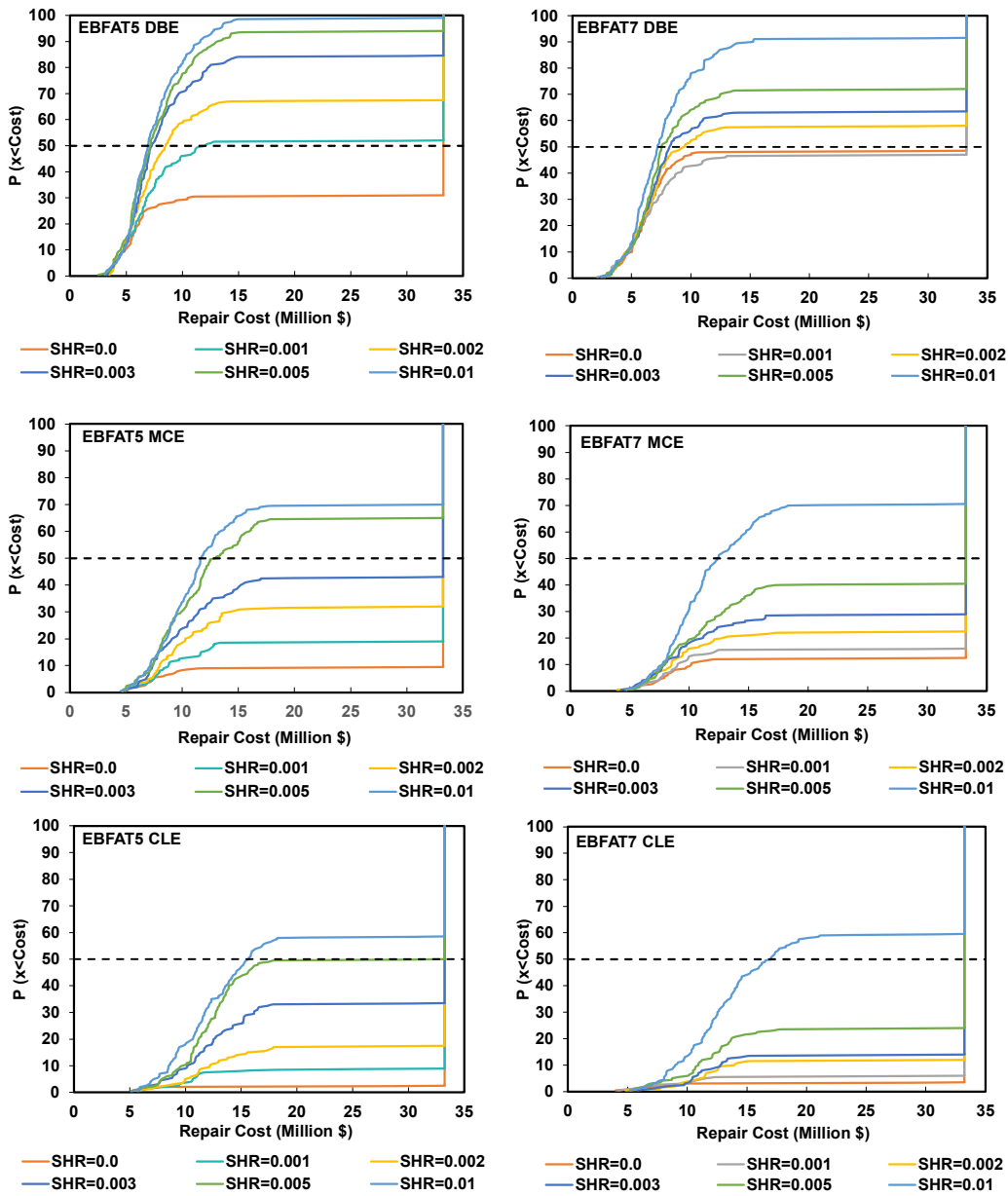


Figure 2.28. Probabilistic Distribution of Repair Costs under DBE, MCE and CLE Level Seismic Events (6-story archetypes)

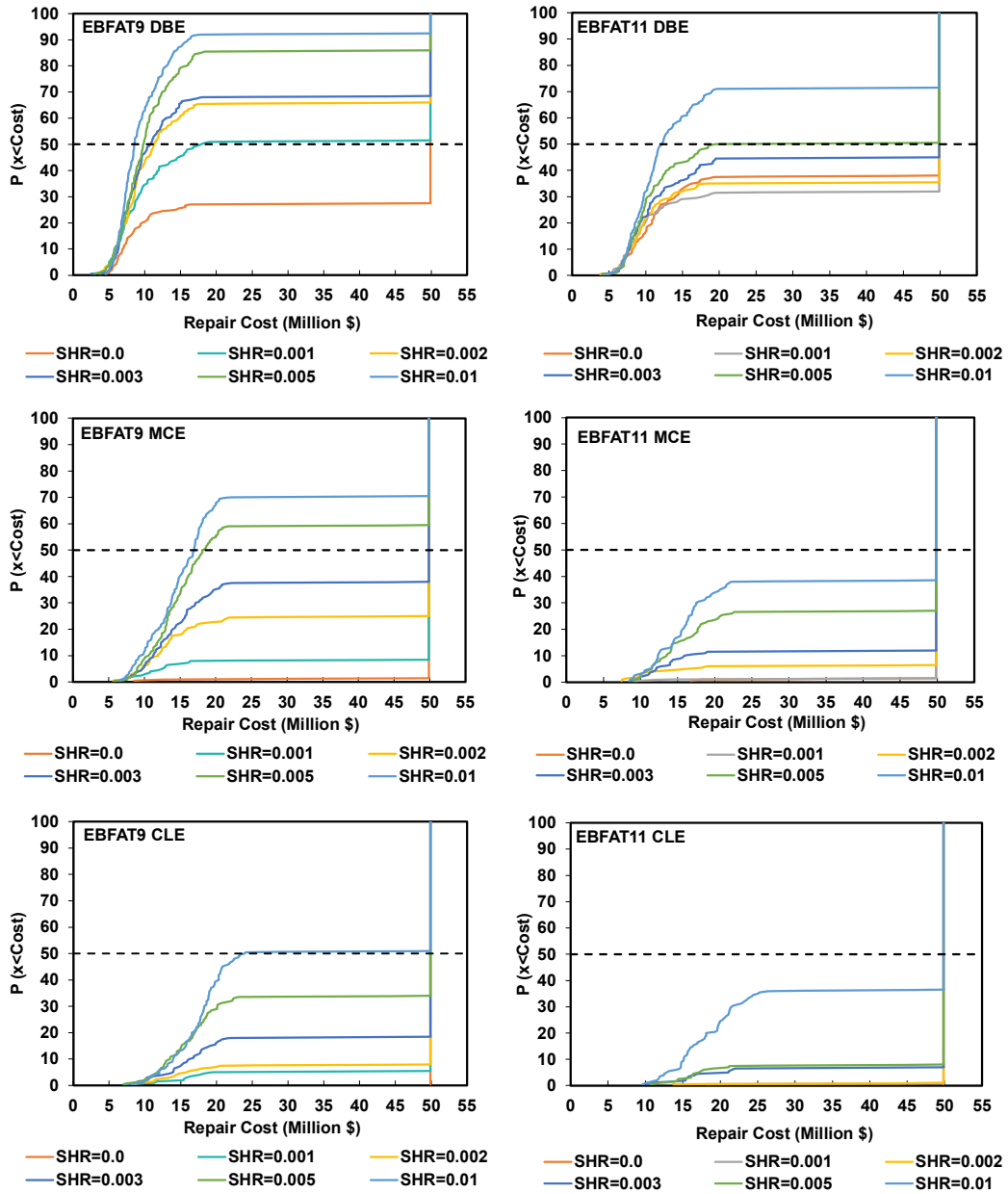


Figure 2.29. Probabilistic Distribution of Repair Costs under DBE, MCE and CLE Level Seismic Events (9-story archetypes)

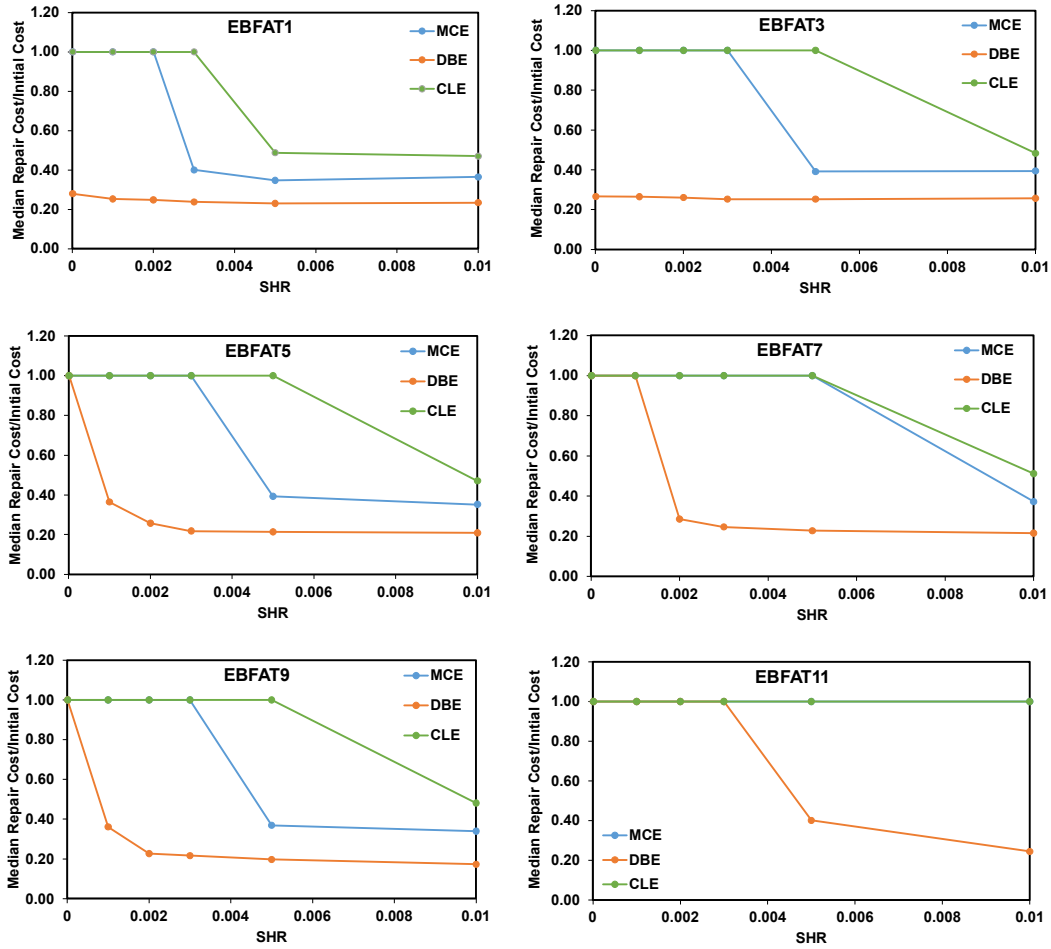


Figure 2.30. Ratio of Median Repair Cost to Initial Cost

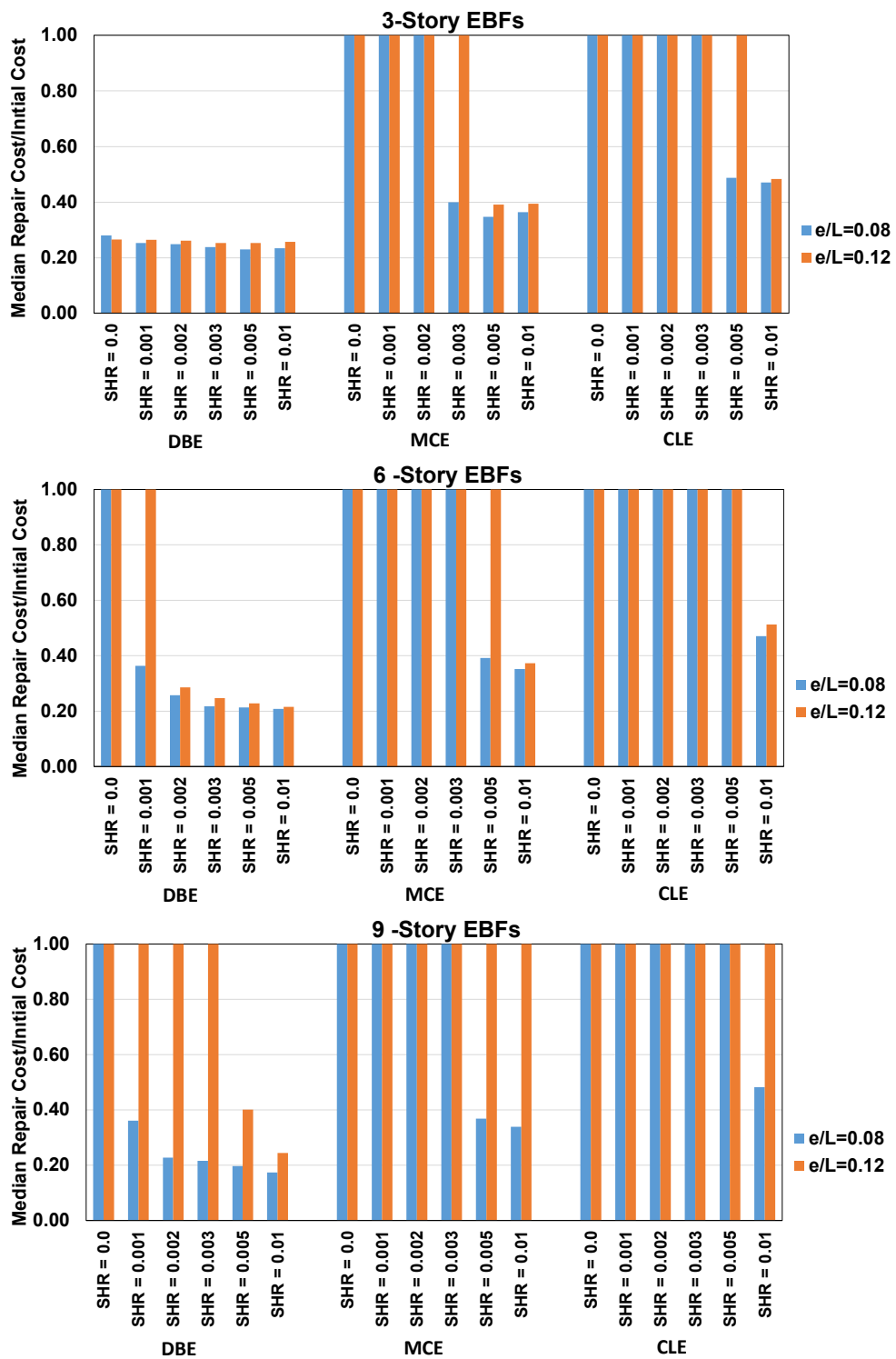


Figure 2.31. Comparison of the Ratio of Median Repair Cost to Initial Cost for EBFs with $e/L = 0.08$ and $e/L = 0.12$

2.6.2 Irreparable Residual Drift

If the maximum residual drift ratio renders a building irreparable, then the computed repair costs and repair times are discarded and the total replacement cost and replacement times are assigned to the realization (FEMA P-58 (2018)). As discussed before, FEMA P-58 (2018) suggests a median irreparable residual drift ratio and dispersion of 1% and 0.3, respectively. Figure 2.32 presents the irreparable residual drift probabilities after 200 Monte Carlo Simulations for each archetype. The probability is observed to be highly sensitive to *SHR* and decreases with increasing *SHR*. Once the irreparable residual drift exceeds 50%, the structure is considered to be irreparable according to PACT analysis. In other words, total replacement is necessary. Irreparable residual drift is the major reason behind the replacement decision and is significantly influenced by *SHR*.

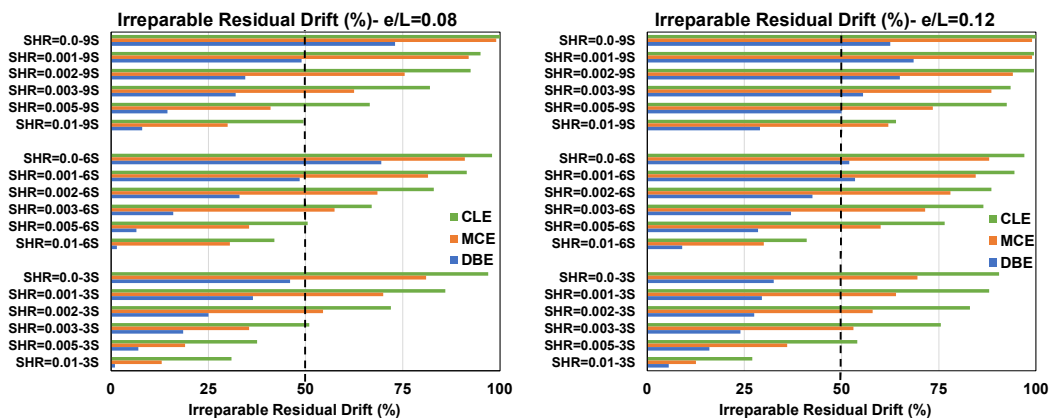


Figure 2.32. Irreparable Residual Drift

FEMA P-58 (2018) allows disregarding irreparable residual deformation if there is no need to use residual drift in the performance assessments. On the other hand, irreparable residual drifts are substantially important in replacement decisions. Jarrett et al. (2015) deliberately excluded residual drifts in performance assessment of seismic resisting systems in order to make a fair comparison of repair costs. The probabilistic distributions of repair costs for AT5 after MCE level events are given in Figure 2.28 for the case where the residual drifts are taken into account. The

distributions were determined for the same archetype without considering the residual drifts and the results are given in Figure 2.33 for comparison. It can be observed that while *SHR* has a major effect on the repair costs when residual drifts are considered, the effect of *SHR* is relatively minor when residual drifts are not considered.

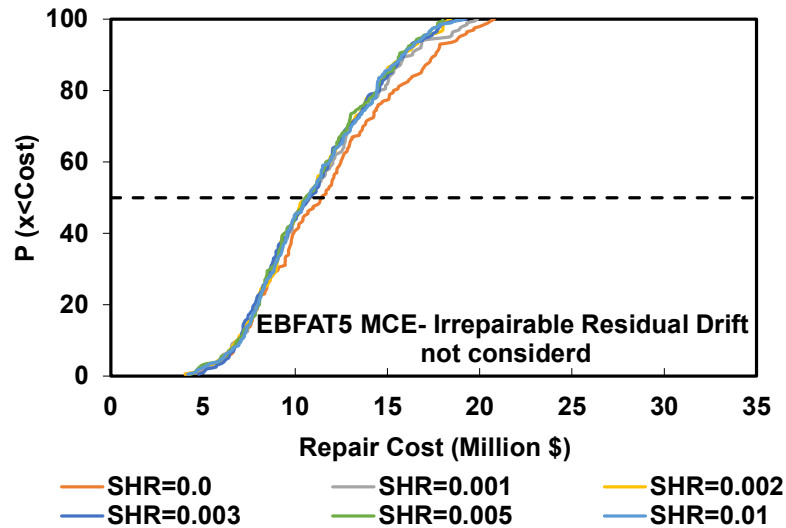


Figure 2.33. Probabilistic Distribution of Repair Costs under MCE Level Seismic Events for AT5 (Irreparable Residual Drifts not Considered)

2.6.3 Unsafe Placards

Unsafe placarding is defined as a post-earthquake inspection rating that deems a building, or portion of a building, damaged to the point that entry, use, or occupancy poses immediate risk to safety (FEMA P-58 (2018)). In this study, link rotation angles were the main reason for the unsafe placarding. In other words, unsafe placarding was observed to depend highly on EBF shear link damage rather than residual frame drift. The percentage of unsafe placarding is given Figure 2.34 for different *SHR* values. The results demonstrate that *SHR* has a minor influence in unsafe placarding.

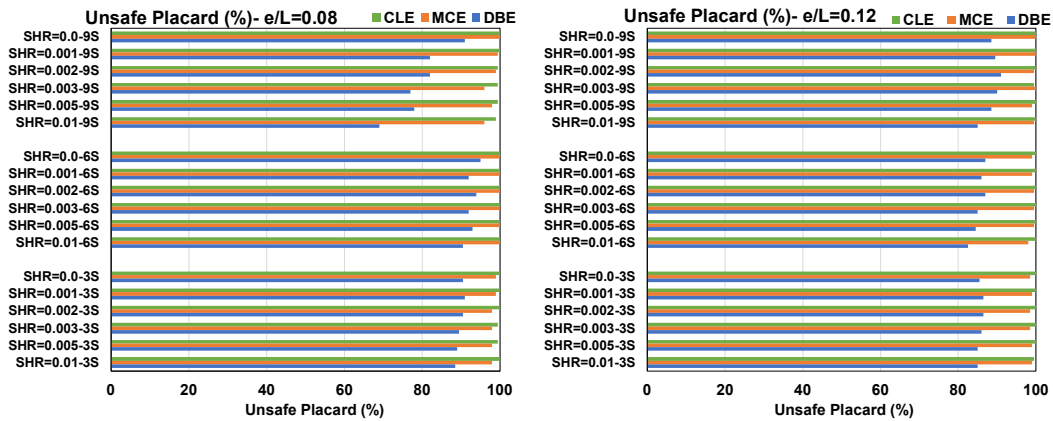


Figure 2.34. Unsafe Placards

2.7 Summary And Evaluation of Results

The results show that the *SHR* has the highest impact on residual interstory drift ratio (RIDR) when compared with other EDPs. Link rotation angle (LRA) and interstory drift ratio (IDR) are also affected from the *SHR* while story acceleration (SA) was observed to be insensitive to post yielding stiffness. Repair costs of the archetype EBFs were calculated using expected damages to structural and nonstructural components defined in Table 2.9. Majority of the component damage fragilities are expressed in terms of story acceleration (SA) which is quite insensitive to the *SHR*. Therefore, if residual drifts are not considered in the performance assessment, then the effects of the *SHR* on the repair costs are negligible. On the contrary, the *SHR* has a significant influence on the replacement decision because irreparable residual drift significantly depends on the *SHR*. The differences in repair costs can be as high as 80% between the cases where the residual drifts are considered or not.

Previous studies on experimental and numerical investigation of material, component, and structure behaviors showed that the post yield stiffness (*SHR*) can vary considerably. The results showed that all of the 3-, 6-, and 9-story archetypes except for one (3-story with $e/L=0.08$) experience total replacement after MCE and CLE events irrespective of the value of *SHR* in the range of 0 and 0.003. For the

highest value of $SHR=0.01$ considered in this study, replacement was not deemed necessary for all archetypes with $e/L=0.08$ subjected to MCE or CLE level events. The same observation is true for archetypes with $e/L=0.12$ except for the 9-story EBFs. An SHR value of 0.05 resulted in replacement for some archetypes but not the others.

MCE and CLE events are extreme hazards and the major concern is life safety rather than economic consequences. Economical loss is the primary concern for more frequent DBE events. The effect of SHR on repair and replacement decisions is much more significant when the archetypes are subjected to DBE level seismic events. The results show that the replacement decision depends on the SHR , the number of stories, and the e/L ratio. None of the 3-story archetypes required replacement. Similarly replacement was not required for 6-story archetypes with $SHR \geq 0.002$. For 9-story archetypes there was a strong dependency on the e/L ratio. While the archetype with $e/L=0.08$ required replacement for $SHR=0$ only, the archetype with $e/L=0.12$ required replacement for $SHR \leq 0.003$.

CHAPTER 3

SEISMIC PERFORMANCE EVALUATION OF ECCENTRICALLY BRACED FRAMES WITH LONG LINKS USING FEMA P695 METHODOLOGY

3.1 Background

3.1.1 Summary of FEMA P-695 Methodology

FEMA P-695 (2009) is a methodology that was developed to evaluate the collapse performance of seismic resisting systems by establishing global seismic performance factors: response modification coefficient (R), the system overstrength factor (Ω_0) and displacement amplification factor (C_d). The methodology considers the potential uncertainties in structural configuration, ground motion and behavior of structural components and systems. The main objective is to set a minimum acceptable design criteria for code-approved seismic designs and evaluations.

FEMA P-695 methodology consists of six basic steps as: obtaining the required system information, archetype development, nonlinear model development, nonlinear analysis, performance evaluation and documentation.

The design requirements and test results in material, component and system levels are the information required by FEMA P-695. The design requirements include the specification of seismic performance factors (R , Ω_0 , C_d), architectural limitations, usage restrictions and drift limits. The test data should include the strength, stiffness and ductility of the components and the system.

An archetype is the prototypical representation of the seismic resisting system. Archetype development includes characterizing the system behavior in terms of building height, fundamental period, structural framing configurations, framing bay size (or wall lengths), magnitude of gravity loads, member and connection design

and detailing conditions. As a result, structural systems are categorized into performance groups which reflect the major response of archetypes in the design space. The variations in the range of each criteria listed above, should also be considered for each applicable Seismic Design Category (*SDC*)

The developed nonlinear models can be two-dimensional or three-dimensional which accounts the seismic mass including the P-delta effects.

Both nonlinear static (pushover) and nonlinear dynamic (response history) analysis are required for the collapse assessment. System overstrength and ductility capacity is provided by the pushover analysis. While the median collapse capacities and collapse margin ratios are estimated by the response history analysis with a pre-defined ground motion set. FEMA P-695 (2009) provides two different sets of ground motions from large-magnitude events in the Pacific Earthquake Engineering Research Center (PEER) Next-Generation Attenuation (NGA) database (PEER, 2006a).

- **Far-field ground motion set:** 22 ground motion record pairs from the sites located ≥ 10 km from fault rupture.
- **Near-field ground motion set:** 28 ground motion record pairs from the sites located < 10 km from fault rupture.

For the collapse assessment, FEMA P-695 (2009) requires only the far-field ground motion set and near-field ground motion records are provided as a supplementary information to investigate near-fault directivity effects, if necessary.

FEMA P695 defines the median collapse as the ground motion intensity at which half of the ground motions cause collapse of an archetype. The ground motions are scaled to larger intensities until median collapse is reached.

The performance evaluation requires both nonlinear static analysis and nonlinear dynamic analysis to determine the value of Ω_0 and check whether the R factor is acceptable respectively. C_d is derived from the R factor considering the effective damping. The acceptability of the R factor is evaluated in terms of collapse margin

ratio (*CMR*). *CMR* is defined by the ratio of the median collapse intensity (\hat{S}_{CT}) to the maximum considered earthquake (MCE) level intensity (S_{MT}) defined by the building code (Equation 3.1) and is the primary parameter that characterizes the collapse safety.

$$CMR = \frac{\hat{S}_{CT}}{S_{MT}} \quad (3.1)$$

Extreme ground motions that cause building collapse are considered by converting the *CMR* into the adjusted collapse margin ratio (*ACMR*). This conversion depends on the shape of the spectrum of these ground motions which is a function of the period-based ductility (μ_T (Equation 3.2)) and fundamental period of vibration. The period-based ductility is determined by making use of static pushover analysis and defined as the ratio of the roof displacement (δ_u) at the point of 20% strength loss ($0.8V_{max}$) and the effective yield displacement given in FEMA P-695 (2009) (Equation 3.3).

$$\mu_T = \frac{\delta_u}{\delta_{y,eff}} \quad (3.2)$$

$$\delta_{y,eff} = C_0 \frac{V_{max}}{W} \left[\frac{g}{4\pi^2} \right] (\max(T, T_1))^2 \quad (3.3)$$

where C_0 is a coefficient used to relate fundamental mode displacement to roof displacement, V_{max} is the maximum base shear capacity, W is the building weight, g is the gravitational constant, T is the approximate fundamental period and T_1 is the fundamental period computed using eigenvalue analysis.

The adjusted collapse margin ratio (*ACMR*) is a function of total system uncertainty (β_{TOT}) and collapse probability at MCE level. β_{TOT} value is a function of record-to-record uncertainty (β_{RTR}), design requirements-related collapse uncertainty (β_{DR}), test data-related collapse uncertainty (β_{TD}) and modeling-related collapse uncertainty (β_{MDL}) (Equation 3.4).

$$\beta_{TOT} = \sqrt{\beta_{RTR}^2 + \beta_{DR}^2 + \beta_{TD}^2 + \beta_{MDL}^2} \quad (3.4)$$

FEMA P-695 (2009) suggests that the probability of collapse at *MCE* seismic level event should be limited to 10% where, each performance group should satisfy this limit on average. If this condition cannot be satisfied, the probability of collapse limit individual archetypes should not exceed the 20% at MCE level earthquake.

If the ACMR is not large enough to satisfy the predefined probability of collapse at MCE level seismic event, than the *R* factor should be redefined and the described procedure should be repeated. Otherwise, the system is asserted to be acceptable and should be documented for the PEER review by independent team of experts.

3.1.2 Summary of Past Research on Long Links

3.1.2.1 Experimental Studies

Engelhardt and Popov (1989, 1992) conducted the first experimental studies on long links attached to columns in late 1980s. A total of 14 tests were conducted on 12 two-third scale subassemblage specimens with ρ varied from 1.45 to 4.25. Based on the test results, it was observed that, as ρ is increased from 1.6 up to 3, the shear-dominant behavior gradually translates to the flexure-dominant behavior and the dominant failure mode to be fracture of link flange at the link-to-column connection. The authors recommended to avoid long links attached to columns in EBFs. There have been a few experimental investigations on long links since then until early 2000s.

Okazaki (2004) and Okazaki and Engelhardt (2005, 2006, 2007, 2009) have tested the seismic performance of long links in EBFs giving particular attention to link-to-column connections. Okazaki and Engelhardt (2005 and 2006) conducted a total of 35 tests on seismic performance of *EBF* links with various lengths (short links to very long links) to evaluate the flange slenderness limits and overstrength factors. They concluded that for the long links ($e > 1.6M_p/V_p$) the flange slenderness effects

are not very clear and further investigation is required. However they highlighted that premature fracture of links is not the concern for only long links, but also for the short links. In 2007, Okazaki and Engelhardt tested 37 link specimens again with varying link lengths constructed from five different wide-flange ASTM A992 steel sections and investigated the effect of loading protocols on the inelastic rotation of the links and the flange slenderness limits for short and long links. The results from the previous publications were also included for the purpose of completeness.

Duscika and Lewis (2010) investigated stiffening alternatives for short and long links with experimentally verified numerical analyses. Their initial results showed that, end stiffeners successfully increased link deformation capacity for the long links and shifted the failure mode away from the welded connections.

Mohammadrezapour and Danesh (2018, 2020) proposed semi-rigid connections for long link-to-column connections by conducting experiments and finite element simulations. Naserifar and Danesh (2018) conducted tests on two full-scale EBFs with different reduced link section (RLS) locations. For the first one, the RLS is placed at both ends of the link, while for the second one, the RLS is only placed at the link end near the column. Both links satisfied the link rotation limits in the provisions, however, at large drifts, the strength of RLS reduced due to the lateral torsional buckling of the link. The authors suggested that the RLS should better be applied to one-end near the column instead of its both ends.

Gulec et al. (2011) have developed fragility functions for short and long links in EBFs by statistical evaluation of test data of 82 links from different experimental programs. The demand parameter is selected to be link plastic rotation and damage states were determined by direct indicators such as web and flange buckling and fracture. Repair methods were discussed and assigned to each damage state selected to develop consequence functions and estimate repair costs.

3.1.2.2 Past Studies on the Comparison of Short and Long Links

First numerical studies on long links were performed by Roeder and Popov (1977, 1978), Hjelmstad and Popov (1983 and 1983). They concluded that, short links perform better than the long links. Engelhardt and Popov (1988 and 1989) proposed to prefer of short links in EBF structures, since they are observed to provide higher stiffness, strength and ductility than the intermediate and long links. In 1991, Ramadan and Ghobarah conducted two studies and on EBF links with various lengths using a finite element model. They have concluded that short links are more efficient than the long ones. However, long links have smaller LRA values with reduced ductility levels. The authors proposed to increase the flange thickness of the link sections to improve the performance of long links.

Richards (2004) developed a general loading protocol to be used for short, intermediate and long EBF links with three- and ten-story archetypes designed according to the International Building Code (2002). Richards (2004) and Richards and Uang (2006) concluded that inelastic rotation capacity of short links is considerably higher than that of intermediate and long links. An extended summary of this study is presented in Section 4.1.1.

Özhendekçi and Özhendekçi (2007) studied the effects of frame geometry on the frame weight and inelastic behavior of EBFs with chevron steel frames where 420 of them are designed with short links, 105 of them are designed with intermediate links and 105 of them are designed with long links. The numerical models were analyzed under 20 SAC ground motions with DRAIN-2DX. The advantages and disadvantages of choosing different link lengths were discussed in terms of mean scale factors and frame weights. The displacement ductilities of long link EBFs were lower than that of the short link EBFs. Longer shear links and shorter intermediate links perform better in terms of seismic performance. However, for the short links, the frame weight increases with increasing link lengths.

Daneshmand and Hashemi (2012) investigated the performance of intermediate and long links in EBFs. A total of 68 European-standard rolled shaped link sections were analyzed by finite element method with 3D solid elements. The authors observed that long links are not sensitive to the existence of one- or two-sided stiffeners as much as the intermediate links. In addition, they propose to further classify long links according to their link lengths and to set a limit to the maximum allowable length of the long links.

Mohebkhah and Chegeni (2014) investigated the applicability of the codified overstrength factor and rotation capacities of EBF links on European IPE sections. IPE sections were observed to sustain larger inelastic rotations than the codified requirements. They have concluded that for the short links with European IPE sections, the overstrength factor proposed by the provisions may result in unconservative designs. However, for the intermediate and long links with European IPE sections, the codified overstrength factors can conservatively be used.

Suswantano et al. (2017) examined the effect of geometry and seismic hazard on the design performances of EBFs with short, intermediate and long links. They have concluded that the short links have higher strength and lower lateral drift than that of intermediate and long links. The authors have also noted that, the addition of diagonal web stiffeners caused long links like a beam. Suswantano et al. (2018) also compared the WF and tubular links on EBFs with variable link lengths (short, long and intermediate). For the long links, neither WF nor tubular link sections could achieve nominal shear force value.

Labed et al. (2020) performed a numerical investigation on the inelastic cyclic behavior of isolated short and long links designed according to Algerian National Seismic Code (RPA 99). They have confirmed that the link length and cross sectional properties are the major parameters that define the stiffness, strength and ductility of the links. The performance of long links were observed to be less effective than the short links. The ultimate state of long links is the formation of plastic mechanisms formed nearly in the flanges where local buckling takes place.

Haris et al. (2020) aimed to determine the effect of link length and brace cross-section on the behavior of EBFs. The authors have concluded that the brace cross section has an effect on the seismic behavior of short-link EBFs, however the ultimate load of intermediate and long links is not observed to show a significant difference. Ductility, on the other hand, is independent on the geometry of the bracing.

3.1.2.3 Numerical Studies:

Some researchers examined the design, modeling and numerical response of EBFs with long links. Verifications of the numerical and analytical models are difficult because of the scarcity in the experimental data.

Malakoutian et al. (2013) developed a modeling technique for short, intermediate and long links to be used with OpenSees (2006) routines where shear and moment responses were uncoupled. The beam-column elements with fiber cross-section were capable of modeling the axial and flexural responses. A shear force versus shear deformation section was aggregated to define the shear response.

Jain et al. (1996) proposed a design procedure for EBFs with flexurally dominated links. They suggested relaxing the usual requirement to restrict inelastic action to the links.

Bosco et al. (2015) developed a model for short, intermediate and long links for EBFs based on the approach proposed by Ramadan and Ghobarah (1991). The long link model of the study was calibrated using the experimental data of Engelhardt and Popov (1989) and Okazaki (2004, 2005, 2006, 2007 and 2009).

Tirca and Gioncu (1999) investigated the seismic behavior of six-story EBFs with a single bay under different ground motions. They concluded that long links should be adopted with caution and should be avoided if possible.

Berman and Bruneau (2008) investigated the performance of long links with tubular sections which do not require lateral bracings using over 200 combinations of geometries and properties such as the compactness range and link length.

Fakharaddini et al. (2019) conducted a parametric study on a group of 30 EBFs of 3, 6, 9, 12 and 15 stories with link length to bay width ratios (e/L) of 0.1, 0.2, 0.3, 0.4, 0.5 and 0.6 to develop a formulation that estimates peak displacement patterns of EBFs.

3.1.2.4 Proposed Methodologies to Improve the Performance of Long Links

Although majority of the past researchers suggest avoiding long links if possible, they provide an advantage of providing large openings in the EBF spans. Some researchers have proposed remedial methods to improve the performance of long link EBFs.

Chegeni and Mohebkhah (2014) developed a three-dimensional finite-element model to investigate the rotation capacity of the link and proved that additional intermediate stiffeners increased the rotation capacity of the long links. However, these investigations did not cover the material failure therefore the authors suggest carrying on further experimental studies for validation of the results.

Naghipour et al. (2011) investigated the application of the reduced beam section (RBS) connection in dual EBFs with long external links. Results of nonlinear static (pushover) analyses on four-, seven-, and ten-story dual EBFs revealed that the RBS connection can increase the ductility of the system (by about 10%) and reduce the demand on link-to-column connections by moving the hinge location away from the column face. The RBS connection was however recommended only for very long links with shallow sections.

Mansouri (2021) proposed to adopt haunched intermediate and long links in EBFs in order to delay yielding of the link and to increase plastic capacity and ductility of the EBF system. The numerical models showed that haunched links provide a higher

inelastic rotation capacity (by 2.12 times on average) and energy dissipation (by 1.79 times on average) than conventional ones. In addition, their inelastic rotation capacity does not decrease with increasing link length. Although the haunched links reduce the lateral stiffness of the EBF, this effect is observed to be negligible. The seismic performance of EBFs with haunched links were observed to be significantly improved.

Danku and Dubina (2013) studied the effects of concrete slabs on the stiffness, drift and rotation demands giving particular attention to long links and reported a 35% reduction in the residual drifts of long links because of the composite action due to the floor slab.

Özkılıç (2022) studied the interaction of flange and web slenderness in long links using numerical analysis and also proposed some stiffening arrangements.

3.1.2.5 Behavior Factors

In the United States, seismic response factors for EBFs are given in Minimum Design Loads for Buildings and Other Structures ASCE7-16 (2016). The recommended values of the response modification coefficient (R), the system overstrength factor (Ω_o), and the deflection amplification factor (C_d) are 8, 2, and 4, respectively. In Europe, seismic response factors for EBFs are given in EC8 (2003), where the behavior factor (q) is calculated based on the ductility classes DCM and DCH. The DCM refers to the Ductility Class Medium with $q=4$. The DCH refers to the Ductility Class High with $q=5 \times \alpha_u / \alpha_1$ where α_u and α_1 are the lateral load factors defined in EC8 with a default α_u / α_1 ratio of 1.2 and a maximum value of 1.6. In short, the ASCE7-16 recommends a force reduction factor of 8 for EBFs while this factor varies between 4 and 8 according to EC8.

Response modification coefficients (behavior factors) for EBFs with long links have been investigated through a number of studies. Bosco et al. (2013 and 2014) proposed an empirical equation to determine the R factor (q factor) for short,

intermediate and long link EBFs as a function of link rotation capacity. For the long link EBFs, the proposed equations of Bosco et al. (2014) and Bosco et al. (2013) calculate q factors as 3.5 and 4.0 respectively. Razavi et al. (2020) proposed an empirical relation to predict behavior factors using the genetic algorithm as a function of number of stories, braces, slenderness, stiffness of the columns, fundamental period of the structure, link beam-to-beam length ratio and roof ductility.

Topkaya and his colleagues (2016, 2021) investigated the seismic performance factors for EBFs with short links using the FEMA P695 methodology (2009). The results showed that the recommended values in ASCE7-16 (2016) result in designs with higher collapse probabilities than expected. Modifications to the response modification coefficient and displacement amplification factor were proposed to satisfy the target collapse probability. Link shear versus link rotation angle responses of short and long links are different from each other as shown in Figure 3.1 in terms of significant strength and stiffness degradation due to local buckling and inelastic rotation capacities. In this figure, experimental data collected by Okazaki and Engelhardt (2007) are presented.

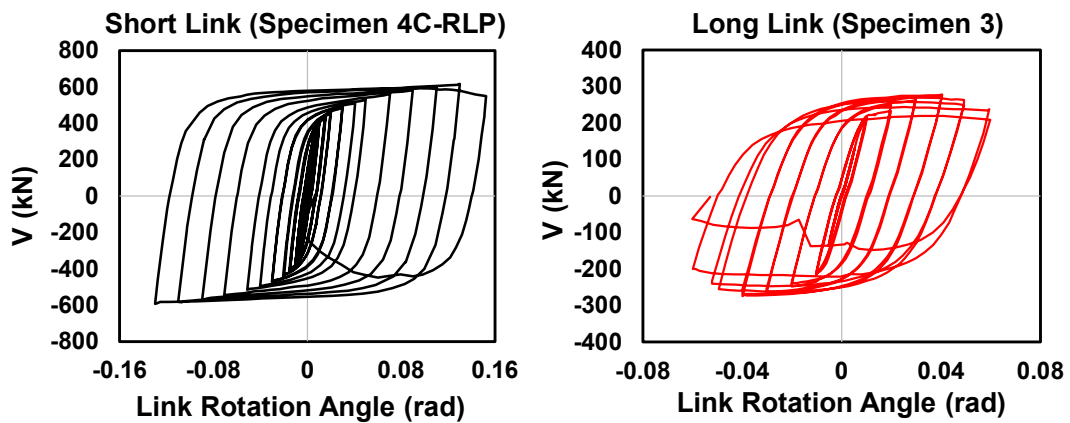


Figure 3.1. Link shear versus link rotation angle responses of short and long links

3.1.3 Link Deterioration Model

Beams experience significant strength and stiffness deterioration as they are subjected to cyclic rotations beyond the yield limit. Ibarra et al. (2005 and 2005) developed a deteriorating model for bilinear, peak oriented and pinching hysteretic models. These models are referred to as Ibarra-Krawinkler (IK) model or Ibarra-Medina-Krawinkler (IMK) model. Lignos and Krawinkler (2009) modified the IK model to address asymmetric component hysteretic behavior, different cyclic deterioration rates for both loading directions, residual strength and an ultimate deformation (θ_u) at where strength of the member vanishes. In 2011, Lignos and Krawinkler developed a database of more than 300 experiments on steel wide flange beams to calibrate the deterioration parameters of the former model. The deterioration model had been implemented in OpenSees (2006) and named as modified-Ibarra-Medina-Krawinkler (modified IMK) model. Figure 3.2 shows the monotonic backbone curve of the modified IMK deterioration model with an elastic branch, strain hardening branch, a negative stiffness branch and a zero-slope residual strength branch. Energy dissipation was used as a deterioration criterion of hysteretic behavior between the bounds presented in Figure 3.3.

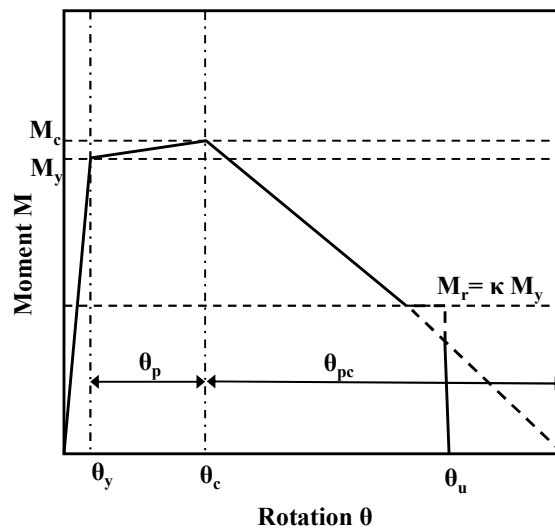


Figure 3.2. Modified IMK model: backbone deterioration curve for monotonic loading

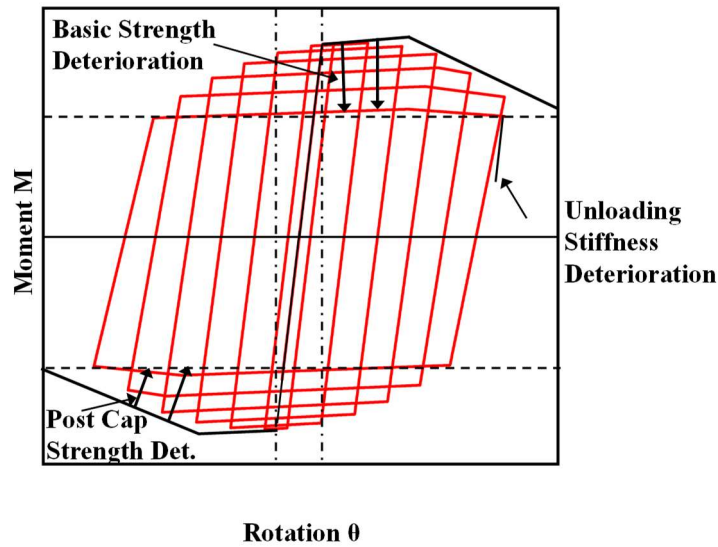


Figure 3.3. Modified IMK model: basic modes of cyclic deterioration

The monotonic backbone curve of the modified IMK should be defined by three strength and four deformation parameters (Figure 3.2). Although the model can be applied to any force-deformation relationship, Lignos and Krawinkler (2011) selected moment-rotation quantities to describe the behavior. The force deformation parameters are the effective yield moment (M_y), capping moment strength (M_c) and residual moment (M_r), the yield rotation (θ_y), pre-capping plastic rotation (θ_p), post-capping plastic rotation (θ_{pc}) and ultimate rotation capacity (θ_u). The following expressions were developed to express the required parameters for wide-flange sections other than reduced beam section (RBS) (2011):

$$M_y = 1.17ZF_y \quad (3.5)$$

$$M_c = 1.1M_y \quad (3.6)$$

$$M_r = \kappa M_y \quad (3.7)$$

$$\theta_y = M_y / (6EI / L) \quad (3.8)$$

$$\theta_p = 0.0865 \left(\frac{h}{t_w} \right)^{-0.365} \left(\frac{b}{2t_f} \right)^{-0.140} \left(\frac{L}{d} \right)^{0.34} \left(\frac{d}{533} \right)^{-0.721} \left(\frac{F_y}{355} \right)^{-0.230} \quad (3.9)$$

$$\theta_{pc} = 5.63 \left(\frac{h}{t_w} \right)^{-0.565} \left(\frac{b}{2t_f} \right)^{-0.800} \left(\frac{d}{533} \right)^{-0.28} \left(\frac{F_y}{355} \right)^{-0.430} \quad (3.10)$$

Where Z = plastic section modulus, h = web depth, b = flange width, L = beam shear span, E = elastic modulus of steel. κ is suggested as 0.4 from the data-sets of W-sections. Yield stress (F_y) and d = beam depth (d) are defined in terms of megapascals and millimeters respectively in Equations 3.9 and 3.10.

Lignos and Krawinkler (2011) followed the rule of cyclic deterioration developed by Rahnema and Krawinkler (1993). They assumed that the hysteretic energy dissipation capacity is an inherent property which is independent of the applied loading history. The following relationship was used to define the reference hysteretic energy dissipation capacity

$$E_t = \lambda \theta_p M_y = \Lambda M_y \quad (3.11)$$

Where Λ = the reference cumulative rotation capacity and defines the rate of cyclic deterioration. For beams other than RBS sections, Λ is defined as:

$$\Lambda = 495 \left(\frac{h}{t_w} \right)^{-1.34} \left(\frac{b}{2t_f} \right)^{-0.595} \left(\frac{F_y}{355} \right)^{-0.360} \quad (3.12)$$

Once the component yields at least in one direction, the cyclic deterioration is activated for the modes of basic strength, post-capping strength, unloading stiffness and reloading stiffness, where all cyclic deterioration modes are represented by the same parameter Λ .

3.1.3.1 The Ultimate Link Rotation Criterion

For beams other than RBS sections, Lignos and Krawinkler (2011) estimated θ_u as 0.05-0.06 rad. AISC 341-16 (2016) limits the inelastic rotation capacity of long links to 0.02 rad. ASCE 41-17 (2017) defines the ultimate link rotation angle as 11 times the yield rotation angle (θ_y) at collapse prevention (CP) performance level. In the current study, the yield rotation angles were calculated using Equation 3.8 for the designed link beams details of which are presented in Section 3.2. The median value of $\theta_u = 11\theta_y$ for the designed archetype links was calculated as 0.0608 rad with a standard deviation of 0.009 rad. The test results of ultimate link rotation angles (LRAs) of long links obtained by other researchers (Okazaki et al. (2007), Hjelmstad and Popov (1983), Engelhardt and Popov (1989), Mohammadrezapour and Danesh (2018)) are presented in Table 3.1. The total LRA values are in the range of 0.029 rad and 0.070 rad. The lowest LRA values of the long links were obtained by Engelhardt and Popov (1989). These are due to premature failures of the links such as lateral torsional buckling or fracture of the link flange at the link-to-column connection. In this study, θ_u was considered as 0.06 rad based on the recommendations of ASCE 41-17 and the experiments on long links. The ultimate rotation capacity ($\theta_u=0.06$ rad) was not defined in the numerical models; however, this limit was used as a failure criterion. Failure of any particular link beam was considered when the median link rotation angle from all considered ground motions exceeds the limit of 0.06 rad.

Table 3.1. Total LRA values of long links from previous experiments

Author	Specimen ID	$e/(M_p/V_p)$	Total LRA (rad)
Okazaki and Engelhardt (2007)	3	3.61	0.060
Okazaki and Engelhardt (2007)	7	3.29	0.068
Hjelmstad and Popov (1983)	12	2.87	0.070
Hjelmstad and Popov (1983)	15	2.87	0.055
Engelhardt and Popov (1989)	5	3.45	0.029
Engelhardt and Popov (1989)	6	3.40	0.046
Engelhardt and Popov (1989)	12	4.25	0.044
Mohammadrezapour and Danesh (2018)	TSAW-PR	3.0	0.070

3.2 Design of Archetypes

A total of 24 archetypes were designed by considering the e/L ratio, number of stories and bay width as the prime variables. The lateral load resisting system of the archetypes consists of EBFs only. The beam-to-column and brace-to-beam connections for the EBF bays were considered as rigid connections with full moment transfer. On the other hand, the gravity beam to column connections were assumed pinned with no moment transfer. The archetypes do not represent dual systems where EBFs are used together with MRFs for lateral resistance.

Two different floor plans shown in Figure 3.4 were selected to be able to have different bay widths. Floor Plan I (FP-I) was 54 m \times 36 m while Plan II (FP-II) was 36m \times 36m. The EBFs with 9 m bay width were designed for FP-I and EBFs with 6 m bay width were designed for FP-II. Twelve archetypes were designed for each floor plan. The column bases were assumed pinned and the story height was considered as 4 m for all stories. Link length to bay width ratios (e/L) of 0.35, 0.40,

0.45 and 0.50 and number of stories of 3, 6 and 9 were considered. Links were positioned in between the ends of braces as shown in the elevation view (Figure 3.5).

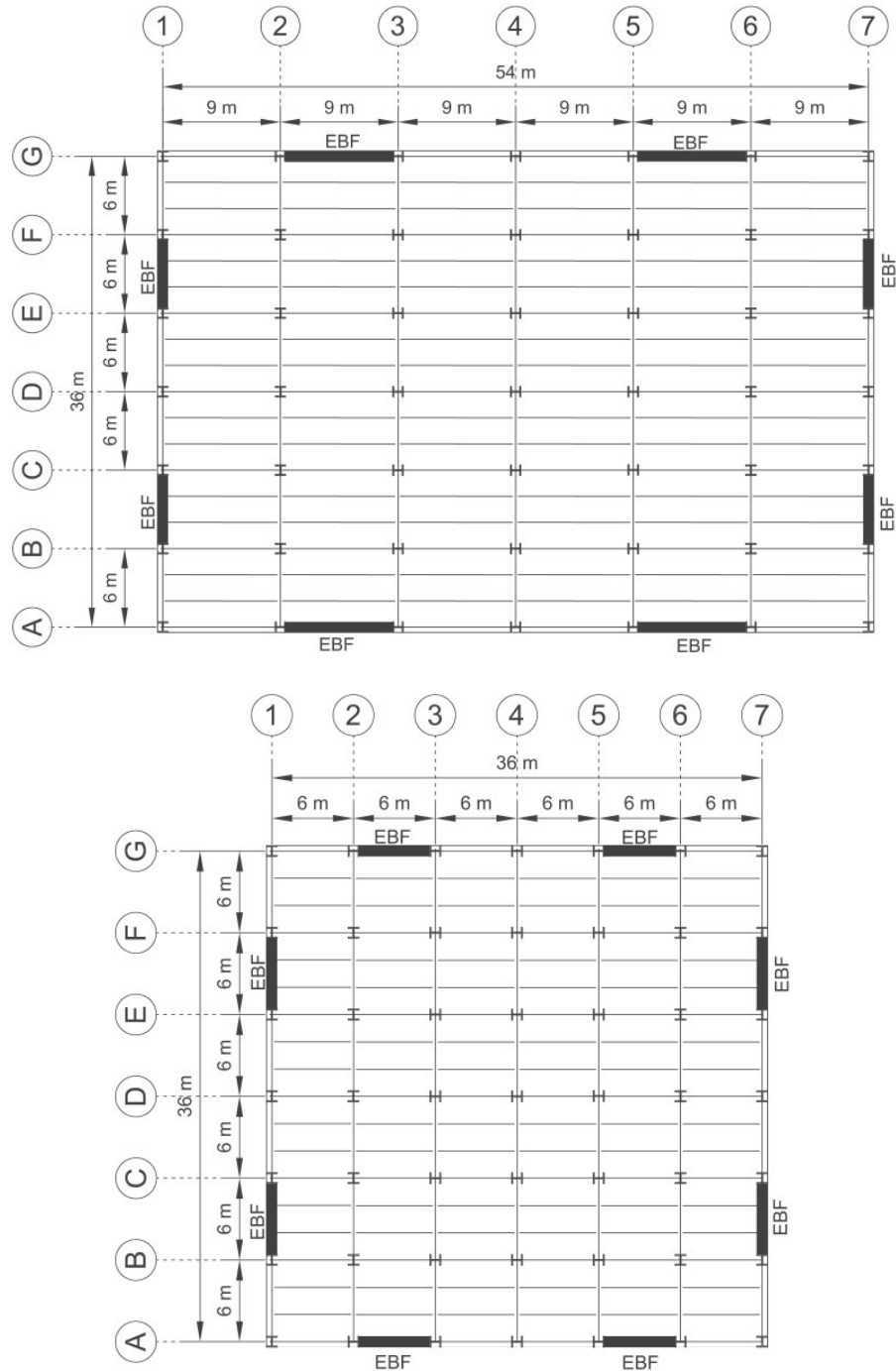


Figure 3.4. Floor plans

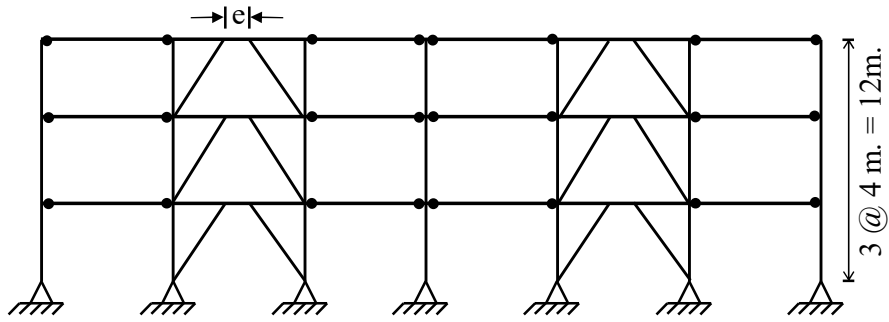


Figure 3.5. Typical elevation view

EBFs were designed to resist gravity and seismic loadings together. The effect of wind was not considered. Story dead loads and live loads were considered as 4.3 kN/m^2 and 2.0 kN/m^2 , respectively which are typical for steel office buildings. Twenty percent of the live load was considered in earthquake load calculations to take into account the contribution of partition walls. Seismic hazard level was determined according to FEMA P695 (2009) methodology. Seismic design category descriptions in FEMA P695 are not specific to a particular location and represent a regional seismic hazard. Seismic Design Category SDC D_{\max} was considered in the present study which is representative of the highest level of shaking expected in the U.S. For SDC D_{\max} S_{MS} and S_{MI} parameters were defined as $1.50g$ and $0.90g$ respectively for maximum considered earthquake (MCE), where S_{MS} is the MCE level 5% damped spectral response acceleration parameter at short periods adjusted for site class effects and S_{MI} is the MCE level 5% damped spectral response acceleration parameter at a period of 1 second adjusted for site class effects.

The archetype EBFs were designed using equivalent lateral force (ELF) procedure proposed in ASCE 7-16 (2016) and considering the provisions of AISC341 (2016) and AISC360 (2016). All members were designed with American wide flange sections (W-sections) with a yield strength of 345 MPa which is typical for A992 grade steel. All links were long links ($e/L > 2.6$). The computer program developed by Kuşyılmaz and Topkaya (2013) was used to design the archetypes. A 9-step

design procedure is used in this program which was specifically tailored for EBF designs. For a particular story, the link and the beams outside the link are selected from the same W section. The idea behind the design process is to optimize the weight of the framing by satisfying all the strength, displacement and link rotation angle requirements. The sub-assembly design concept is adopted in this procedure rather than independently selecting sections for links, braces and columns. The program forms a library of sub-assemblages for a given height and bay width. These are a combination of link sections and suitable brace sections that satisfy the capacity design principles according to the forces produced by the link. The sub-assemblages are sorted from the lightest to the heaviest according to their mass. The program considers the same sub-assembly for all stories and determines the column sections required based on capacity design principles. This process is continued until all design requirements are satisfied. The resulting framing can be considered as a “uniform frame design” where link sections in all stories are identical. The program further modifies the sub-assemblages and columns of this design to obtain a framing with a smaller mass. It should be noted that the column sections are changed at every 3 stories. Detailed information about the archetypes and member sizes are given in Tables 3.2, 3.3 and 3.4. For any number of stories and floor plan, it can be observed that the mass of framings does not change considerably between archetypes with different e/L ratios.

Table 3.2. Archetype Properties and Scaling Factors

AT	F P	N S	e/L	Bay width (m)	Mass (tons)	T_{analysis} (s)	μ_T	MCE Scale Factor	CLE 20% Scale Factor	CLE 10% Scale Factor
AT1-I	I	3	0.35	9	9.17	0.81	4.96	2.42	2.71	3.27
AT2-I	I	3	0.40	9	9.62	0.86	5.93	2.42	2.64	3.17
AT3-I	I	3	0.45	9	9.92	0.90	5.26	2.42	2.69	3.24
AT4-I	I	3	0.50	9	10.22	0.97	6.44	2.42	2.61	3.15
AT5-I	I	6	0.35	9	24.05	1.32	3.37	2.54	2.82	3.38
AT6-I	I	6	0.40	9	23.86	1.44	3.58	2.54	2.79	3.35
AT7-I	I	6	0.45	9	23.56	1.56	3.97	2.54	2.74	3.30
AT8-I	I	6	0.50	9	23.91	1.65	4.44	2.54	2.72	3.25
AT9-I	I	9	0.35	9	49.79	1.79	3.01	2.53	2.73	3.29
AT10-I	I	9	0.40	9	46.92	1.96	3.24	2.53	2.71	3.24
AT11-I	I	9	0.45	9	47.10	2.08	3.62	2.53	2.63	3.19
AT12-I	I	9	0.50	9	50.23	2.23	3.74	2.53	2.63	3.16
AT1-II	II	3	0.35	6	6.40	0.80	5.58	2.42	2.66	3.19
AT2-II	II	3	0.40	6	6.68	0.82	6.04	2.42	2.64	3.17
AT3-II	II	3	0.45	6	6.84	0.91	7.03	2.42	2.57	3.10
AT4-II	II	3	0.50	6	7.14	0.98	7.51	2.42	2.54	3.07
AT5-II	II	6	0.35	6	17.20	1.29	3.53	2.54	2.79	3.38
AT6-II	II	6	0.40	6	17.07	1.43	4.66	2.54	2.69	3.23
AT7-II	II	6	0.45	6	18.53	1.53	5.97	2.54	2.59	3.10
AT8-II	II	6	0.50	6	18.77	1.59	5.44	2.54	2.62	3.15
AT9-II	II	9	0.35	6	42.67	1.70	3.50	2.53	2.66	3.19
AT10-II	II	9	0.40	6	36.77	1.82	2.93	2.53	2.76	3.31
AT11-II	II	9	0.45	6	35.84	2.01	3.86	2.53	2.61	3.14
AT12-II	II	9	0.50	6	36.41	2.18	3.98	2.53	2.58	3.11

Table 3.3. Member Sizes of FP-I Archetypes

AT	S	Links	Braces	Cols.	AT	S	Links	Braces	Cols.
	t					t			
AT 1-I	1	21×68	12×106	14×68	AT 2-I	1	21×73	14×132	14×68
	2	21×62	12×96	14×68		2	24×62	14×109	14×68
	3	18×55	12×87	14×68		3	21×50	12×87	14×68
AT 3-I	1	24×76	14×132	14×68	AT 4-I	1	24×84	14×132	14×68
	2	24×62	12×106	14×68		2	21×83	14×132	14×68
	3	24×62	12×106	14×68		3	21×57	12×87	14×68
AT 5-I	1	24×76	14×159	14×132	AT 6-I	1	24×76	14×145	14×132
	2	24×76	14×159	14×132		2	24×76	14×145	14×132
	3	24×76	14×159	14×132		3	24×76	14×145	14×132
AT 7-I	4	24×62	14×120	14×68	AT 8-I	4	24×76	14×145	14×68
	5	24×55	14×109	14×68		5	24×62	14×109	14×68
	6	16×45	18×86	14×68		6	21×50	12×87	14×68
AT 9-I	1	24×84	14×145	14×132	AT 10-I	1	24×94	14×145	14×132
	2	24×84	14×145	14×132		2	24×94	14×145	14×132
	3	24×84	14×145	14×132		3	24×94	14×145	14×132
AT 11-I	4	24×76	14×132	14×68	AT 12-I	4	24×84	14×132	14×68
	5	24×62	12×106	14×68		5	21×73	14×109	14×68
	6	21×50	12×79	14×68		6	21×50	12×72	14×68
AT 11-I	1	24×94	14×159	14×233	AT 12-I	1	24×94	14×176	14×211
	2	24×94	14×159	14×233		2	24×94	14×176	14×211
	3	24×94	14×159	14×233		3	24×94	14×176	14×211
AT 11-I	4	24×94	14×159	14×159	AT 12-I	4	24×94	14×176	14×132
	5	24×94	14×159	14×159		5	24×94	14×176	14×132
	6	24×84	14×145	14×159		6	24×94	14×176	14×132
AT 11-I	7	24×84	14×145	14×132	AT 12-I	7	24×76	14×145	14×74
	8	24×84	14×145	14×132		8	24×76	14×145	14×74
	9	24×84	14×145	14×132		9	24×76	14×145	14×74
AT 11-I	1	24×103	14×176	14×211	AT 12-I	1	21×122	14×193	14×211
	2	24×103	14×176	14×211		2	21×122	14×193	14×211
	3	24×103	14×176	14×211		3	21×122	14×193	14×211
AT 11-I	4	24×103	14×176	14×132	AT 12-I	4	21×122	14×193	14×132
	5	24×103	14×176	14×132		5	21×122	14×193	14×132
	6	24×94	14×159	14×132		6	21×122	14×193	14×132
AT 11-I	7	24×94	14×159	14×74	AT 12-I	7	24×94	14×145	14×74
	8	24×84	14×145	14×74		8	24×94	14×145	14×74
	9	24×76	14×132	14×74		9	24×94	14×145	14×74

Table 3.4. Member Sizes of FP-II Archetypes

AT	S	Links	Braces	Cols.	AT	S	Links	Braces	Cols.
	t					t			
AT	1	21×44	12×87	14×68	AT	1	21×50	12×87	14×68
1-II	2	18×40	10×77	14×68	2-II	2	21×44	12×79	14×68
	3	16×31	12×58	14×68		3	16×40	10×68	14×68
	AT	1	18×55	12×87		14×68	AT	1	18×60
3-II	2	18×50	12×79	14×68	4-II	2	18×55	12×87	14×68
	3	18×46	12×72	14×68		3	16×50	12×72	14×68
	1	24×55	14×109	14×132		1	21×57	12×106	14×132
AT 5-II	2	24×55	14×109	14×132	AT 6-II	2	21×57	12×106	14×132
	3	21×50	12×96	14×132		3	21×57	12×106	14×132
	4	21×50	12×96	14×68		4	21×50	12×87	14×68
	5	16×45	18×86	14×68		5	21×44	12×79	14×68
	6	18×35	10×68	14×68		6	16×40	10×68	14×68
	1	18×71	12×120	14×132		1	18×86	14×132	14×132
AT 7-II	2	18×71	12×120	14×132	AT 8-II	2	18×86	14×132	14×132
	3	18×71	12×120	14×132		3	16×77	14×109	14×132
	4	18×60	12×96	14×68		4	16×77	14×109	14×68
	5	18×55	12×87	14×68		5	18×55	12×87	14×68
	6	18×50	12×79	14×68		6	18×35	12×53	14×68
	1	21×83	14×159	14×233		1	24×76	14×145	14×211
AT 9-II	2	21×83	14×159	14×233	AT 10-II	2	24×76	14×145	14×211
	3	21×83	14×159	14×233		3	24×76	14×145	14×211
	4	21×83	14×159	14×159		4	24×76	14×145	14×145
	5	21×73	14×145	14×159		5	24×76	14×145	14×145
	6	21×73	14×145	14×159		6	24×76	14×145	14×145
	7	21×73	14×145	14×132		7	21×68	14×132	14×68
	8	21×73	14×145	14×132		8	21×62	14×109	14×68
	9	24×62	14×132	14×132		9	21×57	12×106	14×68
	1	21×83	14×145	14×193		1	18×97	14×145	14×193
AT 11-II	2	21×83	14×145	14×193	AT 12-II	2	18×97	14×145	14×193
	3	21×83	14×145	14×193		3	18×97	14×145	14×193
	4	21×83	14×145	14×132		4	18×97	14×145	14×132
	5	21×83	14×145	14×132		5	18×97	14×145	14×132
	6	21×83	14×145	14×132		6	18×97	14×145	14×132
	7	21×73	14×120	14×68		7	18×86	14×132	14×68
	8	18×71	12×120	14×68		8	16×77	14×109	14×68
	9	18×60	12×96	14×68		9	18×55	12×87	14×68

3.3 Numerical Modeling Details and Verification of Flexural Link Models

The OpenSees computational platform (2006) was used for numerical analysis of the long link EBF archetypes. The schematic diagrams of OpenSees simplified models are given in Figure 3.6. The effect of gravity framing on the lateral resistance was ignored for the most part of the study. For this case where the only resistance is provided by EBFs, an elastic leaning column was used to take into account the P- Δ effects. Stiff truss elements were used to attach the EBF to the leaning column. The beam segments outside the link, columns and braces were modeled with force-based nonlinear beam-column elements with fiber sections. The beam-to-column and brace-to-column connections were modeled as rigid connections. The column bases were considered pinned except for Section 3.6.4 where column bases were considered fixed to investigate the effect of this base condition. The expected yield strength was considered as $F_{ye} = 1.1 \times 345 = 380$ MPa. A 2% stiffness proportional damping in the first mode was assigned to the beam segments outside the link, braces and columns. Links and leaning columns were not assigned any damping. The effects of link deterioration were studied by comparing the responses of degrading and non-degrading models. Therefore, two different link models were adopted for each 24 EBF archetypes which were named as the degrading model and the non-degrading model.

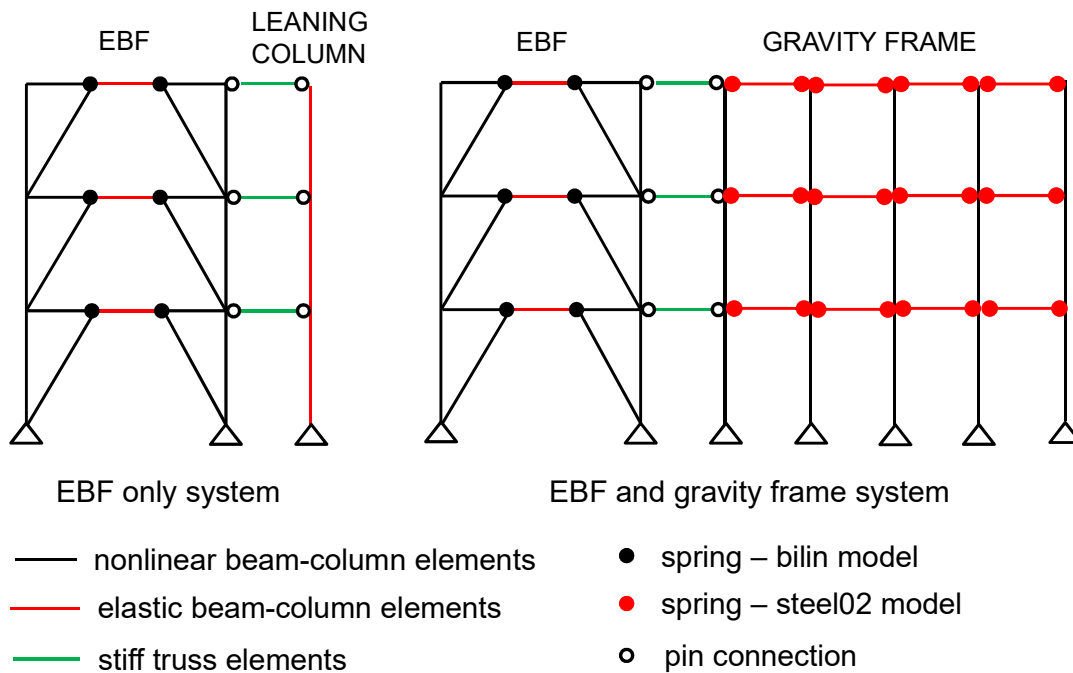


Figure 3.6. Schematic diagram of OpenSees simplified model

In the degrading link model, the link beams were modeled using elastic beam-column elements (Figure 3.6). Zero length rotational spring elements were defined at the end of the links to account for deterioration. The responses of the zero length elements were defined using the modified IMK routines in OpenSees (Bilin material model). Bilin material model parameter definitions are presented in Table 3.5. The default values of deterioration rate parameters (c and D) were used. The initial stiffness reported in Table 3.5 was used for the zero-length elements. The moment of inertia of the links was considered equal to 10 times the original moment of inertia of the link in order to avoid additional flexibility which will be introduced due to the zero-length elements.

Table 3.5. Parameters of bilin material model

Parameter ID	Definition	Value or Equation
K0	elastic stiffness	$6EI/L$
as_Plus, as_Neg	strain hardening ratio for positive and negative loading directions	$(M_c - M_y)/(\theta_p)/K0$
My_Plus, My_Neg	effective yield strength for positive and negative loading directions (negative value in negative direction)	Eq. 3.5
Lamda_S, Lamda_C, Lamda_A, Lamda_K,	Cyclic deterioration parameter for strength, post-capping strength, stiffness and unloading stiffness deteriorations	Eq. 3.12
c_S, c_C, c_A, c_K	rate of strength, post-capping strength, stiffness and unloading stiffness deteriorations	1.0
theta_p_Plus, theta_p_Neg	pre-capping rotation for positive and negative loading directions	Eq. 3.9
theta_pc_Plus, theta_pc_Neg	post-capping rotation for positive and negative loading directions	Eq. 3.10
Res_Pos, Res_Neg	residual strength ratio for positive and negative loading directions	0.40
theta_u_Plus, theta_u_Neg	ultimate rotation capacity for positive and negative loading directions	0.06
D_Plus, D_Neg	rate of cyclic deterioration in the positive and negative loading directions	1.0
nFactor	elastic stiffness amplification factor, optional	NI

The links were modeled with force-based nonlinear beam-column elements with fiber sections for the non-degrading model and the zero length rotational springs at the link ends were removed. The technique developed by Malakoutian (2013) was described in Section 3.1.2.3 and used to represent link behavior in this study. The Giuffre Menegotto-Pinto (Steel02 material model) hysteresis rule was considered to

represent the cyclic shear and flexural behaviors. The yield strength of the link was assumed to be equal to the nominal strength of the link determined according to AISC 341 (2016). The initial stiffness of the link was equal to GA_v where, G is the shear modulus of the steel material and A_v is the shear area of the link which is equal to depth times the thickness of the web. The flexural parameters of Steel02 model b , $R0$, $cR1$, $cR2$, $a1$, $a2$, $a3$ and $a4$ were taken as 0.002, 15, 0.925, 0.15, 0.02, 1, 0.02 and 1, respectively. The parameters of the non-degrading model are selected by trial and error which can verify the experimental data.

The degrading and non-degrading link models were verified using long link test data of Okazaki et al. (2005) and Okazaki and Engelhardt (2007). Specimens 3 and 7 were long links constructed from A992 steel with $e/(M_p/V_p)$ ratios of 3.61 and 3.29 respectively. Figure 3.7 shows the test setup used by Okazaki et al. (2005) and its deformation pattern. One end of the link was connected to a stiff horizontal beam while the other end was connected to a stiff column. The loading was applied from the column base which results in a vertical translation of the column member. The vertical displacements at the link ends were measured in a typical experiment. Low levels of displacements were recorded at the link end attached to the beam due to the vertical restraint present at the link-to-beam joint. The difference in the vertical displacements (Δ) was divided by the link length to calculate link rotation angle (γ). It should be mentioned that the link end rotation (θ) is equal to the link rotation angle (γ) according to the deformation pattern shown in Figure 3.7. The results from numerical simulations are compared with the experimental results in Figure 3.8. The link shear versus link rotation angle responses are presented in Figures 3.8a, 3.8b, 3.8c and 3.8d for specimens 3 and 7. Both the degrading model and non-degrading model simulations are given. The long links clearly showed a deteriorating response. Therefore, the importance of modeling the degradation behavior for long links was highlighted. However, the non-degrading model was also a good estimate of the response especially at the early cycles prior to the commencement of deterioration. As the number of cycles increases, the non-degrading model clearly over-estimates the strength.

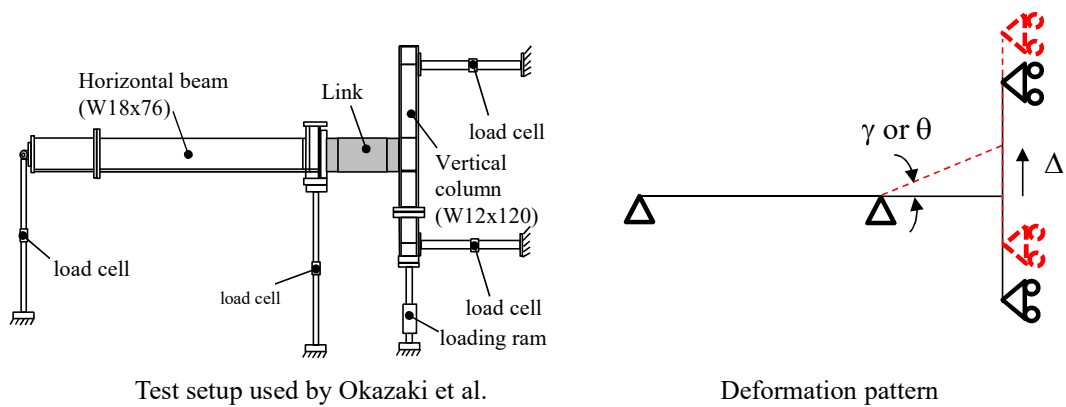


Figure 3.7. Test setup used by Okazaki et al. (2005) and deformation pattern

The bending moments produced at the link ends were back calculated by Okazaki et al. (2005 and 2007) using the load cells mounted on the support points. The numerical simulations for the link end bending moments are compared against the experimental findings in Figures 3.8e, 3.8f, 3.8g, and 3.8h. It should be noted that the bending moments produced at the link ends during the experiments were not equal because of the differences between the stiffnesses of the column and horizontal beam. Therefore, the bending moment versus link rotation responses from both ends are slightly different. Both the bending moments produced at the beam end and the column end are given in Figure 3.8. For specimen 3, the capacities at the final cycles were accurately represented by the degrading model for both the link ends. The ultimate strength was more accurately predicted for the column end moment when compared with the beam end moment. The same observations are valid for specimen 7. It should be noted the ultimate capacities obtained in both loading directions were different from each other, which caused a greater difference between experimental findings and numerical simulations. Overall Figure 3.8 demonstrates that the degrading model parameters developed by Lignos and Krawinkler (2011) are sufficiently accurate for modeling the long link beams considered for the verification study.

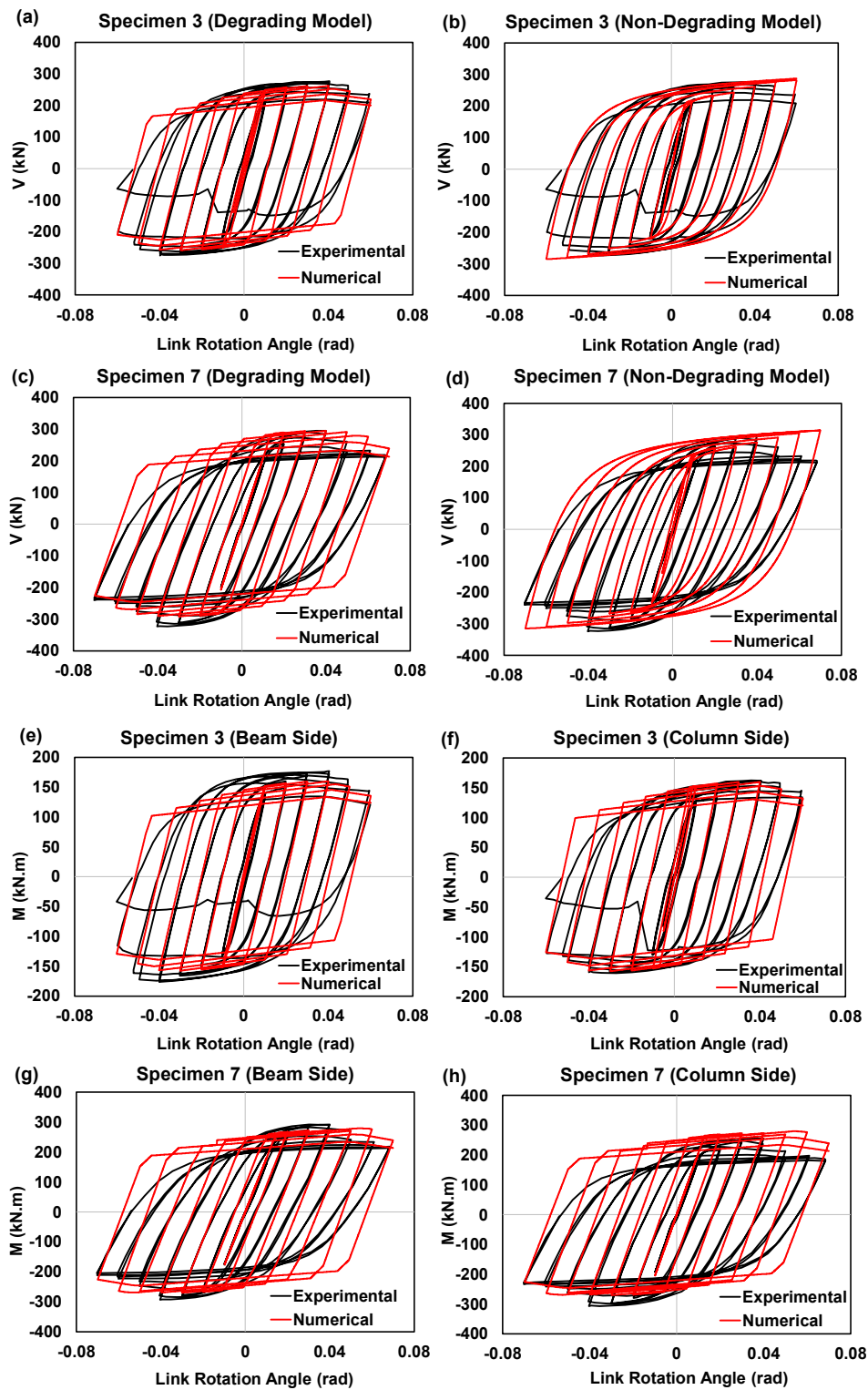


Figure 3.8. Comparison of numerical simulation of degrading and non-degrading models with the experimental results

3.4 Ground Motion Selection and Scaling

The 22 pair ground motions far-field record set of FEMA P695 (2009) was used in time history analysis. The normalized ground motions were scaled up to three different seismic hazards which are the maximum considered earthquake (MCE), the collapse level earthquake with a collapse margin ratio of 20% (CLE20%) and collapse level earthquake with a collapse margin ratio of 10% (CLE10%). The CLE20% and CLE10% represent collapse probabilities of 20% and 10% at MCE level, respectively. The scaling factors for archetypes are given in Table 3.2.

MCE scaling factors were determined by matching the median spectral acceleration of the record set to the MCE spectral acceleration at the modified approximate fundamental period ($T=C_u \times T_a$) where C_u is a modification factor of (1.4) and T_a is the approximate time period as per ASCE7-16 (2016). The MCE scaling factors were amplified by the collapse margin ratios CMR20% and CMR10% to arrive at the CLE scaling factors given in Table 3.2. The following relationship can be used to define the collapse margin ratio:

$$CMR = ACMR / SSF \quad (3.13)$$

where $ACMR$ is the adjusted collapse margin ratio and is a function of total system uncertainty (β_{TOT}) and collapse probability at MCE level as described in Section 3.1.1. In this study, superior model quality (A) was assigned to the archetypes and β_{TOT} was calculated as proposed in FEMA P695. SSF is the spectral shape factor and is a function of period-based ductility (μ_T) and the fundamental period. A representative static pushover analysis result for AT5-I is given in Figure 3.9 to demonstrate the determination of the period-based ductility which is the ratio of the roof displacement (δ_u) at the point of 20% strength loss ($0.8V_{max}$) and the effective yield displacement given in FEMA P-695. Nonlinear static analyses were conducted for all archetype EBFs to determine their period-based ductility (μ_T) which are reported in Table 3.2.

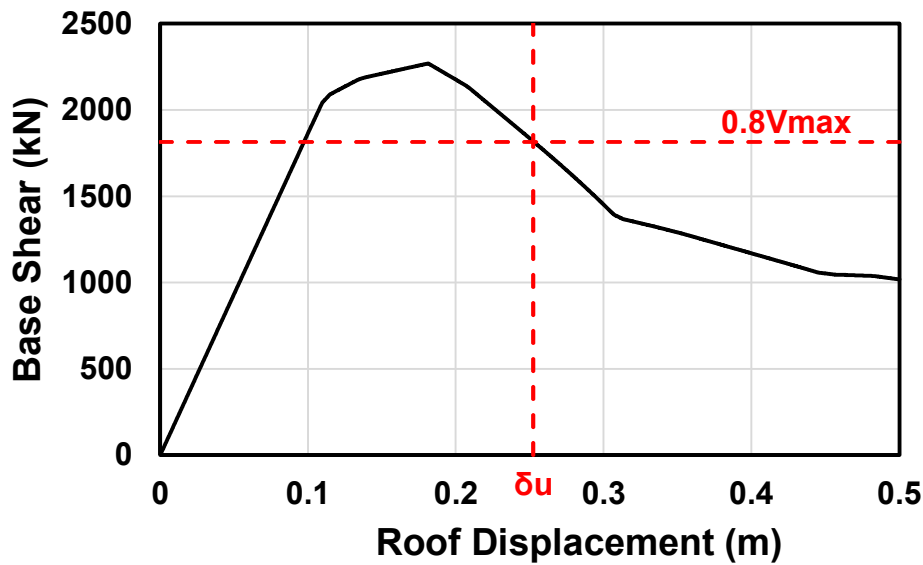


Figure 3.9. Static Pushover Curve of AT5-I

3.5 Results of Time History Analysis

The DesignSafe platform (Rathie et al. 2017) was utilized to conduct most of the OpenSees time history analysis. The results are too voluminous to present in every detail. The effects of degradation, seismic intensity, and floor plan are discussed in the following sub-sections by considering a typical archetype building. The overall results are presented afterwards.

3.5.1 Effects of Strength and Stiffness Degradation

Link rotation angle (LRA) versus link shear (LS) interaction that belongs to the first story link of AT5-I under ground motion 2 (GM02) scaled to CLE10% level seismic intensity is presented in Figure 3.10. Responses of degrading and non-degrading models are given. There are substantial differences between the LRA versus LS plots of degrading and non-degrading models. For both models, maximum link shear values were in the range of -1000 kN and +1000 kN. For the degrading model, once the capping strength was approached, the link experienced a negative stiffness

branch until the predefined residual strength value. After this point, the stiffness drops to zero up to the ultimate rotation. On the other hand, the strain hardening branch of the non-degrading model experiences no strength cap. In addition, for the degrading model, once the component yields at least in one direction, the hysteretic energy dissipation was activated and the peak link shear force reduced to a lower value at each cycle. Conversely, the maximum link shear of the non-degrading model increases at the end of each cycle because of the isotropic hardening. The maximum absolute LRA values for degrading and non-degrading models were 0.15 rad and 0.09 rad, respectively. This considerable difference points out the importance of modeling degradation in long links.

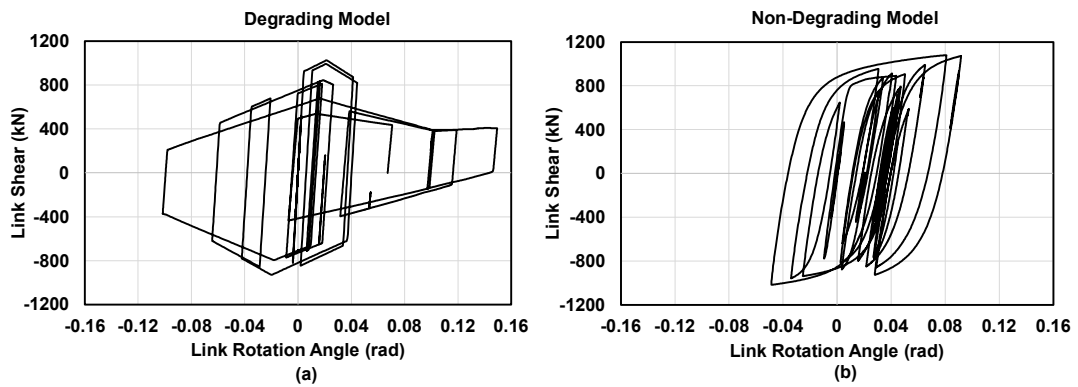


Figure 3.10. LRA versus LS interactions that belong to 1st story link of AT5-I under ground motion 2 (GM02) scaled to CLE10% for (a) degrading model and (b) non-degrading model.

The effects of degradation on typical archetypes building are demonstrated in Figures 3.11 to 3.16. The maximum of the link rotation angles from 44 ground motions were recorded at every story and their median is reported in Figures 3.11-3.16. In these figures, the, 3-, 6-, 9-story FP-I and FP-II archetypes were considered by taking into account both the degrading and non-degrading models. The responses under MCE, CLE20% and CLE10% level earthquakes are presented separately. For the degrading model, the ultimate rotation (θ_u) of all archetypes exceeded 0.06 rad

under CLE10% seismic hazard. For MCE, only the archetypes with $e/L=0.5$ produced link rotations less than 0.06 rad. For example, for 6-story archetypes with FP-I, the maximum reported values are 0.056 rad and 0.059 rad for degrading and non-degrading models, respectively. For CLE20% level events, the 6-story FP-I archetypes with $e/L=0.5$ experienced 0.063 rad of link rotation indicating that the target rotation was exceeded by a slight margin.

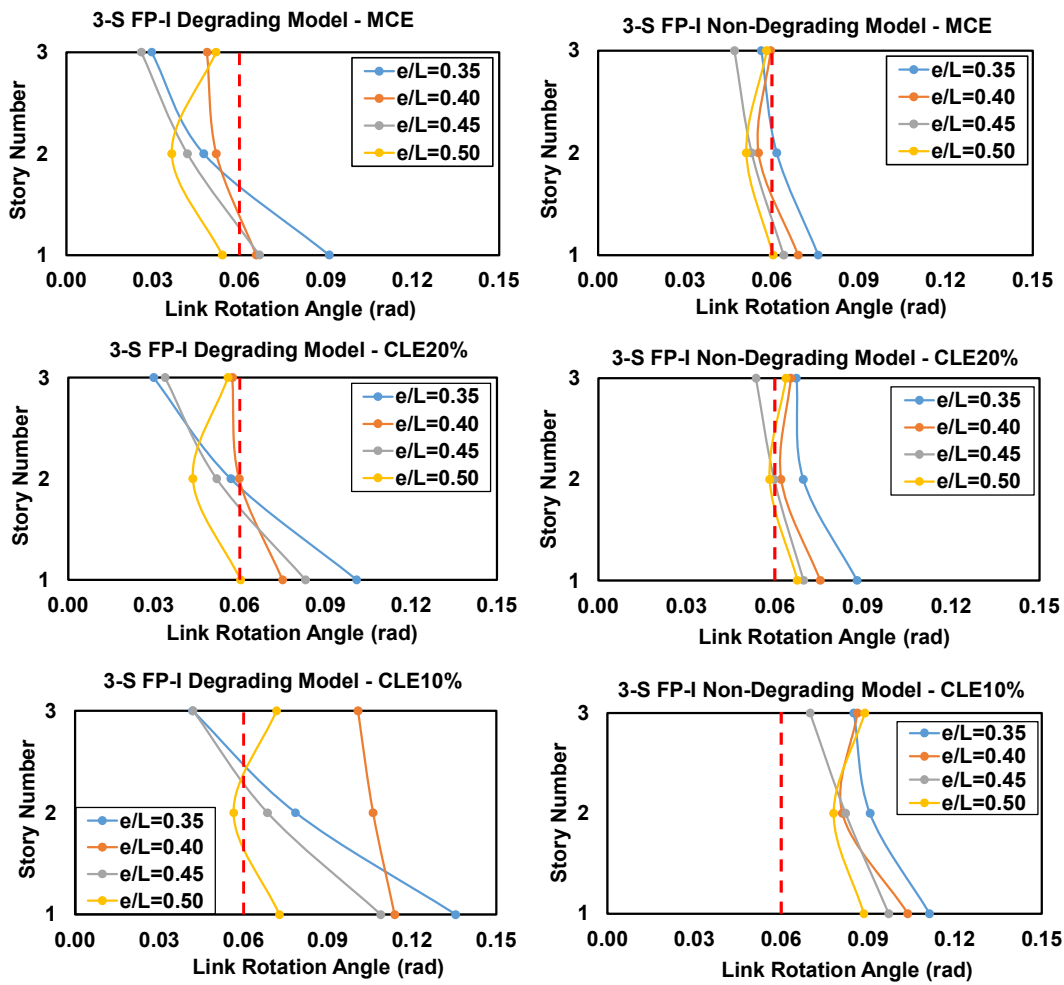


Figure 3.11. The variation of median Link Rotation Angle for 3 story FP-I archetypes

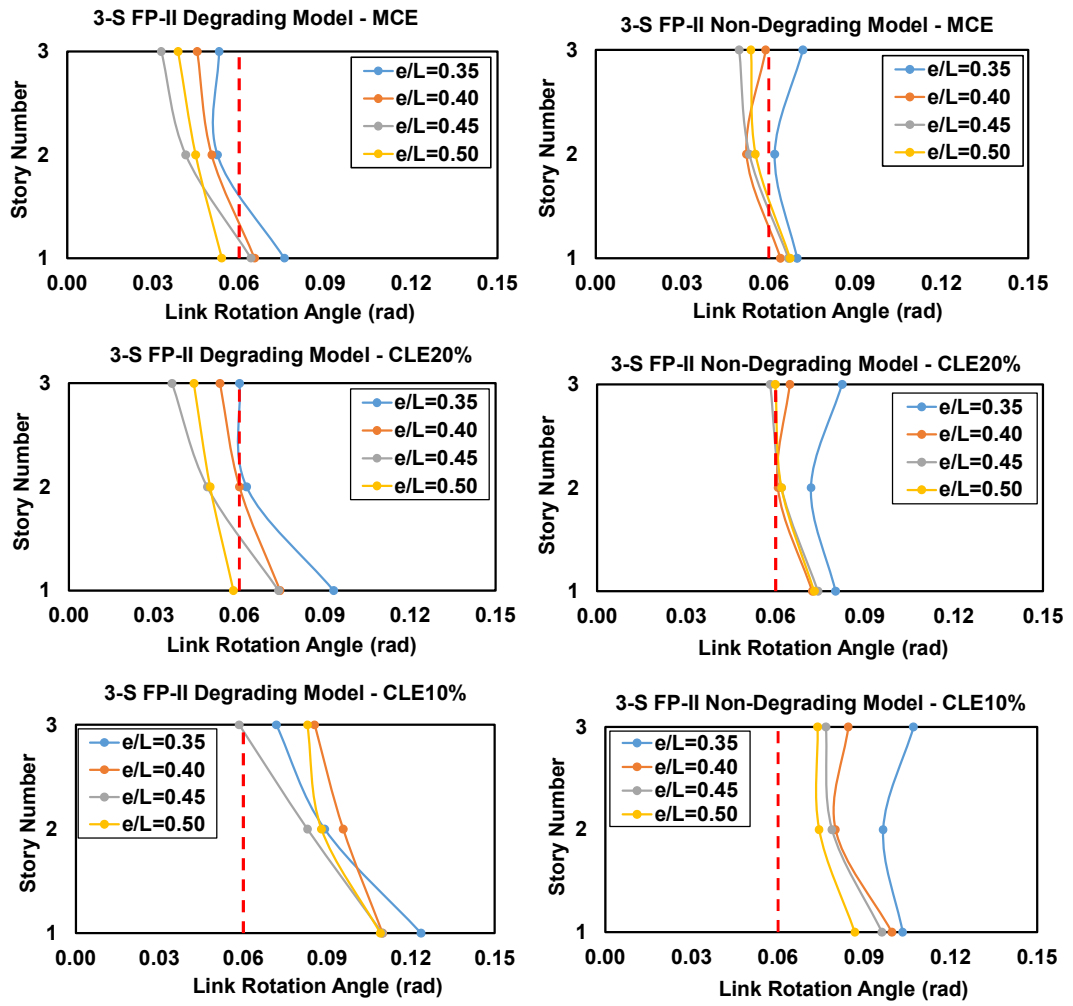


Figure 3.12. The variation of median Link Rotation Angle for 3 story FP-II archetypes

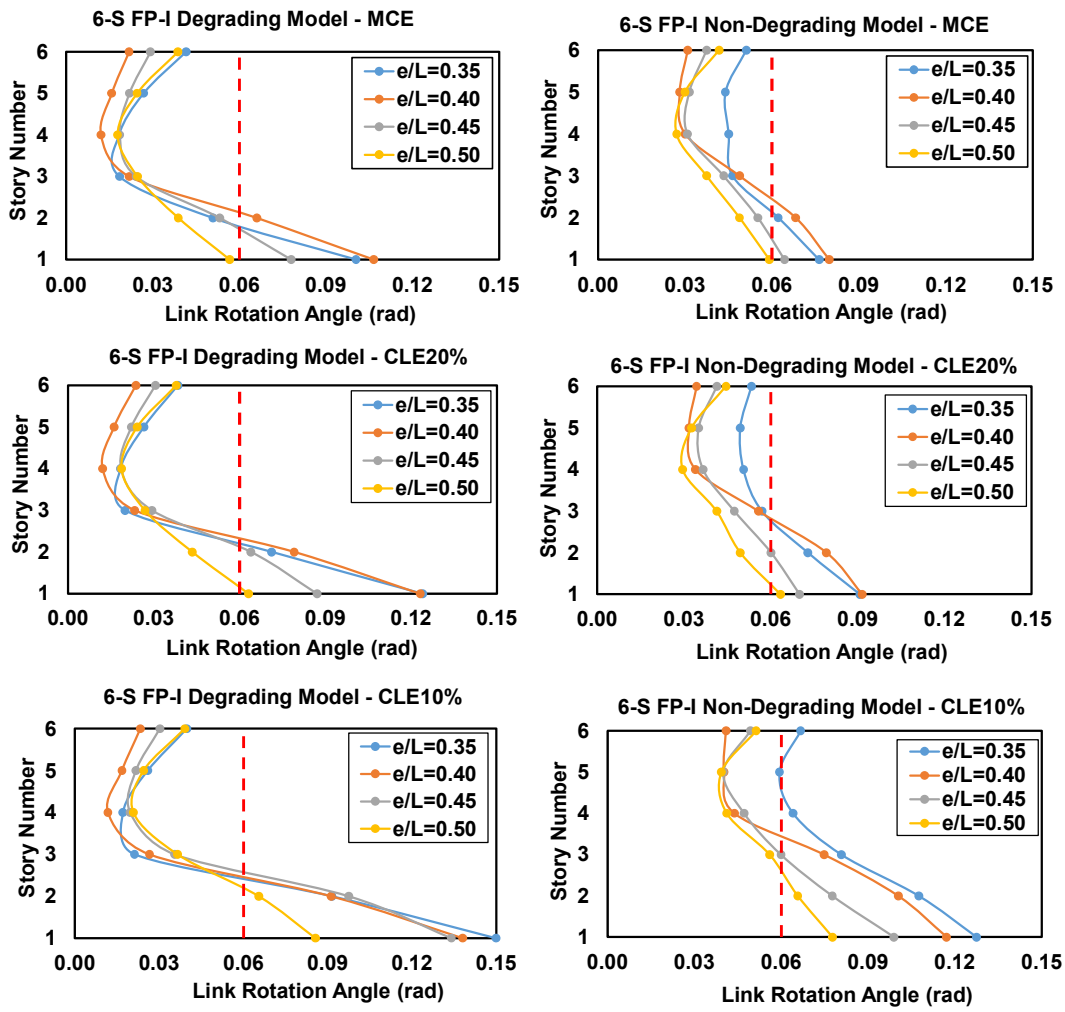


Figure 3.13. The variation of median Link Rotation Angle for 6 story FP-I archetypes

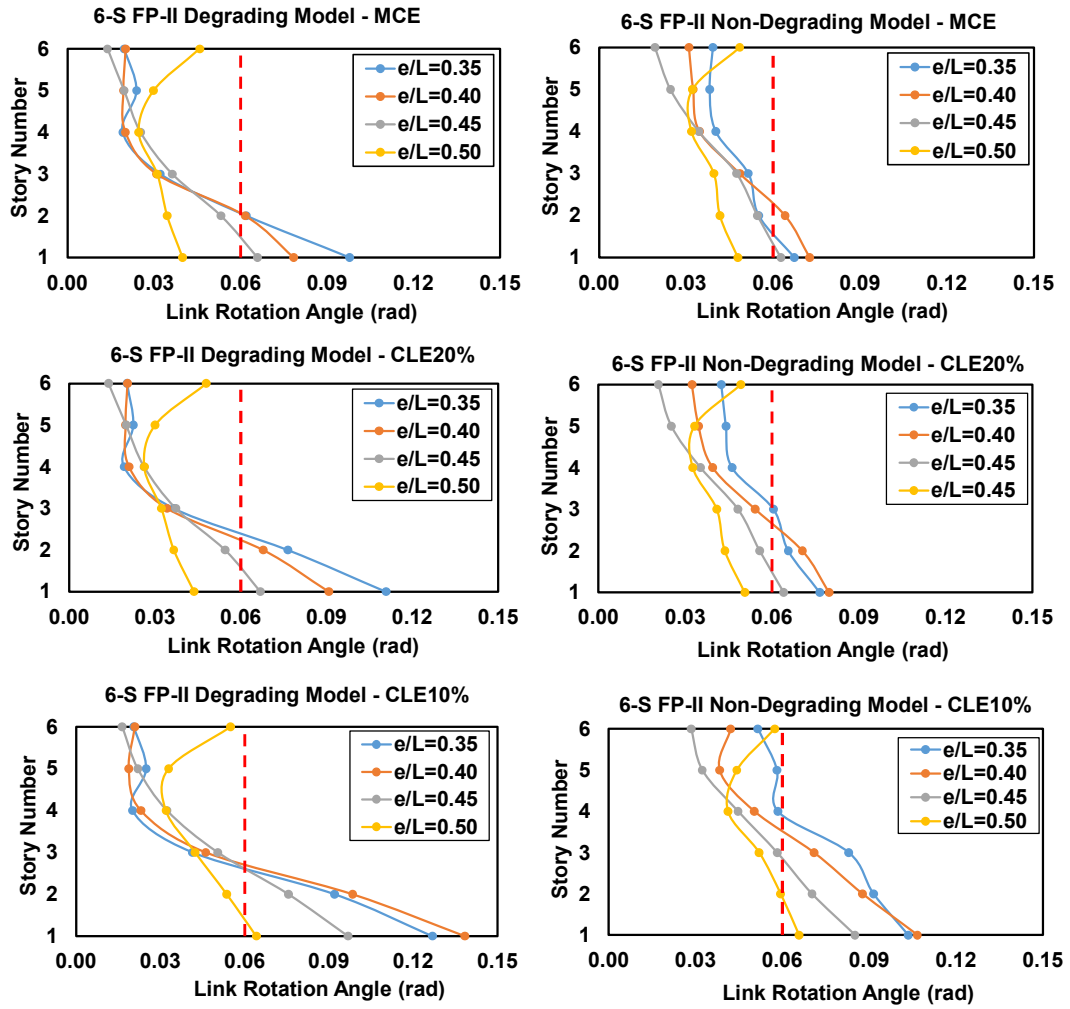


Figure 3.14. The variation of median Link Rotation Angle for 6 story FP-II archetypes

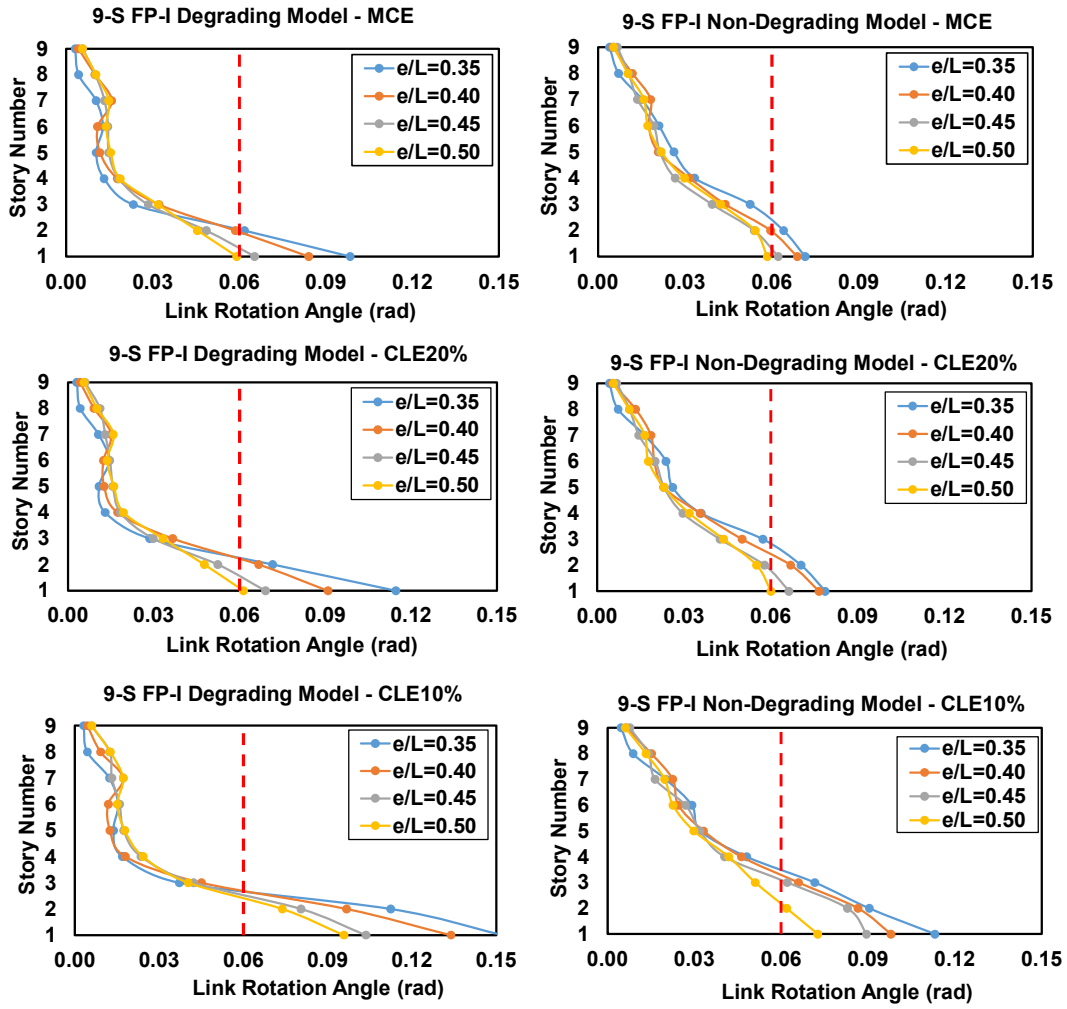


Figure 3.15. The variation of median Link Rotation Angle for 9 story FP-I archetypes

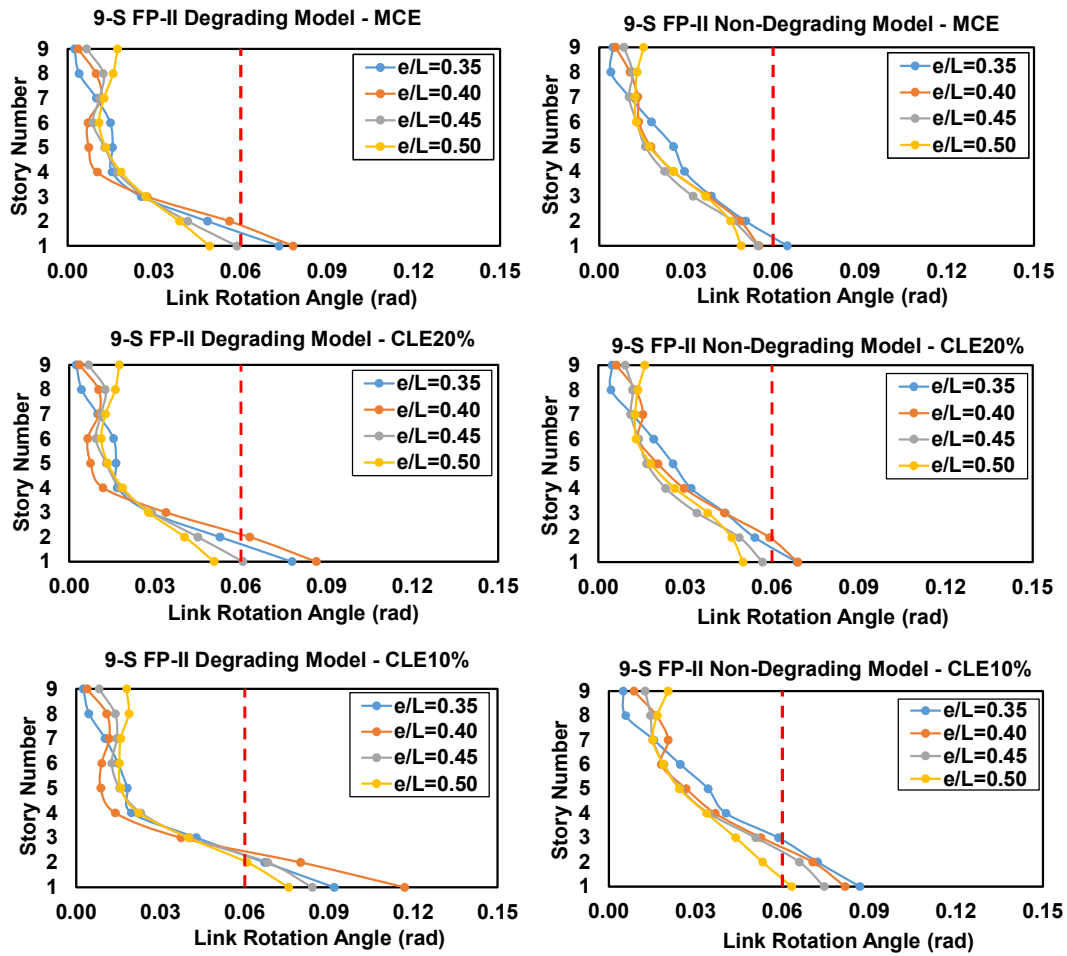


Figure 3.16. The variation of median Link Rotation Angle for 9 story FP-II archetypes

Figures 3.17-3.19 show the LRA ratios of degrading model over non-degrading model for 3-, 6-, 9-story FP-I and FP-II archetypes under MCE, CLE20% and CLE10% events. The use of degrading models does not always result in an increase in the LRA for all stories. In almost all cases the maximum LRA belongs to the first story and there is a clear increase in the LRA of first story links when the degrading model is used. While the LRA of first story links are amplified by using a degrading model, the LRA of links at other stories can experience lower demands. In EBFs with pinned column bases, the damage usually accumulates to the bottom stories. The analysis results showed that the accumulation is more pronounced as degradation is introduced into the system behavior.

A statistical evaluation of the increase in LRA was performed. It was noticed that the increase in LRA due to modeling of degradation is significantly influenced by the e/L ratio with a minor influence of the floor plan or the seismic hazard. When degradation is included in the numerical models, the average increase in maximum LRA is 24%, 19%, 11%, and 0% for e/L of 0.35, 0.40, 0.45, and 0.50, respectively. When all archetypes were considered the average increase is 13% with a standard deviation of 17%. The maximum amount of increase was 46% and observed for AT9-I subjected to CLE20% level seismic hazard.

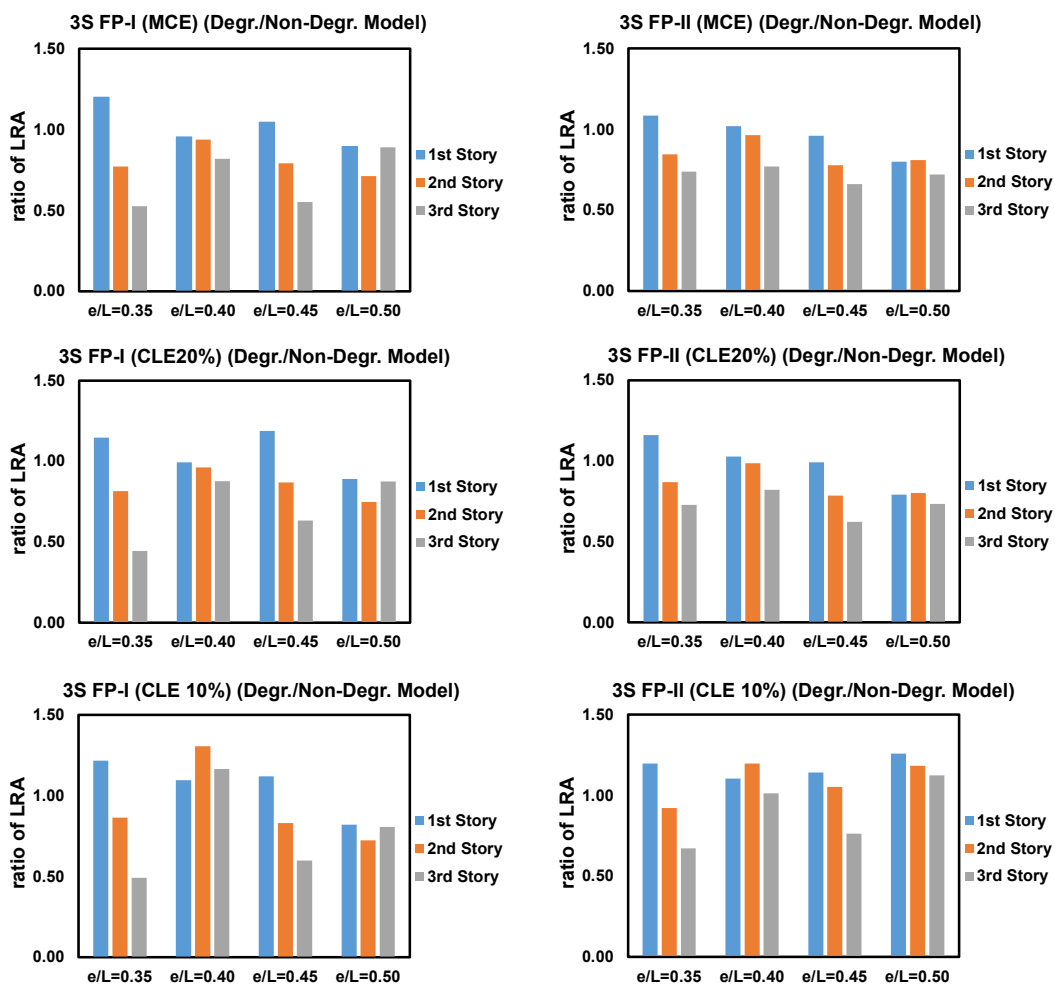


Figure 3.17. Ratios of LRA for degrading model over non-degrading model of 3 story FP-I and FP-II archetypes

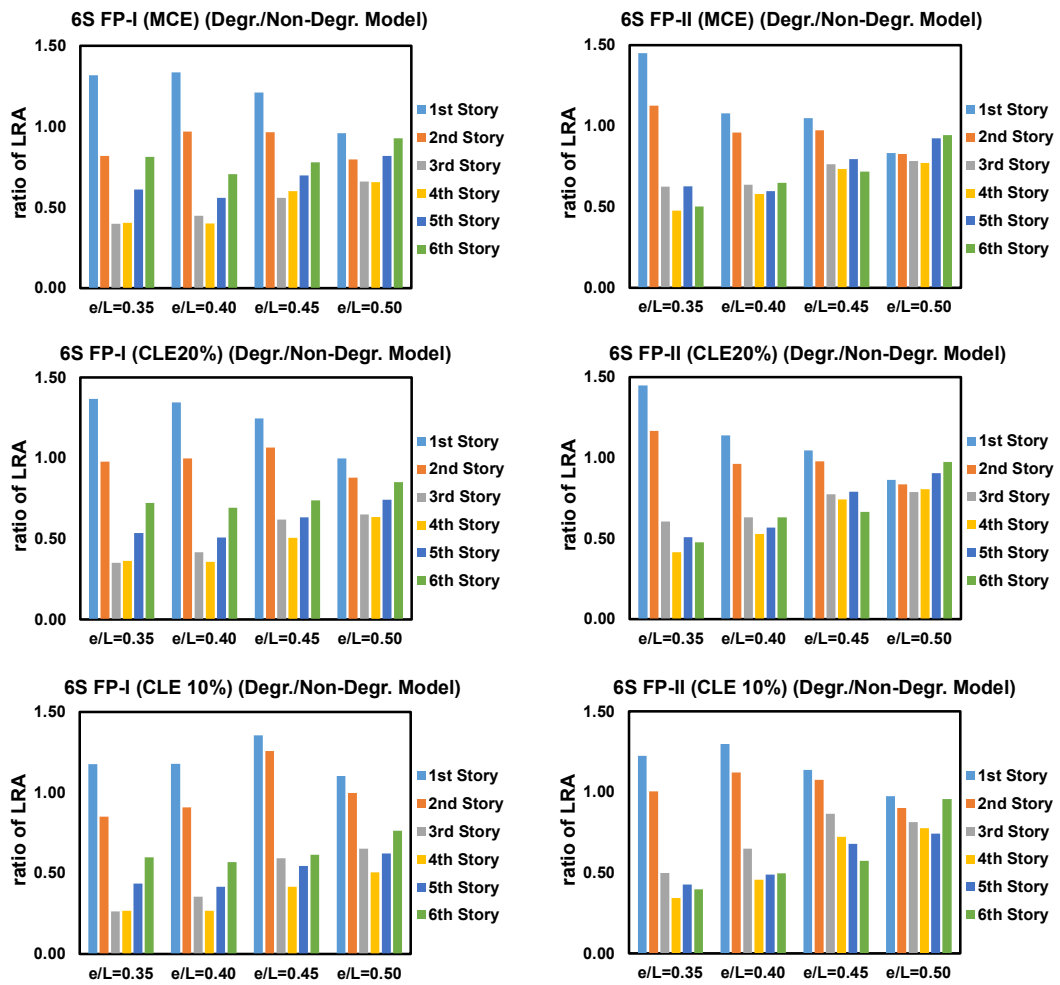


Figure 3.18. Ratios of LRA for degrading model over non-degrading model of 6 story FP-I and FP-II archetypes

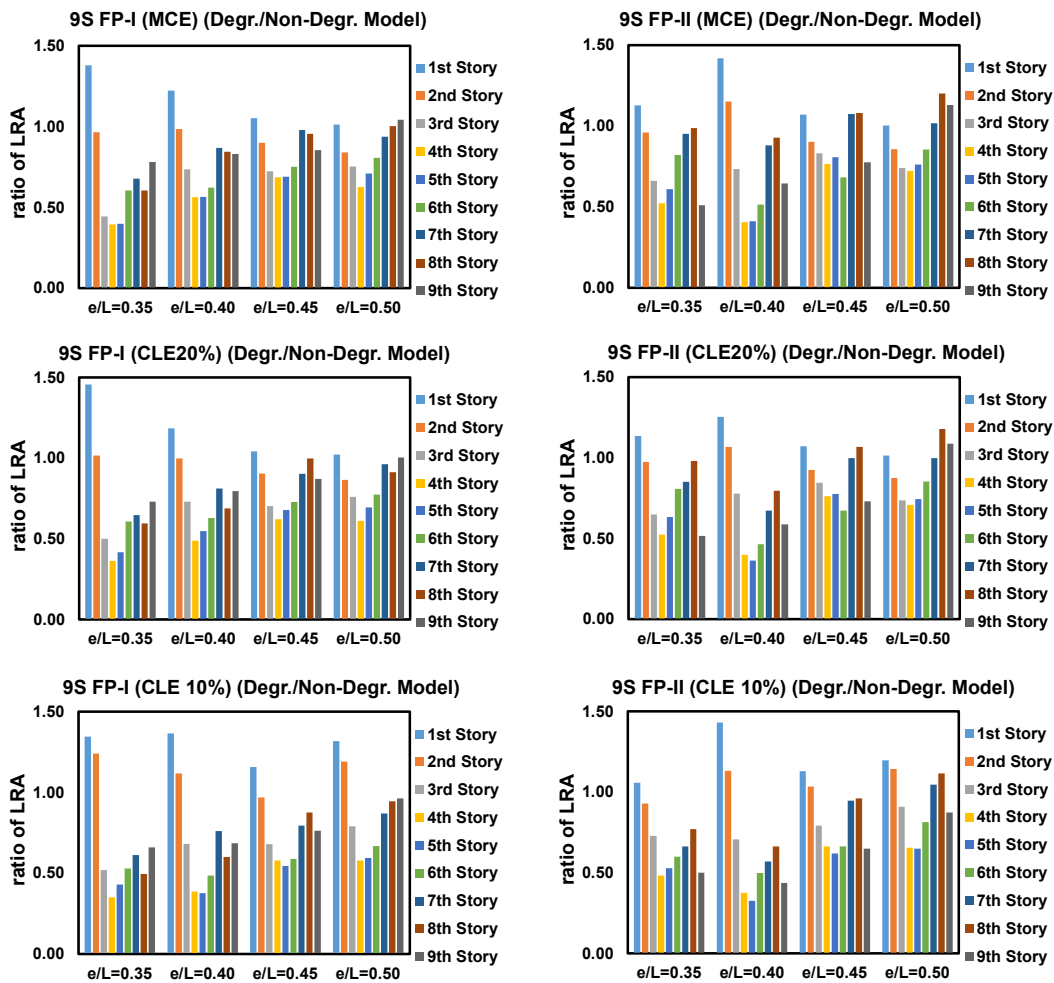


Figure 3.19. Ratios of LRA for degrading model over non-degrading model of 9 story FP-I and FP-II archetypes

3.5.2 Effect of Seismic Intensity

The comparisons of height wise variation of median LRA for three of the 3-, 6-, 9-story FP-I and FP-II archetypes under MCE, CLE20% and CLE10% events are given in Figures 3.20-3.25. An increase in LRA with increasing seismic intensity is apparent. For the non-degrading models and 3-story degrading models, it is observed that the increase in LRA is rather uniform over all stories. On the other hand, for 6- and 9-story degrading model, the increases in LRA are more concentrated to the lower stories and the links in the upper stories do not experience an appreciable

increase in the demands. For the 9-story archetypes especially with $e/L \geq 0.45$, the difference between MCE level and CLE20% is almost negligible for both link models.

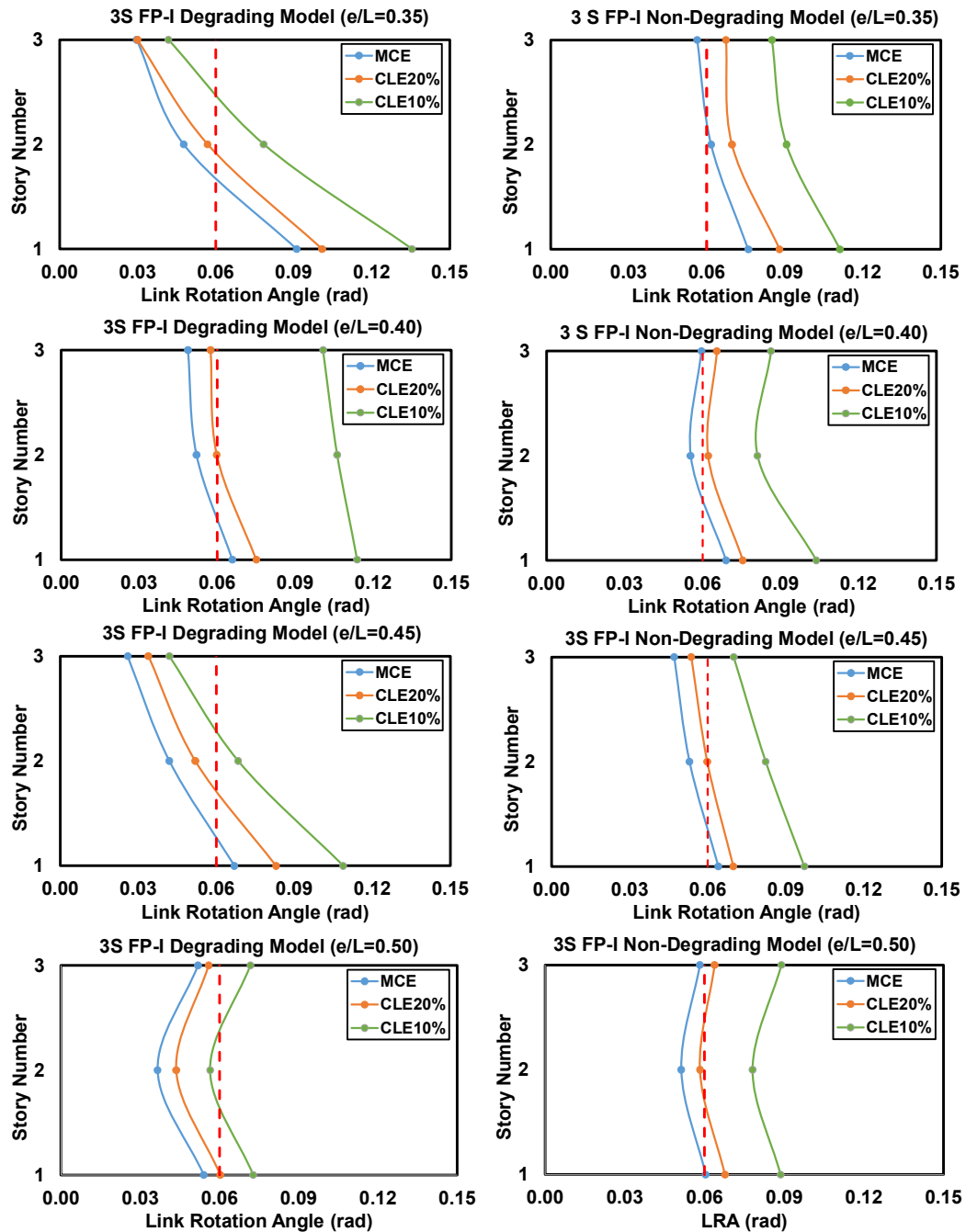


Figure 3.20. Variation of LRA for 3 story FP-I archetypes under MCE, CLE20% and CLE10% events

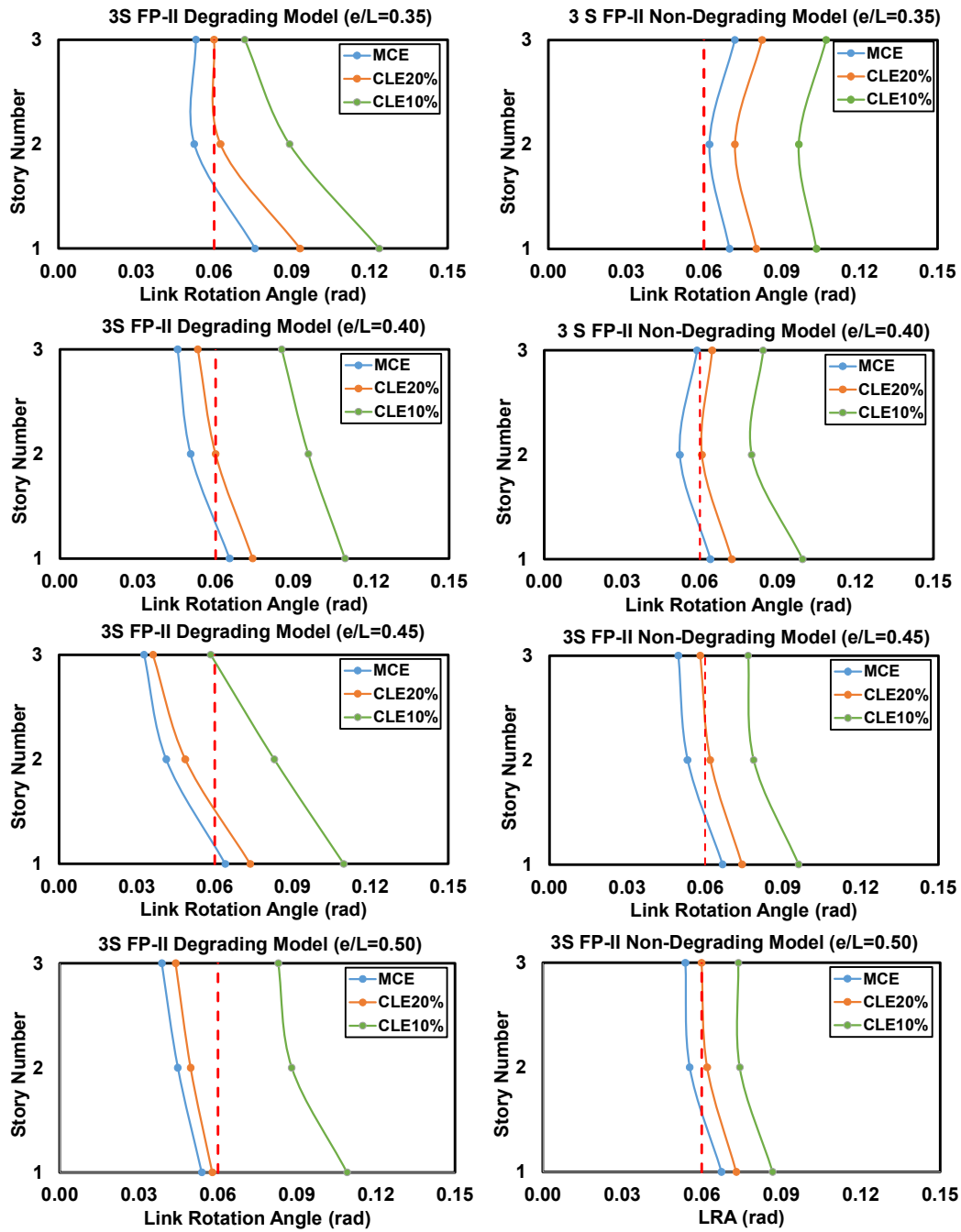


Figure 3.21. Variation of LRA for 3 story FP-II archetypes under MCE, CLE20% and CLE10% events

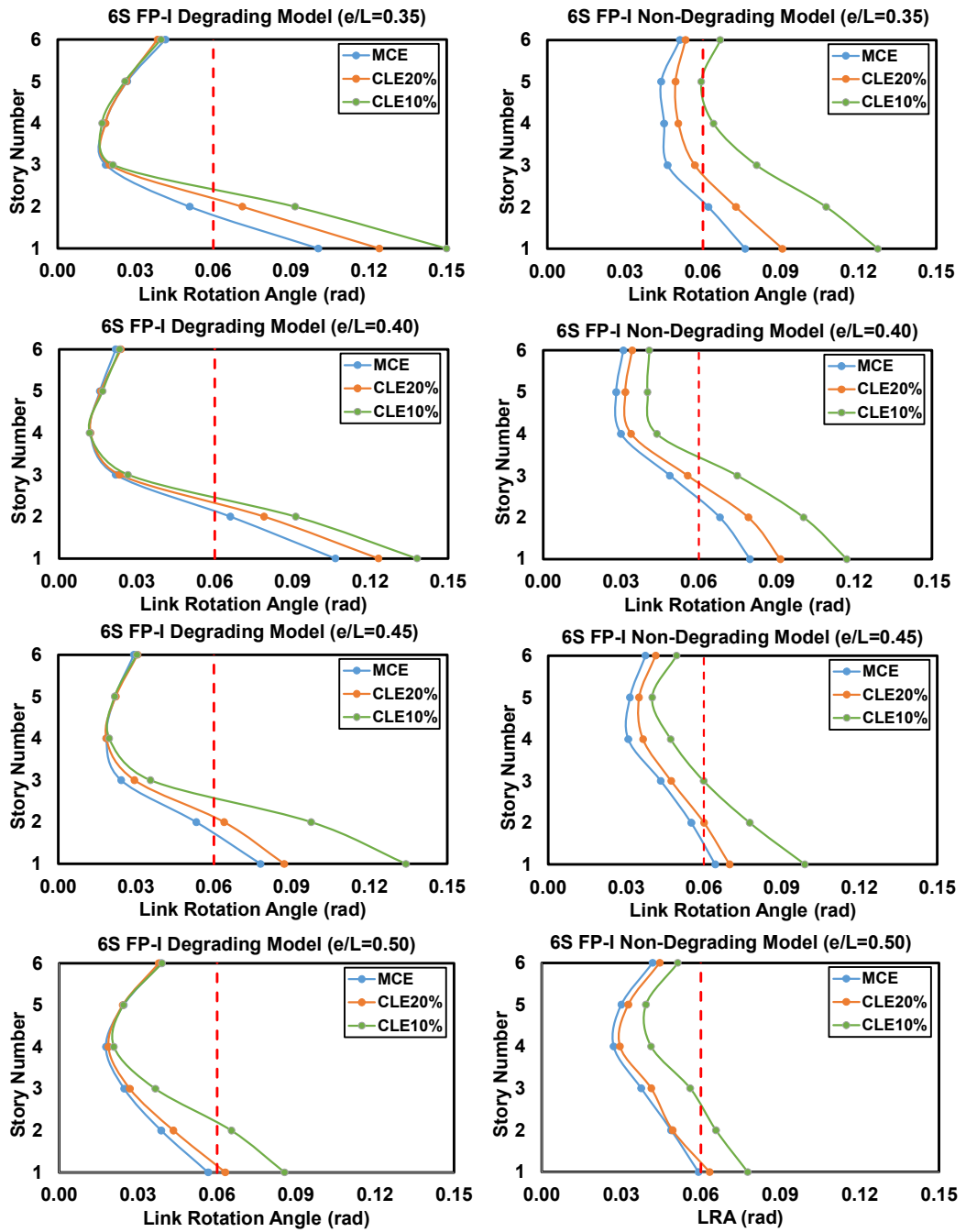


Figure 3.22. Variation of LRA for 6 story FP-I archetypes under MCE, CLE20% and CLE10% events

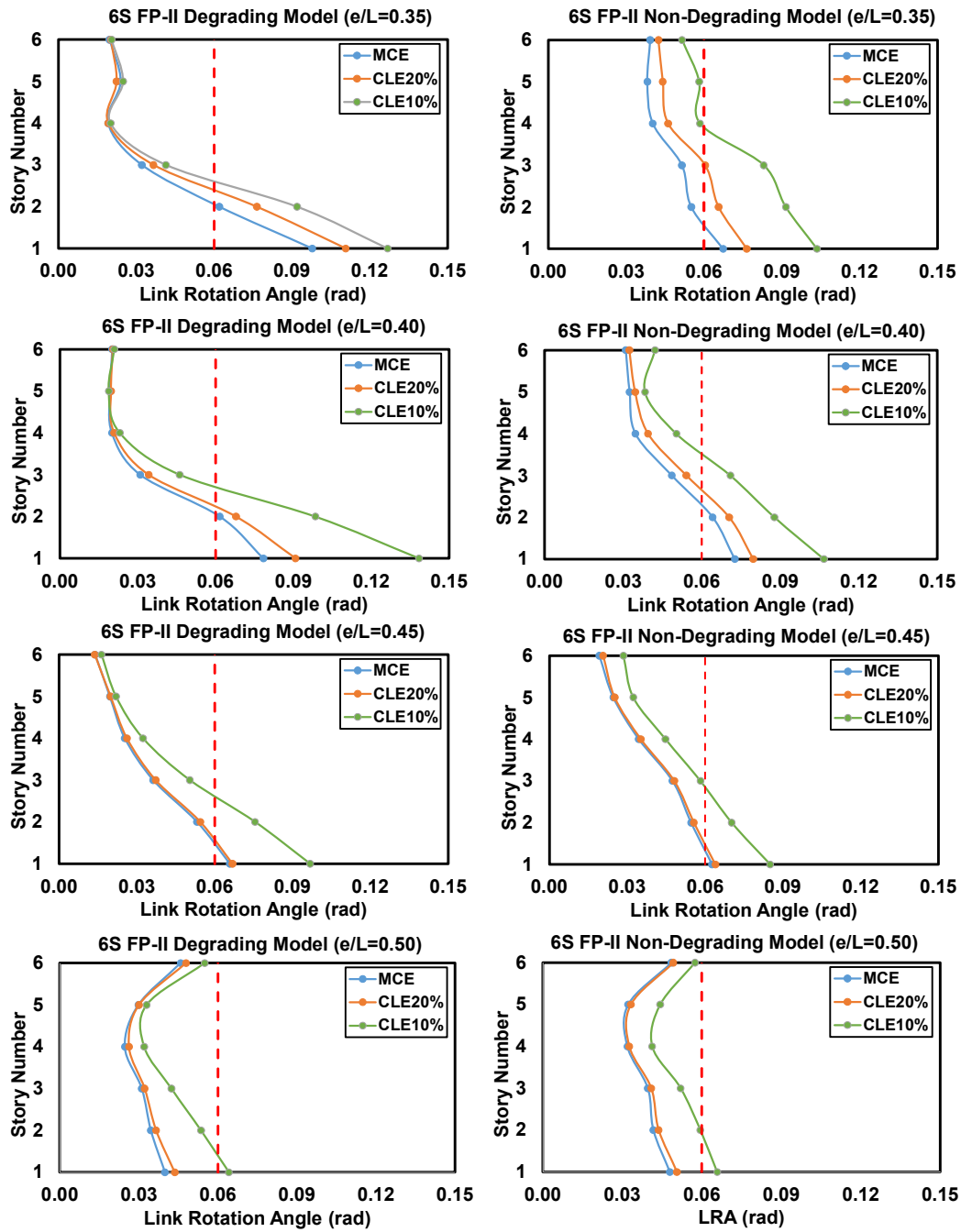


Figure 3.23. Variation of LRA for 6 story FP-II archetypes under MCE, CLE20% and CLE10% events

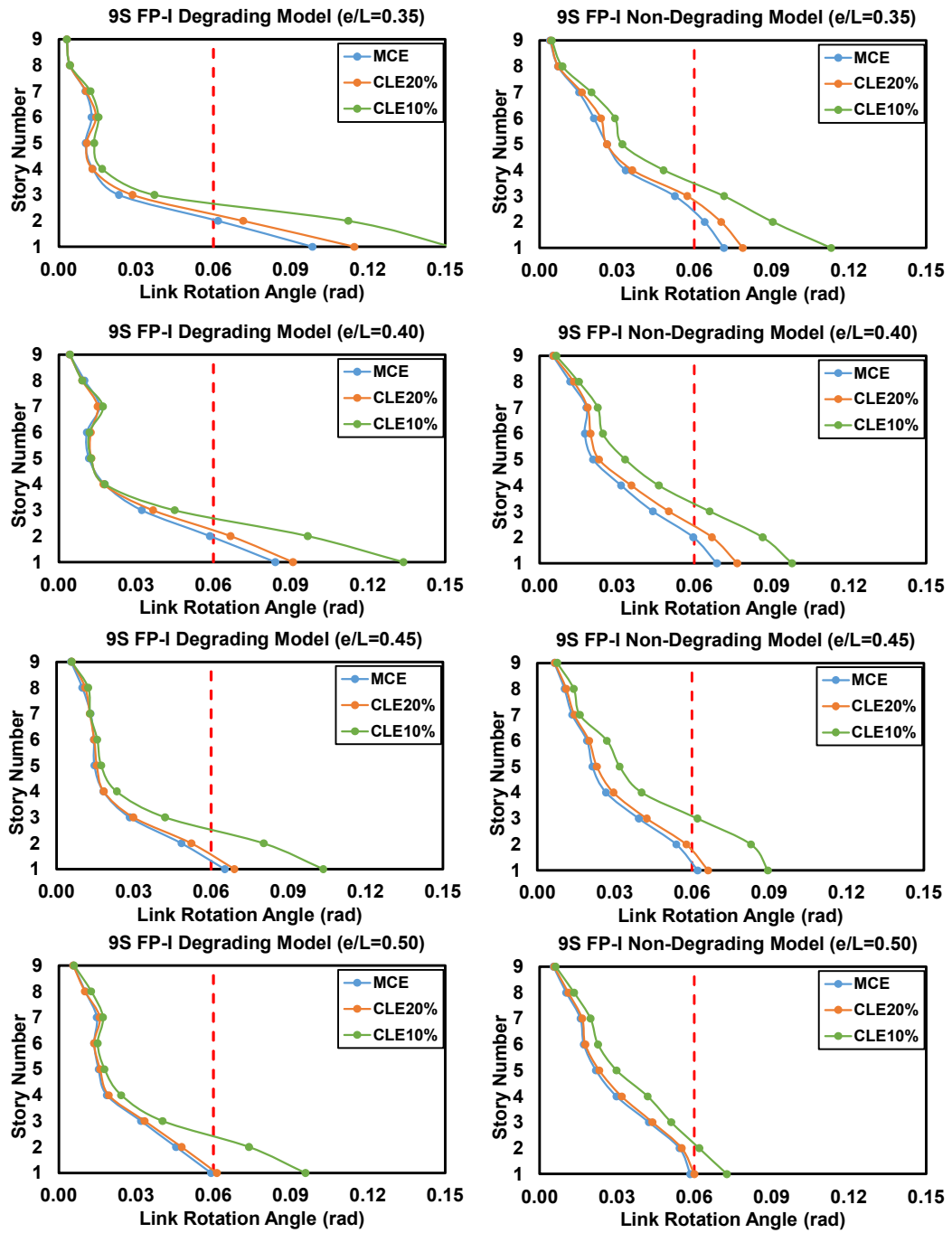


Figure 3.24. Variation of LRA for 9 story FP-I archetypes under MCE, CLE20% and CLE10% events

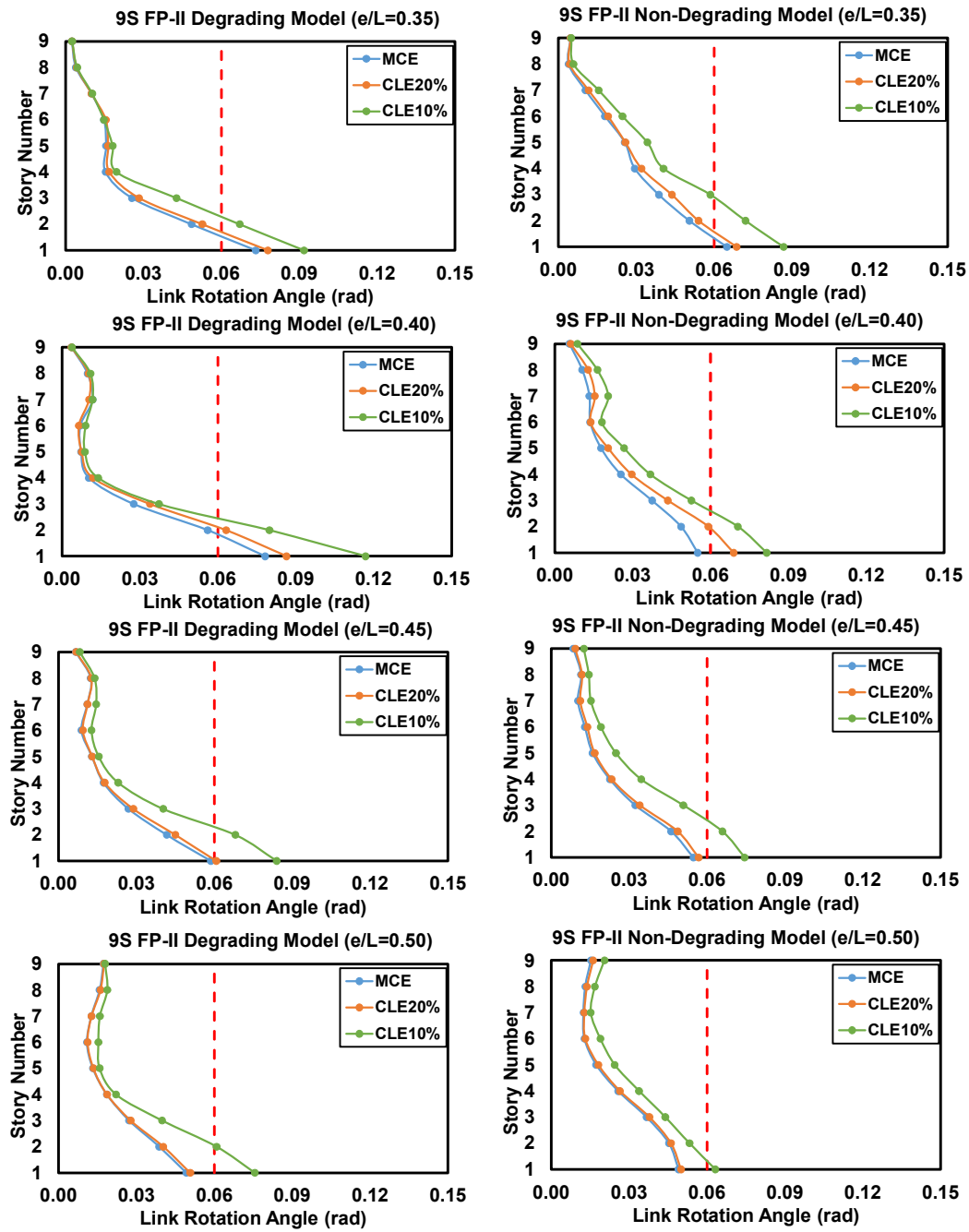


Figure 3.25. Variation of LRA for 9 story FP-II archetypes under MCE, CLE20% and CLE10% events

3.5.3 Effect of Floor Plan

Different floor plans were considered to be able to investigate the influence of having different bay widths for the EBFs. Figures 3.26-3.28 compare the median LRA response of archetypes having two different floor plans for the particular example of 6-story degrading archetypes (AT5 through AT8) subjected to MCE, CLE20% and CLE10% levels. According to the results, the variation of median LRA along the height depends on the floor plan. The maximum LRA reported for the first story also depends on the floor plan considered. FP-II archetypes experienced lower link rotations at the most critical story when compared with FP-I archetypes. For all seismic levels, all archetypes with $e/L \leq 0.45$ experienced link rotations greater than 0.06 rad. For the case with $e/L=0.5$, link rotation angles were recorded lower than 0.06 rad for both floor plans under MCE level seismic event (Figure 3.26). Figure 3.27 shows that FP-II archetype with $e/L=0.5$ (AT8-II) had a much lower link rotation angle than its counterpart (AT8-I) for the CLE20% level earthquake. Although the target link rotation was exceeded by a small amount for AT8-I, the maximum link rotation for AT8-II was well below this limit for this level seismic event. Both archetypes with $e/L=0.5$ (AT8-I and AT8-II) yielded link rotations higher than 0.06 rad under CLE10% level earthquake (Figure 3.28).

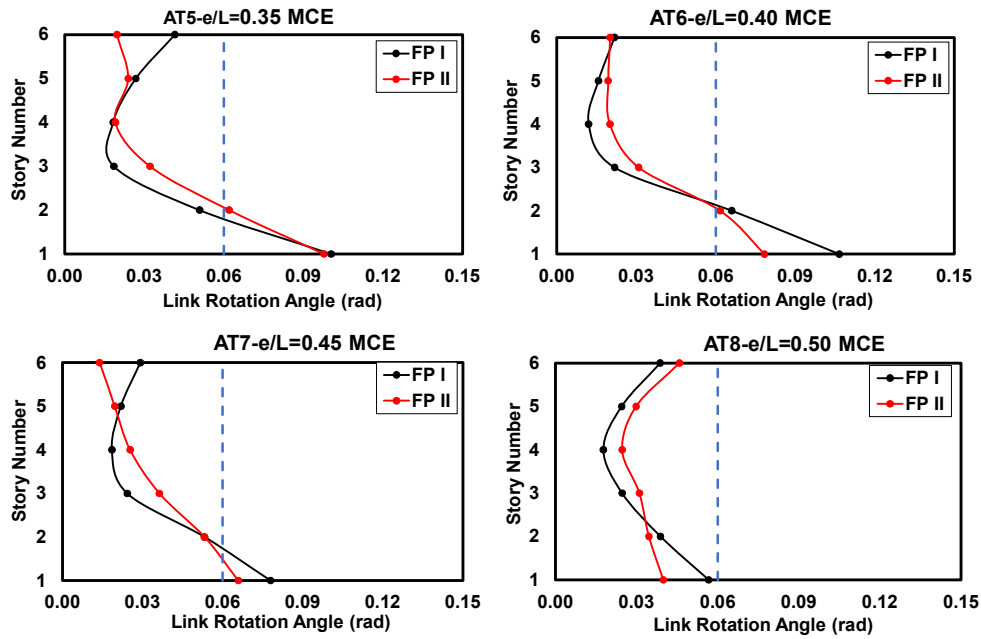


Figure 3.26. Variation of median LRA of degrading model for 6 story FP-I and FP-II archetypes under MCE event

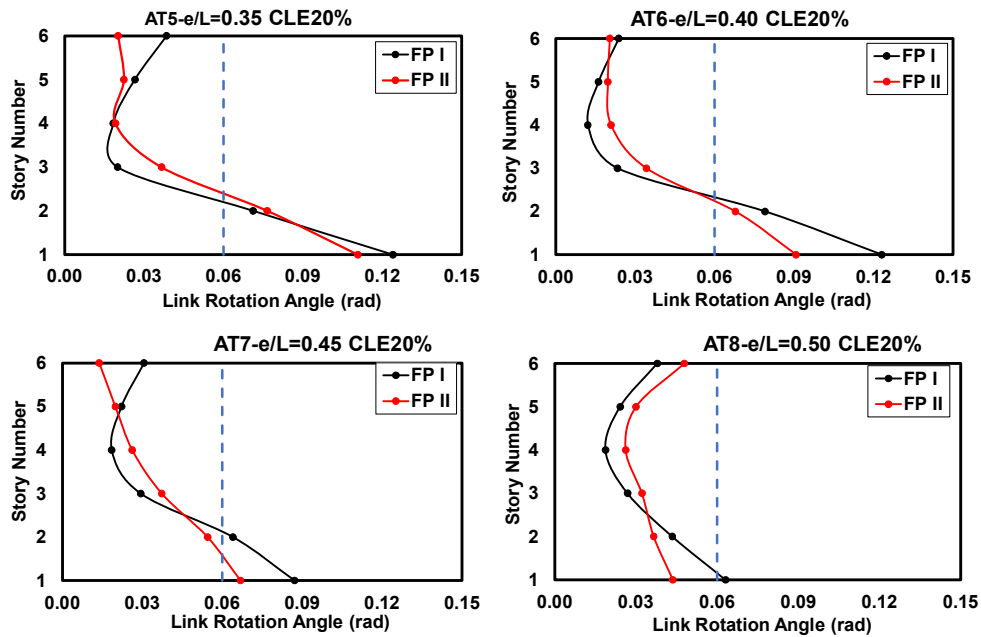


Figure 3.27. Variation of median LRA of degrading model for 6 story FP-I and FP-II archetypes under CLE20% event

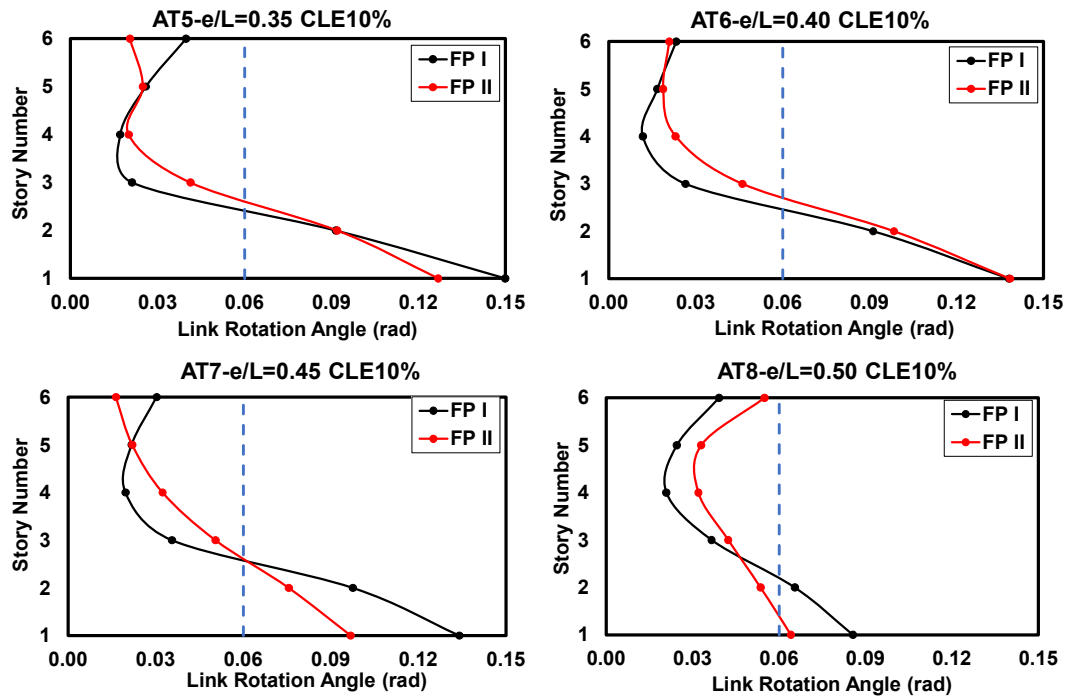


Figure 3.28. Variation of median LRA of degrading model for 6 story FP-I and FP-II archetypes under CLE10% event

3.5.4 Responses of All Archetypes

The link length to bay width ratio (e/L) was observed to be the most influential factor on the response of archetype buildings. Therefore, the archetypes were grouped according to the e/L ratio. The median of maximum LRA responses corresponding to the first story for all archetypes under MCE, CLE20% and CLE10% level seismic events are given in Figure 3.29. Both the degrading and non-degrading model results are presented in this figure. The median values are compared with the ultimate link rotation capacity $\theta_u=0.06$ rad considered in this study.

For MCE level events, all degrading archetypes with $e/L=0.50$ showed satisfactory behavior. The same observation is valid for the non-degrading archetypes except 3S FP-II (AT4-II) where the maximum link rotation was reported as 0.067 rad. Although degrading models give larger link rotations than the non-degrading models in

general, the behavior for this archetype was found to be the opposite. The maximum rotations for degrading archetypes with $e/L=0.45$ exceeded the limit by a slight margin ($\theta_u < 0.07$ rad for most archetypes). On the other hand, the maximum rotations were significantly above the limit for $e/L=0.35$ and 0.40 .

For CLE20% level events all degrading archetypes with $e/L=0.50$ except 6S FP-I (AT8-I) showed satisfactory behavior. As discussed in Sections 3.5.1 and 3.5.3, the maximum rotation for this archetype was 0.063 rad which was slightly above the limit. While it is reasonable to consider that the archetypes with $e/L=0.5$ as satisfactory, the other archetypes with smaller e/L ratios experienced rotations much higher than the target value. The non-degrading models showed a similar trend for $e/L=0.5$ with some archetypes experiencing larger rotations than their counterparts.

For CLE10% level events, none of the archetypes showed satisfactory behavior for both the models. Although cases with $e/L=0.5$ had rotation demands much less than the other EBFs, the maximum rotations reported for the degrading and non-degrading models were 0.11 rad and 0.089 rad, respectively.

The results demonstrated that the link length to bay width ratio (e/L) should be constrained in routine design practice. For 20% probability of collapse under MCE, $e/L=0.5$ seems to be the only solution that provides LRAs less than 0.06 rad for all archetypes considered in this study except for one. All archetypes with $e/L=0.5$ showed satisfactory performance under MCE level events. For 10% probability of collapse under MCE, the current response factors were found to produce link rotation demands that are larger than 0.06 rad for EBFs having $0.35 \leq e/L \leq 0.50$.

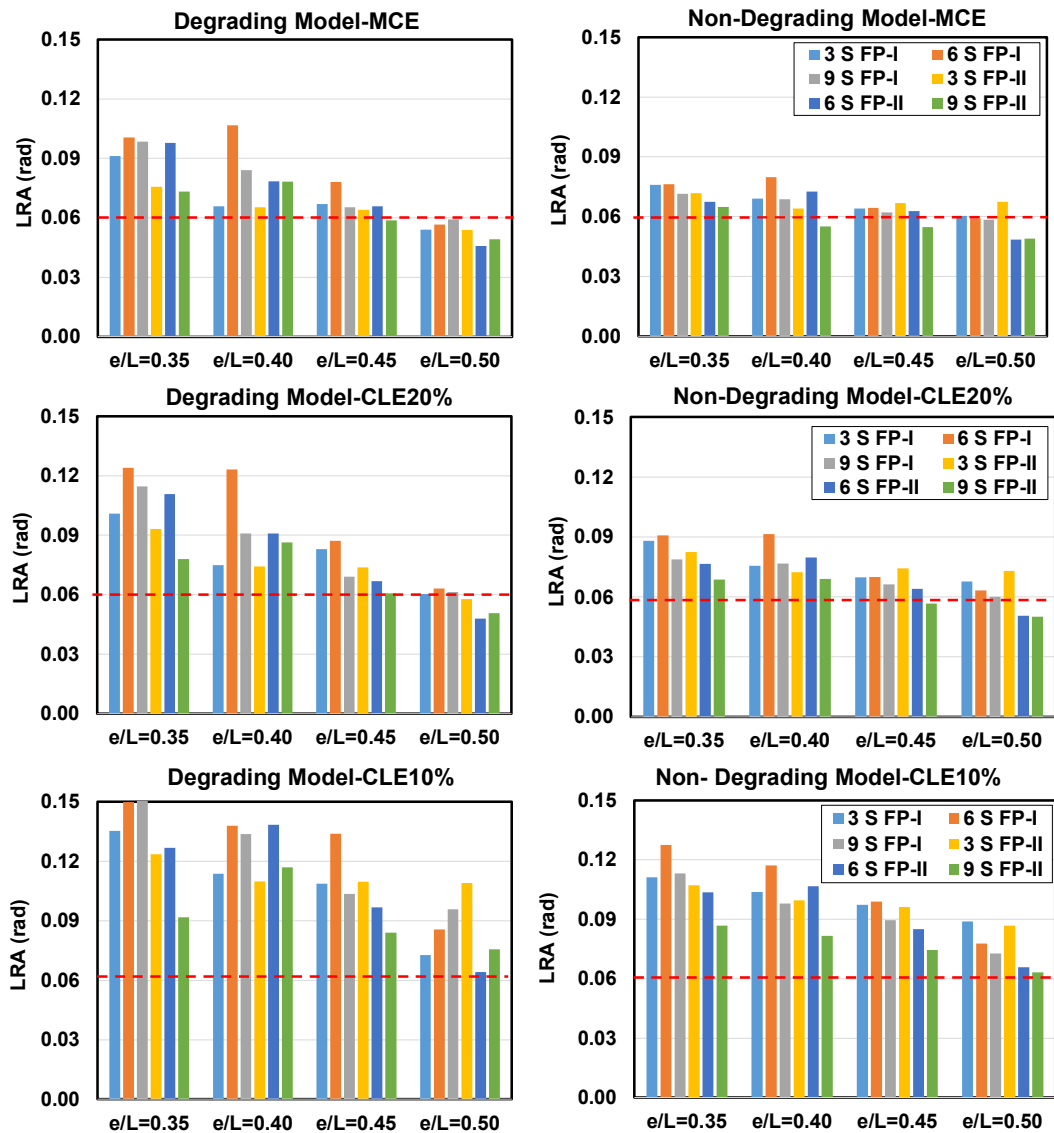


Figure 3.29. Median link rotation angle (LRA) for all archetypes

3.6 Remedial Measures

Based on the findings presented in the previous section, only EBFs with $e/L=0.5$ subjected to CLE20% seismic events were found to be safe according to the current design provisions. Remedial measures were investigated to reduce the level of maximum link rotation angle such that the designs could be found satisfactory under CLE10% seismic events. Five alternatives, details of which are explained in the

following sub-sections, were considered. Degrading models were used in studying the remedial measures.

3.6.1 Modifications to the Response Modification Coefficient

Using response modification coefficients that are less than the recommended value in ASCE7-16 (2016) were investigated. After having several trials, it was observed that using $R=4$ and $C_d=3$ can lead to acceptable solutions for EBFs with $e/L=0.5$. All FP-I and FP-II archetypes with $e/L=0.5$ were redesigned with $R=4$ and $C_d=3$. Representative member sizes are given for two of the redesigned archetypes (9S FP-I (AT12-I) and 3S FP-II (AT4-II)) in Table 3.6. It should be noted that these two archetypes were found to experience the highest link rotation angles under CLE10% events according to the data given in Figure 3.29. The suffix R stands for the redesigned archetypes. The amount of increase in the frame mass varies between 49% and 98% when all archetypes designed with $R=4$ were considered. Figure 3.30a shows the variation of LRA under CLE10% level seismic hazard for $R=8$ (AT12-I) and $R=4$ (AT12-I-R) designs. Similarly, Figure 3.31a shows the variation of LRA for AT4-II and AT4-II-R under the same seismic hazard. From these figures, it is clear that a significant reduction in the R factor can result in link rotation angles being less than 0.06 rad. Although a modification to the R factor can be considered as an option, the significant amount of increase in the frame mass and cost do not make this option feasible.

Table 3.6. Redesigned member sizes of AT1-I-R with R=4 Cd=3 and AT1-I-S with stocky link sections

AT12-I-R				AT12-I-S		
Story	Links	Braces	Columns	Links	Braces	Columns
1	24×192	40×324	14×342	12×279	14×159	14×283
2	24×192	40×324	14×342	12×279	14×159	14×283
3	24×192	40×324	14×342	12×279	14×159	14×283
4	24×192	40×324	14×211	12×279	14×159	14×193
5	24×192	40×324	14×211	12×252	14×145	14×193
6	24×192	40×324	14×211	12×252	14×145	14×193
7	24×192	40×324	14×132	12×252	14×145	14×132
8	24×192	40×324	14×132	14×211	14×132	14×132
9	24×84	14×132	14×132	14×211	14×132	14×132

AT4-II-R				AT4-II-S		
Story	Links	Braces	Columns	Links	Braces	Columns
1	18×119	12×190	14×132	12×106	10×112	14×68
2	18×97	14×145	14×132	12×106	10×112	14×68
3	16×77	14×109	14×132	14×82	12×96	14×68

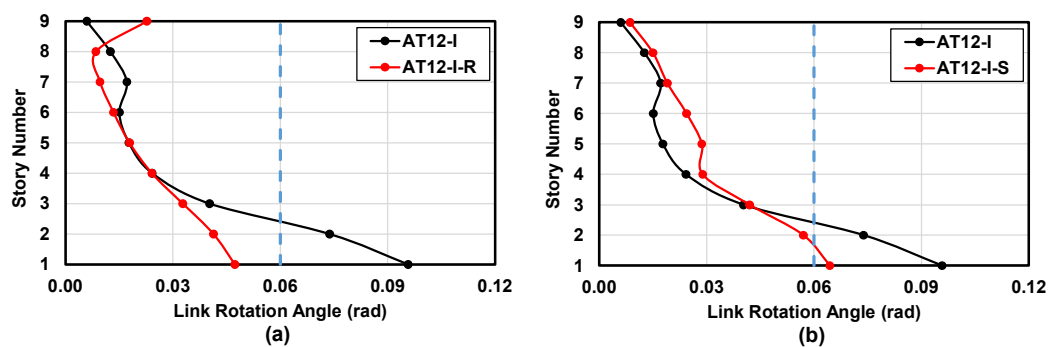


Figure 3.30. Variation of LRA under CLE10% level seismic hazard for AT12-I: a) Modification to response modification coefficient, b) Using stocky link beams

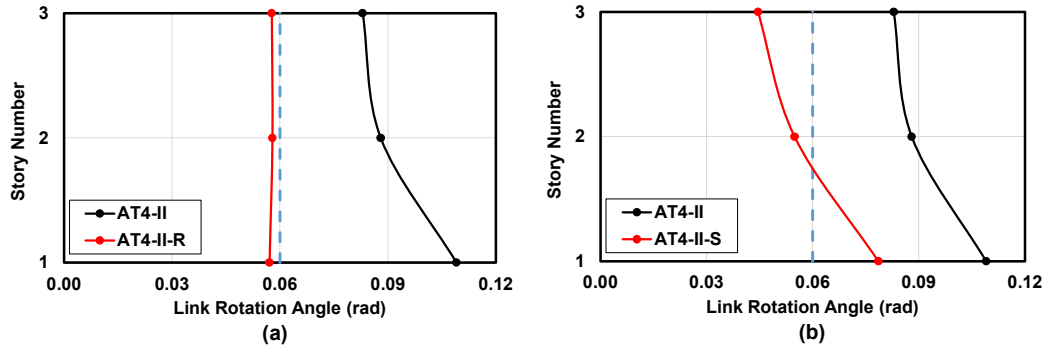


Figure 3.31. Variation of LRA under CLE10% level seismic hazard for AT4-II: a) Modification to response modification coefficient, b) Using stocky link beams

3.6.2 Using Stocky Link Beams

Results presented in Section 3.5.1 proved the importance of modeling deterioration while performing numerical analysis of long link EBFs. The amount of deterioration is a function of the web depth over the web thickness ratio (h/t_w), flange width over two-times flange thickness ($b/2t_f$) and yield stress (F_y). Equation 3.12 shows that the deterioration parameter is inversely proportional to the h/t_w and $b/2t_f$. As the deterioration parameter (Λ) increases, the amount of degradation reduces. Therefore, the effect of deterioration can be minimized by designing the long links with stocky sections ($h/t_w < 20$). Alternative designs were considered for AT12-I and AT4-II. The alternative designs were named as AT12-I-S and AT4-II-S where S stands for stocky sections. In these alternative designs, “column-like” sections with stocky webs were selected as link beams. The member sizes for these alternative designs are reported in Table 3.6. It should be noted that most of the link beams had $h/t_w < 20$. The comparisons of responses of the original and redesigned archetypes are given in Figures 3.30b and 3.31b. Using stocky sections for the link beams has a clear effect on the reduction of link rotation angle demands. On the other hand, the first story link beams are still subjected to a link rotation angle demands that are greater than 0.06 rad. Another detrimental consequence of using stocky sections is the increase in the frame mass and cost. This strategy was applied to all FP-I and FP-II archetypes

with $e/L=0.5$. It was observed that the mass of framing increased by 44% on average. Based on these observations, it can be concluded that using stocky sections for link beams is not a feasible solution either.

3.6.3 Modifying Link Length to Bay Width Ratio

The link length to bay width ratios (e/L) between 0.35 and 0.5 were considered thus far. The use of larger e/L ratios in reducing the link rotation angle demands was considered. After having several trial analyses, it was determined that $e/L=0.65$ can provide acceptable solutions. New archetypes with $e/L=0.65$ were designed using the recommended response factors in ASCE7 and considering the two floor plans. The member sizes of these archetypes are reported in Table 3.7. The archetypes were subjected to CLE10% level seismic events and the variations of link rotation angle along the height of EBFs are reported in Figure 3.32. The maximum link rotations experienced by these archetypes are also reported in this figure in terms of a bar chart. The results indicate that maximum link rotations were bounded by 0.065 rad which is slightly above the target rotation limit. Three of the archetypes experienced link rotations less than the limit considered. The archetypes with $e/L=0.65$ had masses that are 9% to 33% higher than their counterparts ($e/L=0.5$). The average increase in the mass of framing was 23% when all 6 archetypes were considered. From these observations and the analysis results, it can be concluded that $e/L=0.65$ can be a viable option to keep the maximum link rotation to acceptable levels under CLE10% seismic events.

Table 3.7. Member sizes of archetypes with $e/L=0.65$

3 Stories Floor Plan-I			3 Stories Floor Plan-II			
Story	Links	Braces	Columns	Links	Braces	Columns
1	21×122	14×193	14×68	18×86	14×145	14×68
2	21×111	14×176	14×68	18×86	14×145	14×68
3	21×83	14×132	14×68	14×74	14×109	14×68
6 Stories Floor Plan-I			6 Stories Floor Plan-II			
Story	Links	Braces	Columns	Links	Braces	Columns
1	27×161	36×302	14×132	18×97	14×159	14×132
2	21×132	14×211	14×132	18×86	14×145	14×132
3	21×132	14×211	14×132	18×86	14×145	14×132
4	21×111	14×176	14×68	18×86	14×145	14×68
5	21×111	14×176	14×68	18×86	14×145	14×68
6	18×65	12×96	14×68	14×48	12×72	14×68
9 Stories Floor Plan-I			9 Stories Floor Plan-II			
Story	Links	Braces	Columns	Links	Braces	Columns
1	27×161	36×302	14×211	18×119	14×193	14×176
2	27×161	36×302	14×211	18×119	14×193	14×176
3	27×161	36×302	14×211	18×119	14×193	14×176
4	27×161	36×302	14×132	18×119	14×193	14×132
5	27×161	36×302	14×132	18×119	14×193	14×132
6	21×122	14×193	14×132	18×97	14×159	14×132
7	21×111	14×176	14×68	18×86	14×145	14×68
8	21×111	14×176	14×68	18×86	14×145	14×68
9	21×83	14×132	14×68	14×48	12×72	14×68

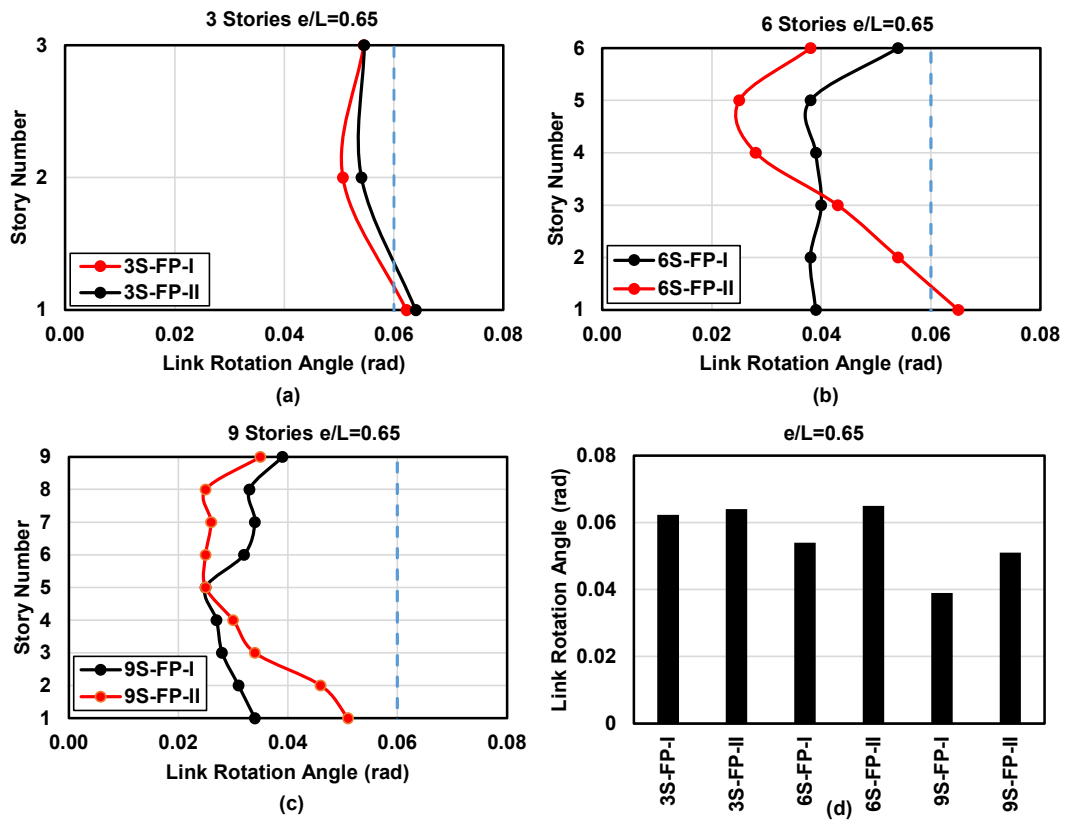


Figure 3.32. Variation of LRA under CLE10% level seismic hazard for $e/L=0.65$:
a) 3 Stories b) 6 Stories c) 9 stories d) Maximum LRA values of all stories for FP-I and FP-II archetypes.

3.6.4 Support Conditions

Pinned column bases were considered for the archetypes that were designed as a part of this study. The effect of support conditions on the LRA demands was studied by considering archetype EBFs with fixed column bases. It was observed that major revisions to member sizes were not required when the column base conditions were modified. This is due to the fact that most of the lateral stiffness of the EBF is influenced by the axial stiffness of braces and columns and bending stiffness of the floor beam. Therefore, the column base condition has a little effect on the internal force distribution and the lateral displacements. Based on these findings, the FP-I and FP-II archetypes presented in Tables 3.3 and 3.4 were considered with only a

modification for the column base condition. The particular example of median LRA distributions of fixed and pin-based 6 story archetypes of FP-I under CLE10% seismic hazard are shown in Figure 3.33. The column base condition has a significant influence on the height wise variation of the link rotation angle. For the pin-based archetypes, the damage concentrates at the lower floors where the maximum demand is on the ground floor. For fixed-based archetypes, the middle floors are subjected to the highest demands. In other words, providing a fixed column base shifts the critical story from the ground level to levels that are 2-3 stories above the ground level. Although a reduction in the maximum link rotation angle was observed for these 6-story archetypes, the limit of 0.06 rad was exceeded in all of them.

The height wise variation of LRA for 9-story FP-I archetypes are given in Figure 3.34a. The results showed that the maximum link rotations for EBFs with $e/L=0.45$ and $e/L=0.5$ were below the limit while the other two archetypes experienced link rotations greater than the limit. The median LRA responses of all archetypes with fixed column bases are given in Figure 3.34b. The link rotation angle limit of 0.06 rad was exceeded in most of the fixed base EBFs as well. The fixed base condition was useful in improving the behavior of 9-story EBFs with $e/L=0.45$ and $e/L=0.5$ for both the floor plans. The maximum link rotation was below 0.06 rad for these archetypes. From these observations, it can be concluded that base fixity cannot be relied upon to reduce the level of link rotations to acceptable levels when CLE10% level seismic hazard is considered.

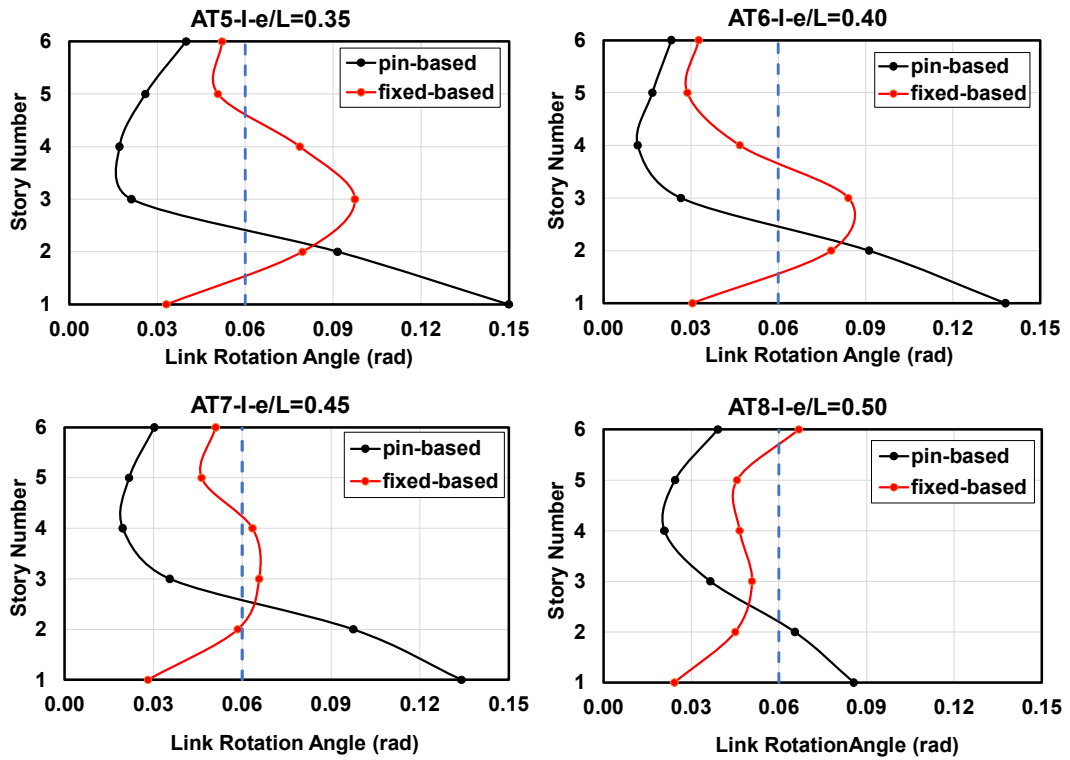


Figure 3.33. Median LRA distribution for fixed and pin-based 6 story archetypes of FP-I under CLE10% seismic hazard

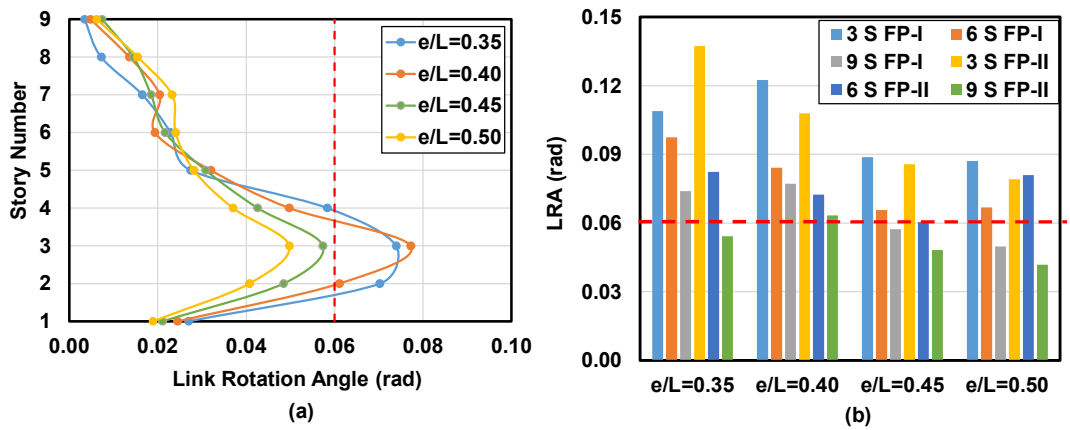


Figure 3.34. Median LRA for fixed-based archetypes: a) Height wise distribution for 9-story buildings, b) Responses of all archetypes

3.6.5 Effect of Gravity Framing

Various research studies pointed out the beneficial effect of the gravity framing on the response of steel lateral load resisting systems (Ji et al. (2009), Flores et al (2016), Imanpour et al. (2016), Hines et al. (2009), MacRae et al. (2004), Flores et al. (2014), Elkady and Lignos (2015)). The effect of gravity framing on the FP-I archetypes was investigated for EBFs with $e/L=0.5$. The 3-, 6- and 9-story archetypes were considered. The gravity column orientations for FP-I are indicated in Figure 3.4. At the core of this floor plan, there are five 2-bay frames where the gravity columns bend with respect to their strong axis under lateral loading that act parallel to the long direction. There are two 4-bay frames gravity frames positioned parallel the short direction. For this floor plan, the long direction, with 9-meter bay width EBFs, was considered and the gravity frames tributary to each EBF were modeled as shown in Figure 3.6. A 4-bay gravity frame was connected to the EBFs by making use of stiff truss elements. Beams of the gravity frames were W21×50 for all stories and for all archetypes. The columns were W12×45 for the 3-story EBF. For the 6-story EBF, W12×72 and W12×45 columns were used for stories 1 through 3 and 4 through 6, respectively. For the 9-story EBF, W12×96, W12×72 and W12×45 columns were used for stories 1 through 3, 4 through 6, and 7 through 9, respectively. The gravity frame columns were modeled using nonlinear beam-column elements with fiber sections. The gravity frame beams were modeled using elastic beam-column elements. Rotational springs were modeled at the ends of the gravity beams to represent the strength and stiffness of connections. Liu and Astanceh (2000) conducted an experimental study to determine the strength and stiffness of gravity frame connections. The behavior depends on the type of connection adopted. Based on the values reported by Liu and Astanceh (2000), the strength of the connections were considered as $0.2 \times M_{p,beam}$ and $0.4 \times M_{p,beam}$, where $M_{p,beam}$ is the plastic bending moment capacity of the gravity frame beams. The stiffness of the connections was considered as $2EI_{beam}/L_{beam}$ where I_{beam} and L_{beam} are the moment of inertia and length

of gravity beams, respectively. The moment rotation response of the connections was modeled using steel02 material model.

The EBFs with gravity frames were subjected to CLE10% level seismic events. The variation of median link rotation angles along the height of AT4-I, AT8-I and AT12-I are given in Figure 3.35. The responses of the EBFs with leaning columns and with gravity frames are compared in this figure. For the EBFs with gravity frame the results are reported for $0.2 \times M_{p,beam}$ and $0.4 \times M_{p,beam}$ separately. The results show that the effect of gravity frame on the LRA depends on the number of stories. For 9- and 6-story EBFs, a reduction in the maximum link rotation was observed where the reduction was more in the 9-story frame. The amount of reduction also depends on the strength of the gravity beam connections where larger strength results in higher reductions. For the 3-story EBF, the maximum link rotation which developed at the first story was observed to increase with the presence of the gravity framing. Conversely, the link rotations of the other two stories were observed to decrease. The maximum link rotation angle was above the limit of 0.06 rad for all the three archetypes considered in this assessment. Therefore, it can be concluded that the effect of gravity framing cannot be relied upon to reduce the link rotations down to acceptable limits.

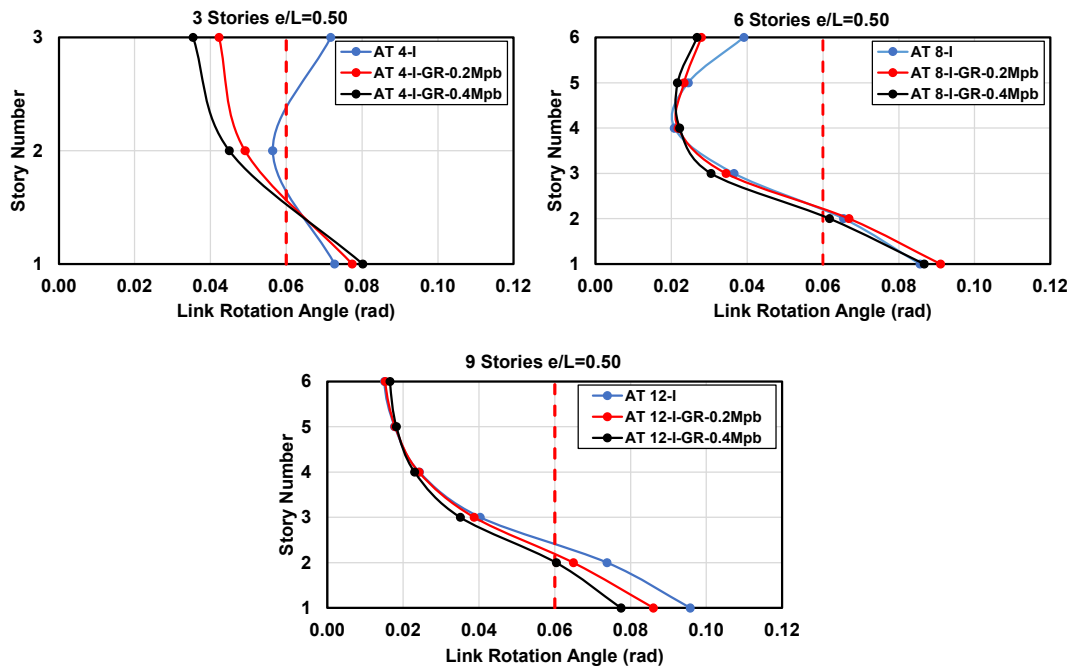


Figure 3.35. Response of EBFs with gravity frames

3.7 Summary

A numerical study was undertaken to evaluate the seismic response factors for EBFs with long links using FEMA P695 methodology. Twenty-four EBF archetypes were designed by considering the bay width, number of stories, the link length to bay width (e/L) ratio and column base condition as the variables. Performances of these archetypes were evaluated under maximum considered earthquake (MCE), and collapse level earthquake (CLE). The effects of degradation were studied by considering degrading and non-degrading responses separately. The results showed that strength and stiffness degradation increases the link rotation angle as much as 46 percent when compared with the non-degrading models. The recommended response factors were found to provide acceptable performance for $e/L=0.5$, when 20% probability of collapse is considered under MCE level events. Remedial measures were investigated to achieve acceptable performance for collapse probability of 10% under MCE level events.

CHAPTER 4

DEVELOPMENT OF A LOADING PROTOCOL FOR LONG LINKS IN ECCENTRICALLY BRACED FRAMES

4.1 Background

Fundamental responses of structural components which are strength and deterioration capacities, ductility, energy dissipation capacity and failure modes depend on cumulative deformation under cyclic loads and are the functions of past damaging cycles. Loading protocols are necessary to examine these responses of structural systems or members under a seismic event. For different structural systems, the loading protocols should be developed separately because of the uncertain natures of the structural response. In order to consider the uncertainty of the earthquakes, a wide range of earthquake data is required. Fang et al. (2020) highlighted the necessity of developing separate loading protocols for different structural systems and earthquakes with different fault distances (near-fault or far-field). The representative loading protocols are much more important in performance-based seismic design where the performance needs to be quantified (Krawinkler et al. (2009)). In addition, loading protocols should especially be developed for the systems where prequalification testing is necessary.

4.1.1 Summary of Past Protocols on Structural Members

Majority of the loading protocols in the literature were developed primarily for steel and wood structures. Examples of the very first loading protocols can be listed as SPD protocol (Porter (1987)), ATC-24 protocol (1992), SAC protocol (Clark et al. (1997)), Cresendo protocol (Behr (1996)), CUREE protocol (Krawinkler (2001)), AISC 341 protocols (2016), FEMA-461 protocol (2007), EN-12512 protocol (2005) and JISF protocol (2002). Separate loading protocols were developed for different

structural systems as well. The CUREE protocol was developed by Krawinkler et al. (2001) for wood frame structures.

Sabelli and Mahin (2003) investigated the seismic demands on 3- and 6-story steel braced frames with buckling restrained braces to determine design procedures and code provisions. Hutchinkson et al. (2011) proposed two drift protocols for representative mid- and low-rise special moment resisting frame (SMRF) building structures based on cycle counting and forward ordering the time histories of interstory drifts.

Mergos and Beyer (2014) evaluated cumulative damage demands of 60 ground motion records. The seismic intensity of the ground motion records correspond to a 2% probability of exceedance in 50 years for a moderate seismicity region in Europe. The loading protocols were developed for a large variety of single degree of freedom systems (SDOF) representing a wide range of existing building stock.

Dehgani and Tremblay (2012) developed a dynamic loading protocol for buckling-restrained brace elements for the eastern and western regions of Canada addressing the effects of local seismicity for different possible hazard scenarios.

Fang et al. (2020) developed loading protocols based on 84th percentile of MCE-level seismic hazard for a series of prototype frames including self-centering braced frames (SCBFs), buckling-restrained braced frames (BRBFs), moment-resisting frames (MRFs) subjected to near-fault and far-field earthquakes.

Suzuki and Lignos (2020) aimed to develop a loading protocol for steel columns whose primary failure mode is local buckling induced softening. The loading protocol reflects the characteristics of the ground motion type (near fault, duration...etc) and the building geometric properties.

Raza et al. (2021) proposed loading protocols for bidirectional cyclic and axial loadings of RC columns using 15 ground motion records that represent typical low-to-moderate seismic regions. The loading protocol was derived based on 3-D analysis of a case study building. Chen and Bai (2022) developed three types of

loading protocols for BRBs in RC frames under far-field, near-fault, and long-duration earthquakes.

Ghassemieh et al. (2021) selected 25 far-field records from more than 2000 recorded accelerograms during 5.5-7.5 magnitude earthquakes and performed 2-D nonlinear analysis to develop a regional loading protocol. The loading protocol is applicable to the steel moment connections considering both the construction conditions and the seismic history of the region.

Hamauzu and Skalomenos (2021) proposed a methodology to evaluate the performance of square tubular steel columns under nonsymmetrical loading. The nonsymmetrical loading is derived by modifying the conventional symmetrical loading protocols.

Jiao et al. (2012) compared the American and Japanese loading protocols for weak-beam moment frames under various earthquakes. For the testing of both single and multiple specimens, they proposed suggestions on selection of loading protocols. and recommended to use one loading protocol from SAC2000, FEMA461 and JISF loading protocols. For the multiple specimen testing program the authors also suggest to adopt a constant amplitude loading protocol and also a monotonic loading protocol or a SAC near fault loading protocol in addition.

4.1.2 Loading Protocol Developed by Richards (2004) and Richards and Uang (2006)

The only loading protocol that can be used for long-link EBFs is developed by Richards (2004). Richards (2004) developed a general loading protocol to be used for short, intermediate and long EBF links. Three and ten-story archetypes were designed according to the International Building Code (2002). The designs employed a redundancy factor (ρ_{IBC}) of 1.47 which essentially resulted in a reduction of the response modification factor (R). The links were modeled by using a multi-linear shear-deformation and bi-linear moment-rotation responses while the strength and

stiffness deteriorations were neglected. The story drift and link rotation angle responses were obtained from time history analysis and a loading protocol based on the story drift was developed.

This protocol can be applied to links with different lengths using a relationship between the story drift and link rotation angle, which was developed as a part of the study. Figure 4.1.a shows the proposed loading protocol for long links which belongs to the most critical link of the archetype EBFs considered with $e/L = 0.32$. The findings from this study were extended by Richards and Uang (2006) to develop a loading protocol for short links only. Different from the original study, the link rotation angle response was considered instead of the story drift. The proposed protocol was adopted with minor modifications by AISC341 for qualifying cyclic tests of link-to-column connections (Figure 4.1.b).

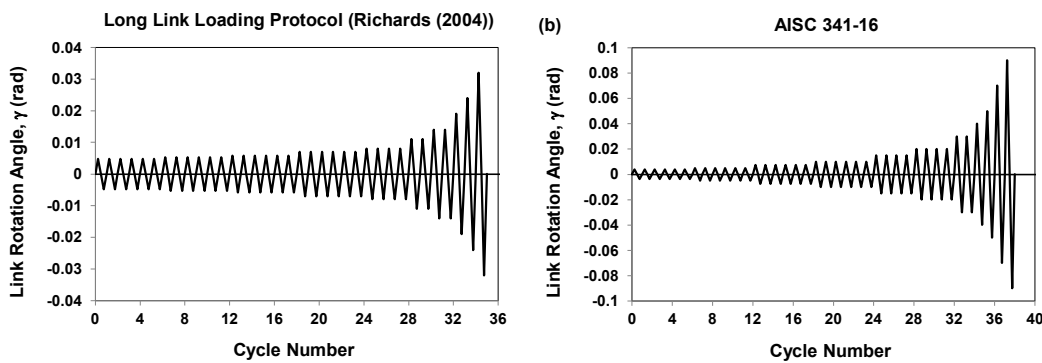


Figure 4.1. Loading Protocols (a) Richards (2004) Loading Protocol for Long links (b) AISC 341-16 Protocol for Short Links

4.1.3 Loading Protocol Developed by Al-Janabi and Topkaya (2020)

Al-Janabi and Topkaya (2020) extended the study of Richards and Uang (2006). The EBF links are generally subjected to one-sided rotations with maximum amount rotation that depends on the e/L ratio. Al-Janabi and Topkaya (2020) proved the importance of considering mean effects for the short EBF links and a nonsymmetrical loading protocol was proposed for short links that take into account

the one-sided nature of rotation demand. Sixteen EBF archetypes with e/L ratio of 0.08, 0.10, 0.12 and 0.14 with number of stories 3, 6 and 9 were designed according to ASCE7-16 standard. Both links positioned in the midspan and attached to columns were considered. In addition, 4 EBF Buildings designed by Speicher and Harris (2016) were selected as a complementary designs. Twenty-two pairs of far-field record set of FEMA P695 (2009) were used and scaled to represent MCE level and collapse level ground motions. The results showed that the link rotation history strongly depends on e/L ratio and ground motion level. The proposed loading protocol was tailored to accommodate different e/L ratios and seismic hazards (Figure 4.2).

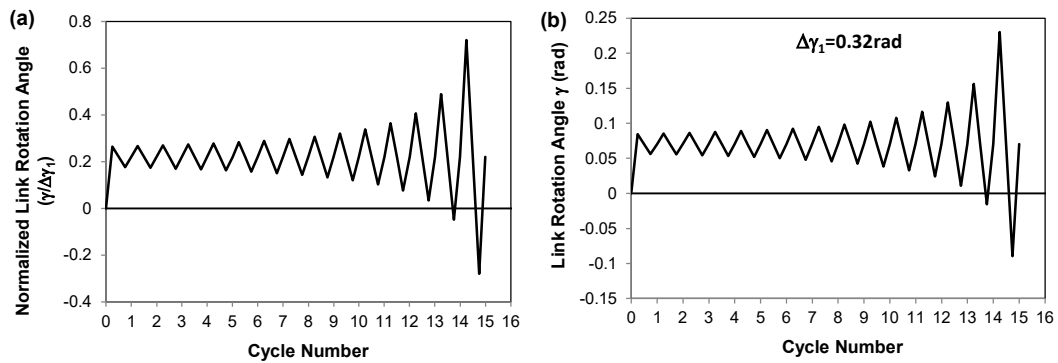


Figure 4.2. Loading protocol proposed for short links for $n_{\max}=15$ (Al-Janabi and Topkaya (2020))

The study described in this Chapter applies the same methodology proposed by Al-Janabi and Topkaya (2020) to long EBF links. The findings of the former study (Al-Janabi and Topkaya (2020)) is also presented and compared with the current study in the following sections.

4.2 Archetype Development

Twenty-four long link EBF archetypes were designed with different e/L ratios, number of stories and floor plans with different bay-widths (Figure 4.3). Floor Plan I (FP-I) was 54 m \times 36 m with 9 m and 6m spans in two perpendicular directions

respectively. EBFs with 9 m bay width were considered for FP-I. Floor Plan II (FP-II) was 36m × 36m with 6m spans in both directions. For each floor plan, 12 archetypes with pinned column bases were designed. The story height was considered as 4 m for all stories. The links were located between the braces as shown in the elevation view (Figure 4.3). Different link length to bay width ratios (e/L) of 0.50, 0.55, 0.60 and 0.65 and number of stories of 3, 6 and 9 were considered. Previous chapter showed that long links with $e/L < 0.5$ experienced very high link rotation angles and, therefore such links were not considered in this study.

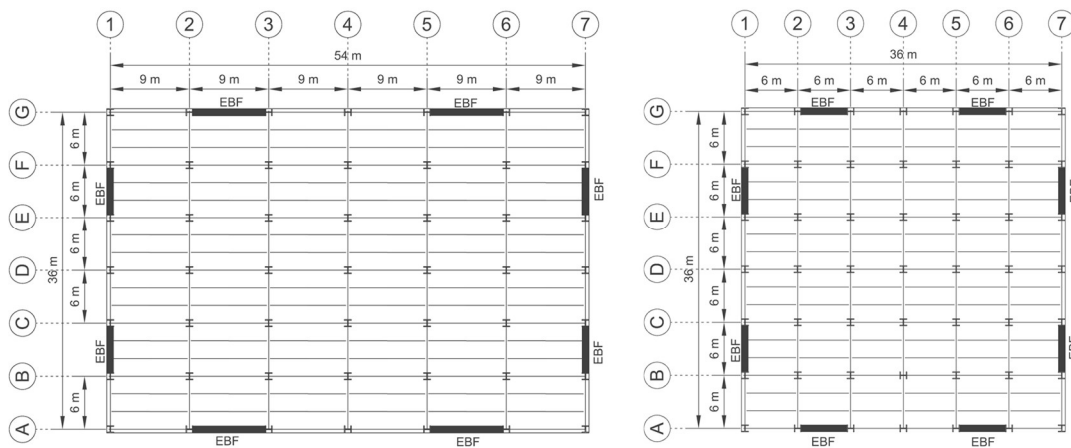


Figure 4.3. Floor plans

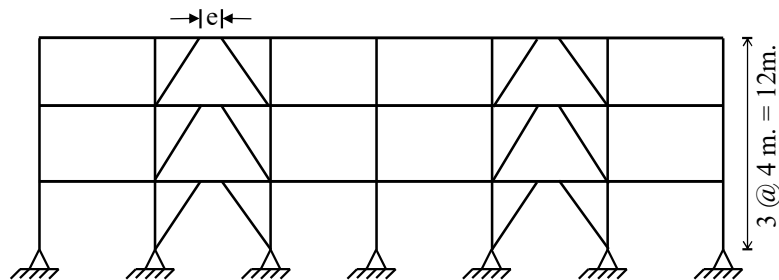


Figure 4.4. Floor plans

EBF bays were designed to resist vertical and lateral loads together however, the wind effect was ignored. Story dead loads and live loads were assumed as 4.3 kN/m² and 2.0 kN/m² respectively. Twenty percent of the live loads were included in earthquake load calculations which accounts for the contribution of partition walls.

FEMA P695 (2009) presents seismic design categories that are compatible with the design spectra used in the United States. Seismic Design Category SDC D_{max} was considered which produces the highest demands. The archetype EBFs were designed using the equivalent lateral force (ELF) procedure given in ASCE 7-16 (2016). The members were designed according to the procedure outlined in Kuşyılmaz and Topkaya (2016) and described in Chapter 3. All members were assumed to have a yield strength of 345 MPa. All members were designed with American wide flange sections and the links were selected to satisfy the long link criterion ($\rho > 2.6$). The details of the archetypes and member sizes are given in Tables 4.1, 4.2 and 4.3.

Table 4.1. Archetype Properties and Scaling Factors

AT	F P	N S	e/L	Bay width (m)	Mass (tons)	T (C _u T _a) (s)	T _{anal} (s)	μ_T	Med. MCE Scale Factor	Med. CLE 10% Scale Factor
AT1-I	I	3	0.50	9	10.22	0.66	0.97	5.15	2.42	3.24
AT2-I	I	3	0.55	9	11.33	0.66	1.02	5.40	2.42	3.22
AT3-I	I	3	0.60	9	11.59	0.66	1.04	5.12	2.42	3.24
AT4-I	I	3	0.65	9	13.07	0.66	1.10	5.31	2.42	3.22
AT5-I	I	6	0.50	9	23.91	1.10	1.65	3.54	2.54	3.38
AT6-I	I	6	0.55	9	27.19	1.10	1.73	3.89	2.54	3.33
AT7-I	I	6	0.60	9	28.24	1.10	1.74	4.47	2.54	3.20
AT8-I	I	6	0.65	9	31.68	1.10	1.78	4.61	2.54	3.18
AT9-I	I	9	0.50	9	50.23	1.50	2.23	2.99	2.53	3.29
AT10-I	I	9	0.55	9	54.00	1.50	2.34	3.26	2.53	3.24
AT11-I	I	9	0.60	9	52.70	1.50	2.31	3.18	2.53	3.26
AT12-I	I	9	0.65	9	59.16	1.50	2.17	4.14	2.53	3.09
AT1-II	II	3	0.50	6	7.14	0.66	0.98	6.00	2.42	3.17
AT2-II	II	3	0.55	6	7.59	0.66	1.01	5.65	2.42	3.19
AT3-II	II	3	0.60	6	8.48	0.66	1.04	6.16	2.42	3.17
AT4-II	II	3	0.65	6	9.54	0.66	1.05	6.02	2.42	3.17
AT5-II	II	6	0.50	6	18.77	1.10	1.59	4.35	2.54	3.28
AT6-II	II	6	0.55	6	18.60	1.10	1.70	4.29	2.54	3.28
AT7-II	II	6	0.60	6	21.23	1.10	1.78	4.68	2.54	3.23
AT8-II	II	6	0.65	6	21.49	1.10	1.87	4.83	2.54	3.23
AT9-II	II	9	0.50	6	36.41	1.50	2.18	3.19	2.53	3.26
AT10-II	II	9	0.55	6	38.49	1.50	2.26	3.66	2.53	3.16
AT11-II	II	9	0.60	6	38.39	1.50	2.42	3.72	2.53	3.16
AT12-II	II	9	0.65	6	39.86	1.50	2.49	4.01	2.53	3.11

Table 4.2. Member Sizes of FP-I Archetypes

AT	S	Links	Braces	Cols.	AT	S	Links	Braces	Cols.
	t					t			
AT 1-I	1	24×84	14×132	14×68	AT 2-I	1	24×94	14×176	14×68
	2	21×83	14×132	14×68		2	21×83	14×145	14×68
	3	21×57	12×87	14×68		3	21×62	12×106	14×68
AT 3-I	1	24×103	14×176	14×68	AT 4-I	1	21×122	14×193	14×68
	2	24×76	14×132	14×68		2	21×111	14×176	14×68
	3	24×76	14×132	14×68		3	21×83	14×132	14×68
AT 5-I	1	24×94	14×145	14×132	AT 6-I	1	24×94	14×176	14×132
	2	24×94	14×145	14×132		2	24×94	14×176	14×132
	3	24×94	14×145	14×132		3	24×94	14×176	14×132
AT 7-I	4	24×84	14×132	14×68	AT 8-I	4	24×94	14×176	14×68
	5	21×73	14×109	14×68		5	21×93	14×159	14×68
	6	21×50	12×72	14×68		6	21×62	12×106	14×68
AT 9-I	1	24×146	14×257	14×132	AT 10-I	1	27×161	36×302	14×132
	2	24×103	14×176	14×132		2	21×132	14×211	14×132
	3	24×103	14×176	14×132		3	21×132	14×211	14×132
AT 11-I	4	24×103	14×176	14×68	AT 12-I	4	21×111	14×176	14×68
	5	24×76	14×132	14×68		5	21×111	14×176	14×68
	6	21×57	12×96	14×68		6	18×65	12×96	14×68
AT 11-I	1	21×122	14×193	14×211	AT 12-I	1	21×132	14×193	14×211
	2	21×122	14×193	14×211		2	21×132	14×193	14×211
	3	21×122	14×193	14×211		3	21×132	14×193	14×211
AT 11-I	4	21×122	14×193	14×132	AT 12-I	4	21×132	14×193	14×145
	5	21×122	14×193	14×132		5	21×132	14×193	14×145
	6	21×122	14×193	14×132		6	21×132	14×193	14×145
AT 11-I	7	24×94	14×145	14×74	AT 12-I	7	21×132	14×193	14×82
	8	24×94	14×145	14×74		8	21×132	14×193	14×82
	9	24×94	14×145	14×74		9	21×111	14×159	14×82
AT 11-I	1	24×146	14×257	14×193	AT 12-I	1	27×161	36×302	14×211
	2	24×146	14×257	14×193		2	27×161	36×302	14×211
	3	24×146	14×257	14×193		3	27×161	36×302	14×211
AT 11-I	4	24×146	14×257	14×132	AT 12-I	4	27×161	36×302	14×132
	5	24×146	14×257	14×132		5	27×161	36×302	14×132
	6	24×103	14×176	14×132		6	21×122	14×193	14×132
AT 11-I	7	24×103	14×176	14×68	AT 12-I	7	21×111	14×176	14×68
	8	24×76	14×132	14×68		8	21×111	14×176	14×68
	9	21×57	12×96	14×68		9	21×83	14×132	14×68

Table 4.3. Member Sizes of FP-II Archetypes

AT	S	Links	Braces	Cols.	AT	S	Links	Braces	Cols.
	t					t			
AT	1	18×60	12×96	14×68	AT	1	21×62	14×109	14×68
1-II	2	18×55	12×87	14×68	2-II	2	18×55	12×96	14×68
	3	16×50	12×72	14×68		3	16×50	12×87	14×68
AT	1	18×86	14×145	14×68	AT	1	18×86	14×145	14×68
3-II	2	16×77	14×120	14×68	4-II	2	18×86	14×145	14×68
	3	16×45	12×72	14×68		3	14×74	14×109	14×68
	1	18×86	14×132	14×132		1	21×68	14×132	14×132
AT	2	18×86	14×132	14×132	AT	2	21×68	14×132	14×132
5-II	3	16×77	14×109	14×132	6-II	3	21×62	14×109	14×132
	4	16×77	14×109	14×68		4	21×62	14×109	14×68
	5	18×55	12×87	14×68		5	18×50	12×87	14×68
	6	18×35	12×53	14×68		6	18×50	12×87	14×68
	1	18×86	14×145	14×132		1	18×97	14×159	14×132
AT	2	18×86	14×145	14×132	AT	2	18×86	14×145	14×132
7-II	3	18×86	14×145	14×132	8-II	3	18×86	14×145	14×132
	4	16×77	14×120	14×68		4	18×86	14×145	14×68
	5	16×77	14×120	14×68		5	18×86	14×145	14×68
	6	14×74	14×109	14×68		6	14×48	12×72	14×68
	1	18×97	14×145	14×193		1	18×106	14×159	14×193
	2	18×97	14×145	14×193		2	18×106	14×159	14×193
	3	18×97	14×145	14×193		3	18×106	14×159	14×193
AT	4	18×97	14×145	14×132	AT	4	18×106	14×159	14×132
9-II	5	18×97	14×145	14×132	10-II	5	18×97	14×145	14×132
	6	18×97	14×145	14×132		6	18×97	14×145	14×132
	7	18×86	14×132	14×68		7	18×86	14×132	14×68
	8	16×77	14×109	14×68		8	18×86	14×132	14×68
	9	18×55	12×87	14×68		9	18×86	14×132	14×68
	1	18×106	14×176	14×176		1	18×119	14×193	14×176
	2	18×106	14×176	14×176		2	18×119	14×193	14×176
	3	18×106	14×176	14×176		3	18×119	14×193	14×176
AT	4	18×106	14×176	14×132	AT	4	18×119	14×193	14×132
11-II	5	18×106	14×176	14×132	12-II	5	18×119	14×193	14×132
	6	18×97	14×159	14×132		6	18×97	14×159	14×132
	7	18×97	14×159	14×68		7	18×86	14×145	14×68
	8	16×77	14×120	14×68		8	18×86	14×145	14×68
	9	16×50	12×79	14×68		9	14×48	12×72	14×68

4.3 Ground Motion Selection and Scaling:

The far-field ground motion record set, recommended by FEMA P695, was considered to be compatible with the selected seismic design category similar to Section 3.4. The set consists of 22 pairs of ground motions. In this study, two seismic hazard levels namely, Maximum Considered Earthquake (MCE) and Collapse Level Earthquake (CLE) were taken into account. The CLE that corresponds to 10% probability of collapse at MCE was considered ($CLE_{10\%}$). The records were scaled to match the median spectral demand from 44 ground motions with the design spectral acceleration at the modified approximate fundamental period ($T = C_u \times T_a$) recommended by ASCE 7-16 (2016). The MCE level scale factors for any given period value are reported in FEMA P695 and these values were directly used (Table 4.1). The scaling for $CLE_{10\%}$, on the other hand, requires further calculations. An Adjusted Collapse Margin Ratio ($ACMR$) is determined according to FEMA P695 in which 50% of the ground motions cause collapse of an archetype. The target $ACMR$ values depend on the probability of collapse and total system collapse uncertainty (β_{TOT}). β_{TOT} (Equation 3.4) is composed of four variables and three of these (β_{DR} , β_{TD} , β_{MDL}) were considered as model quality (A) superior. The record-to-record uncertainty (β_{RTR}) depends on the period based ductility (μ_T) which can be calculated through a nonlinear static (pushover) analysis. The period based ductility can be expressed as in Equations 3.2 and 3.3.

A representative nonlinear static pushover curve for AT5-I is given in Figure 4.5. Based on this response, δ_u and $\delta_{y,eff}$ were calculated as 0.45 m and 0.127 m, resulting in $\mu_T=3.54$. The period based ductility values of all archetypes are reported in Table 4.1. μ_T was used to calculate β_{TOT} and Spectral Shape Factor (SSF) for the archetypes. The relationship between $ACMR$, SSF and Collapse Margin Ratio (CMR) is presented by Equation 3.13.

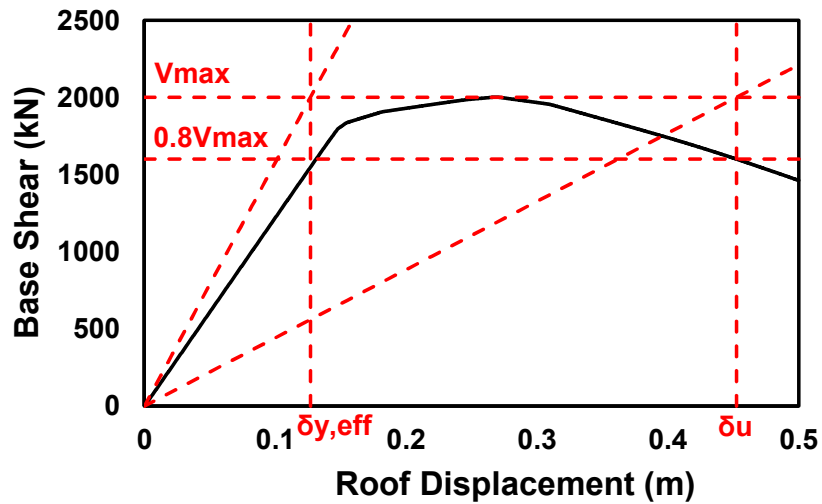


Figure 4.5. Nonlinear Static Pushover Curve of AT5-I

The target $ACMR$ values reported in FEMA P695, which correspond to 10% probability of collapse ($ACMR_{10\%}$), were considered. For the case of AT5-I, $ACMR_{10\%}=1.72$ and $SSF=1.298$ resulting in $CMR=1.33$. The scaling factor for MCE level is 2.54 and the scaling factor for $CLE_{10\%}$ is $2.54 \times 1.33=3.38$. The $CLE_{10\%}$ scaling factors for all archetypes are reported in Table 4.1. The scaling of ground motions are exemplified in Figure 4.6 for AT5-I by plotting the median response spectra. The modified approximate period for this archetype is 1.1 sec.

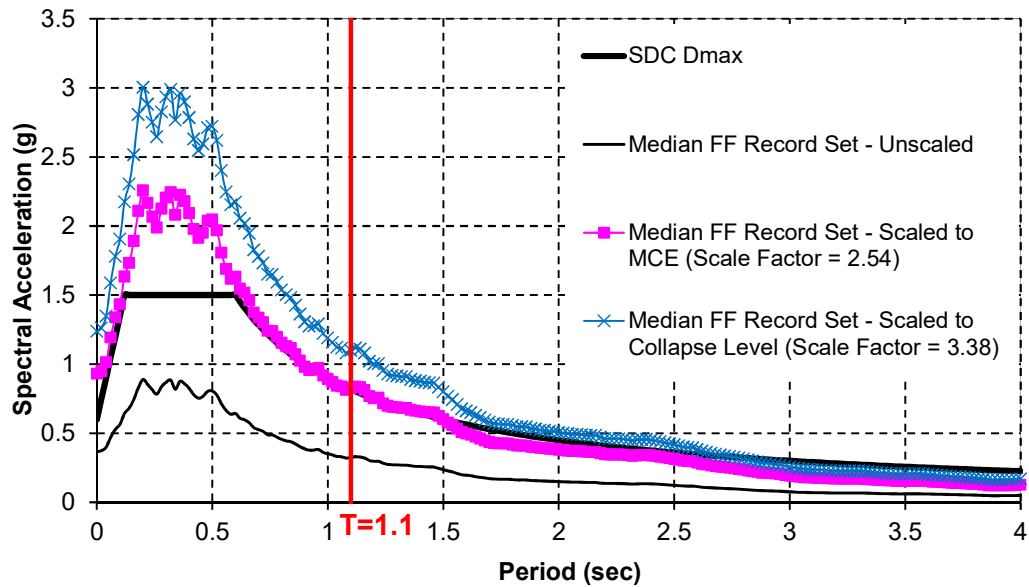


Figure 4.6. Scaling of the far-field record set for AT5-I

4.4 Time History Analysis Results:

Time history analyses of 24 archetypes were conducted by OpenSees on the DesignSafe platform (2017). The very same link deterioration model (Lignos and Krawinkler (2011)) presented in Section 3.1.3 and numerical modeling technique explained in Section 3.3 are adopted in the study described in this Chapter.

For a link beam at a particular story, the maximums of total link rotation angles (LRAs) from the time history analyses were recorded and the medians of the responses from 44 ground motions were calculated. Then, the maximums of these median values from all stories were considered. The time history response of link rotation was converted into ordered cycles using the procedure explained in the following section.

4.4.1 Representation of Time History Response as Ordered Cycles

The time history of link rotation needs to be represented as ordered cycles to be able to develop a loading protocol. In general, the rainflow counting algorithm is used to identify the peaks of the cycles. The JRain Software (2013) was used to apply rainflow counting algorithm to link rotation time history. For any given cycle, the algorithm reports two values of link rotation each of which corresponds to the peaks of that cycle. In general, the peaks are not symmetrically oriented. In other words, the absolute values of the peaks are not equal. The mean effects were generally neglected in most of the studies conducted in the past, except the study conducted by Al-Janabi and Topkaya (2020), where the significance of the mean effects was demonstrated in detail. When the mean effects are neglected, the maximum link rotation angle for a symmetric cycle is equal to the half of the measured peak-to-peak cycle range ($\Delta\gamma$) (Richards and Uang 2006). On the other hand, the differences between the peaks can be considered by taking into account the mean effects.

The differences between the two approaches are exemplified in Figure 4.7. The link rotation time history of the first story link of AT3-I subjected to HECTOR/HEC000 ground motion scaled to CLE10% seismic hazard is given. The peaks of the most damaging cycles were identified by rainflow counting algorithm and ordered from the largest to smallest. Figure 4.7.b shows the ordered cycles which were converted to symmetrical cycles by neglecting the mean effects. Conversely, Figure 4.7.c shows the ordered cycles with their mean effects. The maximum cycle range is equal to 0.128 rad according to the time history response. The absolute maximum link rotation angle (LRA) value is 0.064 rad if mean effects are neglected. However, the peaks of the largest cycle are +0.022 rad and -0.106 rad where the mean of the cycle range is 0.042 rad. The maximum link rotation angles are 0.106 rad and 0.064 rad with and without considering the mean effects, respectively. The one-sided nature of displacement demands is more accurately reflected by considering the mean effects.

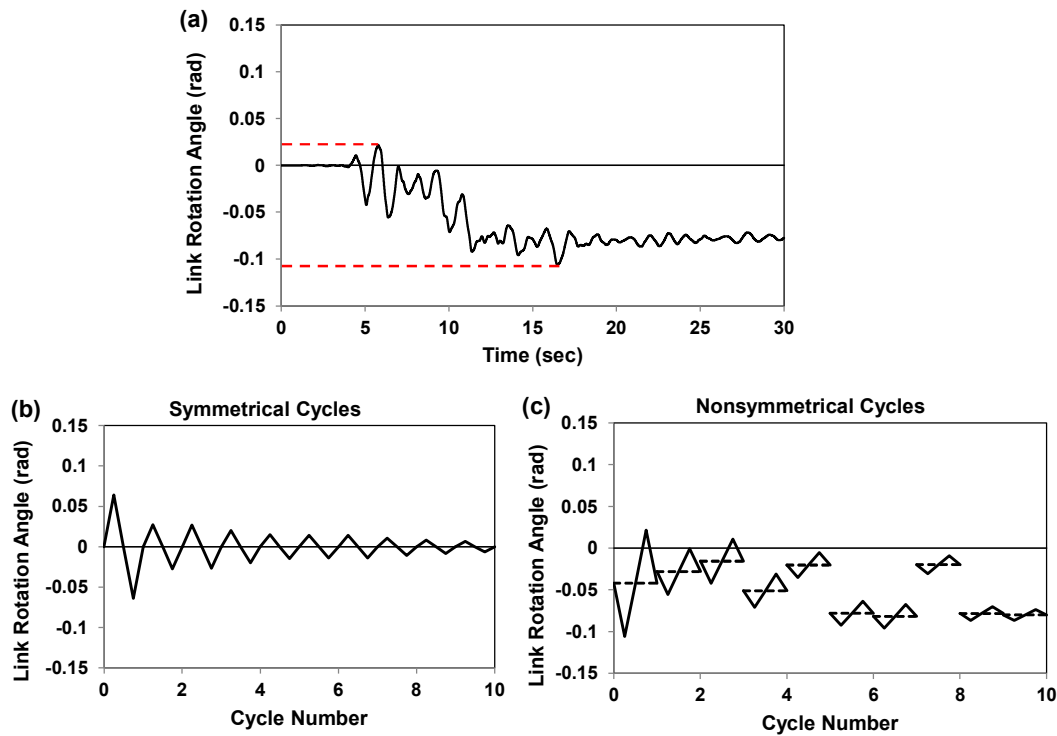


Figure 4.7. Time history analysis results for AT3-I: (a) link rotation versus time, (b) ordered symmetric cycles, and (c) ordered nonsymmetrical cycles

4.4.2 Number of Cycles

Richards and Uang (2006) considered $\gamma=0.0075$ rad as a demarcation point between elastic and inelastic link behavior. Based on this recommendation, cycles with a range greater than 0.015 rad ($\Delta\gamma>0.015$) were considered as inelastic cycles. Cycle ranges having an amplitude of half of the elastic range ($\Delta\gamma>0.0075$) were considered as damaging cycles according to the recommendation of Richards and Uang (2006). The statistical measures of the total number of cycles, number of damaging cycles, and number of inelastic cycles are given in Table 4.4. For any given archetype, the link beam that experiences the highest number of cycles was considered in the statistical analysis.

Table 4.4. Statistical measures for number of cycles, damage index (DI), and maximum LRA

	Total Cycles		Damaging Cycles		Inelastic Cycles	
	MCE	CLE	MCE	CLE	MCE	CLE
Av.	70	72	19	20	8	10
St.D.	4	4	4	4	3	3
Max	78	79	26	27	17	17
Min	63	65	12	14	4	6

	Damage Index (DI)		Maximum Link Rotation (rad)		Ratio CLE/MCE	
	MCE	CLE	MCE	CLE	DI	γ_{max}
Av.	0.012	0.021	0.048	0.070	1.74	1.44
St.D.	0.003	0.006	0.006	0.014	0.27	0.16
Max	0.017	0.031	0.060	0.097	2.32	1.78
Min	0.008	0.009	0.034	0.039	1.25	1.13

The total number of cycles is presented in Figure 4.8.a for all the archetypes subjected to two different seismic hazards. There is not a profound difference in the total number of cycles among the seismic hazard levels. The values varied between 63 and 78 with an average value of 70 under MCE level. The range of values for CLE seismic event varied between 65 and 79 with an average of 72. The total number of cycles for the most critical link of EBFs with short links under MCE level, varied between 80 and 107 with an average of 89 (Al-Janabi and Topkaya (2020)). The average number of total cycles reduced about 21% when long links were considered in EBFs instead of short ones. Richards (2004) reported that 50 percentile values for the total number of rotation cycles for the top story links were around 100 cycles for all link lengths (short, intermediate, and long).

Figures 4.8.b and 4.8.c show the distribution of the number of damaging and inelastic cycles, respectively. A similar observation can be made for the effect of seismic hazard on the number of damaging cycles and inelastic cycles. The number of damaging cycles for the most critical long links varied between 12 and 26 with an average of 19 under MCE level event. For the short links, the number of damaging

cycles varied between 16 and 38 with an average of 28 cycles (Al-Janabi and Topkaya (2020)) for the same hazard level. The number of damaging cycles reduced by 32%, when long links were used instead of short links. The number of damaging cycles was considered as 35 in the study of Richards (2004), by taking into account short, intermediate and long links and without making a distinction among these types of links. In fact, long links were found to experience less number of damaging cycles when compared with short and intermediate links.

According to Figure 4.8.c, the number of inelastic cycles for the most critical link is between 4 and 17 with an average of 8 for MCE level seismic demand. Al-Janabi and Topkaya (2020) reported inelastic cycles varying between 7 and 24 with an average of 17. The number of inelastic cycles for the long links was lower than half of the ones for the short links. The number of inelastic cycles for long links, which correspond to 90 percentile, varied between 5 and 8 in the study of Richards (2004).

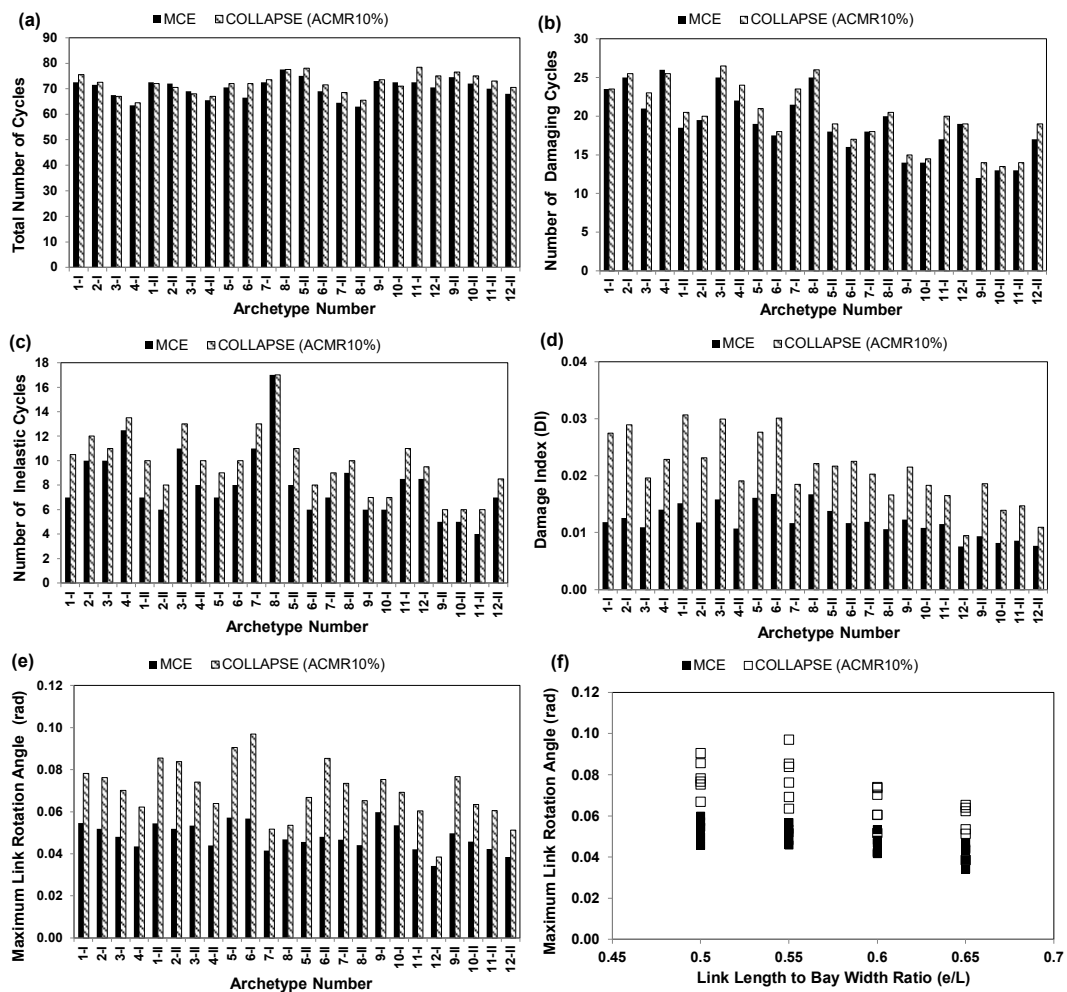


Figure 4.8. Number of cycles, maximum link rotation angle, and damage index

4.4.3 Maximum Link Rotation Angle and Cumulative Damage

The maximum link rotation angle (LRA) experienced by the critical links in all archetypes is given in Figure 4.8.e. The statistical measures are reported in Table 4.4. The maximum LRA varied between 0.034 rad and 0.060 rad, with an average of 0.048 rad under MCE level seismic events. For the collapse level seismic intensity, the same range modified to 0.039 rad and 0.097 rad, with an average of 0.070 rad. According to AISC341, long links are expected to provide stable behavior until 0.02 rad of inelastic rotation. The total rotation demands determined from time history

analysis are significantly higher than the codified limit of 0.02 rad. In the long link loading sequence calculated based on the general loading protocol developed by Richards (2004), the links are loaded up to 0.032 rad which is still lower than the demands from time history analysis. Limited amount of long link tests showed that these links can sustain rotations of the order of 0.07 rad (Table 3.1). As shown in Figure 4.8.f, the link rotation angle demands are a function of the e/L ratio. For both the seismic hazard levels, the maximum LRA tends to decrease with an increase in the e/L ratio. The average of the maximum LRA for all archetypes increases by 44% when collapse level events are considered as opposed to MCE level events (Table 4.4). The ratio of scaling factors (CLE/MCE) is 1.29. The results indicate that the increase in the maximum LRA is more than the increase in the amplitude of spectral accelerations. On the other hand, for the short links, the same ratios for response and demand were calculated as 1.28 and 1.25 respectively (Al-Janabi and Topkaya (2020)).

A damage law is usually adopted to take into account the cumulative damage experienced by a structural member made up of steel. The Miner's damage rule can be combined with the Coffin-Manson relationship to develop the following expression:

$$D = C \sum_{i=1}^N (\Delta\gamma)^c \quad (4.1)$$

where, D is the damage amount that ranges between 0 (undamaged) and 1.0 (damaged), N is the number of damaging cycles and C , and c are the parameters of structural performance and $\Delta\gamma$ is the cycle range at the i th excursion.

Low-cycle fatigue tests must be conducted to obtain the structural performance parameters (C and c). While low-cycle fatigue testing of short links was conducted in the past (Bozkurt et al. (2018)), no such tests exist for long links. The power (c) usually varies around 2.0 for structural steel members and the coefficient (C) depends on the type of member being tested. Bozkurt et al. (2018) recommended

$c=2.0$ for short links and the same value was adopted in the present study. The following damage index (DI), which is the sum of squares of cycle ranges, was considered to take into account the cumulative effect of link rotations:

$$DI = \sum_{i=1}^N (\Delta\gamma)^{2.0} \quad (4.2)$$

Equation 4.2 is not used to detect damage of a long link. The idea here is to calculate the cumulative effects by considering that cycles with a higher range cause significantly more damage to a long link as represented by the power of 2.0. The damage index calculated from time history analysis should be reflected to the loading protocol so that the cumulative effects are correctly taken into account. The average values of DI were 0.012 and 0.021 under MCE and CLE level seismic hazards, respectively (Table 4.4). The DI increases by 74% with an increase of 29% in the ground motion intensity. For the short links, this increase was reported as 71% (Al-Janabi and Topkaya (2020)).

Table 4.5. Statistical measures for rotation range and mean of the rotation range

	$\Delta\gamma_1$		$\Delta\gamma_2$		$\Delta\gamma_3$	
	MCE	CLE	MCE	CLE	MCE	CLE
Av.	0.074	0.102	0.040	0.074	0.102	0.040
St.D.	0.010	0.018	0.006	0.010	0.018	0.006
Max	0.095	0.128	0.052	0.095	0.128	0.052
Min	0.054	0.061	0.030	0.054	0.061	0.030

	Mean of $\Delta\gamma_1$		Mean of $\Delta\gamma_2$		Mean of $\Delta\gamma_3$	
	MCE	CLE	MCE	CLE	MCE	CLE
Av.	0.011	0.018	0.010	0.011	0.018	0.010
St.D.	0.003	0.007	0.003	0.003	0.007	0.003
Max	0.016	0.035	0.015	0.016	0.035	0.015
Min	0.006	0.006	0.005	0.006	0.006	0.005

4.4.4 Maximum Rotation Range, Mean Rotation Range and Distribution of Cycles

The maximum and the mean of rotation ranges and the distribution of cycle ranges were investigated by making use of the ordered cycles. The rotation range of the most damaging cycle (i.e. maximum rotation range) ($\Delta\gamma_1$) and the mean of the rotation range for this cycle are plotted against the e/L ratio in Figures 4.9.a and 4.9.b. The maximum rotation range ($\Delta\gamma_1$) is observed to decrease with an increase in the e/L ratio; however, the mean of the rotation range is relatively unaffected by the e/L ratio. The idea here is to develop a loading protocol as a function of $\Delta\gamma_1$. This requires quantifying $\Delta\gamma_1$ and expressing all other damaging cycles as a ratio of $\Delta\gamma_1$. The following expressions can be used to estimate the maximum rotation range:

$$\Delta\gamma_1 = 0.045 \left(\frac{e}{L} \right)^{-1} \text{ for MCE level seismic events} \quad (4.3)$$

$$\Delta\gamma_1 = 0.060 \left(\frac{e}{L} \right)^{-1} \text{ for CLE level seismic events} \quad (4.4)$$

The maximum rotation range was found to vary with $(e/L)^{-1}$ for short links as well with the coefficients modified as 0.030 and 0.040 for MCE and CLE events, respectively (Al-Janabi and Topkaya (2020)).

For a symmetrical loading, the maximum LRA must be equal to half of the rotation range ($0.5 \times \Delta\gamma_1$). The ratio of maximum $\gamma_{\max}/(0.5 \times \Delta\gamma_1)$ was calculated for all archetypes considering the link that experiences the highest amount of LRA. The averages of the ratios for all archetypes were 1.44 and 1.45 under MCE and CLE events, respectively. These averages clearly indicate that one-sided nature of loadings should be taken into account during the development of the loading protocol.

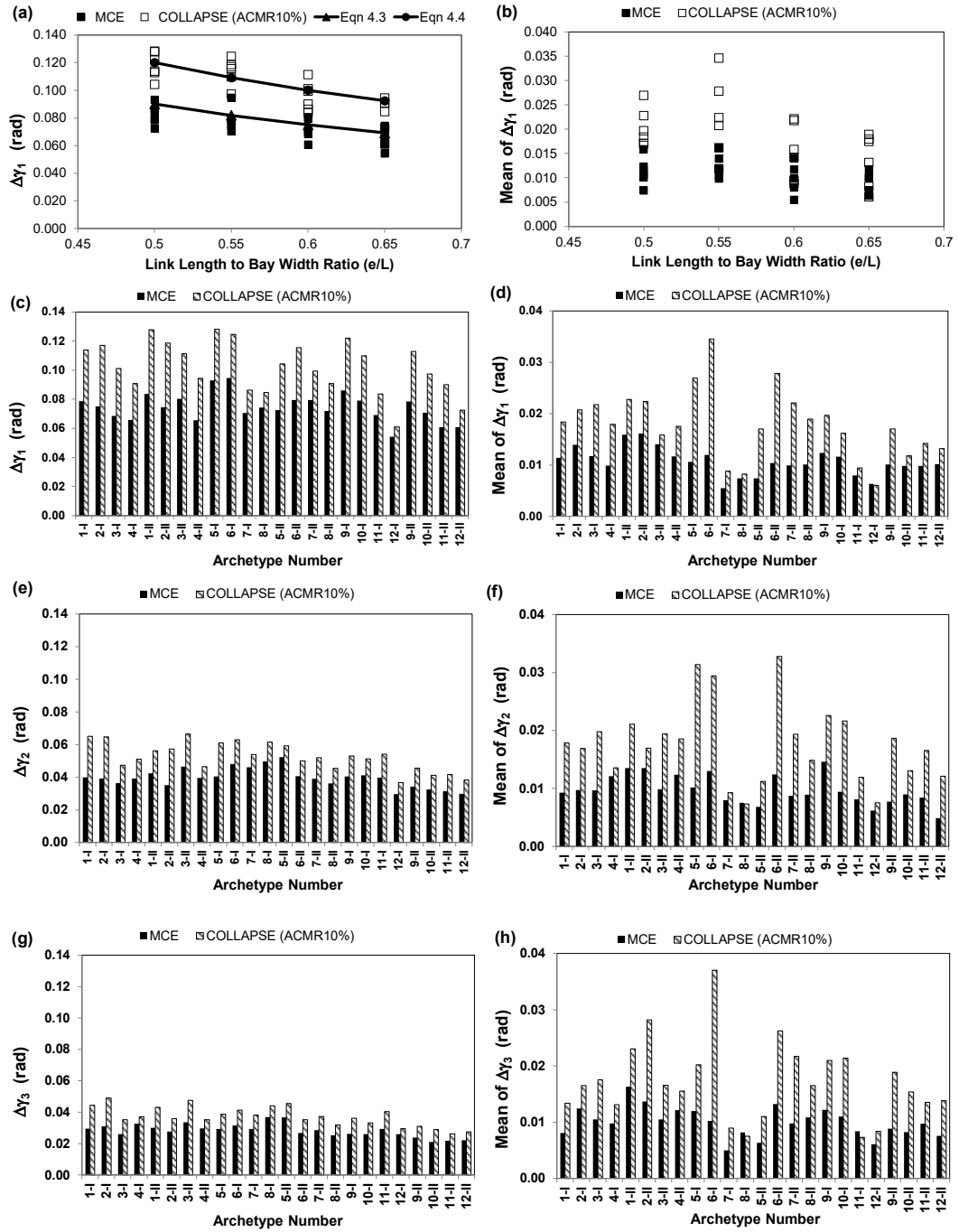


Figure 4.9. Cycle range and mean of cycle range for the three most damaging cycles

The most damaging three cycles ($\Delta\gamma_1$, $\Delta\gamma_2$, $\Delta\gamma_3$) were considered first followed by an in-depth evaluation of the entire cycle distribution. The cycle ranges for all archetypes are given in Figures 4.9.c, 4.9.e, 4.9.g for the most damaging 3 cycles. The cycle means associated with these damaging cycles are given in Figures 4.9.d, 4.9.f, 4.9.h. The statistical measures for the $\Delta\gamma_1$, $\Delta\gamma_2$, $\Delta\gamma_3$ and their mean values are reported in Table 4.5. Under MCE ground motions, the ratios of $\Delta\gamma_2/\Delta\gamma_1$ and $\Delta\gamma_3/\Delta\gamma_1$ are equal to 0.53 and 0.38 respectively. In other words, the amplitude of second cycle is 53% of the most damaging cycle while third cycle has the magnitude of 38% of the first cycle. These values were reported as 0.41 and 0.24 for the short links (Al-Janabi and Topkaya (2020)). The ratios of $\Delta\gamma_2/\Delta\gamma_1$ and $\Delta\gamma_3/\Delta\gamma_1$ do not change significantly if CLE level seismic events are considered. The mean values of $\Delta\gamma_1$, $\Delta\gamma_2$ and $\Delta\gamma_3$ do not show a significant difference among the cycles considered (Table 4.5) for both the seismic hazards. Averages of mean cycle ranges for $\Delta\gamma_1$, $\Delta\gamma_2$ and $\Delta\gamma_3$ were calculated as 0.011 rad, 0.010 rad and 0.010 rad for the MCE level. These values modify to 0.018 rad, 0.018 rad, 0.017 rad for the CLE level.

The complete distribution of the cycle ranges can be represented by making use of the approach proposed by Mergos and Beyer (2014). The most critical link of an archetype was considered as the one having the highest value of DI among all links. The normalized cycle ranges and normalized mean cycle ranges are given in Figures 4.10.a and 4.10.b for MCE and CLE level earthquakes, respectively. The normalized maximum rotation cycle range of long EBF links can be represented as:

$$\frac{\Delta\gamma}{\Delta\gamma_1} = n^{-0.55} \quad (4.5)$$

where n is the cycle number. The power of the cycle number was proposed as -0.90 for short links (Al-Janabi and Topkaya (2020)).

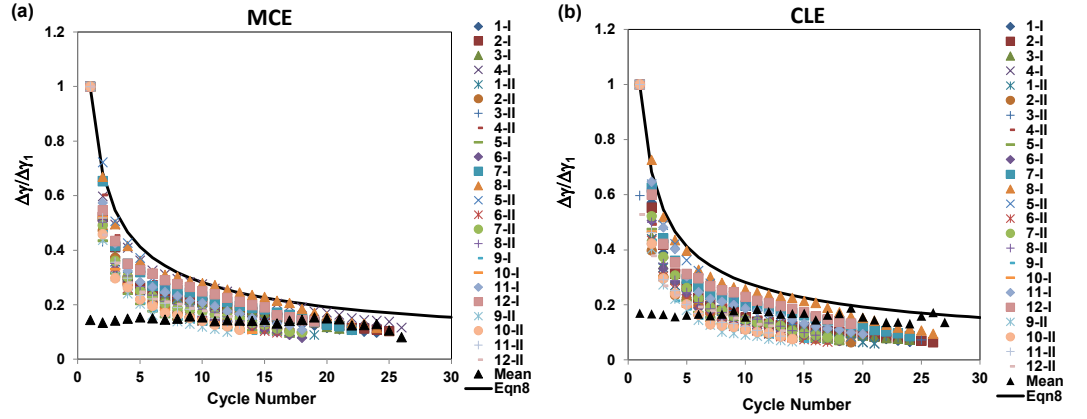


Figure 4.10. Distribution of cycle ranges

4.5 Development of Nonsymmetrical Loading Protocols

The normalized mean cycle ranges for all cycles fall within a narrow band according to the data presented in Figure 4.10. This observation is valid for the two seismic hazards considered in this study. Therefore, the normalized mean cycle range was considered as 0.15 in this study. The loading excursions are expected to alternate around $0.15 \times \Delta\gamma_1$. Al-Janabi and Topkaya (2020) represented the loading protocol for short links as an analytical function. By considering the same approach the loading protocol for long links can be expressed as follows:

$$\gamma_n = \Delta\gamma_1 \times \left(0.15 \pm 0.5 \times (n_{\max} + 1 - n)^{-0.55} \right) \text{ for } n = 1, 2, 3, \dots, n_{\max} \quad (4.6)$$

where n_{\max} is the maximum number of cycles. The maximum numbers of damaging cycles were 19 and 20 under MCE and CLE seismic hazards, respectively (Table 4.4). Therefore, $n_{\max}=20$ was selected for the long link protocol. The maximum number of cycles was considered as 30 for short links; however, the loading protocol can be shortened by applying 15 cycles because the amount of damage does not change significantly for the additional 15 cycles with very low amplitudes (Al-Janabi and Topkaya (2020)). The proposed loading protocol is given in Figure 4.11 in two forms. Figure 4.11.a displays the variation of the normalized link rotation angle for

the 20 cycles. Figure 4.11.b shows a particular example for the case of $e/L=0.6$ under CLE level seismic event, where $\Delta\gamma_1=0.10$ rad according to Equation 4.4.

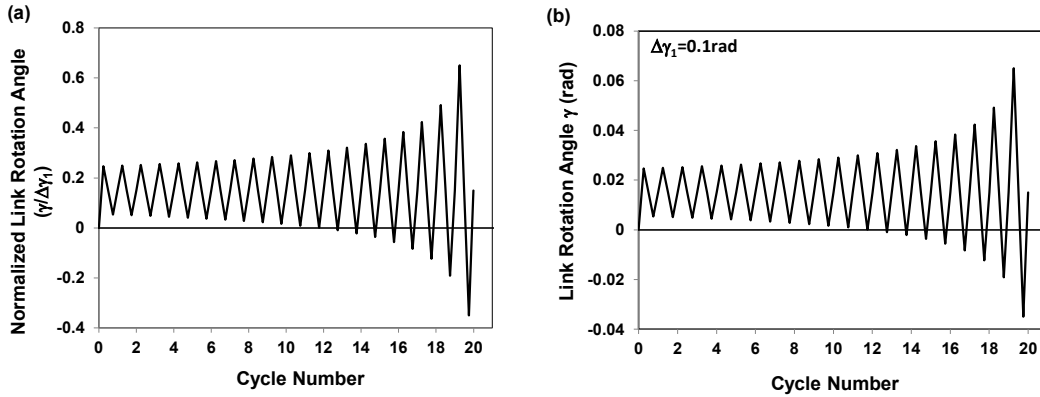


Figure 4.11. Proposed loading protocol for long links

The proposed protocol was compared with the loading protocol proposed by Richards (2004) to identify the differences and similarities. In order to make a fair comparison, the maximum cycle range was selected as $\Delta\gamma_1=0.064$ rad, which was the value considered in the existing loading protocol. The variation of normalized cycle ranges as a function of the ordered cycles is presented in Figure 4.12.a. The proposed protocol is based on 20 cycles while the existing protocol is based on 35 cycles. There is a marked similarity between the two protocols in terms of the change in the normalized cycle ranges. In other words, both the protocols decay in a similar way except that the existing protocol applies 15 additional cycles with $\Delta\gamma/\Delta\gamma_1 < 0.19$. Although additional cycles are required in the existing protocol, their contribution to total damage is quite low. The accumulation of damage with the number of cycles is given in Figure 4.12.b. The proposed protocol produces a damage index of 0.0131 after 20 cycles, whereas the existing protocol produces a damage index of 0.0145 after 35 cycles. Therefore, the proposed protocol and the existing protocol produces similar levels of damage with cycle amplitudes that are similar as well for the 20 most damaging cycles. The proposed nonsymmetrical protocol is less conservative than the existing symmetric protocol for $\Delta\gamma_1=0.064$ because the former imposes similar maximum rotation demand with less cumulative energy dissipation demand

when compared to that of the existing symmetrical protocol. It should be noted that $\Delta\gamma_1=0.064$ rad is rather low compared to what was observed in the present study. According to Figure 4.9.a, only a few archetypes with $0.6 \leq e/L \leq 0.65$ experienced $\Delta\gamma_1 \leq 0.064$ rad under MCE level events. The differences become much more pronounced as CLE level events are considered. The reason for these differences can be attributed to the use of a redundancy factor in the design of archetypes, which essentially reduced the R factor in the former study. If higher values are used ($\Delta\gamma_1 > 0.064$ rad), then the proposed protocol imposes a higher cumulative energy dissipation demand than the existing symmetrical protocol.

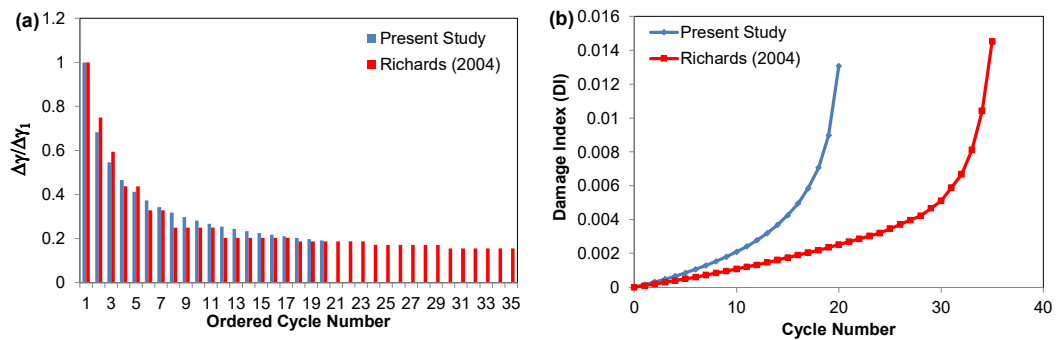


Figure 4.12. Distribution of cycle ranges and accumulation of damage with cycle number

The loading protocols are directly compared with each other in Figure 4.12 for the case of $\Delta\gamma_1=0.064$ rad. Both symmetrical and nonsymmetrical forms of the proposed protocol are presented. In Figure 4.13, the proposed protocol was initiated when the cycle number of Richards protocol equals to 15 (equivalent to $n=1$ in Equation 4.6 for the proposed protocol) considering that any prior cycles have an amplitude equal to zero. The comparisons show that the existing protocol and the proposed protocol are almost identical for the case of $\Delta\gamma_1=0.064$ rad when symmetrical cycles are considered. The protocols differ from each other when the nonsymmetrical nature of loading is considered. While the existing protocol has the most damaging cycle with ± 0.032 rad, the proposed protocol has the most damaging cycle with -0.022 rad and $+0.042$ rad. There are several advantages of the proposed protocol. First of all, the

demands are tailored according to the e/L ratio and the seismic hazard. In addition, the nonsymmetrical nature of loading is taken into account.

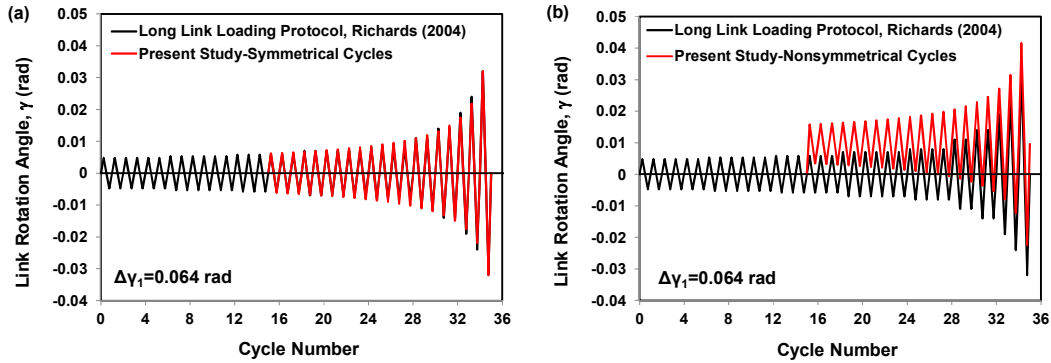


Figure 4.13. Comparison of loading protocols

The Specimen 3 tested by Okazaki et al. (2005, 2007) was considered to compare the link shear versus link rotation behaviors under different loading scenarios. The behavior under the loading protocol proposed by Richards (2004) is given in Figure 4.14.a, while the one under the proposed protocol with symmetrical cycles and $\Delta\gamma_1=0.064$ rad is given in Figure 4.14.b. The behaviors are quite similar except the low amplitude cycles. The response under the proposed nonsymmetrical protocols are given in Figures 4.14.c and 4.14.d for the cases of $\Delta\gamma_1=0.064$ rad and $\Delta\gamma_1=0.10$ rad, respectively. These protocols produce nonsymmetrical demands with higher maximum amount of link rotations (γ_{\max}). In addition, the effects of strength degradation become much more pronounced as the level of γ_{\max} increases.

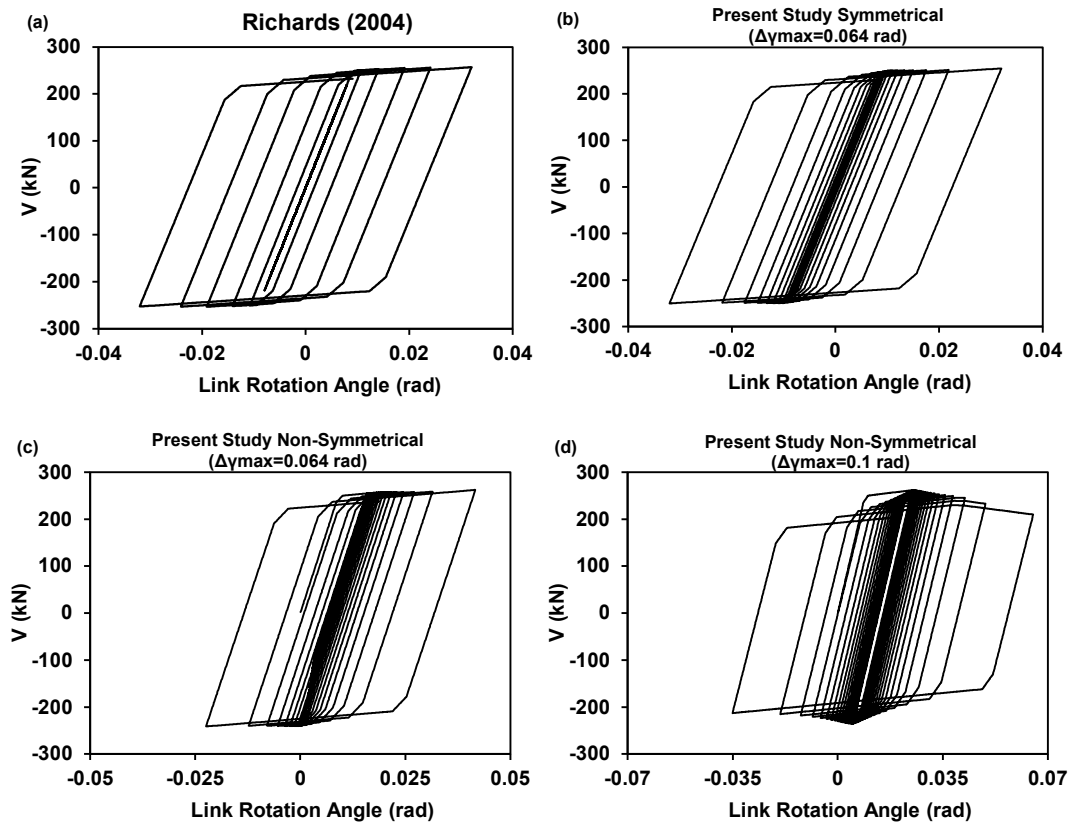


Figure 4.14. Behavior of Specimen 3 under different loading scenarios

4.6 Effects of Column Base Fixity and Link Axial Force

The proposed loading protocol was developed considering long link EBF archetypes with pinned column bases. The archetypes AT1-I, AT4-I, AT5-I, AT8-I, AT9-I, AT12-I (Table 4.2) were reanalyzed with fixed-column bases because the support conditions may influence the collapse mechanism and therefore the cyclic behavior of the links. The member sizes of these archetypes need not be revised due to a modification to the column base condition because the lateral stiffness of EBF structures is mostly influenced by the axial stiffness of braces and columns and the bending stiffness of the floor beam. The number of total cycles, damaging cycles, inelastic cycles, and maximum link rotation (rad) as well as the maximum cycle range of the reanalyzed archetypes were compared with their pin-based counterparts under MCE and CLE seismic events. Table 4.6 shows the statistical information on

the ratio of aforementioned quantities from the fixed archetypes over the pinned ones. The total number of cycles increased on average by 26% and 28% for the MCE and CLE level seismic hazards, respectively. The same values modified to 4% and 10% for the damaging cycles and 14% and 14% for the inelastic cycles. The height-wise variation of maximum LRA is affected by the support conditions where, the pin-based archetypes experience the maximum demand on the first floor while the same demand is experienced at higher floors by the fixed-based archetypes. Modifying the base condition increased the maximum LRA demand by 11% and 2% on average under MCE and CLE seismic events, respectively. The increases in the maximum rotation ranges are 11% and 8% respectively under MCE and CLE level seismic events. It can be concluded that the only major effect of modifying support conditions is on the number of total cycles. Figure 4.15 compares the normalized mean cycle ranges for all cycles for the archetypes AT1-I, AT4-I, AT5-I, AT8-I, AT9-I, AT12-I analyzed under MCE and CLE shaking intensities with both pinned and fixed support conditions. The normalized mean cycle ranges for the first three cycles are 0.13 rad for pin-supported archetypes and 0.11 rad for the fixed supported counterparts. Equation 4.5 is observed to be valid for the archetypes with fixed support conditions. In other words, the proposed loading protocol is applicable to the long link EBF archetypes with both fixed and pinned support conditions.

Table 4.6. The statistical information on the ratio of response quantities (Fixed based archetype over pin-based archetype)

	Total Cycles		Damaging Cycles		Inelastic Cycles		Maximum Link Rotation (rad)		$\Delta\gamma_1$	
	MCE	CLE	MCE	MCE	CLE	MCE	MCE	CLE	MCE	CLE
Av.	1.26	1.28	1.04	1.26	1.28	1.04	1.11	1.02	1.11	1.02
St.D.	0.12	0.10	0.11	0.12	0.10	0.11	0.24	0.25	0.24	0.25
Max	1.41	1.44	1.19	1.41	1.44	1.19	1.35	1.32	1.35	1.32
Min	1.15	1.18	0.93	1.15	1.18	0.93	0.69	0.70	0.69	0.70

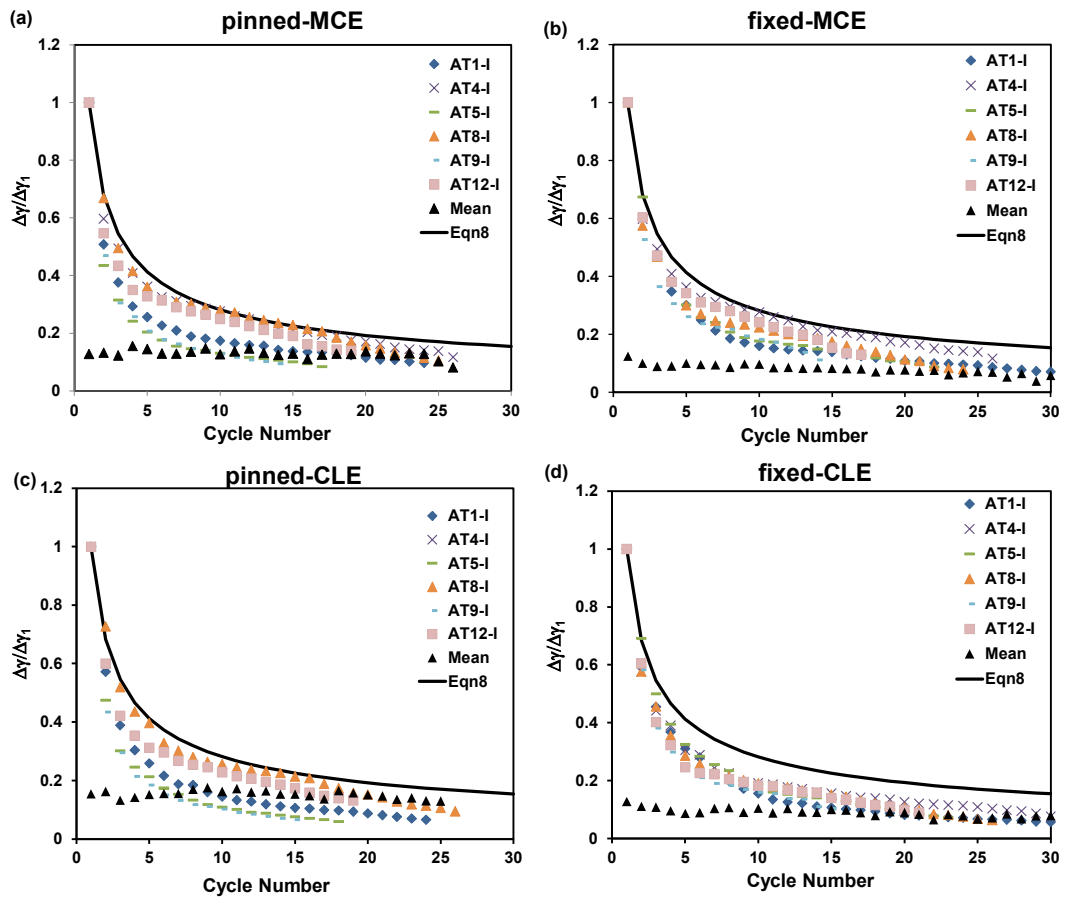


Figure 4.15. Comparisons of the distribution of normalized cycle ranges of pin-based and fixed based archetypes

Past researches revealed that axial loads developed in the EBF links can have an effect on the overall behavior, especially on the overstrength and ultimate plastic rotation. Manganiello et al. (2021) investigated the effect of boundary conditions on very short and short EBF links and concluded the presence of axial restraints increases the overstrength factors by 15% on average. On the contrary, they verified that the boundary conditions do not have an important influence in terms of overstrength and the ultimate rotation for the intermediate links. Della Corte et al. (2013) also carried out a numerical and analytical study on the overstrength of shear links and they have concluded that the axial forces developed in the short links are non-negligible when the link experiences significant plastic deformations. In this study, the order of magnitude of the axial loads developed in long EBF links was investigated. Figure 4.16 shows the variation of normalized link axial forces (axial force divided by the axial yield capacity (P/P_y)) for 6 story FP-I (9m bay) archetypes under CLE10% seismic event. The results show that P/P_y ratio of the links varied between 0.003 and 0.027 for different e/L ratios and maximum P/P_y ratios were 0.027, 0.023, 0.008 and 0.005 for AT5-I, AT6-I, AT7-I and AT8-I respectively. The amount of axial load developed in the long links reduces with increasing e/L ratio. Although the influence of axial forces is non-negligible for the short EBF links; the effect of axial force can be considered negligible for long links. Therefore, no additional requirements are needed to impose any axial loads during the testing of long links.

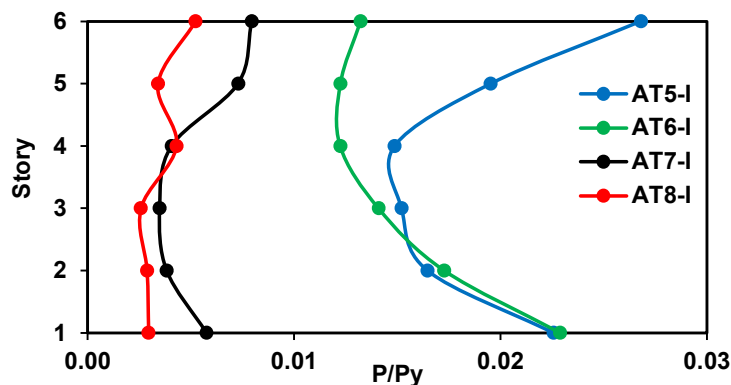


Figure 4.16. Normalized link axial forces for 6 story FP-I archetypes

4.7 Future Research Needs

Bozkurt et al. (2019) conducted low-cycle fatigue tests in order to recommend a damage law for short EBF links. Al-Janabi and Topkaya (2020) calculated the damage indexes for short links according to the low-cycle damage law proposed by Bozkurt et al. (2019) and concluded that short link archetypes with $e/L \leq 0.12$ should be avoided in practice; otherwise the damage indexes would be greater than unity under both MCE and CLE seismic events. AISC341 (2016) defines the inelastic rotation limit for long links as 0.02 rad. This codified limit was developed for design-based earthquakes (DBE) and is expected to be exceeded under MCE and CLE level seismic events. When the maximum inelastic rotation exceeds 0.02 rad, the link behavior can be considered satisfactory if the damage index is proved to be lower than unity. Unfortunately, there exists no known damage law developed for the low-cycle fatigue life of long links in the literature. A low-cycle damage law for long EBF links should be developed in the future. The findings of this study can be used together with this damage law to define the acceptable range of e/L ratio. Precautions should be taken at the design stage in order to reduce $\Delta\gamma_1$ if the damage index of the long links exceeds unity for any given e/L ratio.

The numerical study conducted in Chapter 3 is to evaluate the seismic response of EBFs with long links using FEMA P695 methodology and concluded that none of their archetypes with $e/L=0.35, 0.40, 0.45$ and 0.50 were satisfactory under CLE10% level seismic events. As a remedy, several options were proposed. The first option is, avoiding e/L ratios smaller than 0.65 so that the maximum LRA is kept at acceptable levels under different seismic events. If the use of large e/L ratios is architecturally not applicable, modifying the codified response modification coefficient (using $R=4$) or using stocky link sections which reduces the amount of link deterioration can be considered as alternative options. Kuşyılmaz and Topkaya (2015) presented a numerical study on displacement amplification factors for short, intermediate and long link EBFs. They have concluded that the existing design rules can result in greater LRA values than the design limits. They proposed a

displacement amplification factor (C_d) that varies along the height of the structure. The maximum amount of link rotation angle can be reduced to codified limits by making use of the proposed C_d . Although the aforementioned options provide consistency between the rotation capacity and the demand; they would also introduce additional design effort and an increase in the overall cost of the system. Therefore, cost effective alternatives should be developed to achieve consistency between the maximum link rotation and the codified limit.

4.8 Summary

In this study, a nonsymmetrical loading protocol for long links was developed. Twenty-four long link EBF archetypes with variable floor plans, bay widths, number of stories and link length to bay width (e/L) ratios were designed according to the US standards. The responses of EBFs under maximum considered earthquake (MCE) and collapse level earthquake (CLE) were obtained by making use of numerical analysis employing degrading link models. The link rotation angle time histories were reduced and converted into a series of cycles and the peaks of the LRA response were identified by using the rainflow counting algorithm. The nonsymmetrical loading protocol was represented as a function of maximum rotation range, which depends on the seismic hazard and e/L ratio. A number of future research needs has been identified.

CHAPTER 5

CONCLUSIONS

Three independent studies were conducted on short- and long- link EBFs in the scope of this thesis. In the first part, the effects of strain hardening ratio (*SHR*) on the performance of EBFs with short links by using FEMA P-58 methodology. A comprehensive numerical evaluation of the seismic response of EBFs with long links was presented in the second part. A nonsymmetrical loading protocol was developed in the last part of this thesis. The conclusions of each independent study are presented in the following subsections.

5.1 Conclusions on the Effects of Cyclic Strain Hardening on the Performance of Eccentrically Braced Frames

The effects of post-hardening slope (strain hardening ratio – *SHR*) on the seismic performance assessment of EBF buildings were studied. The investigation required calibration of numerical models, development of a database for *SHR* and a parametric study on archetype EBF buildings.

The shear force versus deformation response with *SHR*=0.002 and proposed by Richards and Uang (2004, 2006) was considered to model the behavior of shear links. The numerical model that adopts this approach was evaluated using the pseudo-dynamic test results of the DUAREM structure. The comparisons showed that the numerical model was able to capture the response, where the maximums of the response quantities are estimated with 10% deviation from the experimental observations.

Based on a survey conducted as a part of this study, it was demonstrated that the *SHR* significantly depends on the grade of steel material, type of steel component and the

structural system. The response of the DUAREM structure was analyzed under different seismic hazards (DBE, MCE, CLE) for SHR ranging between 0 and 0.01. The EDP that is most affected by SHR was found to be the residual interstory drift ratio (RIDR). The responses get more sensitive to SHR as the seismic hazard increases.

Performances of six archetype buildings were evaluated by making use of FEMA P-58 (2018) methodology and considering the 3 seismic hazards. The archetypes differed in the number of stories, link length-to-bay width ratio (e/L) and the SHR . The variation of EDPs as a function of seismic hazard and the SHR are given. The repair costs for all seismic hazard levels were found to be insensitive to the SHR when the residual drifts are not considered in the seismic performance assessment. On the other hand, the SHR was found to significantly influence the repair cost, as for some cases a total replacement was deemed necessary due to large residual frame drift. In general, an increase in the SHR results in a decrease in the residual frame drifts. The repair costs depend significantly on the SHR , seismic hazard level, number of stories and e/L ratio. The results showed that while the residual drifts are more sensitive to SHR for higher ground motion intensities, the repair costs were relatively insensitive. In other words, almost all of the 3-, 6- and 9-story archetypes with $SHR \leq 0.003$ and subjected to MCE and CLE level events required replacement. On the other hand, replacement can be avoided when $SHR > 0.003$ for some of the archetypes. The responses under DBE level seismic events were found to be more sensitive to SHR . While all 3-story archetypes did not require replacement, some of the 6- and 9-story archetypes had to be replaced depending on the value of SHR and the e/L ratio. The study demonstrated the strong influence and sensitivity of the repair cost to the SHR .

The results showed that the SHR value must be carefully selected for the seismic performance assessment of EBF system especially when the response under DBE level events is considered. Engineers must be aware of the consequences of selecting different SHR values. The SHR was found to be quite variable for the link investigated experimentally in the past. A database of link tests should be developed

to more accurately determine the statistical distribution of *SHR*. This will enable a probabilistic evaluation of performance assessment of EBFs taking into account the variability of *SHR*.

The study was limited to EBFs where the link is a horizontal member placed in between the ends of braces. Other EBF geometries with vertical links and links attached to columns require further investigation. The findings of the study can be extended to other steel lateral load resisting systems. The same methodology adopted in this study can be used to investigate the effects of *SHR* on the seismic performance of different structural systems. In addition, the same methodology can be applied with different modelling techniques which will help to investigate the model sensitivity of the results.

5.2 Conclusions on the Seismic Performance Evaluation of Eccentrically Braced Frames with Long Links using FEMA P695 Methodology

Twenty-four EBF archetypes with long links were designed by considering the bay width (9m and 6m), number of stories (3-,6-,9-stories), the e/L ratio (0.35, 0.40, 0.45, 0.50) as the variables. The seismic responses of these archetypes were evaluated by making use of the FEMA P695 (2009) methodology. The archetypes were subjected to MCE, CLE20% and CLE10% level seismic hazards to obtain median link rotation angle (LRA) demands from 44 ground motions. The ultimate rotation capacity of the long links was defined as 0.06 rad, based on the recommendations of ASCE 41-17 (2017) and the experiments on long links. The effects of degradation were investigated by comparing the responses of degrading and non-degrading long link models. For the degrading model, modified IMK deterioration model was adopted. The link rotation histories of degrading and non-degrading models as a function of e/L ratio, seismic intensity, bay width, number of stories are presented. The following can be concluded from this study:

- The importance of modeling deterioration while performing numerical analyses of long link EBFs was highlighted. The results showed that strength and stiffness degradation increases the link rotation angle as much as 46 percent. The amount of increase was found to depend significantly on the e/L ratio. Degradation effects are more pronounced as the e/L ratio decreases. The average amount of increase in the LRA was 13 percent for all the archetypes considered in this study.
- Links with $e/L < 0.50$ should be avoided in practice for acceptable performance under CLE20% level seismic hazards. None of the archetypes were found satisfactory under CLE10% level seismic hazards.
- Design using $e/L = 0.5$ is recommended for pin-based EBFs with long links. Choosing this ratio does not adversely affect the mass and cost of framing and results in acceptable link rotation angle demands.
- Design of EBFs with long links using a response modification coefficient of $R = 4$ can result in acceptable performance for EBFs with $e/L = 0.5$ subjected to CLE10% level seismic events. This alternative, however, was not found feasible due to the excessive increase in the frame weight and cost.
- Selecting link beams with stocky webs can be considered as a remedy to decrease the link rotation angle demands. This alternative was found to be unfeasible as well due to the increase in the frame weight and cost.
- Under CLE10% level seismic events, EBFs with $e/L = 0.65$ were found to provide satisfactory behavior with link rotations slightly exceeding the limit.
- Providing fixed column bases was found to be an effective solution in reducing the link rotation angle demands especially for 9-story EBFs with $e/L = 0.5$. Base fixity, however, cannot be relied upon to reduce the level of link rotations to acceptable levels when all archetypes were considered.
- The effect of gravity framing was found to reduce the level of link rotation angle demands particularly for 9- and 6-story EBFs. On the other hand, the link rotations cannot be reduced to acceptable levels by making use of the strength and stiffness of gravity framing.

The study was limited to EBFs designed according to the US provisions. Future research should extend the findings to EBFs designed according to other specifications which were not considered herein. The study considered the effects of gravity framing to a limited degree. Additional studies are required to investigate the effect of gravity framing in more detail and the effects of adopting a dual system of EBFs and MRFs.

5.3 Conclusions on the Development of a Loading Protocol for Long Links in Eccentrically Braced Frames

A numerical study was undertaken to develop loading protocols that can be used in the performance evaluation of long links in EBFs. The study followed the procedure adopted by Al-Janabi and Topkaya (2020) which was used to develop loading protocols for short links. Twenty-four EBF archetypes with different bay widths, number of stories and e/L ratios were designed and analyzed under MCE and collapse level seismic events to obtain median link rotation angle (LRA) demands from 44 ground motions. The numerical modeling technique included strength and stiffness degradation for the long links by adopting modified IMK deterioration model. The link rotation time history responses were processed by making use of the rainflow counting algorithm to identify the loading cycles, their mean values and amplitudes. The study demonstrated the importance of mean effects in the loading history. A nonsymmetrical loading protocol was developed and is represented by an analytical function given in Equation 4.6. This function requires the range of the most damaging cycle ($\Delta\gamma_1$), which was represented by Equations 4.3 and 4.4, for MCE and collapse level events, respectively. $\Delta\gamma_1$ was found to depend on the seismic hazard and the e/L ratio.

The proposed loading protocol was compared with an existing general symmetrical loading protocol developed by Richards (2004). The symmetrical parts of these two protocols were found to be very similar for the case of $\Delta\gamma_1=0.064$ rad, with the existing protocol requiring 15 more low amplitude cycles to be applied. The

proposed protocol provides the advantage of tailoring the demands according to the e/L ratio and seismic hazard and also accounts for the mean effects.

REFERENCES

- AISC. 2016. Seismic Provisions for Structural Steel Buildings. American Institute of Steel Construction. ANSI/AISC 341-16. Chicago, IL.
- AISC. Specification for structural steel buildings. American Institute of Steel Construction. ANSI/AISC 360-16. Chicago, IL. 2016.
- Akkar, S., Sandıkkaya, M.A., Şenyurt, M., Azari, Sisi A., Ay, B.Ö., Traversa, P., Douglas, J., Cotton, F., Luzi, L., Hernandez, B., Godey, S. (2014). Reference database for seismic ground-motion in Europe (RESORCE) Bulletin of Earthquake Engineering, DOI: 10.1007/s10518-013-9506-8, 12 (1) ,v 11-339.
- Al-Janabi, M.A.Q., Topkaya, C. 2020. Nonsymmetrical loading protocols for shear links in eccentrically braced frames. Earthquake Engng. Struct. Dyn., 49, 74-94.
- Al-Janabi, M.A.Q., Topkaya, C. 2021. Seismic performance of eccentrically braced frames designed to AISC341 and EC8 specifications. Structures, 29, 339-359.
- American Society of Civil Engineers and Structural Engineering Institute (ASCE/SEI). 2016. Minimum Design Loads for Buildings and Other Structures ASCE7, American Society of Civil Engineers, Reston, VA.
- Arce, G. 2002. Impact of higher strength steels on local buckling and overstrength of links in eccentrically braced frames. Thesis for Master's Degree. University of Texas at Austin: Department of Civil, Architectural and Environmental Engineering.
- Arifin, F.A. 2017. Identification of Cost-Effective Retrofit and/or Rehabilitation Strategies for Steel Buildings. Thesis for Master's Degree. University of Canterbury: Department of Civil and Natural Resources Engineering.

- Arifin, F.A., Sullivan, T.J., MacRae, G., Kurata, M., Takeda, T. 2021. Lessons for Loss Assessment from the Canterbury Earthquakes: a 22 storey Building. *Bulletin of Earthquake Engineering*, <https://doi.org/10.1007/s10518-021-01055-7>
- Ariyaratana, C., Yakhchalian, M., Mohebi, B. 2020. Evaluation of approximate methods for estimating residual drift demands in BRBFs. *Engineering Structures*. 224(2020): 110849.
- ASCE. 2017. Seismic evaluation and retrofit of existing buildings, American Society of Civil Engineers, ASCE/SEI 41-17 Virginia, VA.
- ASCE. 2017. Design loads on buildings and other structures. American Society of Civil Engineers, ASCE/SEI 7-16. Reston. 2017.
- Asgarkhani, N., Fahnestock, L.A. 2011. Evaluation of buckling-restrained braced frame seismic performance considering reserve strength. *Engineering Structures*, 33(2011): 77-89.
- ATC. 1992. Guidelines for Cyclic Seismic Testing of Components of Steel Structures for Buildings, ATC-24. Applied Technology Council, California.
- Behr, R.A., Belarbi, A. 1996. Seismic Test Methods for Architectural Glazing Systems. *Earthq Spectra*, 12(1), 129– 143.
- Berman, J.W., Bruneau, M. 2008. Tubular links for eccentrically braced frames. II: experimental verification. *J. Struct. Eng. ASCE*. 134 (5), 702–712.
- Black, G.R., Wenger, B.A., Popov, E.P. 1980. Inelastic buckling of steel struts under cyclic load reversals. UCB/EERC-80/40, Earthquake Engineering Research Center, Berkeley, Calif.

- Bojórquez, E., Ruiz-García, J. 2013. Residual drift demands in moment-resisting steel frames subjected to narrow-band earthquake ground motions. *Earthquake Engineering and Structural Dynamics*, 42:1583-1598.
- Bosco, M., Marino, E.M., Rossi, P.P. 2014. Proposal of modifications to the design provisions of Eurocode 8 for buildings with split K eccentric braces. *Eng. Struct.*, 61, 209–223.
- Bosco, M., Rossi, P.P. 2013. A design procedure for dual eccentrically braced systems: numerical investigation. *J. Constr. Steel Res.*, 80, 453–464.
- Bosco, M., Marino, E.M., Rossi, P.P. 2015. Modelling of steel link beams of short, intermediate or long length. *Eng Struct.*, 84, 406–418.
- Bozkurt, M.B., Topkaya, C. 2018. Replaceable links with gusseted brace joints for eccentrically braced frames. *Soil Dynamics and Earthquake Engineering*, 115 (June), 305–318.
- Bozkurt, M.B., Kazemzadeh Azad, S., Topkaya, C. 2018. Low-cycle fatigue testing of shear links and calibration of a damage law. *J Struct Eng.*, 144(10), 04018189-1–04018189-20
- Building Research Institute Japan Iron and Steel Federation. 2002. *Testing Methods of the Evaluation of Structural Performance for the Steel Structures*.
- Cardone, D., Perrone, G. 2015. Damage and Loss Assessment of Pre-70 RC Frame Buildings with FEMA P-58: A Case Study. Second ATC & SEI conference on improving the seismic performance of existing buildings and other structures, p. 363–74.
- Carreño, R., Lotfizadeh, K.H., Conte, J.P., Restrepo, J.I. 2020. Material Model Parameters for the Giuffrè-Menegotto-Pinto Uniaxial Steel Stress-Strain Model. *Journal of Structural Engineering*, 146(2): 04019205.

- Carr, A.J. 2005. Ruaumoko program for inelastic dynamic analysis: User manual, Dept. of Civil Engineering, Univ. of Canterbury, Christchurch, New Zealand.
- Chegeni, B., Mohebkhah, A. 2014. Rotation capacity improvement of long link beams in eccentrically braced frames. *Sci Iran*. 21 (3), 516–524.
- Chen, H., Bai, J. 2022. Loading Protocols for Seismic Performance Evaluation of Buckling-Restrained Braces in RC Frames. *J Build Eng.*, 45, 103522.
- Christopoulos, C., Pampanin, S., Priestley, M.J.N. 2003. Performance-Based Seismic Response of Frame Structures Including Residual Deformations. Part I: Single-Degree of Freedom Systems. *Journal of Earthquake Engineering*, 7:1: 97-118.
- Clark, P., Frank, K., Krawinkler, H., Shaw, R. 1997. Protocol for Fabrication, Inspection, Testing and Documentation of Beam-Column Connection Tests and Other Experimental Specimens. Report No. SAC/BD-97/02, Steel Project Background Document.
- Cofie, N.G., Krawinkler, H. 1985. Uniaxial cyclic stress-strain behavior of structural steel. *ASCE Journal of Engineering Mechanics*, 111(9): 1105-1120.
- Cook, D., Fitzgerald, K., Chrupalo, T., Haselton, C.B. 2017. Comparison of FEMA P-58 With Other Building Seismic Risk Assessment Methods.
- Cook, D.T., Liel, A.B., DeBock, D.J., Haselton, C.B. 2021. Benchmarking FEMA P-58 repair costs and unsafe placards for the Northridge Earthquake: Implications for performance-based earthquake engineering. *International Journal of Disaster Risk Reduction*, 56(October 2020), 102117.
- Cremen, G., Baker, J.W. 2018. Quantifying the benefits of building instruments to FEMA P-58 rapid post-earthquake damage and loss predictions. *Engineering Structures*, 176(July), 243–253.

- Dafalias, Y.F., Popov, E.P. 1975. A model for nonlinearly hardening materials for complex loading. *Acta Mechanica*, 21, 173-192.
- Daneshmand, A., Hashemi, B.H. 2012. Performance of intermediate and long links in eccentrically braced frames. *J. Constr. Steel Res.*, 70, 167–176.
- Danku, G., Dubina, D., Ciutina, A. 2013. Influence of steel-concrete interaction in dissipative zones of frames: II-numerical study. *Steel Compos. Struct.*, 15 (3),323–342.
- Dehgani, M., Tremblay, R. 2012. Standard Dynamic Loading Protocols for Seismic Qualification of BRBFs in Eastern and Western Canada. 15th World Conference on Earthquake Engineering, Lisbon.
- Del Gobbo, G.M., Williams, M.S., Blakeborough, A. 2018. Seismic performance assessment of Eurocode 8-compliant concentric braced frame buildings using FEMA P-58. *Engineering Structures*, 155, 192–208.
- Dusicka, P., Itani, A., Buckle, I. 2007. Cyclic response of plate steels under large inelastic strains, *J. Constr. Steel Res.*, 63, 156–164.
- Dusicka, P., Lewis, G. 2010. Investigation of replaceable sacrificial steel links. Proceedings of the 9th US National and 10th Canadian Conference on Earthquake Engineering, Toronto, Canada.
- Elkady, A., Lignos, D.G. 2015. Effect of gravity framing on the overstrength and collapse capacity of steel frame buildings with perimeter special moment frames. *Earthquake Eng. Struct. Dyn.*. 44 (8),1289-1307.
- EN1993-1-8. Eurocode 3. 2005. Design of steel structures. part 1-8: design of joints, European Committee for Standardization, Brussels, Belgium.
- EN-12512. 2005. Timber structures-test methods. Cyclic testing of joints made with mechanical fasteners, European Committee for Standardization, Brussels.

- Engelhardt, M.D., Popov, E.P. 1989. Behavior of long links in eccentrically braced frames, Earthquake Engineering Research Center, University of California, Berkeley, CA, Report No. UCB/EERC-89/01.
- Engelhardt, M.D., Popov, E.P. 1992. Experimental performance of long links in eccentrically braced frames. *J Struct Eng. ASCE*, 118 (11), 3067–3088.
- Erochko, J., Christopoulos, C., Tremblay, R., Choi, H. 2011. Residual Drift Response of SMRFs and BRB Frames in Steel Buildings Designed according to ASCE 7-05. *Journal of Structural Engineering*, 137(5): 589-599.
- Eurocode 8. 2004. Design of structures for earthquake resistance - part 1: general rules, seismic actions and rules for buildings, EN 1998-1, European Committee for Standardization.
- Fakhraddini, A., Hamed, S., Fadaee, M.J. 2019. Peak displacement patterns for the performance-based seismic design of steel eccentrically braced frames. *Earthq. Eng. Vib.*, 18(2), 379–393. <https://doi.org/10.1007/s11803-019-0510-0>
- Fang, C., Ping, Y., Chen, Y. 2020. Loading protocols for experimental seismic qualification of members in conventional and emerging steel frames. *Earthquake Engng Struct Dyn.*, 49, 155-174.
- FEMA. 2000. State of the art report on systems performance of steel moment frames subject to earthquake ground shaking: FEMA 355C. Washington DC.
- FEMA. 2007. Interim protocols for determining seismic performance characteristics of structural and non-structural components through laboratory testing: FEMA-461. Federal Emergency Management Agency, Washington.
- FEMA. 2018. Seismic Performance Assessment of Buildings Volume 1-Methodology. FEMA P-58. Second Edition. Washington DC.

- FEMA. 2009. Quantification of building seismic performance factors. Building Seismic Safety Council for the Federal Emergency Management Agency. FEMA P695. Washington, DC.
- Flores, F.X., Charney, F.A., Lopez-Garcia, D. 2014. Influence of the gravity framing system on the collapse performance of special steel moment frames. *J. Constr. Steel Res.* 101, 351–362.
- Flores, F.X., Charney, F.A., Lopez-Garcia, D. 2016. The influence of gravity column continuity on the seismic performance of special steel moment frame structures. *J Constr Steel Res.*, 118: 217–230.
- Gade, V.P., Sahoo, D.R. 2016. Evaluation of Collapse-Resistance of Special Truss Moment Frames as per FEMAP695 Approach. *Engineering Structures*, 126, 505–515.
- Ghassemieh, M., Sokhtesaraei, M.H., Akbarpour, H. 2021. Development of a New Cyclic Loading Protocol for Seismic Performance Assessment of Steel Moment Connections. *J Earthq Eng.*, DOI: 10.1080/13632469.2021.1991514
- Ghobarah, A., Ramadan, T. 1991. Seismic analysis of links of various lengths in eccentrically braced frames. *Can. J. Civ. Eng.*, 18 (1), 140–148.
- Ghowsi, A.F., Sahoo, D.R. 2019. Effect of Loading History and Restraining Parameters on Cyclic Response of Steel BRBs. *International Journal of Steel Structures*. 19(4), 1055–1069.
- Ghowsi, A.F., Sahoo, D.R. 2013. Seismic Performance of Buckling-Restrained Braced Frames with Varying Beam-Column Connections, *Journal of Steel Structures*, 13(4), 607–621.
- Gray, M.G., de Oliveira, J.C., Christopoulos, C., Binder, J.I. 2014. Effects of Post-Yield Stiffening and Strengthening on the Collapse Performance of Non-Buckling Braced Frames. *Proceedings of the 10th National Conference in Earthquake Engineering*, Earthquake Engineering Research Institute, Anchorage, AK.

- Guerrero, H., Terán-Gilmore, A., Ji, T., Escobar, J.A. 2017. Evaluation of the economic benefits of using Buckling-Restrained Braces in hospital structures located in very soft soils. *Eng Struct.*, 136:406–19.
- Guerrero, H., Ji, T., Teran-Gilmore, A., Escobar, J.A. 2016. A method for preliminary seismic design and assessment of low-rise structures protected with Buckling-Restrained Braces. *Engineering Structures*. 123:141–54.
- Gulec, C.K., Gibbons, B., Chen, A., Whittaker, A.S. 2011. Damage states and fragility functions for link beams in eccentrically braced frames. *J. Constr. Steel Res.*, 67(9), 1299–1309.
- Güner, T., Topkaya, C. 2020. Performance Comparison of BRBFs Designed Using Different Response Modification Factors. *Engineering Structures*, Vol. 225, 111281.
- Hamauzu, S., Skalomenos, K.A. 2021. Cyclic Behavior of Tubular Steel Columns with High Yield-to-Tensile Strength Ratio under Asymmetric Loading Protocols. *ce/papers*, Nos. 2 – 4.
- Hamburger RO, Rojahn C, Heintz JA, Mahoney MG. FEMA P58 : Next-generation building seismic performance assessment methodology. *Proceedings of the 15th World Conference on Earthquake Engineering*. 10, 10. 2012.
- Haris, S., Nidiasari Putri S.T.P. 2020. Numerical study of bracing section variations in an eccentrically braced frame. *E3S Web of Conferences* 156, 05012. <https://doi.org/10.1051/e3sconf/202015605012>.
- Hines, E.M., Appel, M.E., Cheever, P.J. 2009. Collapse performance of low-ductility chevron braced steel frames in moderate seismic regions. *Eng. J. AISC*, Third Quarter:149-180.

- Hjelmstad, K.D., Popov, E.P. 1983. Seismic behavior of active beam link in eccentrically braced frames. Earthquake Engineering Research Center, University of California, Berkeley, CA, Report No. UCB/EERC-83/15.
- Hjelmstad, K.D., Popov, E.P. 1983. Cyclic behavior and design of link beams. *J. Struct. Eng. ASCE*, 109 (10), 2387–2403.
- Hoveidae, N., Tremblay, R., Rafezy, B., Davaran, A. 2015. Numerical investigation of seismic behavior of short-core all-steel buckling restrained braces. *Journal of Constructional Steel Research*. 114(2015): 89-99.
- Hutchinson, T.C., Zhang, J., Eva, C. 2011. Development of a Drift Protocol for Seismic Performance Evaluation Considering a Damage Index Concept. *Earthq Spectra*, 27(4), 1049-1076.
- Ibarra, L.F., Krawinkler, H. 2005. Global collapse of frame structures under seismic excitations. The John A. Blume Earthquake Engineering Center, Stanford University, Stanford, CA. Rep. No. TB 152.
- Ibarra, L.F., Medina, R.A., Krawinkler, H. 2005. Hysteretic models that incorporate strength and stiffness deterioration. *Earthquake Eng. Struct. Dyn.*, 34(12), 1489–1511.
- Imanpour, A., Auger, K., Tremblay, R. 2016. Seismic design and performance of multi-tiered steel braced frames including the contribution from gravity columns under in-plane seismic demand. *Adv. Eng. Softw.*, 101, 106-122.
- International Code Council (ICC). 2000. International Building Code. International Code Council, Inc., Whittier, Calif.
- Ioan, A., Stratan, A., Dubina, D, Poljansek, M., Molina F.J., Taucer, F. Pegon, P., Sabau G. 2016. Experimental validation of re-centring capability of eccentrically braced frames with removable links. *Eng. Struct.*, 113, 335-346.

- Iraj, H.P., Mamaghani, T., Usami, T., Mizuno, E. 1996. Inelastic large structural steel cyclic loading. *Engineering Structures*, 18(9): 659-668.
- Jain, A., Koboevic, S., Redwood, R. 1996. Design and behavior of eccentrically braced frames with flexural links. In: *Advances in Steel Structures (ICASS '96)*, Proceeding of International Conference on Advances in Steel Structures, Hong Kong. 233–237.
- Jalali, A., Daie, M., Nazhadan, S.V.M., Kazemi-Arbat, P., Shariati, M. 2012. Seismic performance of structures with pre-bent strips as a damper. *International Journal of the Physical Sciences*, 7 (26), 4061–4072.
- Jarrett, J.A., Judd, J. P., Charney, F.A. 2015. Comparative evaluation of innovative and traditional seismic-resisting systems using the FEMA P-58 procedure. *J. Constr. Steel Res.*, 105, 107–118.
- Ji, X., Kato, M., Wang, T., Hitaka, T., Nakashima, M. 2009. Effect of gravity columns on mitigation of drift concentration for braced frames. *J. Constr. Steel Res.* 65, 2148–2156.
- Jiao, Y., Kishiki, S., Yamada, S. 2012. Loading Protocols Employed in Evaluation of Seismic Behavior of Steel Beams in Weak-Beam Moment Frames. 15th World Conference on Earthquake Engineering, Lisbon.
- JRain. Jesmond Engineering Ltd. 2013.
- Kasai, K., Popov, E.P. 1986. General Behavior of WF Steel Shear Link Beams, *J. Struct. Eng. ASCE*. 112 (2), 362-382.
- Kawashima, K., MacRae, G.A., Hoshikuma, J.I., Nagaya, K. 1998. Residual Displacement Response Spectrum. *Journal of Structural Engineering*, 124 (5):523-530.
- Kelly, J. M. 1997. *Earthquake-resistant design with rubber*, 2nd Ed., Springer, New York.

- Khorami, M., Khorami, M., Alvansazyazdi, M., Shariati, M., Zandi, Y., Jalali, A., Tahir, M.M. 2017. Seismic performance evaluation of buckling restrained braced frames (BRBF) using incremental nonlinear dynamic analysis method (IDA). *Earthquake and Structures*, 13 (6), 531–538.
- Khorami, M., Khorami, M., Motahar, H., Alvansazyazdi, M., Shariati, M., Jalali, A., Tahir, M.M. 2017. Evaluation of the seismic performance of special moment frames using incremental nonlinear dynamic analysis. *Structural Engineering and Mechanics*, 63 (2), 259–268.
- Koboevic, S., Rozon, J., Tremblay, R. 2012. Seismic Performance of Low-to-Moderate Height Eccentrically Braced Steel Frames Designed for North American Seismic Conditions. *Journal of Structural Engineering*, 138 (12), 1465-1476.
- Krawinkler, H., Parisi, F., Ibarra, L., Ayoub, A., Medina, R. 2001. Development of a Testing Protocol for Woodframe Structures. CUREE. publication No. W-02.
- Krawinkler, H. 2009. Loading Histories for Cyclic Tests in Support of Performance Assessment of Structural Components. In: *Proceedings of the 3rd International Conference on Advances in Experimental Structural Engineering*, Pacific Earthquake Engineering Research Center, San Francisco, USA.
- Kuşyılmaz, A., Topkaya, C. 2013. Design overstrength of steel eccentrically braced frames. *Int J Steel Struct.*, 13 (3), 529-545.
- Kuşyılmaz, A., Topkaya, C. 2016. Evaluation of Seismic Response Factors for Eccentrically Braced Frames using FEMA P695 Methodology. *Earthq. Spectra.*, 32 (1), 303–321.
- Labeled, A., Benmansour, T., Abu Halaweh, A.M.I. 2020. A numerical investigation of the inelastic cyclic behaviour of short and long links designed according to RPA 99 provisions. *Asian J Civ Eng.*, 21(2), 217–228.

- Lamarche, C.P., Tremblay, R. 2008. Accounting for residual stresses in the seismic stability of nonlinear beam-columns elements with cross-section fibre discretization. Structural Stability Research Council (SSRC) - Proceedings of the 2008 Annual Stability Conference, (pp. 59-78). Nashville
- Lamarche, C.P., Tremblay, R. 2010. Experimental and Numerical Study on the Potential for Column Size Reduction in Capacity Designed Multi-Story Braced Steel Frames. Proceedings of the 9th U.S National and 10th Canadian Conference in Earthquake Engineering, Toronto, Ontario, Canada.
- Lignos, D.G., Krawinkler, H. 2009. Sidesway collapse of deteriorating structural systems under seismic excitations. The John A. Blume Earthquake Engineering Center, Stanford University, Stanford, CA. Rep. No. TB 172.
- Lignos, D.G., Krawinkler, H. 2011. Deterioration modeling of steel components in support of collapse prediction of steel moment frames under earthquake loading. J Struct Eng. ASCE, 137(11), 1291-1302.
- Liu J, Astaneh-Asl A. Cyclic testing of simple connections including effects of slab. J Struct Eng ASCE 2000; 126 (1): 32-39
- MacRae, G.A., Kimura, Y., Roeder, C. 2004. Effect of column stiffness on braced frame seismic behavior. J. Struct. Eng., ASCE 130 (3), 381-391.
- Mahdavi-pour, M.A., Deylami, A. 2014. Probabilistic assessment of strain hardening ratio effect on residual deformation demands of Buckling-Restrained Braced Frames. Engineering Structures, 81(2014):302-308.
- Majdi, A., Isa-Said, A., Vacareanu, R., Obied, W. 2021. Earthquake loss estimation for an educational reinforced concrete building by using FEMA P-58 methodology. IOP Conference Series: Earth and Environmental Science, 664(1).

- Malakoutian, M., Berman, J.W., Dusicka, P. 2013. Seismic response evaluation of the linked column frame system. *Earthquake Engng Struct Dyn.*, 42, 795-814.
- Malley, J.O., Popov, E.P. 1984. Shear Links in Eccentrically Braced Frames, *J. Struct. Eng, ASCE.*, 110 (9), 2275-2295.
- Mansouri, A. 2021. Development of a novel haunched link for eccentrically braced frames. *Eng. Struct.* 245: 112870.
- Mazzoni, S., McKenna, F., Scott, M.H., Fenves, G.L. 2006. Open system for earthquake engineering simulation (OpenSees) user command language manual. Berkeley: Pacific Earthquake Research Center, University of California.
- McCormick, J., Aburano, H., Ikenaga, M., Nakashima, M. 2008. Permissible Residual Deformation Levels for Building Structures Considering Both Safety and Human Elements. *Proceedings of the 14th World Conference on Earthquake Engineering*, Beijing, China.
- Mergos, P.E., Beyer, K. 2014. Loading Protocols for European Regions of Low to Moderate Seismicity. *B Earthq Eng.*, 12, 2507-2530.
- Merrit, S., Uang, C.M., Benzoni, G. 2003. Subassemblage testing of core brace bucklingrestrained braces. La Jolla (California): University of California, San Diego; 2003.
- Mohammadrezapour, E., Danesh, F. 2018. Experimental investigation of bolted link-to-column connections in eccentrically braced frames. *J. Constr. Steel Res.*, 147, 236–246.
- Mohammadrezapour, E., Danesh, F. 2020. Experimental and numerical study of semi-rigid connection for long link-to-column joints. *Proceedings of the Institution of Civil Engineers: Structures and Buildings.* 173 (7), 488–500.

- Mohebkah, A., Chegeni, B. 2014. Overstrength and rotation capacity for EBF links made of European IPE sections. *Thin Wall Struct*, 74, 255–260.
- Mondkar D.P., Powell G.H. 1975. ANSR-I general purpose program for analysis of nonlinear structural response. Rep. EERC 75-37, Earthquake Research Center, College of Engineering, University of California, Berkeley, CA.
- Naghipour, M., Javadi, N., Naghipour, A. 2011. Investigation of RBS connection ductility in eccentrically braced frame. *Proceedings of the Twelfth East Asia-Pacific Conference on Structural Engineering and Construction - EASEC12*, Hong Kong, 743–752.
- Naserifar, A., Danesh, F. 2018. Experimental study on the behavior of EBFs with reduced link sections. *16th European Conference on Earthquake Engineering Thessaloniki*, 18-21 June, 2018.
- Okazaki, T. 2004. Seismic Performance of link-to-column connections in steel eccentrically braced frames. PhD Thesis, Department of Civil Engineering, University of Texas at Austin, Austin, TX.
- Okazaki, T., Arce, G, Ryu, H.C., Engelhardt, M.D. 2005. Experimental study of local buckling, overstrength, and fracture of links in eccentrically braced frames. *J Struct Eng ASCE*, 131 (10), 1526-1535.
- Okazaki, T., Engelhardt, M.D., Nakashima, M., Suita, K. 2006. Experimental performance of link-to-column connections in eccentrically braced frames. *J Struct Eng ASCE*, 132 (8), 1201–1211.
- Okazaki, T., Engelhardt, M.D. 2007. Cyclic loading behavior of EBF links constructed of ASTM A992 steel. *J Constr. Steel Res.*, 63 (6), 751–765.
- Okazaki, T., Engelhardt, M.D., Drolas, A., Schell, E., Hong, J.K., Uang, C.M. 2009. Experimental investigation of link-to-column connections in eccentrically braced frames. *J Constr Steel Res.*, 65 (7), 1401–1412.

- O'Reilly, G.J., Sullivan, T.J. 2016. Direct displacement-based seismic design of eccentrically braced steel frames. *J Earthq Eng*, 20, 243-278.
- Özhendekci, D., Özhendekci, N. 2008. Effects of the frame geometry on the weight and inelastic behaviour of eccentrically braced chevron steel frames. *J. Constr. Steel Res.*, 64 (3), 326–343.
- Özkılıç, Y.O. 2022. Interaction of flange and web slenderness, overstrength factor and proposed stiffener arrangements for long links. *J. Constr. Steel Res.*; 190:107150.
- Pandikkadavath, M.S., Sahoo, D.R. 2016. Analytical Investigation on Cyclic Response of Buckling-Restrained Braces with Short Yielding Core Segments. *International Journal of Steel Structures*, 16(4), 1273–1285.
- Pandikkadavath, M.S., Sahoo, D.R. 2017. Mitigation of Seismic Drift Response of Braced Frames Using Short Yielding-Core BRBs. *Steel and Composite Structures*, 23(3), 285–302.
- Papadopoulos, A.N., Vamvatsikos, D., Kazantzi, A.K. 2019. Development and application of FEMA P-58 compatible story loss functions. *Earthquake Spectra*, 55 (1), 95–112.
- Popov, E.P., Engelhardt, M.D. 1988. Seismic eccentrically braced frames. *J. Constr. Steel Res.*, 10, 321–354.
- Popov, E.P., Engelhardt, M.D., Ricles, J.M. 1989. Eccentrically braced frames: US Practice. *Eng. J. AISC*. 26 (2), 66-80.
- Porter, M.L. 1987. Sequential Phased Displacement (SPD) Procedure for TCCMAR Testing. In: 3rd Meeting of the Joint Technical Coordinating Committee on Masonry Research US-Japan coordinated program.

- Prakash, V., Powell, G.H. 1993. DRAIN-2DX, DRAIN-3DX and DRAIN BUILDING: Base program design documentation. Rep. UCB/ SEMM-93/17, Univ. of California, Berkeley, CA.
- Prasai, A. 2021. Numerical Simulation Study of Ten Steel Eccentrically Braced Frames and Evaluating Its Resilience using FEMA P-58 Procedure. MS Thesis, University of Maryland, College Park.
- Rahnama, M., Krawinkler, H. 1993. Effect of soft soils and hysteresis models on seismic design spectra. Rep. No. TB 108, The John A. Blume Earthquake Engineering Center, Stanford Univ., Stanford, CA.
- Ramadan, T., Ghobarah, A. 1991. Prediction of the ultimate capacity of wide flange link beams under cyclic loading. *Comput Struct.* 40 (2), 409–418.
- Ramadan, T., Ghobarah, A. 1995. Analytical model for shear-link behavior. *J. Struct. Eng. ASCE*, 121 (11), 1574-1580.
- Rathje, E.M., Dawson, C., Padgett, J.E., Pinelli, J-P., Stanzione, D., Adair, A., Arduino, P., Brandenberg, S.J., Cockerill, T., Dey. C., Esteva, M., Haan,, Jr. F.L., Hanlon, M., Kareem, A., Lowes. L., Mock. S., Mosqueda, G. 2017. DesignSafe: A new cyberinfrastructure for natural hazards engineering. *Nat Hazards Rev ASCE*, 18(3), 06017001. doi:10.1061/(ASCE)NH.1527-6996.0000246.
- Raza, S., Tsang, H.H., Menegon, S.J., Wilsin, J.L. 2021. Generalized Loading Protocols for Experimentally Simulating Multidirectional Earthquake Actions on Building Columns in Regions of Low-to-Moderate Seismicity. *J Struct Eng.*, 147(7), 04021082.
- Razavi, S.A., Siahpolo, N., Adeli, M.M. 2020. A new empirical correlation for estimation of EBF steel frame behavior factor under near-fault earthquakes using the genetic algorithm. *J. Eng.* 2020, 1-13. <https://doi.org/10.1155/2020/3684678>.
- Richards, PW. 2004. Cyclic stability and capacity design of steel eccentrically braced frames. Ph.D. dissertation. La Jolla (CA, USA): University of California, San Diego.

- Richards, P.W., Uang CM. 2006. Testing protocol for short links in eccentrically braced frames, *J. Struct. Eng. ASCE*, 132(8): 1183-1191.
- Roeder, C.E., Popov, E.P. 1977. Inelastic behavior of eccentrically braced steel frames under cyclic loading. University of California, Berkeley, UCB/EERC-77/18.
- Roeder, C.W., Popov, E.P. 1978. Cyclic shear yielding of wide-flange beams. *J. Eng. Mech. Div. ASCE*, 104 (4), 763–780.
- RSMeans Online Square foot estimator. [Online]. Available: <https://www.rsmeans.com/>. [Accessed: 09-Feb-2020].
- Sabau, G.A., Polijanšek, F.T., Pagon, P., Molina, F.J., Tirelli, D., Viaccoz, B., Stratan, A., Chesoon, A.I., Dubinã, D. 2014. DUAREM Full-scale experimental validation of dual eccentrically braced frame with removable links. JRC Science and Policy Reports: Seismic Engineering Research Infrastructures for European Synergies, Italy.
- Sabelli, R., Mahin, S., Chang, C. 2003. Seismic demands on steel braced frame buildings with buckling-restrained braces. *Eng Struct*, 25, 655-666.
- Sahoo, D.R., Chao, S-H. 2015. Stiffness-Based Design for Mitigation of Residual Displacements of Buckling-Restrained Braced Frames. *Journal of Structural Engineering*, 141(9), 04014229.
- Saldana, D. 2018. Simplified Analysis Response Models for SCBF and BRBF Compliant With FEMA P-58 Simplified Procedures. MS thesis California State University, Long Beach, December, 2018.
- Sani, H.P., Gholhaki, M., Banazadeh, M. 2018. Simplified direct loss measure for seismic isolated steel moment-resisting structures. *Journal of Constructional Steel Research*, 147, 313–323.

- Shariati, M., Ghorbani, M., Naghipour, M., Alinejad, N., Toghroli, A. 2020. The effect of RBS connection on energy absorption in tall buildings with braced tube frame system. *Steel and Composite Structures*, 34(3), 393–407.
- Shen, C., Tanaka, Y., Mizuno, E., Usami, T. 1992. A two-surface model for steels with yield plateau. *Japan Society of Civil Engineers, Structural Engineering and Earthquake Engineering*, 8(4): 179-188.
- Shen, C., Mamaghani, I.H.P., Mizuno, E., Usami, T. 1995. Cyclic behavior of structural steels II-theory. *ASCE Journal of Engineering Mechanics*, 121(11): 1165-1172.
- Silva, A., Macedo, L., Monteiro, R., Castro, J.M. 2020. Earthquake-induced loss assessment of steel buildings designed to Eurocode 8. *Eng Struct.*, 208(October 2019): 110244.
- Sullivan, T., Asisi, F.A., MacRae, G.A., Kurata, M., Takeda, T. 2018. Cost-effective consideration of non-structural elements: Lessons from the Canterbury earthquakes. *16th European Conference on Earthquake Engineering*, pp: 1–12.
- Suswanto, B., Amalia, A.R., Wahyuni, E., Wilson, J. 2017. Numerical behavior study of short link, intermediate link and long link in eccentrically braced frame steel structure. *Int. J. Appl. Eng. Res.*, 12(21), 11460–11471.
- Suswanto, B., Amalia, A.R., Wahyuni, E., Al Farisy, N. 2018. Comparison of WF & tubular links on the eccentrically brace frame system due to cyclic loads. *Int J. Adv. Sci. Eng. Inf. Technol.*, 8(3), 799–804. <https://doi.org/10.18517/ijaseit.8.3.4337>.
- Suzuki, Y., Lignos, D.G. 2020. Development of Collapse-Consistent Loading Protocols for Experimental Testing of Steel Columns. *Earthquake Engineering & Structural Dynamics*. 49(2), 114-131.

- Tirca, L., Gioncu, V. 1999. Ductility demands for MRFs and LL-EBFs for different earthquake types. *Proceedings of the Stability and Ductility of Steel Structures (SDSS'99)*, 429–438.
- Tong, L., Zhang, Y., Zhou, X., Keivan, A., Li, R. 2019. Experimental and Analytical Investigation of D-Type Self-Centering Steel Eccentrically Braced Frames with Replaceable Hysteretic Damping Devices. *Journal of Structural Engineering*, 145 (1), 04018229.
- Tremblay, R., Bolduc, P., Neville, R., DeVall, R. 2006 Seismic Testing and Performance of Buckling Restrained Bracing Systems. *Canadian Journal of Civil Engineering*, 33 (1), 183–198
- Uriz, P., Filippou, F.C., Mahin, S.A. 2008. Model for Cyclic Inelastic Buckling of Steel Braces. *Journal of Structural Engineering*, 134 (4), 619-628.
- Usami, T., Gao, S., Ge, H. 2000. Elastoplastic analysis of steel members and frames subjected to cyclic loading. *Engineering Structures*, 22: 135-145.
- Wang, Y.B., Li, G.Q., Cui, W., Chen, S.W., Sun, F.F. 2015. Experimental Investigation and Modeling of Cyclic Behavior of High Strength Steel. *Journal of Constructional Steel Research*, 104(2015): 37-48
- Xu, Z., Zhang, H., Lu, X., Xu, Y., Zhang, Z., Li, Y. 2019. A prediction method of building seismic loss based on BIM and FEMA P-58. *Autom Constr.* 102(February): 245–57.
- Zienkiewicz, OC. 1977. *The finite element method*" (3rd edn) McGraw-Hill, New York
- Zimbru, M., D'Aniello, M., Stratan, A., Landolfo, R., Dubină, D. 2017. Numerical investigation of composite detachable short links *Composite Construction in Steel and Concrete VIII - Proceedings of the 8th International Conference on Composite Construction in Steel and Concrete*, 678.699.

Zimbru, M., D'Aniello, M., Stratan, A., Landolfo, R., Dubina. 2017 Finite element modelling of detachable short links D. COMPDYN 2017 - Proceedings of the 6th International Conference on Computational Methods in Structural Dynamics and Earthquake Engineering, 2017, 1, pp. 790-199-699.

Zimbru, M., D'Aniello, M., Stratan, A., Landolfo, R. Dubină, D.Finite. 2018. element analysis of composite replaceable short links Key Engineering Materials, 763, 576-583.

CURRICULUM VITAE

PERSONAL INFORMATION

Surname, Name: Ün, Elif Müge
Nationality: Turkey
Date and Place of Birth: 25 July 1988, Amasya, Turkey
Marital Status: Married
Email: elifun88@yahoo.com

EDUCATION

Degree	Institution	Year of Graduation
MSc	METU Civil Engineering	2011
BSc	METU Civil Engineering	2009
High School	TED Ankara College	2005

EXPERIENCE

Year	Place	Enrollment
2009-2011	METU Department of Civil Engineering	Research Assistant
2012	Northeastern University	Teaching Assistant
2013-2015	PROMER Cons. Eng. Inc.	Structural Engineer
2017-	METU Department of Civil Engineering	Research Assistant

FOREIGN LANGUAGES

Turkish (Native), English (Fluent)

PUBLICATIONS

1. Ün EM, Erberik MA, Askan A. "Performance assessment of Turkish residential buildings for seismic damage and loss estimation", Journal of Performance of Constructed Facilities, 29(2):04014063 (2015).
2. Ün EM., Topkaya C. "Effects of cyclic strain hardening on performance of eccentrically braced frames", Journal of Constructional Steel Research, 187:106948 (2021)

3. Ün EM., Al-Janabi MAQ., Topkaya C. "Seismic performance evaluation of eccentrically braced frames with long links using FEMA P695 methodology", *Engineering Structures*, 258:114104 (2022)
4. Al-Janabi MAQ., Ün EM., Topkaya C. "Development of a loading protocol for long links in eccentrically braced frames", *Journal of Constructional Steel Research*, 193:107278 (2022)